A Numerical and Experimental Investigation of Free-Cylinder Stirling Engine Operation

Douglas Ian Bank

A thesis submitted to the Faculty of Engineering, University of the Witwatersrand, Johannesburg, in fulfilment of the requirements for the degree of Doctor of Philosophy.

Johannesburg, April 25, 1994

Declaration

I declare that this thesis is my own, unaided work. It is being submitted for the Degree of Doctor of Philosophy in the University of the Witwatersrand, Johannesburg. It has not been submitted before for any degree or examination in any other University.

D M Bard

29th day of April 1994

Abstract

A numerical and experimental investigation of free-cylinder Stirling engines is reported. This work evolved from an attempt to develop a particular free-cylinder Stirling engine concept, such that commercial manufacture and application as the power source for a water pump could be considered. Available design tools were not directly applicable to the engine being considered. The linear analysis technique (coupled with second order heat transfer, thermodynamic and loss analysis) developed and implemented as a computer programme by D M Berchowitz was therefore extended to allow the simulation of free-cylinder engines. The solution procedure follows a more generalized form than that adopted by Berchowitz. As a result symbolic manipulation and solution of the equations was impractical. However numerical root map generation and the simple production of force vector diagrams allows useful design information to be obtained.

Experimental work was carried out on two very different machines. A Sunpower free-cylinder Stirling engine prototype yielded disappointing results, as the engine did not run satisfactorily. However the data gathered provides a useful check of the general applicability of the coupled analysis method. The second engine, a modified Sunpower Model B-10 Demonstrator yielded motion and pressure data over a wide range of operating conditions. The effects of changes in parameters such as the case–ground spring stiffness, displacer spring stiffness, case mass, charge pressure, hot-end temperature and load were explored. Agreement between experimental results and simulation results using the coupled analysis is reasonable, particularly when one considers the wide range of operating conditions over which the comparison is made.

Acknowledgements

The advice, encouragement and friendship of my supervisors, Professor Costa Rallis and Dr Harald Jawurek is greatly appreciated. William Beale and members of Sunpower Inc., allowed me to spend a short period of intense learning in the stimulating Sunpower environment during the early part of this research. Sunpower Inc. supplied both the engines on which the experimental work reported here was carried out. Finally, the SAUCE programme, developed by David Berchowitz and other members of the Sunpower team provided a solid base for the development of the free-cylinder analysis presented in this work.

Thanks are also extended to the Structural Dynamics unit of the University for the loan of the hydraulic ram and control system. A variety of people assisted with advice, particularly in the setting up and trouble-shooting of experimental rigs. I would particularly like to thank Charles Constancon, Don Kilgour, Paul Roberts, George Gibbon, Mike Nethersole and the Mechanical Engineering Workshops team. Mr Bateman of Plascoat Engineering assisted with the Teflon coating of seal surfaces.

This work is part of a wider on-going experimental and theoretical programme on Stirling engines being conducted in the School of Mechanical Engineering of the University. This has been partially funded over the years by the Anglo American Corporation of South Africa and by the Foundation for Research Development. The Foundation for Research Development and the University assisted with study bursaries. Their assistance is gratefully acknowledged.

I was employed by Wits Rural Facility, of the University of the Witwatersrand, for a period of 30 months halfway through the work reported here. Although this slowed progress considerably, they provided important financial assistance, and allowed me sufficient time at the main campus and through undergraduate project supervision to continue the development of the second experimental rig.

Finally I would like to thank my wife, Hélène, and my parents Jane and Ian Banks for their love and support.

Contents

Declaration i

Abstract ii

Acknowledgements iii

Contents iv

List of Figures xii

List of Tables xx

List of Symbols xxii

1 Introduction 1

1.1 Objectives of the study 1

1.1.1 Thesis structure 2

1.2 The Stirling engine 2

1.3 Some Stirling engine types and projects 6

1.3.1 An older generation 6

1.3.2 The Philips initiative 7

1.3.3 Modern kinematic engines suitable for application in rural areas . . . 8
1.3.4 Hybrid engines . . . 9
1.3.5 Free-piston Stirling engines . . . 12
1.3.6 Free-cylinder Stirling engines . . . 14
1.3.7 Fluidyne engines . . . 15
1.4 Summary . . . 17

2 The free-cylinder Stirling engine **18**
2.1 The Sunpower free-cylinder Stirling engine . . . 19
2.1.1 Case (or cylinder) . . . 19
2.1.2 Piston and centering port cylinder . . . 21
2.1.3 Displacer . . . 22
2.1.4 Centering ports . . . 22
2.1.5 Gas springs (or bounce spaces) . . . 22
2.2 Possible heat sources for a free-cylinder engine . . . 23
2.2.1 Solar concentrator and tracker . . . 23
2.2.2 Gas burner . . . 25
2.2.3 Solid fuel . . . 27
2.3 Water pump designs . . . 28
2.3.1 Induced flow pump . . . 28
2.3.2 Down-well pump . . . 29
2.3.3 Sprag clutch system . . . 31
2.4 Other applications . . . 31
2.5 Summary . . . 32

3 Free-cylinder Stirling engine analysis 34

3.1 Linear dynamics approach 40

3.1.1 Closed-form solutions 47

3.2 Thermodynamic, heat transfer and parasitic loss analysis 49

3.2.1 Work-space pressure vector 50

3.2.2 Adiabatic analysis 53

3.2.3 Heat transfer analysis 54

3.3 The spring matrix 55

3.3.1 Gas springs 56

3.3.2 Work-space gas pressure 58

3.3.3 Case-ground spring 60

3.4 The damping matrix 60

3.4.1 Simple friction losses 61

3.4.2 Bounce-space hysteresis loss 63

3.4.3 Pumping losses 65

3.4.4 Work-space hysteresis loss 68

3.4.5 Displacer appendix gap loss 69

3.4.6 Seal leakage losses 70

3.4.7 A note of caution 71

3.4.8 Power delivered to load 71

3.5 The mass matrix 73

3.6 Use of the 3-D SAUCE programme as a design tool 74

3.6.1 Sensitivity and optimization using the full simulation . . 74

3.6.2 Using the root maps as a design tool 75

3.6.3 Force vector plots 81

4 Experimental results: 'water pump' engine 84

4.1 Apparatus 84

4.1.1 Drive unit and supporting frame 84

4.1.2 Instrumentation 87

4.1.3 Data capture 89

4.1.4 Routine data processing 90

4.2 Typical engine performance 92

4.2.1 Absolute motion of the engine components 93

4.2.2 Relative motion of components 94

4.2.3 Force between case and ram 96

4.2.4 Pressure–volume diagrams 97

4.2.5 Phase angles 99

4.2.6 Work flow paths 99

4.3 Performance curves 102

4.3.1 Amplitude ratios 103

4.3.2 Phase angles 106

4.3.3 Indicated work 107

4.4 Possible engine performance 107

4.5 Summary: 'Water pump' engine experimental and simulation results 113

5 Experimental results: Model B-10 engine 114

5.1 Introduction 114

5.1.1 B-10 engine 116

5.1.2 Instrumentation 116
5.1.3 Data processing methods 119
5.1.4 Data presentation 121
5.2 A detailed look at one test 121
5.2.1 Derived data 123
5.2.2 Profile of the complete test 131
5.3 Presentation and discussion of general results 135
5.3.1 Variation of hot-end temperature and charge pressure . . 135
5.3.2 High pressure tests 136
5.3.3 Series BE16N tests 140
5.3.4 Series BE19N tests 149
5.4 Summary 154

6 Simulation of the B-10 engine 160

6.1 Introduction 160
6.1.1 Approximations and assumptions 161
6.2 Simulation of series BE09N tests 162
6.3 High pressure tests 165
6.4 Simulation of the series BE16N tests 173
6.4.1 Unstable engine operation 176
6.4.2 Test BE16N27 177
6.5 Simulation of series BE19N tests 177
6.6 Summary 179

7 Closure 180

7.1 Conclusions 180
7.1.1 3-D linear dynamics simulation of free-cylinder Stirling engines (3-D SAUCE) 180
7.1.2 Sunpower prototype free-cylinder Stirling engine 181
7.1.3 Model B-10 Demonstrator engine as a free-cylinder Stirling engine 181
7.1.4 Free-cylinder Stirling engine as a power source for a rural water pump 182
7.2 Recommendations for further work 182
7.2.1 3-D Linear dynamics approach 182
7.2.2 Free-cylinder Stirling engines 183

A Instrumentation: 'water pump' engine 184

A.1 Displacement transducers 184
A.1.1 Case motion 184
A.1.2 Displacer and piston motion 185
A.2 Force between case and ram 185
A.3 Pressure transducers 186
A.3.1 Bounce-space pressure 186
A.3.2 Work-space pressure 187
A.4 Computer-scope card 187
A.5 Temperature measurement 187

B Apparatus and methods: Model B-10 188

B.1 Apparatus 188
B.1.1 Model B-10 engine 188
B.1.2 Engine heat source 188

B.1.3 Cooling 190
B.1.4 Load device 190
B.1.5 Mechanical springs 190
B.2 Instrumentation 194
B.2.1 Motion data 194
B.2.2 Pressure transducers 198
B.2.3 Force transducer 198
B.2.4 Temperature measurement 198
B.3 Data capture 198
B.3.1 Synchronization of the recording devices 199
B.4 Routine data processing 200
B.4.1 Translation of the video data 200
B.4.2 Translation of the computer-scope data 203
B.4.3 Motion data conditioning 204
B.4.4 Synchronization 205
B.4.5 Least squares analysis 206

C Computer simulations **209**

C.1 Engine data 209
C.2 'Water pump' engine 209
C.3 Model B-10 engine 211

D Model B-10 simulation: equation modifiers **214**

D.1 Bounce-space spring and damping coefficient calculation 214
D.2 Heat exchanger friction losses: sensitivity to gap dimension and eccentricity 215

D.3 Investigation of the force balance method 220

E Regenerator effectiveness calculation **230**

F Copy of publication **233**

F.1 Errata 233

References **241**

List of Figures

1.1 Simple Stirling engine configuration 3

1.2 Stirling water pump: Housed in the private Stirling machine collection of Ms K Chagnot of Athens, Onio 6

1.3 Stirling Technology Incorporated stationary Stirling engine. . . . 9

1.4 A drawing produced by Senft [49] based on Ossian Ringbom's 1907 patent 10

1.5 Rallis Stirling engine 11

1.6 Schematic diagram of a free-piston Stirling engine 13

1.7 Combination wood stove/solid-fuel Stirling engine. [5, p 268] . . 14

1.8 Free-cylinder water pump 15

1.9 Fluidyne Engine 16

2.1 System block diagram 19

2.2 Schematic drawing of 'water pump' free-cylinder Stirling engine 20

2.3 Small free-cylinder Stirling engine water pump and inflated Mylar collector mounted on a z-crank tracking mechanism. 24

2.4 Constant pressure digester built at the Mathabela homestead, Acornhoek, RSA 27

2.5 Integral induction pump design concept 29

2.6 Cable linked induction pump design concept [35] 30

2.7 Inertia pump design concept 31

2.8 Sprag clutch drive (Redrawn from [6]) 32

3.1 The two halves of a free-cylinder Stirling engine simulation process 35

3.2 Location of roots of characteristic equation in the complex plane. 44

3.3 Root locus map, for values of D_{cg} from 150 to 400 Ns/m 46

3.4 Real component of above plotted roots versus D_{cg} 46

3.5 Simulation of FCSE: flow chart 48

3.6 Temperature distribution and volume space labels: Isotherma analysis (Redrawn from Urieli & Berchowitz [57, p 21]). 51

3.7 The displacer-piston friction loss 61

3.8 Regenerator gas flow losses 66

3.9 Effect of work-space gas hysteresis losses on pressure phase angle 69

3.10 Root map showing effect of increasing displacer gas spring volume 77

3.11 Close up of figure 3.10 77

3.12 Real component of roots plotted against D_{cg} (region of interest only) 78

3.13 Approximate amplitudes of oscillation: root map technique . . . 79

3.14 Approximate phase angles: root map technique 79

3.15 Root locus map showing condition in which engine is unstable for all values of D_{cg}. 80

3.16 Displacer force polygon 82

3.17 Piston force polygon 82

3.18 Case force polygon 83

4.1 'Water pump' engine, with instrumentation and burner, mounted on the hydraulic shaker. 86

4.2 Displacer displacement transducer mounting 88

4.3 Absolute motion of 'water pump' engine components 93

4.4 Phasor representation of experimental and simulation results. . . 95

4.5 Phasor representation of relative motion, volumes and pressures 95

4.6 Motion of piston and displacer relative to the case 96

4.7 Case force versus case motion 97

4.8 Pressure–volume diagram 98

4.9 Piston amplitude/case amplitude versus frequency: nitrogen . . 104

4.10 Piston amplitude/case amplitude versus frequency: helium . . . 104

4.11 Displacer amplitude/piston amplitude versus frequency: nitrogen 105

4.12 Displacer amplitude/case amplitude versus frequency: nitrogen . 105

4.13 Displacer–piston relative motion phase angle versus frequency . 106

4.14 Displacer (d) and piston (p) absolute motion phase versus frequency: nitrogen 108

4.15 Displacer (d) and piston (p) absolute motion phase versus frequency: helium 108

4.16 Output work ratio $((-\oint f_{sc} dx_c)/X_o)$ versus piston phase: helium 109

4.17 Indicated and measured works versus frequency: nitrogen 110

4.18 Indicated and measured works versus frequency: helium 111

4.19 Engine power and efficiency as a function of case amplitude . . . 112

4.20 Load damping coefficient versus case amplitude 112

4.21 Engine frequency versus case amplitude 113

5.1 Drawing of B-10 engine before modification 115

5.2 Photograph of Model B-10 free-cylinder rig 117

5.3 B-10 engine mounted such that free-cylinder motion is possible . 118

5.4 Instrumentation block diagram 119

5.5 Calibrated data and sine wave approximation: low load condition 122

5.6 Calibrated data and sinusoidal approximation: high load condition 124

5.7 Absolute motion phasors, low and high load condition 126

5.8 Relative motion phasors, low and high load condition 126

5.9 Volume and pressure phasors, low and high load condition . . . 127

5.10 pV diagram for low and high load conditions: Test BE16N27 . . 128

5.11 Measured data for complete test BE16N27 132

5.12 Further results for test BE16N27 133

5.13 Variance expressed as a percentage of the relevant amplitude ($\frac{\varepsilon \times 100}{|X|}$) for test BE16N27 134

5.14 Engine power as a function of temperature difference and charge pressure. 137

5.15 Engine frequency as a function of temperature difference and charge pressure 137

5.16 Amplitudes of motion as a function of temperature difference and charge pressure 138

5.17 Motion phase angles as a function of temperature difference and charge pressure 138

5.18 Output power versus load damping coefficient 139

5.19 Motion and force phasors, magnitude increases with increased D_{lc} 141

5.20 Relative motion and expansion and compression space phasors, magnitude increases with increased D_{lc} 141

5.21 Motion data for case external spring and case mass investigation 143

5.22 Case, piston and displacer motion versus w_c 144

5.23 Frequency response to changes in case mass and external spring stiffness 145

5.24 Quasi-stable engine operation: Phases and amplitudes 147

5.25 Quasi-stable engine operation: Frequency, output power and spring and damping coefficients 148

5.26 Cyclic variation in operation: Phase and amplitude data 150

5.27 Cyclic variation in operation: Frequency data 151

5.28 Cyclic variation in operation: Phase and amplitude data (relative motion) 151

5.29 Calibrated data and sine wave approximation: high amplitude helium test (BE19N24) 153

5.30 Pressure–volume diagram: high amplitude helium test (BE19N24) 154

5.31 Calibrated data and sine wave approximation: lower amplitude helium test (BE19N15) 155

5.32 pV diagrams: lower amplitude helium test (BE19N15) 156

5.33 Series BE19N: Engine frequency versus rigid body natural frequency 157

5.34 Series BE19N: Amplitude ratios ($|X_p/X_c|, |X_d/X_a|$) versus rigid body natural frequency 157

5.35 Series BE19N: Phase angles 157

5.36 Response of engine to increase in load: motion data 158

5.37 Response of engine to increase in load 159

6.1 Simulation and experimental results: low pressure range of test series BE09N 163

6.2 Simulation and experimental results: Output power, low pressure range of test series BE09N 164

6.3 Engine power as a function of temperature difference and charge pressure (simulation results). 166

6.4 Engine frequency as a function of temperature difference and charge pressure (simulation results). 166

6.5 Amplitudes of motion as a function of temperature difference and charge pressure (simulation results). 167

6.6 Motion phase angles as a function of temperature difference and charge pressure (simulation results). 167

6.7 Root locus diagram, test BE14N14 at initial conditions 170

6.8 Real component of roots versus load damping coefficient, conditions as for above figure. 170

6.9 Output power versus load damping coefficient 172

6.10 Motion phasors, magnitude increases with increased D_{cg} 172

6.11 Load versus case amplitude curve 173

6.12 Motion data for series BE16N simulation: K_{cg} and M_c varied . . 175

6.13 Series BE19N simulation: Engine frequency versus rigid body natural frequency 178

6.14 Amplitude ratios $(|X_d/X_c|)$, $(|X_p/X_c|)$ versus rigid body natural frequency 178

6.15 Series BE19N simulation: Phase angles 178

B.1 Engine and instrumentation 189

B.2 An example of the data from a case-ground spring stiffness check 191

B.3 An example of the data from a piston-case spring stiffness check 192

B.4 An example of the data from a displacer-case spring stiffness check 193

B.5 Instrumentation block diagram 194

B.6 A typical video frame, showing the composite image produced during $\frac{1}{50}$ of a second 196

B.7 The strobe light pulse intensity as a function of time 197

B.8 Piston search band on the video image 201

B.9 Displacer search algorithm (examples of possible keys) 202

D.1 Comparison of linearized adiabatic simulation and measured bounce-space pressure amplitude (Series BE09N). 216

D.2 Comparison of bounce-space hysteresis loss: simulation and experimental data (Series BE09N). 216

D.3 Comparison of linearized adiabatic simulation and measured bounce-space pressure amplitude (Series BE14N). 217

D.4 Comparison of bounce-space hysteresis loss: simulation and experimental data (Series BE14N). 217

D.5 Comparison of linearized adiabatic simulation and measured bounce-space pressure amplitude (Series BE16N). 218

D.6 Comparison of bounce-space hysteresis loss: simulation and experimental data (Series BE16N). 218

D.7 Heat exchanger flow losses as a function of annular gap dimension 219

D.8 Free body diagram of B-10 engine 221

D.9 Piston force vector diagram: Test BE16N27 , high load condition 223

D.10 Enlarged view of portion of piston force polygon 223

D.11 Displacer force polygon: Test BE16N27, high load condition. . . 225

D.12 Case force polygon: Test BE16N27, high load condition. 225

D.13 Piston force polygon: Test BE09N06 (low mean pressure) 226

D.14 Displacer force polygon: Test BE09N06 (low mean pressure) . . 226

D.15 Case force polygon: Test BE09N06 (low mean pressure) 227

D.16 Pressure drop across the annular heat exchangers: low pressure range of test series BE09N 228

D.17 Pressure drop across the annular heat exchangers: high temperature range of test series BE14N 228

E.1 Approximate phase relationships between mass flow and temperature 231

F.1 Corrected drawing to replace figure 1 of published paper 234

List of Tables

1.1 Comparison of system costs: from Beale [6], Prices in 1979 US$ . . . 16

3.1 Sunpower M100 free-cylinder engine: comparison of simple linear analysis and experimental results [57] 87

4.1 Data summary 100

4.2 Work flow paths, helium test 101

5.1 Instrumentation resolution 119

5.2 Measured and calculated external forces 129

5.3 Work flow paths: Test BE16N27, segment 1–2 seconds 130

5.4 Work flow paths: Test BE16N27, segment 19–20 seconds 130

5.5 Series BE09N spring and mass parameters 136

5.6 Series BE14N spring and mass parameters 139

5.7 Comparison of motion data: selected helium and nitrogen test . 152

6.1 Comparison of motion data: unstable operation, experimental and simulation results 176

6.2 Comparison of key data: Test BE16N27, experimental and simulation results 177

C.1 Matrix of input variables for computer code 210

C.2 Matrix of input data for 3-D SAUCE: File FCHELBAS.DAT . . 212

C.3 Matrix of input data for 3-D SAUCE: File 09N09BE.DAT . . . 213

D.1 Estimates of pressure drop across the annular heat exchangers: Test BE16N27 229

F.1 Corrected table to replace Table 2 of published paper 235

List of Symbols

Standard symbols

A	area
A_c	area of case (cylinder)
A_d	area of displacer (including displacer rod area)
A_p	area of piston (excluding displacer rod area)
A_r	displacer rod area
c_p	specific heat capacity at constant pressure
c_v	specific heat capacity at constant volume
$\mathbf{D}$	damping matrix
d	derivative with respect to independent variable
d_1,d_2	temporary variables used to simplify presentation of equations
f	force
$[\mathrm{G}(s)]$	Laplace domain: combined spring, damping and mass matrix
k	thermal conductivity
k_1,k_2	temporary variables used to simplify presentation of equations
$\mathbf{K}$	spring matrix
m	mass
$\mathbf{M}$	mass matrix
p	pressure
N	NTU for the regenerator (E.2)
$\triangle p$	pressure drop across regenerator
Q	heat transfer
R	the ideal gas constant
t	time
T	temperature
T_c	temperature of the working gas in the compression space
T_e	temperature of the working gas in the expansion space
T_h	temperature of the working gas in the heater
T_k	temperature of the working gas in the cooler
T_r	temperature of the working gas in the regenerator space

V	volume
V_c	compression space volume
V_e	expansion space volume
V_T	total working gas volume
V_r	void volume of regenerator open to flow
W	mechanical work done
W_c	mechanical work done in the compression space
W_e	mechanical work done in the expansion space
w	amplitude of mass flow rate through heat exchangers
x	displacement
X	amplitude of displacement

Greek letters

α	volume phase angle
β	angle by which working space pressure phasor leads the case motion phasor
β'	angle by which the working space pressure phasor leads the volume phasor
γ	specific heat capacity ratio c_p/c_v
ϵ	regenerator effectiveness, variance (eqn. B.3)
η	efficiency
$\Im$	take the imaginary part of a complex expression
θ	angular position corresponding to ωt
κ	thermal diffusivity
π	3.141592654...
ϕ	phase angle
Φ	dissipation
$\dot{\Phi}_H$	gas space hysteresis loss
$\Re$	take the real part a complex expression
ρ	density
ω	angular velocity

Subscripts

- b bounce space
- c cold, compression space, case
- d displacer
- dc motion (phasor, amplitude or phase angle) relative to the case
- ds displacer spring
- e expansion space
- g gas, ground
- h hot, heater
- k cooler
- l loss
- m mean
- p piston
- pc motion (phasor, amplitude or phase angle) relative to that of the case
- r regenerator
- w wall, working space

Other symbols

- $\mathcal{L}$ Laplace transform
- $[V]$ matrix
- $|\,|$ absolute value, amplitude of phasor, determinant of matrix
- $\bar{\ }$ complex phasor or spatially averaged value
- $\dot{\ }$ first derivative with respect to time
- $\ddot{\ }$ second derivative with respect to time

Chapter 1

Introduction

1.1 Objectives of the study

The original objective, when starting this work, was to continue the development of a Stirling engine suitable for application in the rural areas of underdeveloped or developing countries. In order to successfully design such an engine three important areas of knowledge and understanding are required:

1. An understanding of the engine design principles, thermodynamics, heat transfer, dynamics, stress, materials and fabrication.
2. An understanding of the system components: energy source, heater, coolant, mounting supports and useful load device.
3. An understanding of the market: the people, their attitude to technology, the environment, the technical and economic constraints, the specific needs and the support systems available.

My aim was to produce a system design, in which a good understanding of the above components had been integrated successfully. This has not been achieved, as the development of a thorough understanding of the class of Stirling engines selected, and of the necessary design tools, has required considerable experimental, analytical and computational work. The development of this understanding is the work presented here. I hope that it will assist in the process of developing an integrated design in the future.

1.1.1 Thesis structure

This chapter serves to introduce Stirling engines, with particular emphasis on those aspects which make them attractive for application in rural areas. A number of engine concepts and projects are briefly reviewed. The free-cylinder Stirling engine (FCSE) is described in some detail in chapter 2, possible design configurations, and the reasons for more detailed study are presented.

Chapter 3 presents the analysis model used, and the principal extensions to the model made by this author. The methods which allow the analysis to be used as a design tool are presented in section 3.6.

In order to gain an experimentally based understanding of free-cylinder engines, and to provide data for evaluation of the above model, two sets of experimental work were conducted. The first was carried out on a Sunpower prototype free-cylinder water pump engine (referred to as the 'water pump' engine). The experimental results, as reported in chapter 4, were somewhat disappointing. True free-cylinder operation could not be obtained, although positive output power was recorded. Agreement between the analysis model and experimental results is fair, while predictions of potential performance by the analysis model are quite promising (section 4.4). However the particular engine being used had significant drawbacks, and it was thus decided that further work should be conducted on a more flexible rig which operated independently of an external oscillator.

For this purpose a small Sunpower demonstration engine (a 1987 Model B-10 Demonstrator) was modified so that it could be run as a free-cylinder engine. Tests were run on the engine under a wide variety of operating conditions (chapter 5). The suitability of the analysis model for this engine is demonstrated in chapter 6.

The concluding chapters refer to the successes and failures of the analytical and experimental work, drawing attention to avenues requiring further work.

The appendixes provide more detail on the instrumentation used for the experimental work, the data processing techniques used, and some specific investigations carried out using the Model B-10 engine data.

1.2 The Stirling engine

Robert Stirling, a Scottish minister, was the inventor of the air engine and heat regenerator (or economizer as he called it). He filed the first patent, No 4081

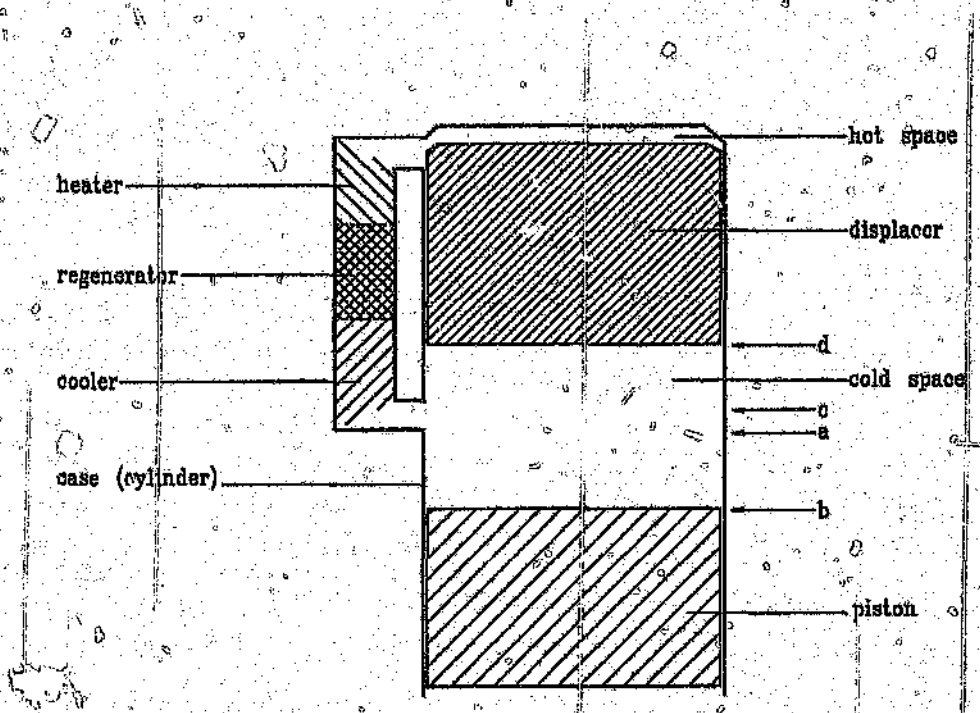

Figure 1.1: Simple Stirling engine configuration

of 1816, only two months after becoming the junior minister of Laigh Kirk, Kilmarnock [59].

Walker, in his review of Stirling engine technology [59] defines the Stirling engine as follows:
'A Stirling engine is a mechanical device which operates on a *closed* regenerative thermodynamic cycle, with cyclic compression and expansion of the working fluid at different temperature levels. The flow is controlled by *volume changes,* and there is a net conversion of heat to work or vice versa.'

There are many different configurations which satisfy the broad definition of a Stirling engine given above. Some of these will be noted in section 1.3. However, the basic principle of operation is the same, and is presented in a qualitative manner below.

Figure 1.1 shows a possible configuration of a Stirling engine. A fixed mass of gas is enclosed within the engine. Volume changes occur only as a result of the motion of the piston. The displacer can move freely up and down as the resistance to gas flow in the cooler, heater and regenerator is small enough to be ignored in this description. There is very little volume change in the engine as a result of displacer motion, thus the work required to move the displacer

is negligible.

In the position shown the work-space volume is at its maximum value, and most of the gas is on the cold side of the displacer. If the piston is now pushed in to position *a*, the gas will be compressed and the pressure will rise. Pushing the piston up against the pressure exerted by the gas will require work. If the displacer is then moved until it almost touches the top of the piston, most of the gas will be forced out of the cold space, through the cooler, through the regenerator and the heater, and into the hot space. As the mean gas temperature rises, so the pressure rises, and the piston will be forced outwards, with more force than was required to push it in. The gas does work on the piston. If the displacer is then moved back towards the hot end, the gas will flow back towards the cold end, releasing some of its stored energy to the regenerator, and cooling as it passes through the cooler. The mean gas temperature lowers, hence the pressure drops, and the piston can once again be pushed in, compressing the gas, and continuing the cycle. Thus, compression of the gas takes place at a relatively low temperature (and hence lower pressure), while expansion takes place at a higher temperature (and thus at a higher pressure). As a result, the work done on the gas during compression is less than that which the gas does on the piston during expansion. The net work output is positive.

The regenerator is extremely important as it stores energy as the gas is cooled (displacer moving from *c* to *d*), and then releases energy to the gas during the heating part of the cycle (displacer moving from *d* to *c*). The theoretical efficiency of the ideal cycle in the above engine is the 'Carnot' efficiency, $\eta = (T_h - T_c)/T_h$. Since the working gas can not be cooled below the ambient temperature, increasing the hot-end temperature remains one of the important goals of Stirling engine development work.

In figure 1.1, the gas space above the displacer is referred to as the expansion space, as it is the area in which most of the working fluid should be located during the expansion process. The ideal cycle which yields the above Carnot efficiency assumes that all the gas is in this space during expansion, and that all of the gas is in the compression space during the compression process. For this and other reasons practical engines cannot follow the ideal cycle. More realistic analyses of the cycles have been developed, some of which are outlined in section 3.2.

If the piston and displacer of the above engine are driven by an external power source, then heat will continue to flow into the expansion space from the surroundings, and out of the compression space into the surroundings, even if the expansion end temperature drops below that of the compression end. Stirling cycle machines can thus be used as coolers, or as heat pumps.

Stirling engines have a number of inherent advantages, particularly when considering their appropriateness for application in rural areas:

- As Stirling engines require only a heat source and a heat sink, they can be designed to run off a wide range of fuels. Engines have been run on solar energy or the combustion heat of biomass fuels such as rice husks or wood. Coal can be used, as well as biogas (see 2.2.2) or any of usual gas or liquid fuels. Nuclear heat sources have also been utilized.
- The engines potentially have very low maintenance requirements as the number of moving parts can be kept to a minimum, and if lubricants are used they are not exposed to the products of combustion.
- Although most of the modern engines require sophisticated manufacturing technology, some extremely simple Stirling engines have been built, so that manufacture and maintenance in underdeveloped economies should be possible.
- Stirling engines characteristically have much lower noise levels than their spark or compression ignition counterparts.

Disadvantages include:

- As the Stirling engine has struggled to compete with the spark or compression ignition engines in the developed areas, there is no strong base from which to branch out into poorer rural ares. Furthermore, the technology may be seen as a 'second best', with the associated marketing difficulties. Thus even though the rural environment may provide a market niche which is not available in more developed areas, it will be difficult to penetrate this market directly. These considerations are particularly important in countries such as South Africa, where the main access to technology in rural areas will be through people visiting and or working in the more developed areas.
- In the case of engines consuming biomass, the variable nature of the available fuel may provide severe difficulties, particularly as skilled technicians will not be on hand to solve problems as they arise, or to monitor fuel quality and engine performance.
- Even an engine designed specifically for the rural market is likely to be significantly more expensive than a spark or compression ignition engine of similar power.

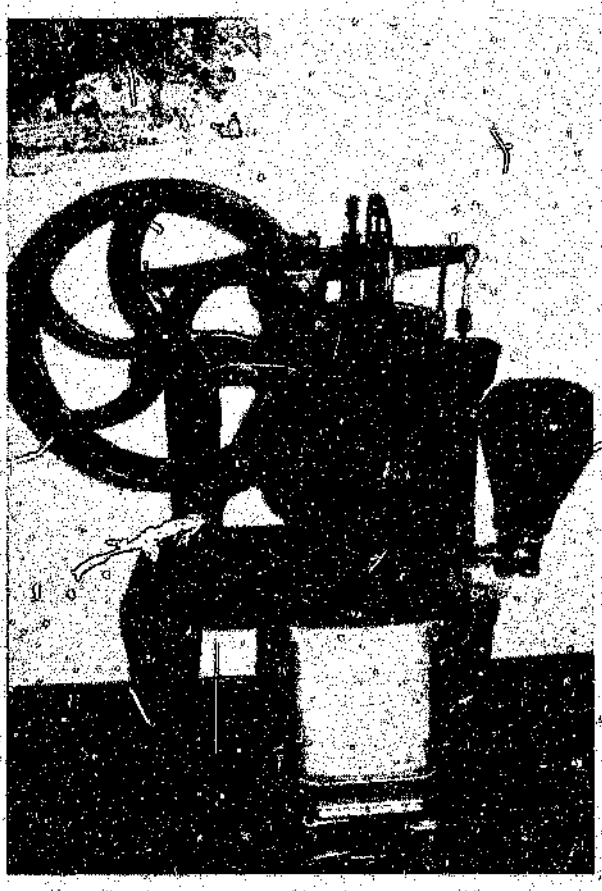

Figure 1.2: Stirling water pump: Housed in the private Stirling machine collection of Ms K Chagnot of Athens, Ohio

1.3 Some Stirling engine types and projects

1.3.1 An older generation

During the latter half of the nineteenth century and the early part of the twentieth century, Stirling engines were successfully employed to provide mechanical power in a great variety of applications including: water pumps, ship engines, sewing machines, milk churns and even to rotate hairbrushes in a barbers shop! [43]. Figure 1.2 illustrates one of these older engines. Such machines were even available through mail order companies [59]. The materials available at the time severely limited the maximum operating temperature and pressure. Thus the older Stirling engines had a low power to mass ratio, of the order of 1 kW per tonne and efficiencies of the order of 1% [43, p 143]. However, their ability to burn readily available fuels (coal, solid fuel, kerosene)

and their relative reliability made them excellent contenders in the developing semi-industrial environment. Such machines, if available today at reasonable cost could well have a place in rural areas of the developing world. Indeed they formed the starting point of a recent initiative by Intermediate Power Technology to design a fractional horsepower Stirling engine suitable for use in developing countries [20].

The advent of the more compact, and at the time more efficient, spark ignition and compression ignition engines, as well as the increased availability of electrical machines, was largely responsible for the loss of the Stirling engine market at the turn of the century. The ready availability of liquid fuels for the internal combustion engines reduced the comparative advantage of the omnivorous Stirling engine still further. Despite significant technological developments, and many promising projects, the Stirling engine has not yet managed to regain a significant market foothold. Elusive though the goal of successful commercialization may have been, it has remained sufficiently near to entice students, engineers, governments and even private enterprise to keep trying.

1.3.2 The Philips initiative

The earliest of the modern Stirling initiatives was typical of many to follow, in that impressive performance goals were achieved, but the necessary factors required to institute large scale commercial production were not all present at the right time. The Philips Research Laboratory in Eindhoven identified a need for a quiet electric power generator, suitable for powering field-radios. They were also aware of the potential for significant improvements which could be made to the existing Stirling engine machines. By the end of the war, Philips were able to produce compact generators, far superior to the older generation Stirling engines. They had increased the power per kilogramme by a factor of 50, reduced the physical size per unit power by a factor of 125, and improved engine efficiency by a factor of 15 [43]. Fifty 200 W generator sets were constructed. The need had by then faded, due to the invention of the transistor, and improved dry cell batteries. The engine designers had produced an excellent machine for a market niche that no longer existed.

Since then, Stirling engine development has branched out into many areas, such as space power, vehicle and marine vessel power, artificial heart power systems, and stationary power systems. There have been many technologically successful engines, but practically no commercially successful engines. The following section reviews some of these projects, with an emphasis on those suitable for application in underdeveloped rural areas.

1.3.3 Modern kinematic engines suitable for application in rural areas

Various teams have, or are working on Stirling engines suitable for stationary power applications in rural areas. Beck [8] reported recently on the development of a prototype engine of 'robust construction', using biogas as fuel (see section 2.2.2). The prototype produced a mechanical output power of 170 W at a speed of 100 rpm. IT Power [20] released a project bulletin in 1988 which described a 500 W engine running at 850 rpm, and with a prototype mass of 60 kg. This engine used the mechanical drive components of a Vee-Twin piston air compressor, thereby taking advantage of the design and development work already done. At the time it was hoped that with appropriate financial support the engine could be in production within two years. This author is not aware of further development work on this engine.

Kinnersly [31] reported in 1993 that an engine designed by Dr G Rice of Reading University, with significant later developments carried out by Kinnersly, was undergoing trials. The original design was commissioned in response to the need for small electricity generating systems, fuelled by solid biomass, in rural areas of developing countries. At the time of preparing the above cited report the engine was undergoing preliminary trials, and had produced 0.45 kW at a charge pressure of 3 bar. The design is intended to produce 5 kW at a charge pressure of 10 bar.

A mature engine which was specifically designed with the developing areas of the world in mind is the 3.5 kW STI engine. This engine was designed by Sunpower Inc. and then further developed by Stirling Technology Inc. (See figure 1.3). A plant was set up in Madras, India to manufacture the engines for use by farmers. The combustion chamber is designed to burn solid fuels such as wood, rice-husks or coal. Envisaged applications included water pumping, electricity generation and rice hulling. The latter application has the appealing characteristic that a portion of the husks obtained from the process provides sufficient fuel to drive the engine [16, 50]. In a recent independent evaluation carried out by Gaugauf [22], an engine purchased from the Indian plant yielded an output power of 2 kW electrical, and an overall efficiency of 8 to 10%. The engine was heated using wood chips in a modified stoker type wood chip furnace. Gaugauf felt that engine reliability did not meet the required standards for the application, although improvements were being undertaken by the manufacturer.

An easily constructed engine, using flat plate heat exchangers, a discontinuous displacer motion and a simple diaphragm type piston has been developed by Kolin [32, 34]. These engines use very simple technology, the basic frame

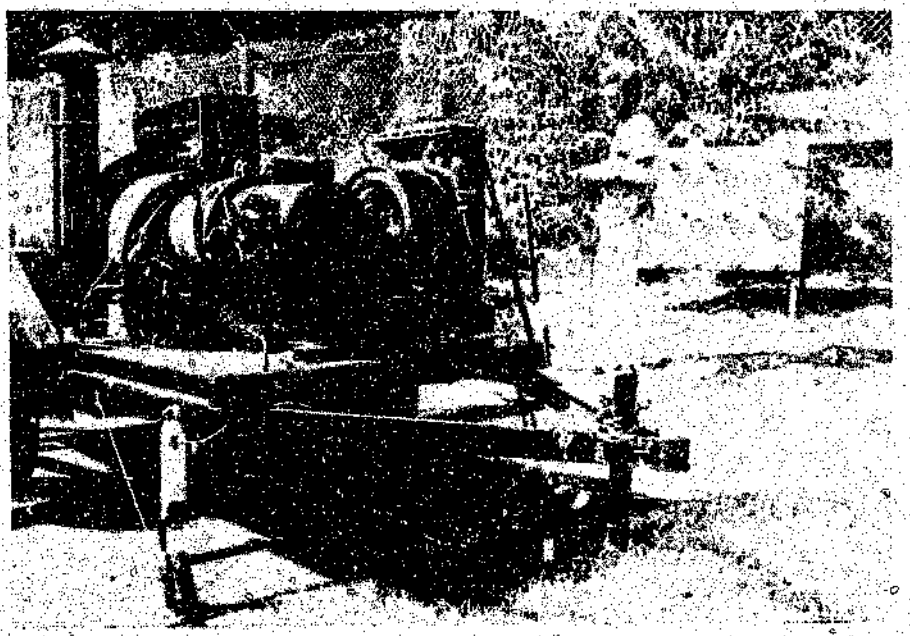

Figure 1.3: Stirling Technology Incorporated stationary Stirling engine.
[Photograph courtesy Sunpower Inc.]

being wooden, with a flexible rubber seal between the wood and the flat plate cooler/piston. They are able to run at low hot-end temperatures, and are thus particularly suitable for solar powered applications, as a concentrator would not be required.

1.3.4 Hybrid engines

All of the engines referred to above rely on mechanical linkages to move the piston and displacer in the pattern required. Some of these engines do not even have a displacer as such. In the IT Power engine the gas is moved between a hot and cold cylinder as a result of the motion of a single piston in each cylinder. There are a wide variety of linkages and engine configurations which can be used to achieve the required volume variations and gas transfer. All such engines fall into the general group referred to as kinematic engines [13, p 7]. It is however not always necessary to kinematically link the moving components. There are a number of engine designs in which one or more of the components are 'free' and move under the influence of gas pressure and forces transmitted by springs. Projects involving some of these engines are referred to below. For a basic text on 'free' and hybrid Stirling engines see Walker and Senft [61].

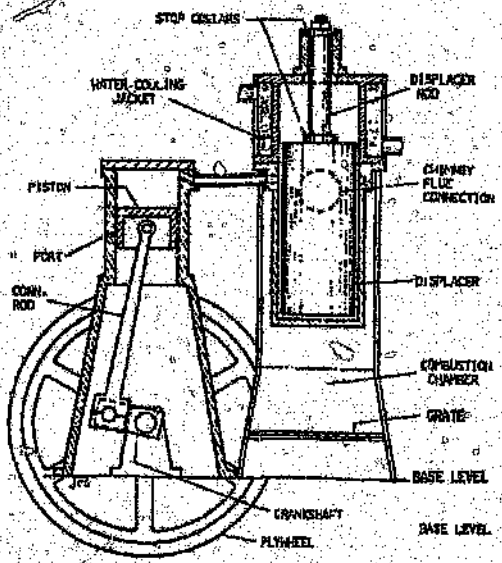

Figure 1.4: A drawing produced by Senft [49] based on Ossian Ringbom's 1907 patent

In the engine illustrated in figure 1.4, the displacer is not restrained in the axial direction and can therefore move under the differential pressure acting on the displacer rod. This type of hybrid engine, with a free-displacer and a disciplined piston, has been called a Ringbom engine, after Ossian Ringbom, who in 1905 applied for a patent 'on a hot air engine in which the movement of the displacing piston is obtained without the connection of rods or cranks or eccentric or other mechanical parts.' [61]. This introduces a new aspect into the understanding and design of Stirling engines. The mass of the displacer, the differential area exposed to the working space, and the spring constant of any attached spring or bounce space become extremely important factors in the determination of the dynamic operation of the displacer. Typically this type of engine will have a specific operating frequency range, outside of which the dynamics of the displacer are no longer satisfactory. Senft presented a mathematical model describing the operation of these models in 1985 [49].

A Ringbom Stirling engine which had a coal combustor was developed by Sunpower Inc. [51]. Urieli and Chen [58] have proposed a Ringbom Stirling engine combined with a solar pond, a concept which would be particularly well suited to utilization in rural areas. Senft has designed and built Ringbom engines capable of running at very low temperature difference (hot-end to cold-end temperature difference as low as 4°) [60]. Although such engines would have a low power to mass ratio, the fact that they could run on the

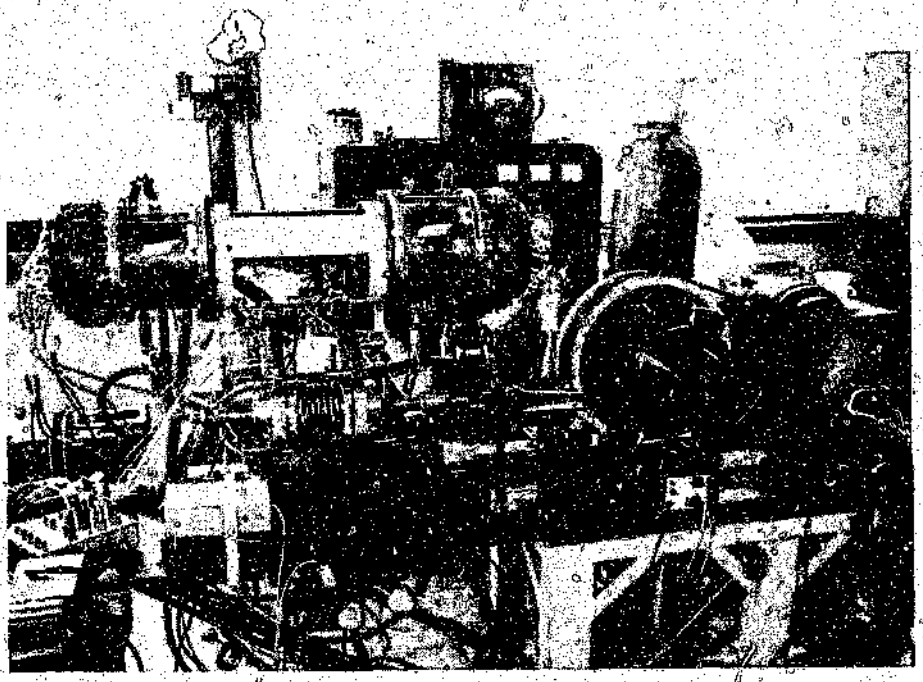

Figure 1.5: Rallis Stirling engine

energy gathered by a simple flat plate collector makes them very attractive for applications in rural areas.

Rallis *et al* [41, 42] have studied a free-displacer disciplined-piston back-to-back Stirling machine (figure 1.5), now widely referred to as the 'Rallis Stirling engine', at the University of the Witwatersrand. Although still at a pre-prototype stage, the experimental rig has performed adequately, delivering a peak indicated power of 320 W at a hot-end temperature of 450°C. The power piston is well removed from the hot end, allowing the use of a slightly modified pneumatic cylinder. The displacer housing can be completely sealed. Furthermore, the present engine does not have any gas springs, which would require close tolerance seals and cause dissipation. Although Rallis originally conceived the engine as being suitable for underdeveloped areas, it does have the severe disadvantage of requiring two heaters, and hence two burners. The engine has undergone preliminary tests as a refrigerator, with one side being heated, while the other side draws heat from the surroundings. Temperatures of -10 °C were obtained, although the engine did not self-sustain in this mode [45]. If this concept can be developed further it may prove useful for refrigeration of medical supplies.

Although both the Ringbom and the Rallis engine have a free displacer, their power output is through a rotating shaft, and could thus be turned to a range of purposes. These might include the generation of electricity, pumping water

or the direct driving of small scale industrial or milling equipment.

1.3.5 Free-piston Stirling engines

It is possible to design an engine in which both the piston and displacer are 'free'. William T. Beale produced such a concept in March 1964. A quickly constructed prototype 'produced nothing but despair' [61, p 129]. However by the summer of 1966 Beale and his team at the University of Ohio had produced a single cylinder engine which worked. It used rubber bands to suspend the piston and displacer in position, and a simple annular gap regenerator. By 1969, when Beale published a review of various investigations carried out in the context of undergraduate projects [3], they had started the exploration of most of the important application concepts for free-piston engines, including:

- free-piston engine driving a linear alternator
- duplex heat engine driven refrigerator
- double ended fluid pump
- free-cylinder water pump (see section 1.3.6)

In this type of engine, the link between dynamics and thermodynamics becomes very important. Conceptually the engine can be thought of as comprising of two masses, suspended in space by springs (see figure 1.6). The springs and the damping coefficients are designed so that the natural mode of vibration of the system causes volume variations within the engine which approximate those required for the Stirling cycle as described above. Some of the work output from the cycle maintains oscillation of the components, while the rest is available as useful work output. The motion of the piston of this type of engine is typically used to drive a linear alternator, or [illegible] some sort of fluid pump. Such an engine can be hermetically sealed, as loads on bearing surfaces are minimal. It should be noted that some free-piston engines, particularly those developed in earlier years, operate in a 'bang-bang' mode, the displacer running up against the piston, or the end of the cylinder for part of the cycle.

While most free-piston projects have been orientated towards very sophisticated space or defense applications, some of these engines may be suited to application in rural areas, provided that they are sufficiently reliable to be treated as a 'black box' with no maintenance requirement between long service intervals. A number of papers have been written by Sunpower staff,

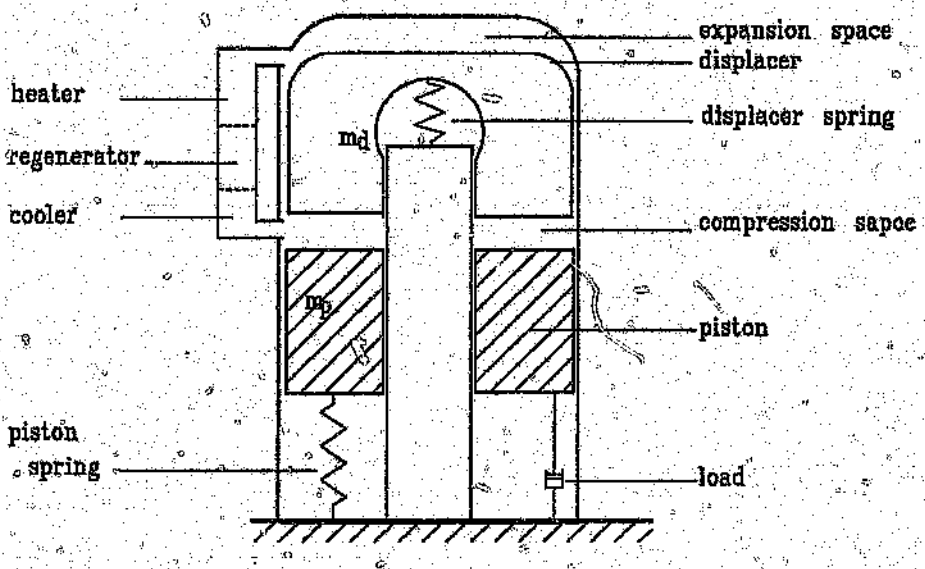

Figure 1.6: Schematic diagram of a free-piston Stirling engine

with a specific emphasis on Stirling engines for developing countries on rural areas [4, 7, 5, 12]. Some of their hardware projects have been specifically aimed at the developing country market. Figure 1.7 illustrates a solid-fuels stove/engine combination. Such a combination is particularly attractive for a number of reasons. Fuelwood for cooking is the major energy source used by rural dwellers in developing countries. The use of fuelwood in open fires often leads to severe health risks due to the smoke build-up indoors. Thus the stove with chimney, apart from being desirable, does make a positive contribution to health. High quality energy for lighting or for running items such as radios and television sets is a small fraction of the overall energy consumption of rural families. However, it does form a significant component of the household expenditure on energy. (See Griffin *et al* [23] for a report on the fuel use in six rural settlements in a rural area of South Africa as an example).

Recent high efficiency solar powered Stirling power generation developments have been particularly promising. Cummins Engine Company, Inc. plan to manufacture dish-Stirling systems for public electric utilities and remote power application in 1996. The engine is a 7.5 kW Sunpower design, driving a linear alternator. Transfer of the heat from the collector to the engine is via a heat pipe. With projected costs approximately 50% less than the equiva-

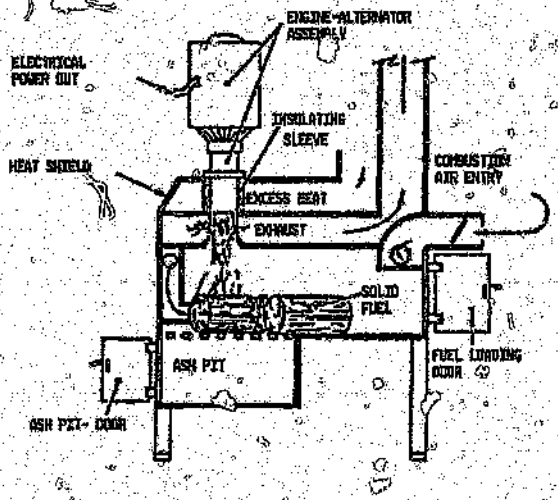

Figure 1.7: Combination wood stove/solid-fuel Stirling engine. [5, p 268]

lent photovoltaic system, such systems should be eminently viable [46]. They are however quite complex machines, and will almost certainly require highly trained personnel to supervise their operation.

1.3.6 Free-cylinder Stirling engines

If the case of the free-piston Stirling engine as shown in figure 1.6 is made relatively light, and mounted on a spring, and if the piston is made relatively heavy, then the case will tend to oscillate. The lighter the case, the larger the oscillation amplitude. Useful work can then be extracted from the case motion instead of the piston motion. As noted above, the free-cylinder concept was first developed during the years preceding 1969 by Beale and his students, the concept emerging almost by chance when Beale observed that the moving cylinder of an unbalanced pressurized free-piston engine was capable of delivering significant work [6]. Despite the successful operation of a complete solar powered water pump system comprising a Fresnel lens, engine, pump, polar mount and tracker in 1971, no sponsors were found for further work.

The concept was again taken up by Beale and the Sunpower team in 1979. Beale reported on successful engine development and trials in June of 1979 [6], presenting impressive achieved and potential performance. A comparison of expected system costs yielded system costs per watt of pumped water significantly lower than that of a Rankine or a photovoltaic system (see table 1.1). Presumably on the basis of this promising work, further development work was carried out in the period 1979 to 1984. Free-cylinder powered water pumps

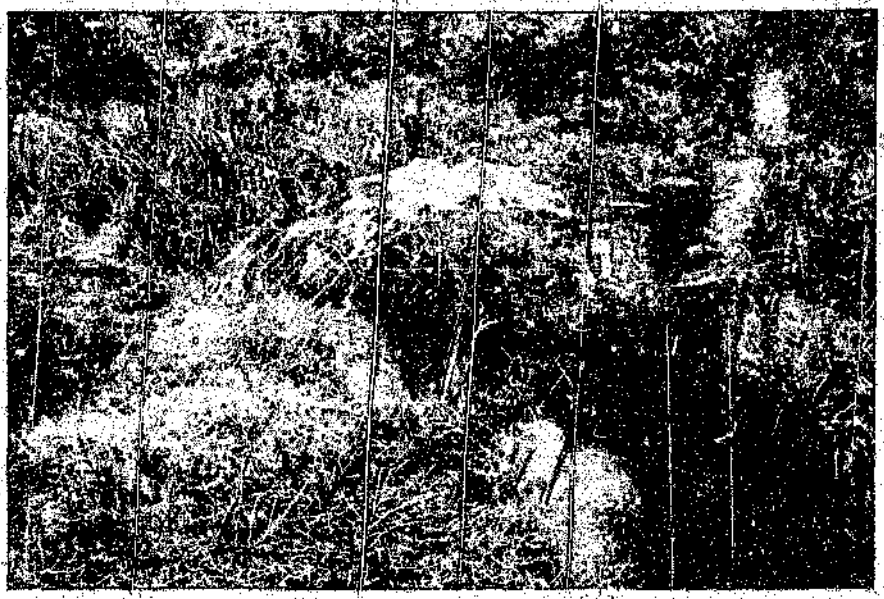

Figure 1.8: Free-cylinder water pump
[Photograph courtesy Sunpower Inc.]

of approximately 100 watts output were developed and demonstrated. (See figure 1.8.) Sadly, the work was halted at this stage, despite the significant promise shown by the so-called 'Red Water Pump'. This engine, a reliable and impressive performer, was still being demonstrated occasionally by Sunpower Inc. in 1988 [51]. At the end of this development stage, the most recent of the Sunpower free-cylinder Stirling engines was designed and built. Unfortunately this engine was never thoroughly tested or proved. Furthermore there is little public documentation regarding the design procedure followed, or its intended operating characteristics. This engine was donated to the University of the Witwatersrand in May 1988, and formed the principal focus of the first set of experimental work reported in section 4. In the following chapters the 'water pump' engine refers to this particular machine.

1.3.7 Fluidyne engines

The last class of Stirling engines which is significantly different to the above described types, is the fluidyne engine. West [62] gives a thorough account of their development and describes many design variations. Fluidyne engines use a column of liquid as the displacer/piston (see figure 1.9). The liquid column

Table 1.1: Comparison of system costs: from Beale [6]. Prices in 1979 US$

Stirling free-cylinder 600 °C Hot-end				Rankine [52] 350 °C Hot-end				Photovoltaic 3$/PW Photocells			
Component	Eff.	Power out W/m^2	$/m^2	Component	Eff.	Power out W/m^2	$/m^2	Component	Eff.	Power out W/m^2	$/m^2
Collector	0.7	450	50	Collector	0.7	450	50	Photocells	0.1	100	300
Absorber	0.7	313	5	Absorber	0.7	313	5	Meter	0.8	80	30
Engine	0.25	78	80	Engine & Thermo Cycle	0.10	31	40	Pump	0.8	36	8
Mount & Tracker			20	Mount & Tracker			20	Auxiliaries			15
Pump	0.6	47	5	Pump	0.6	18	5				
Net power to water		47		Net power to water		18		Net power to water		36	
System cost				System cost				System cost			
$/m^2			110	$/m^2			120	$/m^2			350
$/W			2.55	$/W			6.67	$/W			9.8
Relative cost $/W			1	Relative cost $/W			2.6	Relative cost $/W			3.64

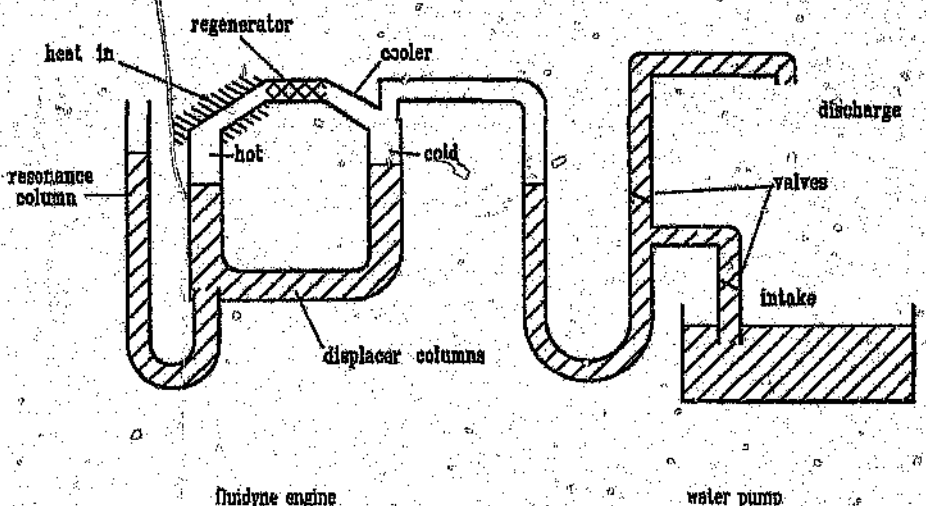

Figure 1.9: Fluidyne Engine

is in the from of a U, which oscillates back and forth, moving the gas from the hot side to the cold side, and back again. Compression of the working space is achieved by injecting liquid into the oscillation column from the resonance column during the compression stroke. During expansion, the volume of the liquid in the U is reduced as liquid flows out into the resonance column. Liquid piston Stirling engines may have application in rural areas for water pumping, as they require readily available and often cheap components. Efficiency has been extremely low to date. Typical values are less than 1%, although a large machine with an efficiency of 7% and a pumping rate of 11250 l/hour at a head of 3 m has been reported [62, p 122 & 130]. Hot-end temperatures have to be kept quite low, and evaporation of the liquid results in a significant enthalpy flux out of the hot space. Pressurization is also difficult, so these engines usually have a low power to mass ratio. However, if low grade biomass 'waste' products or solar energy at a low concentration factor can provide the heating requirements, these engines may yet find their niche.

An alternative engine configuration, proposed by William R Martini and subsequently simulated and investigated by Goldberg and Rallis at the University of the Witwatersrand [24] is the liquid-piston, free-displacer engine. The engine is essentially a free-piston engine, with a liquid column instead of a solid piston. As the liquid column is well removed from the hot end, the problem of evaporation is reduced or even eliminated.

1.4 Summary

From this brief introduction to Stirling engine technology, it is apparent that various types of Stirling engines have characteristics which attest to their suitability in rural areas. The free-cylinder Stirling engine does not come out as a clear leader, it is merely one of many which seems poised on the brink of commercial success. Thus it is important to explain why it was chosen as the subject for detailed investigation and research. Perhaps the most important reason is that an engine was made available to the School of Mechanical Engineering by Sunpower Inc. of Athens, Ohio. Furthermore, the potential for a significant advance in the analytical approach to the simulation of the free-cylinder Stirling engines was perceived by Dr Berchowitz and the author during discussions in Athens during 1988. However, other factors including its simplicity, the proven track record of the previous prototypes, the importance of water supply in southern Africa, and the robustness of the engine were important considerations in the decision process. In the subsequent chapters further advantages and disadvantages are highlighted.

Chapter 2

The free-cylinder Stirling engine

The preceding chapter has outlined some of the roles that Stirling engines could play in the rural environment. The remainder of this dissertation considers aspects of a particular class of Stirling engine, and a possible application system. No further attempt is made to justify the selection of the free-cylinder Stirling engine for detailed research. Prior research by Sunpower has been promising, and in the words of Beale [7], 'The most promising Stirling engines for these purposes have been found to be the free-cylinder water pump, the simple low pressure crank drive hot air engine, and the air charged free piston-linear alternator combination for generation of electricity.' It is one type of engine which may be able to fill an important niche in the rural environment. Detailed knowledge of the characteristics and costs of free-cylinder Stirling engines is required before it will it be possible to fully evaluate their suitability for application.

The three major components of a free-cylinder Stirling engine powered water pump suitable for use in rural areas are discussed below. The first section details the design concept of the free-cylinder Stirling engine. Various heat sources are then discussed, and lastly, some of the proposed water pump designs are presented. Figure 2.1 shows how the components fit together in a block format.

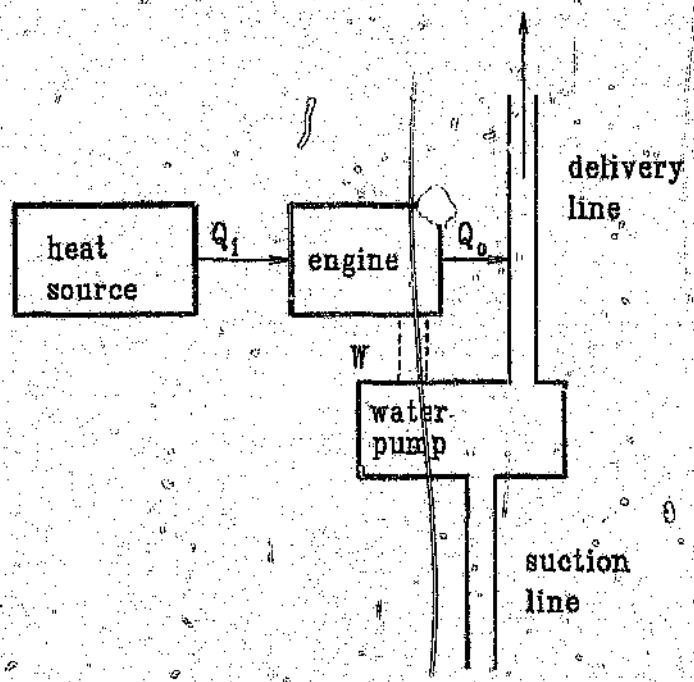

Figure 2.1: System block diagram

2.1 The Sunpower free-cylinder Stirling engine

Figure 2.2 shows the principal components of the engine, and the nomenclature used in this discussion. Detailed dimensions are given in table C.2.

2.1.1 Case (or cylinder)

The external shell of the engine is a stainless steel case, which is hermetically sealed. The prototype engine has two 'O-ring' seals, one at the bottom of the engine, the other is located immediately below the cooler. The engine is pressurized through a non-return valve of the type used for automobile tyres. Thus the engine should remain pressurized for months without need of recharging. In the final application form, it may be possible to weld the entire engine closed, forming a sealed, and hopefully maintenance free unit. In any event the unit would certainly never be opened on site. Thus, as far as those who would use the FCSE in the field are concerned, the engine is

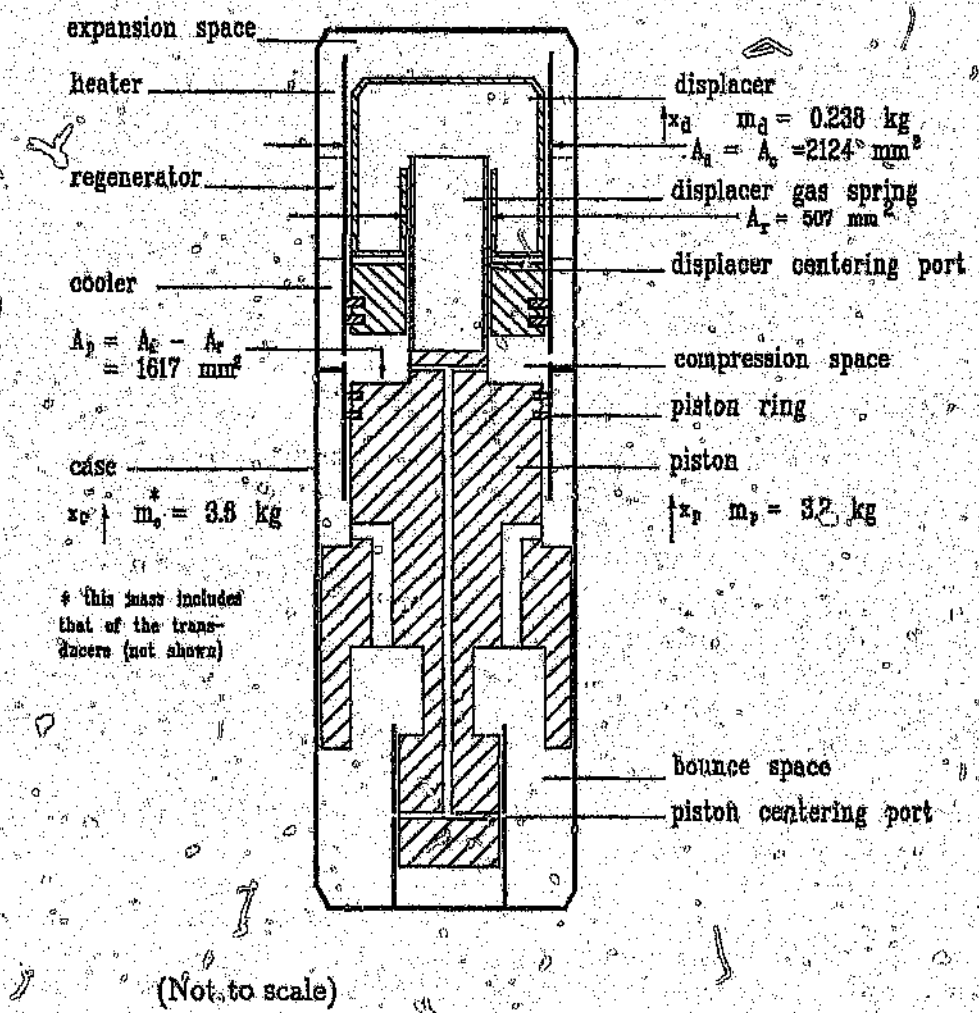

Figure 2.2: Schematic drawing of 'water pump' free-cylinder Stirling engine

an extremely robust unit, impervious to dirt or water and not requiring any maintenance except possible recharging with air (using a device as simple as a bicycle pump), or in more sophisticated applications, with helium.

The heat exchanger units, the heater, regenerator and cooler are integral with the case. Both the heater and cooler are finned, while the regenerator is filled with a random wire matrix. Although the exact dimensions of the heat exchangers in the prototype engine are not known by this author (drawings could not be located, and the engine would have to be machined open in order to measure them) the construction details have been deduced from a engineering drawing of a very similar Sunpower engine. These assumed details are given in the engine data table C.2. The inner cylinder is welded in place, thus the entire top end of the engine is a single welded unit.

The entire engine would normally be supported on a spring, and held such that the case could oscillate in the vertical plane. The motion of the case would then transfer work from the engine to the load device, the water pump.

2.1.2 Piston and centering port cylinder

The piston comprises the displacer rod, piston crown, skirt and centering port spindle. The various sections are screwed together. The displacer rod is a fine tolerance component, as it forms the inner spool of the displacer gas spring clearance seal. It is manufactured from anodised aluminium, coated with a low friction Teflon-based product. The crown section is brass, with two grooves cut into it for the Rulon piston-rings. The piston skirt slides inside the main cylinder, and is the principal guide surface to maintain coliniarity of the engine components. The prototype skirt is manufactured from brass. The wear surfaces are coated with a Teflon-based film. The present piston centering port spool is stainless steel. It is also coated with a Teflon film.

The centering port cylinder is not located in the case, it is held down by the light spring which supports the piston in the mid-stroke position.

Given the long life without maintenance requirement, seals and bearing surfaces in a production engine will have to be appropriately designed and manufactured. The solutions applicable to free-piston engines will also be applicable to free-cylinder engines.

2.1.3 Displacer

The displacer comprises two drawn stainless steel shells which surround an anodised aluminium hollow shaft. The inner shell defines the volume of the displacer gas spring. The displacer ring seals are mounted in the base of the aluminium shaft, well away from the hot end of the engine.

Concentricity of the engine components is thus not extremely critical as the alignment of the close tolerance seals (displacer rod and piston centering port) is relieved, the former by the use of a ring seal on the displacer seal, and the latter by the use of a floating centering port cylinder.

2.1.4 Centering ports

Clearance or ring seals do leak slightly, and the oscillatory motion of the components often causes a differential pumping action which tends to result in a higher pressure on one side of a seal than the other [13, p 226]. Such a differential pressure causes the engine components to drift from the desired mean positions. A simple and effective way of controlling this drift is to fit centering ports, which open as the components move past the desired mean position. The free-cylinder engine has centering ports located on the displacer rod and cylinder, which allow gas flow between the working space and the displacer gas spring at displacer mid-stroke. The piston centering ports connect the bounce space, via the piston central shaft, to the working space at piston mid-stroke.

2.1.5 Gas springs (or bounce spaces)

The displacer gas spring, and the piston bounce space are closed volumes of gas, which have no role in the thermodynamic Stirling cycle. However, they act as springs, which are very important contributors to the dynamic characteristics of the engine. Gas springs have associated hysteresis losses, which must also be considered in the engine analysis.

2.2 Possible heat sources for a free-cylinder engine

The free-cylinder engine requires a high temperature heat source. Under optimum conditions, assuming an engine efficiency (excluding the burner) of 20% (this should be easily obtainable, see section 4.4) the engine would require 1.5 kW of heat input, while delivering 300 W. The required wall temperature is of the order of 600 °C. An important complication is that the surface to be heated oscillates. It is beyond the scope of this dissertation to discuss heater design in detail, or even to present all the options which may be suitable. The paragraphs below serve to introduce the concepts and present an idea of some of the possibilities.

2.2.1 Solar concentrator and tracker

Solar energy is an extremely attractive energy form for a rural water pump in southern Africa. There is abundant sunshine, and furthermore, water demand is often partially dependent on the sunshine. Cloudy weather will result in less pumped water, but the demand, particularly in irrigation schemes will also be lower under such conditions. Water can also be stored fairly easily. Photovoltaic pumping sets are becoming popular in the rural application, despite their high capital cost [36].

The high temperature requirement of the FCSE necessitates a concentrator and associated tracking equipment if solar energy is to be used. Standard mirror concentrators, multiple faceted hand placed mirrors or even a Fresnel lens could provide adequate concentration factors [6].

A concentrator design, which may be particularly suited to third world applications, simply on account of its low cost, is that of an inflated Mylar film collector. Sunpower Inc. have manufactured some effective concentrators, which comprise two sheets of Mylar film, sandwiched between two supporting rings. One layer of Mylar is aluminised, acting as a reflective surface. The concentrator is inflated slightly, which results in a semi-parabolic surface, yielding an acceptable concentration factor (see figure 2.3).

Figure 2.3 also shows a z-crank support for the concentrator, and a tracking system. The z-crank allows simple adjustment of the angle of the collector with respect to the axis of rotation of the tracker to accommodate seasonal variations in the sun's path across the sky. A small photovoltaic panel and DC stepper motor provide accurate tracking. Diurnal rotation could equally well

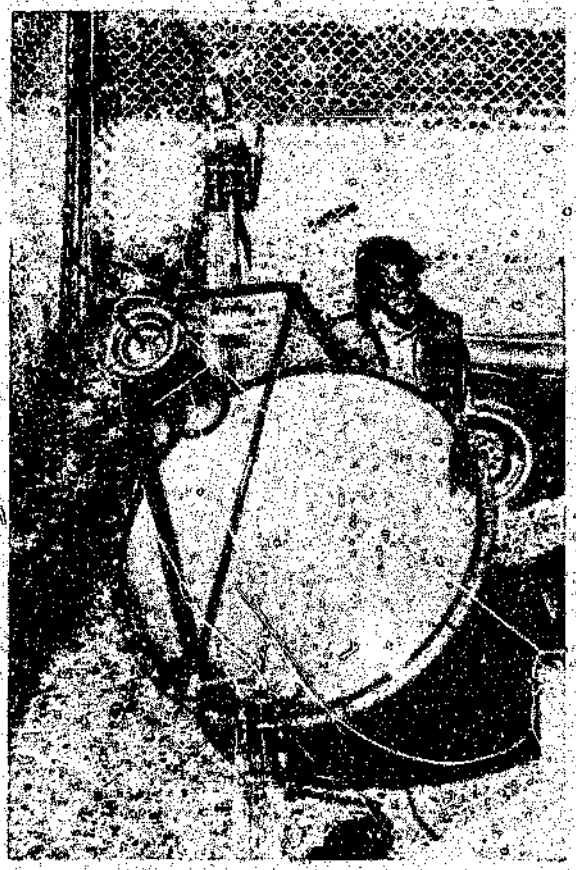

Figure 2.3: Small free-cylinder Stirling engine water pump and inflated Mylar collector mounted on a z-crank tracking mechanism.
[Photograph courtesy Sunpower Inc.]

be powered by a heat activated mechanism using shade plates (a passive solar tracker), a clockwork mechanism or a gravity escapement driven system.

Concentrators would normally focus the solar energy directly on to the engine heater, requiring that the entire engine be mounted close to the focal point of the concentrator. An alternative which has been used on bigger free-piston and kinematic engines is to use a liquid metal heat pipe to transfer the heat from a collector at the focal point of the concentrator to the engine heater.

In a system cost breakdown presented by Beale [6], the collector, absorber and tracker (excluding the mounting) comprise more than 50% of the entire system cost (pump, mounting and engine comprising the remainder of the system). Beale's choice of collector for this exercise was a second surface glass mirror. A gas burner of the type described below would certainly be cheaper. However, where the cost of alternative fuels are highly significant, or where long term availability of biomass is threatened, then the initial extra cost of the solar system may be justified.

If solar energy is used then the engine has to be able to self-start reliably, as the hot end would be severely damaged should the full power of the concentrator be focused on a stationary engine for any length of time. Although free-cylinder Stirling engines can be made such that they will self-start on the application of heat [6, 44], this does not appear to be perfectly reliable and was never recorded in the experimental work reported here. The non-vertical attitude of an engine mounted on a solar concentrator will also make self-starting more difficult. Beale does however report that self-starting can be assured [6, p3]. The methods are however proprietary and have not been explored by this author.

2.2.2 Gas burner

The simplest way to heat the engine would be to use a gas burner. This is the system used on the prototype 'water pump' engine rig (see section 4.1.1). Possible fuels are liquefied petroleum gas (LPG) which is available and used in some rural areas (see Griffen *et al* [23]), natural gas or biogas. The latter option is discussed in a little more detail here, as the association of biogas with the free-cylinder Stirling engine water pump seems to form a very viable and attractive system for a variety of reasons.

Biogas as a Stirling engine fuel

Biogas is the common name given to a multicomponent gas, which usually comprises: 50–70% methane (CH_4), 25–50% carbon dioxide (CO_2), 1–5% hydrogen (H_2), 0.3–3% nitrogen (N_2) (gas compositions in volume percent), and various impurities, the most notable being hydrogen sulphide (H_2S) [28]. There are a number of installations in which biogas is tapped from wells sunk into municipal waste dumps. The gas is usually purified, and used to power internal combustion truck engines. In a rural village situation, biogas can be produced by the anaerobic digestion of animal wastes, plant wastes, and in some cases human excreta. Typically a high quality liquefied fertilizer is produced as a byproduct. The effluent has a lower pathogen count than the raw feed material. The gas is usually used for household cooking and lighting, and in communal installations may be used to power spark or compression ignition engines. The biogas digester is thus, a waste disposal system, an energy source and a producer of fertilizer. A plethora of different digester designs has been developed, the most commonly known household scale units being the fixed dome constant volume digesters. Sasse [47] gives detailed construction and management information. Another common type is shown in figure 2.4. This digester was built at the home of a family living in a rural area of the Eastern Transvaal lowveld (South Africa) by a team which included this author [54]. The type of digester is usually referred to as a floating dome, or constant pressure design, with many variants being in existence. There is a considerable literature base regarding biogas production in rural areas. Fulford [21] and Sasse [48] provide good overviews. Thom [55] has recently concluded a project which specifically considered biogas as an energy source in rural areas of South Africa.

The energy content of methane is 37.3 MJ/m^3. At an overall burner-engine-pump efficiency of 12% one would therefore require 0.8 m^3 of methane per kWh. At a concentration of 60% methane this corresponds to 1.34 m^3 raw biogas. A 300 W machine, running for 6 hours a day would thus require approximately 2.4 m^3 per day. Gas production is highly variable, depending on the feed material, the temperature at which the digestion process takes place, the retention time of the system, and the degree of agitation within the system. Sasse gives data in litres gas/kilogrammes feed material/day (l/kg/d) for a range of retention times. Using a retention time of 60 days (quite common in rural installations), and an operating temperature of 26° – 28° C one could expect a production rate of 34 l/kg/d for cattle dung. The 300 W machine running at the above duty cycle thus requires a daily feed of 71 kg dung. Cattle dung would be mixed with water in a ratio of approximately 1:1. The required digester volume would thus be approximately 8.5 m^3.

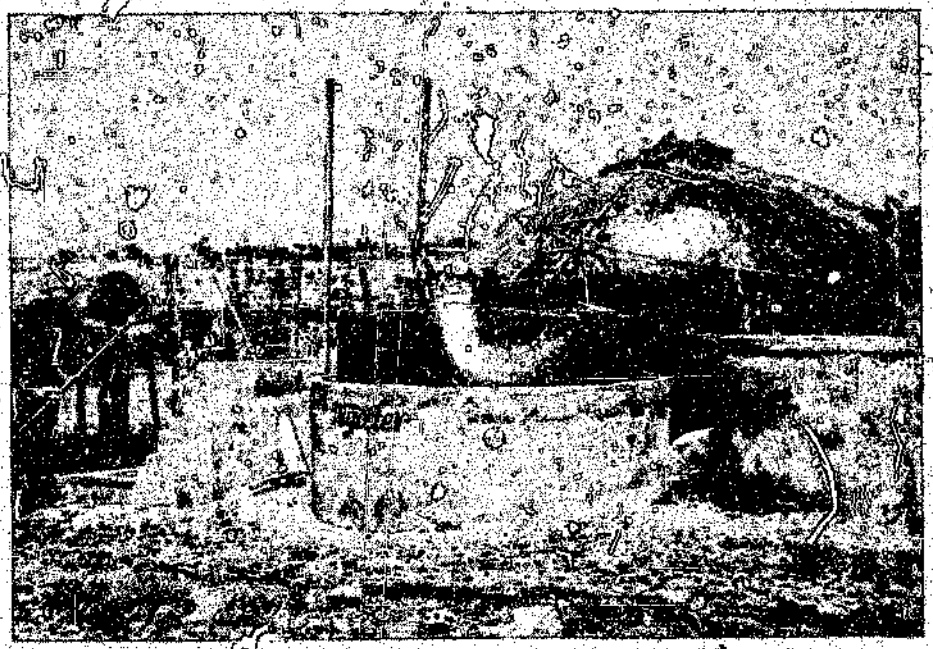

Figure 2.4: Constant pressure digester built at the Mathabela homestead, Acornhoek, RSA
[Photograph courtesy C Thom]

Non-ferrous metals are quickly corroded by the H_2S component of biogas, ferrous metals being less severely attacked. The combustion product SO_2 combines with water vapour which badly corrodes the exhaust side of burners. It also dissolves in the lubricating oil of internal combustion engines, reducing the interval between oil changes under continuous operating conditions to about 200–250 hours [39]. It is thus advisable to remove the H_2S from the gas in internal combustion engine applications. Low cost methods are well described by Muche & Zimmermann [39]. However a free-cylinder Stirling engine would be able to tolerate unpurified gas, as the burner could be manufactured from stainless steel, and the internal components are isolated from the products of combustion.

2.2.3 Solid fuel

There are possibilies of using solid fuels for a free-cylinder Stirling engine. One option would be to design the engine such that it can be operated with the head inside a fire box (heater end pointing downwards, or with the cylinder on its side.) This would entail a completely different system concept, and has not been seriously considered in this work. Alternative concepts include the

use of a heat pipe to transfer heat from the fire box to the heater, or to have a short insulated passageway leading from the fire box to the heater. Thermal gasification of biomass would also be technically feasible. This technology has been successfully employed to run internal combustion engines [29]. As in the case of biogas, the purification normally required before such gases can be used in internal combustion engines would not be required in the case of a Stirling engine.

2.3 Water pump designs

The most likely application of the free-cylinder Stirling engine is as the power source for a water pump for rural areas, (or of course any other application where a small, robust, multifuel pump is required). Whereas the engine falls into the 'black box' category of technology, the proposed water pump designs are relatively simple from a technical point of view, although not always from a design point of view. Maintenance by users or technicians in the field would certainly be possible. Since the free-cylinder Stirling engine has a relatively high operating frequency, and small stroke, it is not suitable for a conventional reciprocating pump. The following design concepts are presented to give an indication of some of the avenues which could be followed in the pump development process.

2.3.1 Induced flow pump

Burton and Lobo-Guerrero [14] describe a high frequency reciprocating diaphragm pump which uses the inductance effect of a short, rigid discharge tube and an air filled bladder as a capacitance in order to obtain a low head pump with a high resonance frequency. If the pump is operated near this frequency then it is possible to obtain volumetric efficiencies much greater than one. Lobo-Guerrero and Burton indicate discharge heads of between 5.2 and 27 m for their '3 inch Spate' induced flow pump. However, the volumetric efficiency advantages of the induced flow principle are lost at the higher discharge head, with the volumetric efficiency of the pump reducing from 2.3 at the lower discharge head to 1.2 at a 27 m discharge head. Their operating frequency was 25 Hz, which is fairly close to the expected operating frequency of a free-cylinder Stirling engine. Figure 2.5 indicates a possible pump design concept using the induction flow principle. Mitchell [37], Beale, Chagnot and other members of the Sunpower team designed and built a number of induction pumps coupled directly to free-cylinder Stirling engines. The pump shown in

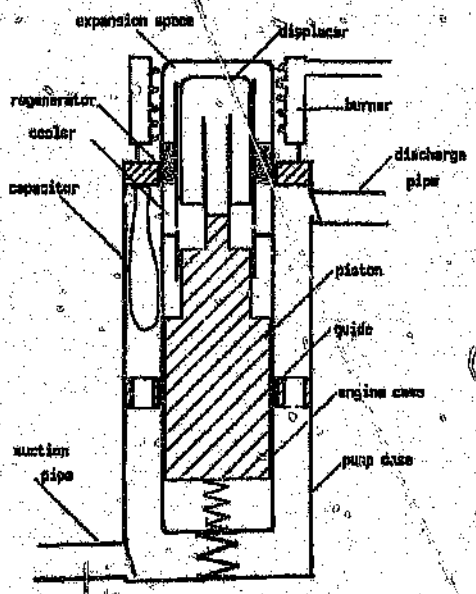

Figure 2.5: Integral induction pump design concept

figure 1.8 is an example of this work.

2.3.2 Down-well pump

Any pump which is located at the engine can only have a maximum suction head of about 6 m. This would restrict application to water supply from rivers, dams or shallow wells. A further disadvantage of any pump with a negative suction head is that the pump will require priming before each use, unless equipped with extremely efficient valves.

Beale [6] illustrates a cable linked pump system, although no pump details are given. Mclean [35], with this author as one of her supervisors, investigated the concept as shown in figure 2.6 . This allows the pump to be placed down a well, with the engine located at the top. Mclean used a discharge head of 10 m for her design calculations, thus slightly extending the range of the pump. The results for the 3 inch Spate pump quoted above indicate that water could be drawn from a depth of 25 m or more using such a cable linked system. The diaphragm return spring shown in figure 2.6 serve two purposes. The first is simply to keep the cable in tension at all times, as the cable cannot push the diaphragm down. However, the mass of the cable and the diaphragm will also affect the resonant frequency of the engine, to which they are attached. It will

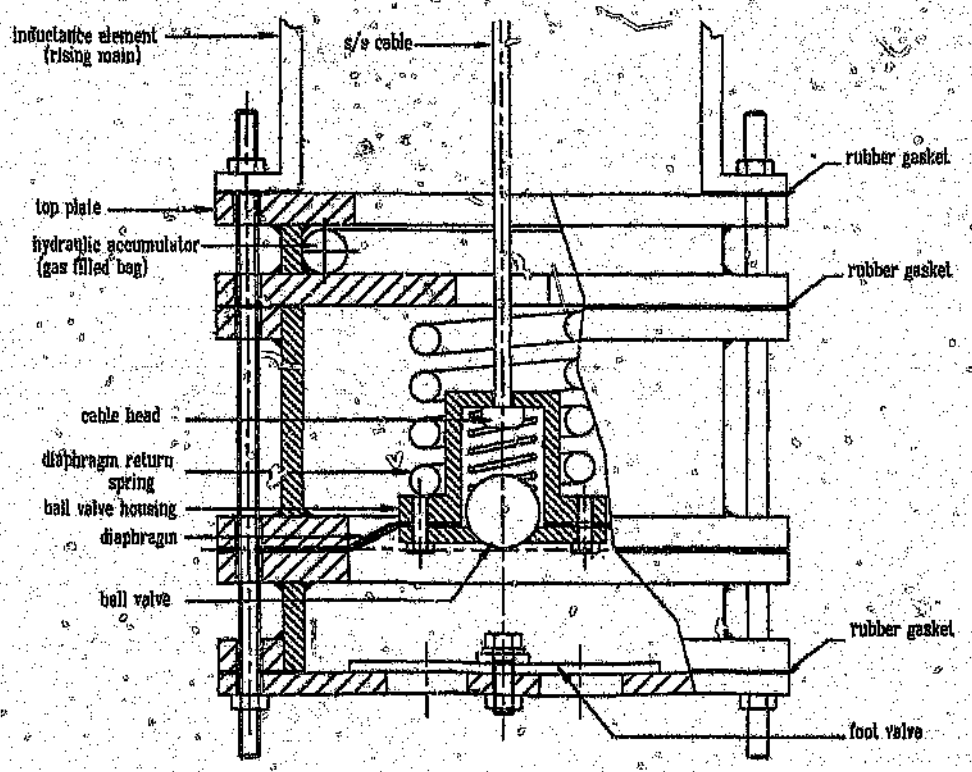

Figure 2.6: Cable linked induction pump design concept [35]

therefore be necessary to choose the spring stiffness appropriately to ensure correct matching of the pump and engine (see section 3.5).

An alternative down-well concept is shown in figure 2.7. This pump is similar to the 'Blair' hand pump described by Morgan [38]. The 'Blair' pump was designed as a low cost, simple pump for use in shallow tube wells. It has two valves, a foot valve and a piston valve, with the tube through which the water flows up the pipe acting as the pump rod. If the pump frequency is high enough, such that the acceleration of the tube downwards is far greater than the acceleration of the water column under free fall conditions, then the foot valve becomes superfluous.[1] The resulting pump thus has only one valve and no piston or diaphragm, with a consequent reduction in cost and maintenance requirements. The principle disadvantage of such a pump would be the provision of springs of sufficient stiffness to maintain a high resonant frequency of the pump components (see section 3.5).

[1]The downwards acceleration of the free-cylinder Stirling engine operating at a frequency of 33 Hz and an amplitude of 8.5 mm reaches a peak of 365 $m.s^{-2}$.

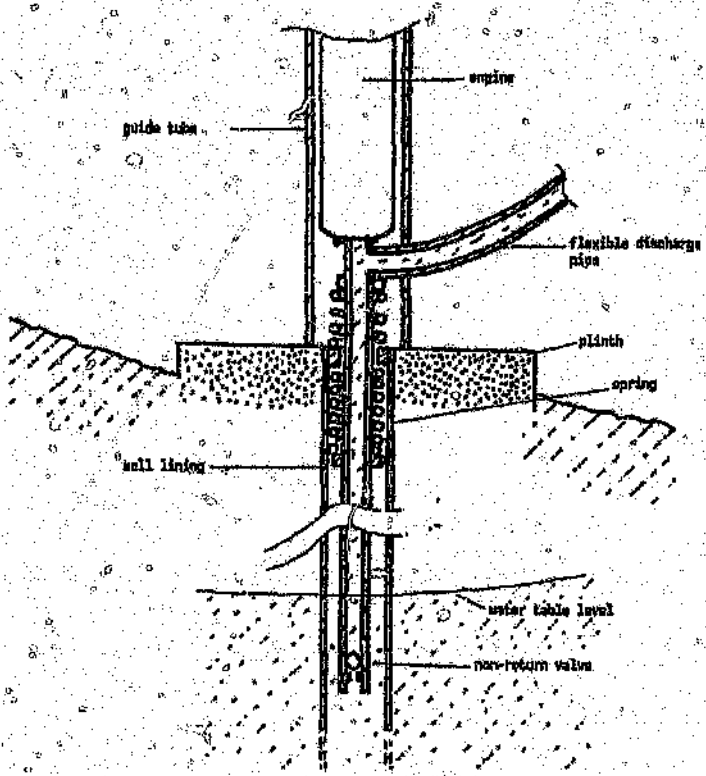

Figure 2.7: Inertia pump design concept

2.3.3 Sprag clutch system

Beale [6] describes a sprag clutch drive system which would allow the conversion of the variable amplitude oscillation of the free-cylinder engine to a lower frequency rotary motion (see figure 2.8). Such a system could be used for a variety of purposes, including the powering of a deep well reciprocating or rotary pump. As noted by Beale, in solar concentrator applications, the minimum cost per kilowatt is achieved for relatively small units (of the order of a few kilowatts). In systems requiring higher power a number of engines could be connected to a common shaft using the sprag clutch system.

2.4 Other applications

Although the water pump concept seems the most viable application of the free-cylinder Stirling engine, other possibilities may exist. Beale *et al* [4] have suggested that free-cylinder Stirling engines could be used for grinding corn, digging or post driving, or even as the power source for a jack hammer. A portable low cost vibrator would allow considerable improvements to the brick

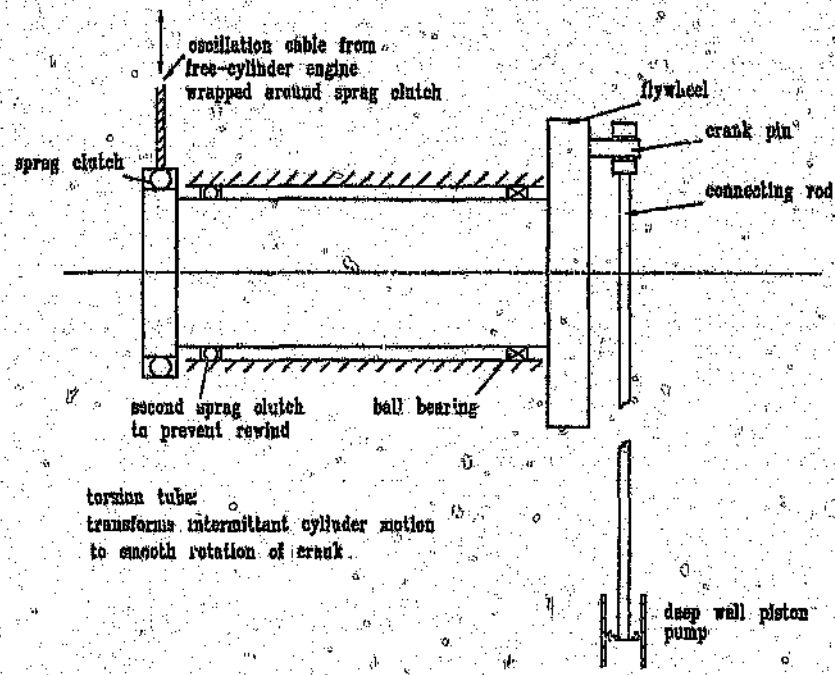

Figure 2.8: Sprag clutch drive (Redrawn from [6]).

making processes carried out in the rural areas of many developing countries[2]. A mechanical mechanism which converts the oscillatory motion to rotary motion, (such as the sprag clutch system described above) opens up a host of possibilities. Ringbom or kinematic engines may however be more suitable in such applications, although the free-cylinder engine has the considerable advantage of being able to provide shaft power from a hermetically sealed unit.

2.5 Summary

Given the above listed attributes and possible applications of free-cylinder Stirling engines, it is apparent that they are an attractive concept, reasonably well proven and worth developing further. Designs and working prototypes of all the components of the possible system have been presented in the past, and complete systems have already been produced. It should be a relatively straightforward process to design and integrate a system suitable for a specific application. With potential efficiencies similar to those of their free-piston

[2] A lower ratio of cement to sand can be used if the mixture can be vibrated in the process of moulding bricks.

counterparts, their robust attributes, as well as the economic advantages they have over other systems (table 1.1), it seems strange that they have not been commercially developed. In seeking to develop a design suitable for commercial development, this author started with an unproven Sunpower prototype. Early attempts at running the engine were a failure and the promises and hopes of developing an integrated system became trapped in the quagmire of trying to understand the fundamental operation of free-cylinder Stirling engines a little better, and to develop the tools whereby such engines could be readily designed. The focus has been on that aspect of free-cylinder engine technology which is not shared with other Stirling engines, the dynamics of the three-degree-of-freedom system.

Chapter 3

Free-cylinder Stirling engine analysis

The free-cylinder engine comprises three oscillating masses, the forces driving the oscillations being a function of time and the motion of the oscillations. Typically these force functions have small but significant nonlinear components. The thermodynamic, mechanical and heat transfer mechanisms resulting from a particular dynamic motion of the engine components are of the same form as that found in most other Stirling engines. The techniques developed in the greater Stirling engine field are therefore applicable. However, the motion of the components is, in a free-cylinder engine, a function of those forces. It is therefore necessary to couple the conventional thermodynamic, heat transfer and fluid flow models to a suitable model of the dynamic motion, and then to solve for the system as a whole. As the engine comprises three masses, with no fixed relationship to each other (such as would be provided by cranks and connecting rods), the development of a suitable model is quite complex.

Other Stirling engines, such as the free-piston, liquid piston, the Harwell thermomechancial generator and duplex free-piston Stirling refrigerators require a similar dynamic-thermodynamic coupled analysis. The problem can be tackled in a number of different ways, as described briefly below.

For some of the methods, the process can conveniently be divided into two halves, as shown in figure 3.1. Each can be solved independently, although it will usually be necessary to circle around figure 3.1 a number of times before the results of the dynamics calculations yield the same motion parameters as were used to calculate the forces acting on the components.

Accurate modelling of both paths is essential for the successful simulation

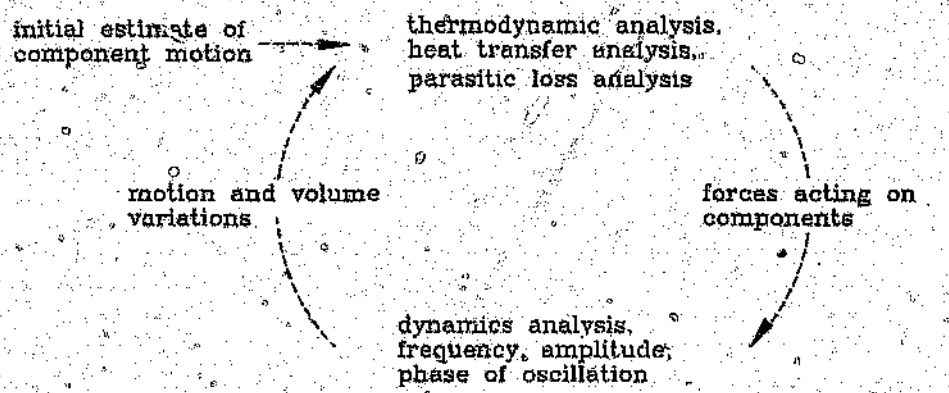

Figure 3.1: The two halves of a free-cylinder Stirling engine simulation process

of free-cylinder or free-piston Stirling engines. However, as noted above, the top path of figure 3.1 is common to all Stirling engines, while the lower path is specific to the class of engine being studied. The focus of this work has therefore been on the dynamic model, and its coupling to the upper half of the figure.

A variety of methods is available to model the lower path. The thermodynamics can be hypothetically decoupled, such that the force resulting from the work-space pressure variations is used as an external driver. If the other interactions between components are expressed as linear functions of the position, velocity or acceleration of the components, then the response of the system to the driving force can be determined analytically. Kaźmierczak and Żmudzki applied this method to free-piston Stirling engines, using it to investigate the effect of changing piston and displacer spring stiffness constants [30]. This approach, although useful in determining relative amplitudes and phases of the components at different frequencies, fails to directly predict the actual operating frequency of an engine.

A similar approach, which makes use of the sophisticated capabilities of available electrical network analysis programmes, has been presented by Cooke-Yarborough [18]. Mechanical interactions are expressed in terms of their electrical analogues. The response of the network to an alternating voltage (excitation) at a particular frequency can then be determined. Under oscillatory conditions a feedback loop in the circuit would provide the necessary excitation, provided that loop gain and phase are correct. Adjustment of the gain

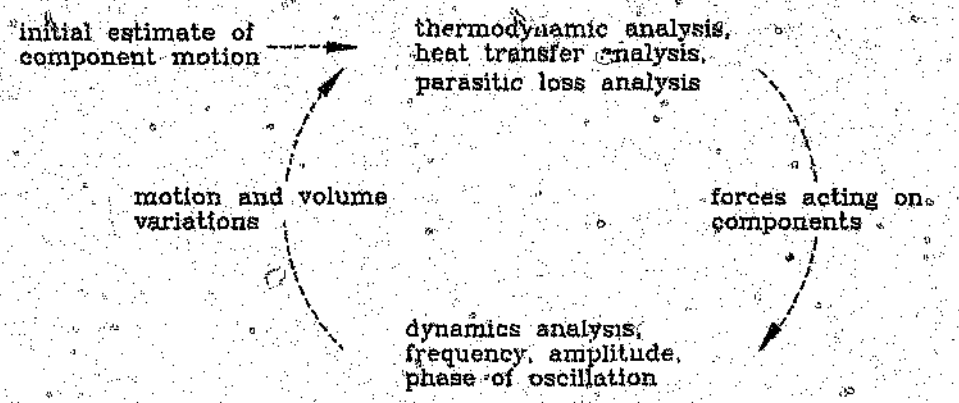

Figure 3.1: The two halves of a free-cylinder Stirling engine simulation process

of free-cylinder or free-piston Stirling engines. However, as noted above, the top path of figure 3.1 is common to all Stirling engines, while the lower path is specific to the class of engine being studied. The focus of this work has therefore been on the dynamic model, and its coupling to the upper half of the figure.

A variety of methods is available to model the lower path. The thermodynamics can be hypothetically decoupled, such that the force resulting from the work-space pressure variations is used as an external driver. If the other interactions between components are expressed as linear functions of the position, velocity or acceleration of the components, then the response of the system to the driving force can be determined analytically. Kaźmierczak and Żmudzki applied this method to free-piston Stirling engines, using it to investigate the effect of changing piston and displacer spring stiffness constants [30]. This approach, although useful in determining relative amplitudes and phases of the components at different frequencies, fails to directly predict the actual operating frequency of an engine.

A similar approach, which makes use of the sophisticated capabilities of available electrical network analysis programmes, has been presented by Cooke-Yarborough [18]. Mechanical interactions are expressed in terms of their electrical analogues. The response of the network to an alternating voltage (excitation) at a particular frequency can then be determined. Under oscillatory conditions a feedback loop in the circuit would provide the necessary excitation, provided that loop gain and phase are correct. Adjustment of the gain

would be provided by changing load and/or control circuit resistors. Phase of the feedback loop would have to be adjusted either by modifying the tuning of components in the loop, or by modifying the excitation frequency (this corresponds to a change in engine frequency).

A 'state space analysis' approach was presented by Goldberg [25, pages 22 to 131]. This involves linearization of all equations, including the thermodynamic and flow loss equations, and then solving for the system as a whole. It is a somewhat abstract method of analysis, which may have particular application at the concept design stage of an engine.

A closed form linearized solution method has been presented by Redlich and Berchowitz [44, 13]. This is one of the few analyses which has been directly applied to a free-cylinder Stirling engine. It allowed useful qualitative and quantitative assessment of the operational characteristics of free-cylinder Stirling engines. In simplifying the equations in order to produce a tractable system, Berchowitz and Redlich assumed that the case–ground spring stiffness could be ignored. The inclusion of this term, (which is significant in the engines considered here) results in significant complication of the equations. For this and other reasons noted below, their closed form approach has not been adopted here, although the Redlich and Berchowitz method still forms the foundation of the analysis used.

Benvenuto *et al* [9] have used a similar approach to investigate free-piston engine behaviour. Case motion was not included in their analysis.

A similar approach was also published by Berchowitz and Urieli [57, pages 76–80]. They analyzed a specific free-cylinder Stirling engine, the Sunpower M100. For this engine the piston motion was sufficiently small that it could be assumed to be stationary (the piston mass was 3 times that of the case), thereby allowing significant simplification of the analysis. Bounce-space pressure was assumed constant. An isothermal model assuming fixed gas-space temperatures was used. Damping coefficients were also fixed. The engine was not fully instrumented, thus detailed comparison of experimental and simulation results was not possible. However, agreement on frequency, approximate displacer–piston stroke ratio and approximate output power was quite good, as shown in table 3.1.

The linear analysis technique can be applied in an iterative form, the upper part of figure 3.1 being analyzed for an estimated set of component dynamics using *any* applicable combination of analyses, the results of this analysis being used to determine equivalent linearized coefficients for the equations of motion of the components. These equations are then used to determine a better estimate of the component dynamics, and the cycle repeated until convergence

Table 3.1: Sunpower M100 free-cylinder engine: comparison of simple linear analysis and experimental results [57].

	Linear analysis	Experiment
Frequency (Hz)	22.4	23.0
Amplitude ratio	2.25	2.5*
Output power (W)	58.5	40.0*
* Approximate values		

occurs. This allows the effect of nonlinearities to be simulated, although in an approximate form, as the coefficients representing forces which are dependant on amplitude of oscillation, such as gas-flow losses, work-space pressure variations, seal leakage, etcetera are iteratively determined as the solution converges to steady state component dynamics. This approach was applied by Berchowitz [13] and codified in a comprehensive computer programme suitable for the analysis of free-piston machines. The programme, referred to as SAUCE, has been successfully used during the development of various machines at Sunpower Inc [51]. An early version of this programme was published by Berchowitz as part of his PhD thesis [13]. More recent work by Benvenuto *et al* [10] also uses equivalent linear terms, the nonlinear terms of the analysis being represented by linear terms which result in the same contribution to power and mean pressure (or force).

If all interactions can be expressed as a function of the motion of the components, it is possible to write out equations of motion for the components, and solve these. A set of initial conditions can be selected, and a nonlinear technique used to solve the set of equations at time $t + \Delta t$. After a number of cycles, (if the initial conditions were appropriately chosen and the engine design is one that will run stably) transients should die out and the steady state oscillation of the engine will be simulated. Such an approach would require significant computational power, and is rather similar to running an experiment. The design insight available is limited, particularly if the engine configuration being modelled is not one that will allow stable oscillation. With the recent surge in personal computer capability this approach may however become more readily used, as small nonlinear components are indeed vital to the steady state operation of free-piston or free-cylinder engines, and larger desirable or undesirable nonlinear interactions are often significant. Carlini and Kucharski [15] used an unconditionally stable scheme of the Newmark method to solve a general nonlinear free-piston engine dynamic model. Their analysis was applied to a Model 10-B engine (different to the Model B-10 used for the work reported here). The engine had an inertia pump which was driven by the piston oscillations. The system thus had four moving masses, and the model

so formed is from a dynamic point of view more complete than the others presented above. Comparative simulation and experimental results were only presented at one operating point. It is not clear whether the motion of the case was significant or not, as only a single amplitude ratio and phase angle were presented. Agreement between experimental and simulation results at this operating point was good.

Beale [3], in one of the first papers to present the free-cylinder concept, discussed the use of the IBM 1130 Continuous System Modelling programme to carry out a nonlinear simulation of a free piston engine. This early engine operated in a non-sinusoidal mode, the displacer running up against an end stop at the top of its stroke, and against the piston for part of its downward stroke. A simple isothermal model was used, with the assumption that hot- and cold-space gas temperatures were at fixed temperatures. The piston and displacer were assumed to move under the influence of pressure, externally applied load, drag forces proportional to velocity, and with the geometrical restraints on motion assumed equivalent to short stiff springs and dashpots. The simulation did not attempt to determine the value of the drag force coefficients, these were inputs to the programme. The simulation predicted the dynamic motion and the frequency of the engine reasonably well. (A second experimental run did have a significantly different frequency, although this may have been due to a different charge pressure, absolute pressure instrument drift being a problem).

A similar example of a nonlinear simulation which focuses primarily on the motion of the components was presented by Ikaj *et al* [27]. They used the IBM Continuous System Modelling programme to simulate a Sunpower Model-100 free-piston engine (no case motion). Although the motion of this engine was reasonably sinusoidal, the principal nonlinearity included in their model was that induced by the centering ports. Frequency was well simulated, the piston–displacer phase angle was significantly underpredicted and the amplitudes did not agree completely. The effects of the centering ports were simulated with moderate success.

Fine resolution of the processes within the engine can be obtained by dividing the system into discrete cells, to which the state, continuity, momentum and energy equations are applied. An iterative solution procedure is normally used to solve the equations for the entire system. This is the so called third order approach to the analysis of Stirling machines. It is often applied to particular areas of interest in the engine, rather than for solving the entire engine design at once. An example of this type of computer simulation is that presented by Berchowitz *et al* [11]. An indication of the computing power required for this sort of approach is given by Bauwnes [2]. The MS*2 code, which only claims to model the thermodynamic aspects of Stirling engines, performs as follows: 'For

a moderately accurate model, in which an engine is divided in 200 volumes, with four time steps per crank angle degree, about 200 revolutions are required for the solution to reach a reasonably periodic behaviour. That takes about 6 minutes of cpu time on a CRAY X-MP, running at approximately 100 Mflops (millions of floating point operations per second), and costs less than $200.'

Such a third order system could be structured to include calculation of the motion of the components in a free-piston or free-cylinder engine, although this author has not identified any published or reported simulation programme which does this.

This author is not aware of any available package (of any order) which is directly suitable for the analysis of free-cylinder Stirling engines. A slightly modified version of the SAUCE computer programme referred above was made available to this author by Sunpower Inc. during 1988. SAUCE is an ever growing package, and has been further developed since 1986 by Berchowitz and other members of the Sunpower team. The package has been successfully used in the design and development of a number of free-piston Stirling engines. The programme's use of the linear analysis method for determining the component dynamics, its tried and tested thermodynamic and heat transfer components, coupled with its ability to run quickly on personal computers made it an attractive tool with which to explore the operational characteristics of free-cylinder Stirling engines.

SAUCE is a design tool used by Sunpower, and the code is proprietary. Thus, no computer code is presented as part of this dissertation. However, that portion of the programme which deals with the upper part of figure 3.1 is essentially that presented by Berchowitz [13], while the lower half, and the linearization techniques, are described in detail below. Gas-inertia terms, centering-port losses and cooler-port cut off effects have not been included in the free-cylinder analysis, although they were present in the free-piston version supplied to this author. The original programme was written in 'Microsoft Basic' as used on the Apple Macintosh computer. Apple computers were not readily available to this author. The programme has therefore been transcribed so that it can be run using the 'Quickbasic' programming language in an MS-DOS environment. This allowed the maintenance of maximum compatibility between the original programme and that developed for FCSE analysis. As an extra set of motion equations have been included in the free-cylinder analysis, it is referred to as 3-D SAUCE for ease of reference.

3.1 Linear dynamics approach

As noted above, the analysis below is based primarily on that presented by Redlich and Berchowitz [44, 13]. Some aspects of the presentation by Benvenuto *et al* [9] are used as they help to explain the commonly accepted role of the characteristic equation a little better.

In the discussion below, any force, acceleration or motion in an upwards direction is considered positive (where upwards refers to the hot end of the engine). The system of interest has three moving masses, the displacer, piston and cylinder (sometimes referred to as the case). There is a fourth mass, the earth, which is sufficiently massive such that any accelerations imparted to it by the smaller three masses will be negligible. An equation of motion can be written for each of the smaller masses. From Newton's second law, the sum of all the forces acting on each mass, including the inertia terms, must be zero at any instant in time. The forces acting on a particular mass could be the result of its position, its velocity, its acceleration and also the position, velocity and acceleration of the other masses interacting with it. The forces interacting between the masses will also depend on the state of the working fluid inside the engine, and the resulting pressures acting on the components. In order to apply the linear analysis method, these forces are represented as a function of the position, mass or acceleration of the three masses, as will be shown later. Solution of the equations of motions is considerably simplified by the process of linearization. This will introduce error. Provided that the real processes being simulated are reasonably linear, and that linearization is carried out at the operation amplitudes and frequencies, this induced error will be acceptable. The extensive application of the SAUCE simulation by Sunpower Inc. in the design of free-piston Stirling engines has clearly demonstrated the utility and reasonable accuracy of the method. As shown in section 6.5, even where significant nonlinearities are present in the system, the linearized method may still yield useful results. The determination of the linear coefficients is discussed in more detail in section 3.3, 3.4 and 3.5.

Since the connection of the engine to the earth is only made through a spring, and a load device attached to the case, any force on the piston or displacer must be balanced by corresponding forces on the other two masses. No force can be transmitted from the earth outside, except through the terms which relate to x_c in the equation of motion for the case. In the process of forming the matrix equations which represent the forces acting on the components, a check can be made to ensure that all the forces are indeed balanced. The full equations of motion can be presented in a matrix form as shown below.

$$[\mathbf{M}]\ddot{\mathbf{x}} + [\mathbf{D}]\dot{\mathbf{x}} + [\mathbf{K}]\mathbf{x} = \mathbf{0} \tag{3.1}$$

where **M**, **D**, and **K** represent 3×3 matrixes and **x** is the column vector of motion functions:

$$\begin{bmatrix} x_d(t) \\ x_p(t) \\ x_c(t) \end{bmatrix}$$

The Laplace transform of this matrix equation can be expressed as follows:

$$[s^2\mathbf{M} + s\mathbf{D} + \mathbf{K}]\hat{\mathbf{x}} = [\mathbf{A}_{I.C}] \tag{3.2}$$

or :

$$[\mathbf{G}(s)]\hat{\mathbf{x}} = [\mathbf{A}_{I.C}] \tag{3.3}$$

$[\mathbf{A}_{I.C}]$ will be a column vector of the form $[s\mathbf{M} + \mathbf{D}]\mathbf{x}_{t=0} + [\mathbf{M}]\dot{\mathbf{x}}_{t=0}$.

If known initial conditions exist, since $[\mathbf{G}(s)]$ is known, it is possible to solve for $\hat{\mathbf{x}}$ as a function of s, although the algebraic manipulation involved would be daunting. The inverse Laplace transform of $\hat{\mathbf{x}}$ would then yield **x**.

Although initial conditions are not normally known, a heuristic analysis allows one to gain insight into the solution procedure, and indirectly to determine suitable initial conditions. Cramer's rule can be applied to the system (3.3) yielding:

$$\hat{x}_d = \frac{|[\mathbf{A}_{I.C.}\ \mathbf{G}(s)_{1:3,2}\ \mathbf{G}(s)_{1:3,3}]|}{|[\mathbf{G}(s)]|} \tag{3.4}$$

$$\hat{x}_p = \frac{|[\mathbf{G}(s)_{1:3,1}\ \mathbf{A}_{I.C.}\ \mathbf{G}(s)_{1:3,3}]|}{|[\mathbf{G}(s)]|} \tag{3.5}$$

$$\hat{x}_c = \frac{|[\mathbf{G}(s)_{1:3,1}\ \mathbf{G}(s)_{1:3,2}\ \mathbf{A}_{I.C.}]|}{|[\mathbf{G}(s)]|} \tag{3.6}$$

$$\tag{3.7}$$

As an example of the notation used above, $\mathbf{G}(s)_{1:3,2}$ refers to the second column of matrix $[\mathbf{G}(s)]$.

The numerators of each of the above expressions will be functions of s of order 5, while the denominators are functions of s of order 6. Provided that $|[\mathbf{G}(s)]|$ has distinct roots (s_1, s_2, ... s_6), the above expression can be decomposed

into partial fractions. The form of the equations is the same for all three components, that for the displacer being presented below:

$$\hat{x}_d = \frac{R_{d1}}{s-s_1} + \frac{R_{d2}}{s-s_2} + \frac{R_{d3}}{s-s_3} + \frac{R_{d4}}{s-s_4} + \frac{R_{d5}}{s-s_5} + \frac{R_{d6}}{s-s_6}$$

The residues, $R_{di\,(i=1\ldots6)}$ can often be determined symbolically in a simple system. They will usually be complex numbers. In the general form they are:

$$R_{di} = \lim_{s \to s_i}(s-s_i)\frac{|[\mathbf{A}_{I.C.}\,\mathbf{G}(s)_{1:3,2}\,\mathbf{G}(s)_{1:3,3}]|}{|[\mathbf{G}(s)]|}$$

The inverse Laplace transformation of $\hat{\mathbf{x}}$ gives the motion of the components in the time domain (displacer used as an example, piston and case equations have the same form):

$$x_d(t) = R_{d1}e^{s_1 t} + R_{d2}e^{s_2 t} + R_{d3}e^{s_3 t} + R_{d4}e^{s_4 t} + R_{d5}e^{s_5 t} + R_{d6}e^{s_6 t} \qquad (3.8)$$

The motion of each of the components is thus a combination of six exponential functions, each multiplied by a complex number R_{di}. Although known initial conditions are required to determine the values of R_{di}, the exponents of each term are a function of the roots $s_1 \ldots s_6$ of $|[\mathbf{G}(s)]|$ only. They determine the behaviour as a function of time, and are therefore of great interest.

Although $[\mathbf{G}(s)]$ is a function of s, the coefficients, which come directly from the matrixes **M**, **D** and **K** (equation 3.2) are all real, thus the coefficients of the characteristic equation $|[\mathbf{G}(s)]| = 0$ are all real. The roots of this equation are therefore either real or must occur in complex conjugate pairs (so that the factors when multiplied together yield a polynomial with real coefficients only). If a particular root pair is chosen as an example, it follows that the residues must also occur in complex conjugate pairs so that the final solution for $x(t)$ is in the real domain only. The combined effect of such a root pair can then be represented as follows.

$$x(t) = (A + jB)e^{(a+jb)t} + (A - jB)e^{(a-jb)t}$$

where $R_1 = A + jB$, $R_2 = A - jB$, $s_1 = a + jb$, $s_2 = a - jb$. By substituting Euler's formula ($e^{jbt} = \cos bt + j \sin bt$) and simplifying we can obtain, for each

such root pair and its associated complex conjugate residues, a deceptively simple term:

$$A_r e^{at} \cos(bt + \phi)$$

where $A_r = \sqrt{(2A_2 + 2B_2)}$ and $\phi = \arctan(B/A)$. (Care should be taken to ensure that the correct quadrant for ϕ is determined from A and B).

Any real roots must be associated with real residues in order to obtain real $x(t)$. Expressed with real coefficients, the contribution of such roots would be: $A_i e^{a_i t}$, $A_i = R_i$ (real) and $a_i = s_i$ (real). The complete equation of motion for each component therefore contains terms of the form $A_{r_i} e^{a_i t} \cos(b_i t + \phi_i)$ and/or $A_i e^{a_i t}$.

The behaviour of the system can thus be deduced from the location (in the complex plane) of the roots of the characteristic equation:

$$|[G(s)]| = 0 \tag{3.9}$$

Any root with a positive real component (a_i) will lead to unbounded displacement of the components as $e^{a_i t} \to \infty$ for $a > 0$ as t increases. Thus occurrence of such roots implies unstable behaviour. The contribution of any term with a negative real component will gradually disappear as $e^{a_i t} \to 0$ for $a < 0$ as t increases.

Complex conjugate root pairs will contribute an oscillatory motion to the system, the frequency of oscillation being determined by the magnitude of their imaginary component b. The amplitude of oscillation will either decay or grow, depending on the value of the real component a. If $a = 0$ then steady oscillation at a constant amplitude and frequency will occur. Motion of the components resulting from such a root would be sinusoidal at a frequency $b/2\pi$ Hz.

In summary: for stable oscillation it is necessary that there be no roots of the characteristic equation with positive real values, and at least one root pair with a non-zero imaginary component and a zero real component. At first this seems very unlikely. Would the coefficients of [G] be precisely those required to obtain a purely imaginary root of equation (3.9)? In the solution procedure followed below it will be seen that the coefficients of $[G(s)]$ are modified to obtain just this special condition. In the real Stirling engine, it is the nonlinearities of the engine which do this subtle modification of the coefficients, ensuring stable oscillation at a constant amplitude. Figure 3.2 shows a typical root map for the 'water pump' engine. The matrix coefficients were calculated, and substituted into the matrix equation of motion (3.2) and the determinant ($|[G(s)]|$)

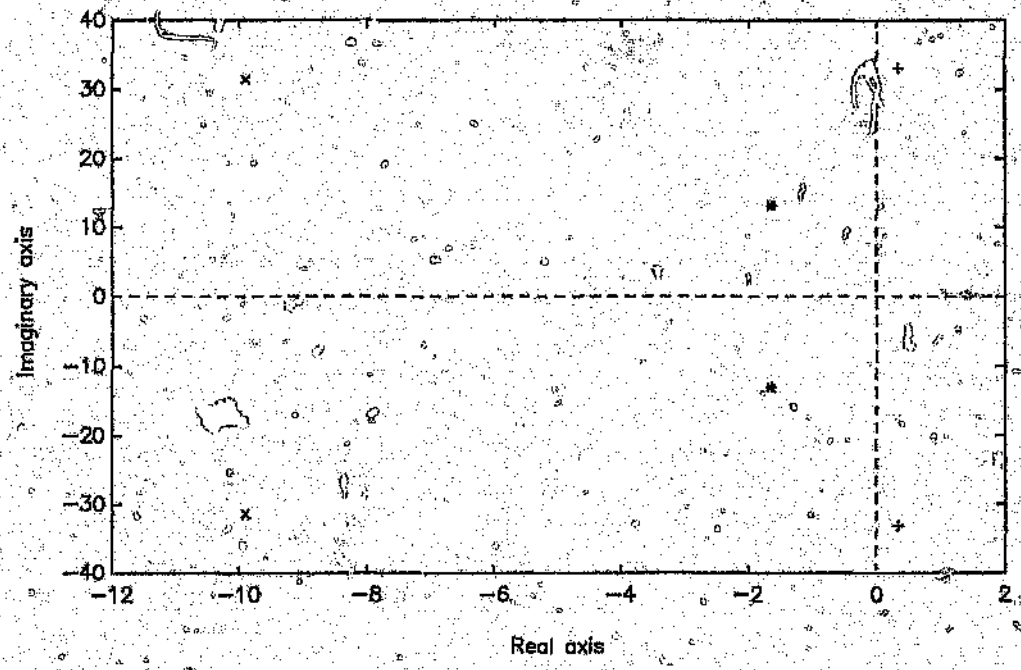

Values have been divided by 2π to yield oscillation frequency in Hz

Figure 3.2: Location of roots of characteristic equation in the complex plane.

evaluated. A standard subroutine given by Tse [53] (and incorporated into the 3-D SAUCE programme) was used to find all six of the complex roots of the characteristic equation. There are no real roots, and two of the complex conjugate root pairs occur in the left hand plane, thus their effects will die away and can be ignored. The third root pair lies close to the imaginary axis, but not on it, indicating that for the given linear coefficients, the system is not stable. Oscillations would gradually increase, and if the engine were a perfectly linear device the oscillations would become unbounded. Fortunately, there are usually processes in the engine which are not perfectly linear. Turbulent flow losses, (as an example), will increase according to the square of the component oscillations. As the amplitudes increase, so the linearized coefficients reflecting these losses in the matrix equations of motion will change, moving the location of the root pair towards the imaginary axis, until stable oscillation is achieved with the roots located on the imaginary axis. Should the amplitude increase too much, (or the hot-end temperature be reduced), then the roots would move to the left of the imaginary axis. The negative real component of the root pair would then cause the oscillations to die down. Nonlinearities of the engine would hopefully result in the roots moving back towards the imaginary axis, restoring stable oscillation. If the amplitude-linked changes to the matrix coefficients as a result of the nonlinearities are insufficient, or in the

wrong direction, then the oscillations will simply die away.

In the linear analysis model, the nonlinear variation of the coefficients is not included directly, (although, as will be shown later, they are indirectly included through an iterative process). It is thus necessary to relax at least one of the terms of $[\mathbf{G}(s)]$. Iterative (or in simpler cases, analytical) techniques can then be used to determine a value for this term which results in the required root map . In the free-cylinder engine analysis utilized here, it was convenient to vary the case-ground damping coefficient (D_{cg}), using a simple iterative procedure to find an appropriate value which yields four roots with negative real components, and one pair with zero real components. In a free-piston simulation it would be convenient to relax the damping coefficient which accounts for the load between the piston and the case, (D_{pc}). Figure 3.3 shows the root locus as a function of D_{cg} for the same engine configuration as in the previous figure. Figure 3.4, which shows only the real components of the roots, is easier to interpret. For the given linear coefficients the engine would only operate stably if the load damping coefficient was 308.189... Nm/s, the point at which one of the root pairs crosses the imaginary axis.

At this stage in the analysis procedure we now have knowledge of the frequency of operation, but not yet of the amplitudes and phases of oscillation. Uncertainty about the initial conditions makes the determination of the residues R_{di}, and hence of the amplitude and phase of oscillation impossible. However, since the form of the steady state solution is now known (sinusoidal at a frequency b rad.s^{-1}), it can be substituted into the time domain equation of motion. If one amplitude is assumed fixed, then these equations can be used to determine the other two amplitudes and their phase relative to the fixed amplitude. This is equivalent to substituting $s = jb$ into any two of the rows of equation (3.2) (or equation (3.3)) and setting $[\mathbf{A}_{1C}] = [\mathbf{0}]$. (Since $|[\mathbf{G}(s)]| = 0$ for $s = jb$ the three rows of $[\mathbf{G}(s)]$ are no longer independent). This process yields complex amplitudes $\overline{X}_d$, $\overline{X}_p$ and $\overline{X}_c$. It is convenient to express jb as $j\omega$. The motion $x_i(t)$ of a particular component can then be expressed as the real part of the equation below.

$$x_i(t) = \overline{X}_i e^{j\omega t} \tag{3.10}$$

The real part of equation (3.10) can be expressed as:

$$x_i(t) = X_i \cos(\omega t + \phi_i) = \Re(\overline{X}_i e^{j\omega t}) \tag{3.11}$$

where $\overline{X}_i = A + jB$, $X_i = \sqrt{A^2 + B^2}$, $X_i \cos(\phi_i) = A$ and $X_i \sin(\phi_i) = B$.

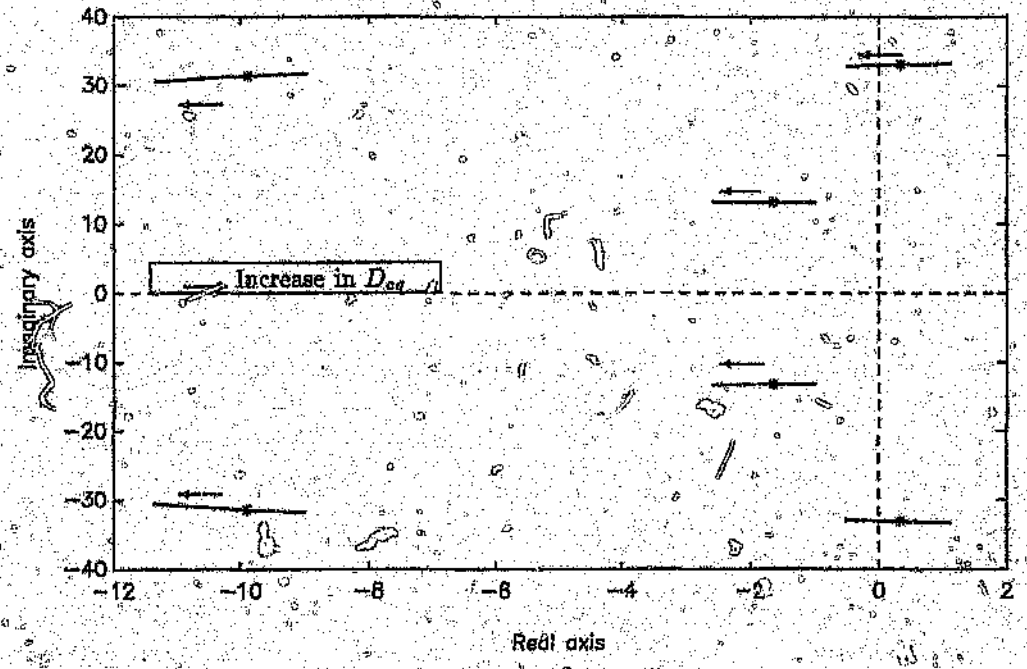

Values have been divided by 2π to yield oscillation frequency in Hz

Figure 3.3: Root locus map, for values of D_{eq} from 150 to 400 Ns/m

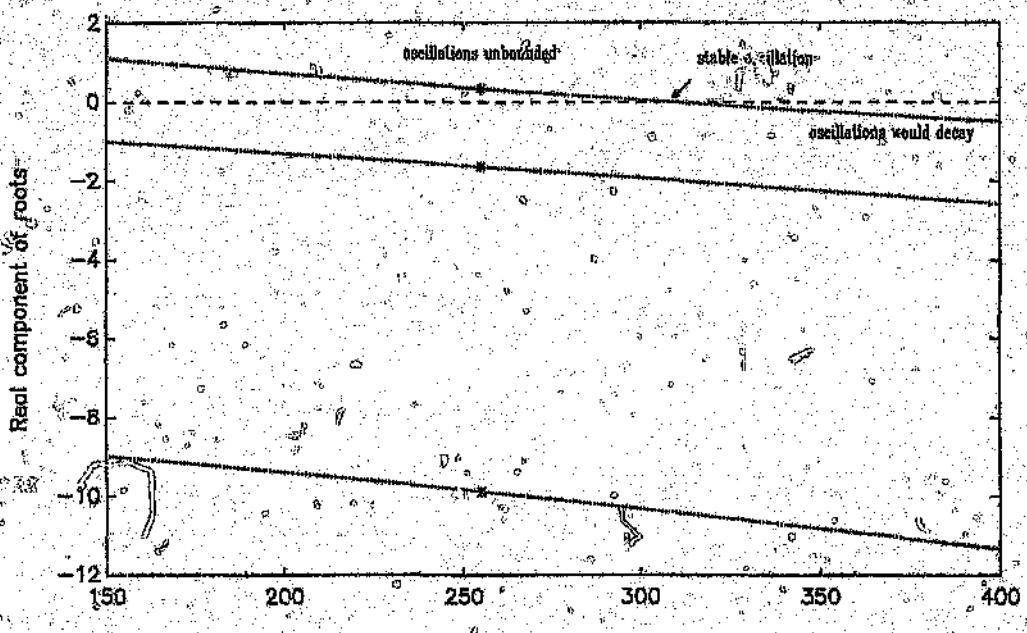

Values have been divided by 2π to yield oscillation frequency in Hz

Figure 3.4: Real component of above plotted roots versus D_{eq}

In equations (3.12) to (3.20) the position, velocity and acceleration equations for each component are set out for easy reference.

$$x_d = X_d \cos(\omega t + \phi_d) \tag{3.12}$$
$$\dot{x}_d = -\omega X_d \sin(\omega t + \phi_d) \tag{3.13}$$
$$\ddot{x}_d = -\omega^2 X_d \cos(\omega t + \phi_d) \tag{3.14}$$

$$x_p = X_p \cos(\omega t + \phi_p) \tag{3.15}$$
$$\dot{x}_p = -\omega X_p \sin(\omega t + \phi_p) \tag{3.16}$$
$$\ddot{x}_p = -\omega^2 X_p \cos(\omega t + \phi_p) \tag{3.17}$$

$$x_c = X_c \cos(\omega t + \phi_c) \tag{3.18}$$
$$\dot{x}_c = -\omega X_c \sin(\omega t + \phi_c) \tag{3.19}$$
$$\ddot{x}_c = -\omega^2 X_c \cos(\omega t + \phi_c) \tag{3.20}$$

The solution could now be considered complete, if the Stirling engine was a simple linear machine. However, there is a strong interaction between the actual dynamics of the components and the values of the coefficients in the spring [**K**], and damping [**D**], matrixes. In sections 3.3 and 3.4 the procedures used to determine these linear coefficients will be discussed. Suffice it then to say here that it is necessary to determine new values for the coefficients of [**G**(*s*)] using the above calculated dynamic motions. These can then be substituted back into the characteristic equation and the cycle repeated until conversion of both the thermodynamic and dynamic systems occurs. A further consequence of the nonlinearity of the interactions in the engine is that starting values for the dynamic system must be assumed in order to calculate the matrix coefficients for the first iteration.

Figure 3.5 shows the simulation algorithm.

3.1.1 Closed-form solutions

The above description of the linear analysis method does not include any simplification of the characteristic equation. All the terms of the mass, damping and spring matrixes have been included in the numerical simulation. Previous workers have made some assumptions which have allowed them to reduce the order of the characteristic equation to 5 (Redlich & Berchowitz) [44] or 4 [57]. The latter analysis assumed that the piston motion was insignificant, thereby reducing the number of degrees of freedom from 3 to 2. Redlich and Berchowitz

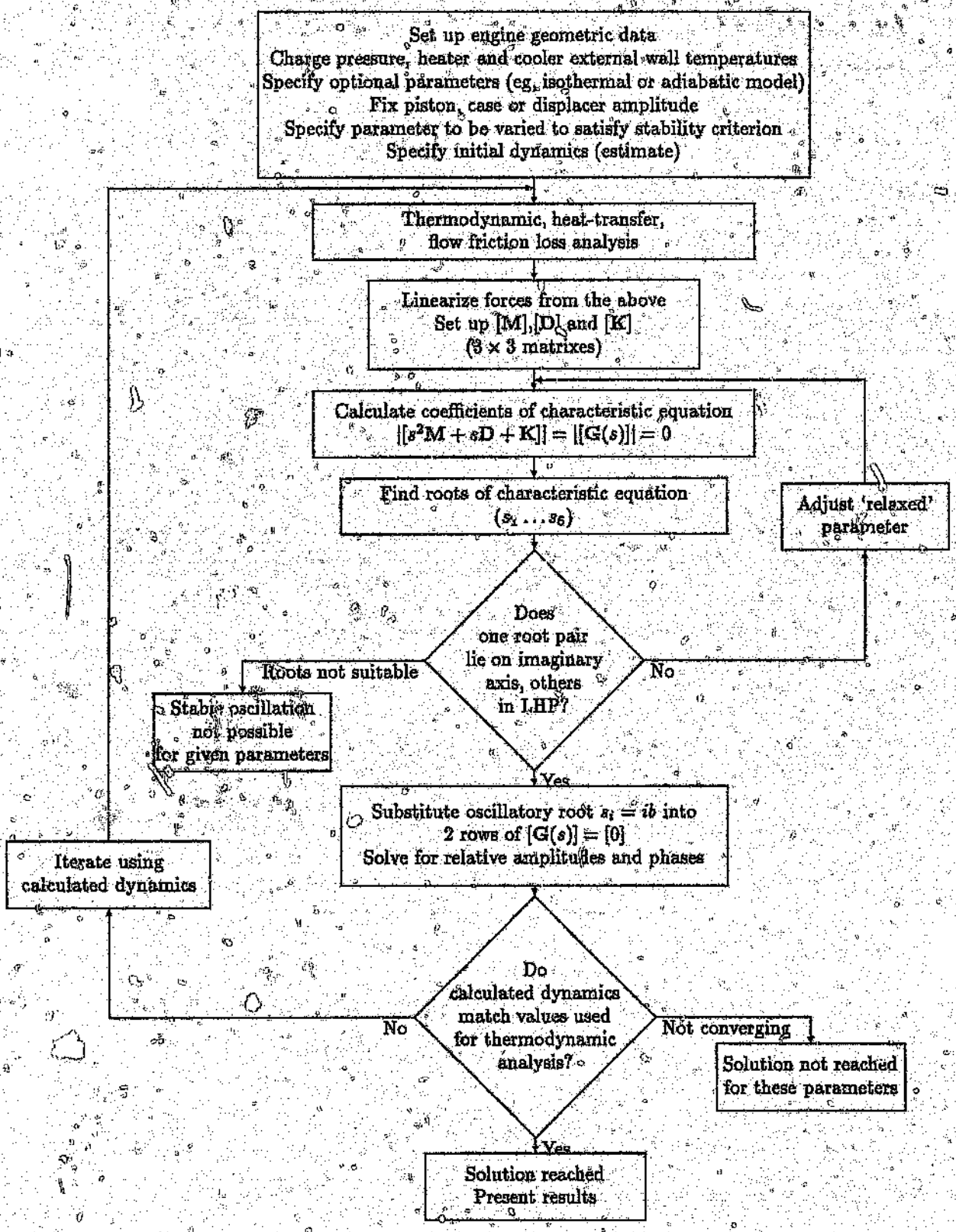

Figure 3.5: Simulation of FCSE: flow chart

included the casing motion, but used the force balance on the entire system to simplify the case equation of motion to:

$$\hat{x}_c = -\frac{m_p s \hat{x}_p}{m_c s + D_{cg}}$$

This was then substituted into the piston and displacer equations to yield a tractable system. This simplification, which has significant advantages as it allows elegant closed-form analysis of the general behaviour of the machine, was unfortunately not applicable to the two engines analyzed here. The full equation for the motion of the centre of mass of the system is:

$$m_d \ddot{x}d + D_{cg}\dot{x}_c + K_{cg}x_c + m_p\ddot{x}_p + m_d\ddot{x}_d = 0$$

Thus, using the Laplace domain form:

$$\hat{x}_c = -\frac{m_p s^2 \hat{x}_p}{m_c s^2 + D_{cg}s + K_{cg}} - \frac{m_d s^2 \hat{x}_d}{m_c s^2 + D_{cg}s + K_{cg}}$$

Both engines investigated had significant values of K_{cg}. The inclusion of this term increases the order of s from 5 to 6. Furthermore, although the displacer of both engines was significantly lighter than the other components, its amplitude of oscillation was sometimes much higher than that of the other components, making the second term on the right hand side of the above equation important. Elegant simplification was therefore not achieved. However, some of the behavioural information can still be obtained, as shown in section 3.6. The general format of the solution procedure used here (and incorporated into the 3-D SAUCE programme) does make it much easier to investigate different configurations, or to investigate the effect of even minor terms, as the solution is applied to the complete damping and spring matrixes.

3.2 Thermodynamic, heat transfer and parasitic loss analysis

Berchowitz, in developing the original version of the SAUCE programme, presented (and where necessary derived) a number of equations and techniques which allowed closed form, or else quick iterative procedures to be used to calculate the gas pressures, gas flow rates, and the magnitude of the various

loss mechanisms required in order to generate the mass, spring and damping matrixes described in the preceding sections. These equations all assumed sinusoidal motion of the piston and displacer and zero case motion. These subroutines have been left almost entirely unaffected by the modification of the program to allow simulation of free-cylinder Stirling engines. The free-cylinder absolute motions of the piston, case and displacer were simply translated to motions relative to the case. These relative motions of the piston and the displacer with respect to the case could then be passed to Berchowitz's original subroutines, and the system treated as if it were a standard free-piston engine. Where necessary, results returned from Berchowitz's subroutines were transferred back to the absolute motion co-ordinates prior to determining coefficients of the mass, spring or damping matrixes.

The reader is therefore referred to Berchowitz's PhD dissertation [13] for a detailed development of the analysis used, and for a listing of the subroutines in their original form. The sections below are intended to provide a short description of the capabilities and options provided by Berchowitz.

It is however important to state that almost any Stirling engine simulation or analysis programme could be linked to the linear dynamics approach described in the preceding sections. Provided that linearized forces acting on all components of the engine can be obtained from the Stirling engine simulation, then the linear analysis can be used to predict the resulting motion of the components, which could be fed back to the Stirling engine simulation, and the process cycled through until convergence is reached.

3.2.1 Work-space pressure vector

In section 3.3.2 the assumption is made that a linearized pressure vector could be determined for given volume variations of the working spaces. This assumption has often been accepted, and is used in the works already mentioned Berchowitz [13], Urieli & Berchowitz [57], Redlich & Berchowitz [44]. The SAUCE programme has two options available to determine this pressure vector. One can either assume isothermal working spaces, or adiabatic working spaces. The basic assumptions of each are reviewed below.

Isothermal analysis

In a real Stirling engine, there is some gas in each of the working spaces at any given time. The gas is certainly not at some uniform state. If the total mass of gas (m_i) is known, and the temperature and volume of the various spaces is

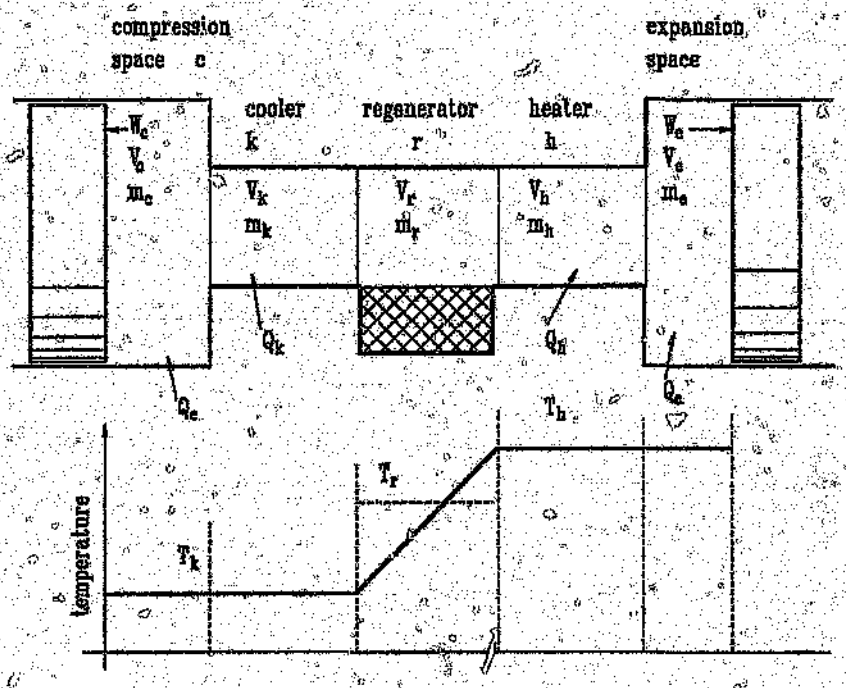

Figure 3.6: Temperature distribution and volume space labels: Isothermal analysis (Redrawn from Urieli & Berchowitz [57, p 21]).

known, then it is possible to express the gas pressure (assuming an ideal gas) as:

$$p = \frac{m_t R}{\frac{V_c+V_k}{T_k} + \frac{V_r}{T_r} + \frac{V_h+V_e}{T_h}} \tag{3.21}$$

If the temperature distribution in the regenerator is linear, then T_r can expressed as:

$$T_r = \frac{T_h - T_k}{\ln(T_h/T_k)}$$

The principle assumption made is that the gas temperatures in each of the spaces are constant throughout the cycle. This implies heat exchangers capable of infinite heat transfer rates. Other assumptions which are made in the isothermal analysis are:

- There is no spatial pressure drop.
- There is no leakage of working fluid.
- Cyclic steady state is established.
- Gas kinetic and potential energy is neglected.

The known volume variations can then be substituted into the above equation for the pressure, and the linearized pressure vector can then be determined.

The linearized pressure vector used in the SAUCE programme is derived by assuming sinusoidal volume variations of the compression and expansion spaces. This follows the Schmidt analysis, after Gustav Schmidt who published the basis of the analysis in 1871 [59, p 47]. The reader is referred to Berchowitz [13, pp 47–78] for a full derivation of the isothermal analysis used in the SAUCE programme. The coded subroutine is listed as subroutine *Isothermal:* [13, pp 400–401].

Given the pressure vector, the energy equation can be applied to the cells of the engine shown in figure 3.6 to obtain the instantaneous heat transfer required in the regenerator, and across the expansion and compression space boundaries. A consequence of assuming expansion and compression spaces at constant temperatures, is that the heater and cooler heat transfer rates calculated from the energy equation are zero. All external heat transfer takes

place across the compression and expansion space boundaries. Integrating the equations for the latter two spaces allows one to obtain the approximate heating and cooling requirements of the engine. To these must be added that portion of the required regenerator heat transfer which does not take place in the actual regenerator (as a result of its effectiveness being less than one), as well as conduction, hysteresis and other parasitic losses.

The Schmidt analysis, as extended by Berchowitz, also allows one to calculate linearized gas flow rates through the heater, cooler and regenerator (see section 3.2.3).

3.2.2 Adiabatic analysis

In a practical engine heat transfer will occur both across the boundaries of the expansion and compression space, and the surfaces of the heater and cooler. However the expansion and compression space walls are usually not effective heat exchangers, and it has thus been argued that it is more appropriate to treat the working spaces of Stirling engines as adiabatic [57, p 86]. This implies that all external heat transfer must occur at the heater and cooler heat exchangers. The adiabatic analysis is more difficult to treat analytically, and closed form exact solutions can not be obtained. However, numerical techniques can be used to solve the nonlinear differential equations. A clear exposition of this method is presented by Urieli and Berchowitz [57, pp 86–91]. Urieli and Berchowitz also note that the adiabatic analysis does not result in significantly different performance to that predicted by the isothermal analysis. Although efficiency is lower due to the irreversibilities introduced, the indicated power is usually higher as a result of higher pressure swings.

Berchowitz [13, pp 361–381] has presented an adiabatic analysis of the cycle which can be used in the SAUCE programme as listed [13, pp 401–402]. The solution is approximate, relying on linearization of equations where necessary. Iteration is required, however convergence is rapid and the computational time required is more than an order of magnitude less than for the numerical method. The two methods have similar accuracy [13, p 379].

The basic assumptions of the analysis are:

- The temperature of the gas in the cooler is constant (T_k),
- The temperature of the gas in the heater is constant (T_h),
- Regeneration is perfect.

- A linear temperature profile is assumed along the regenerator.
- There is no spatial pressure drop or leakage of the working gas.
- Gas kinetic and potential energy is neglected.
- The working gas is ideal.
- Volume variations are sinusoidal.
- The expansion and compression spaces are adiabatic and perfectly mixed.

The enthalpy of gas crossing the boundary between working space and heat exchanger is assumed equal to that of the gas in the space which it is leaving. One thus requires flow reversal points, with different equations being applicable for different portions of the cycle.

The principle results of the analysis are:

- The mean temperatures of the gas in the expansion and compression spaces,
- Compression and expansion space temperature amplitudes and phase,
- Mass flow amplitudes and phase,
- The cyclic work in the compression and expansion spaces (from which by inspection of a control volume containing either the heater or the cooler the required heater and cooler loads can be deduced),
- The amplitude and phase of the pressure wave (if required then the second harmonic of this pressure wave can also be evaluated).

3.2.3 Heat transfer analysis

Either of the above analyses will provide the basic data necessary for the calculation of the heat exchanger performance. Heat exchanger analysis involves a number of steps. Firstly, it is necessary to determine the actual heat loads on the three heat exchangers. The above analysis yields the thermodynamic load on the cooler and heater. However to this must be added gas and internal wall conduction losses, shuttle losses, expansion and compression space hysteresis losses, the gas flow losses, and the displacer appendix gap losses. Although the regenerator heat capacity is usually assumed to be sufficient such that the

matrix temperature remains constant, the heat transfer rate will not be sufficient to maintain the assumed constant linear temperature profile shown in figure 3.6. During the cold blow the gas temperature will be lower than that of the matrix, while during the hot blow the temperature will be higher than that of the matrix. The cooler and heater must make up for this extra heat load as well. A small modification was made to the subroutine dealing with regenerator effectiveness, as a discrepancy was noted between the equations as coded in the subroutine and those derived by Berchowitz in the body of his thesis [13]. Details are given in appendix E.

Given the final heat loads, and the gas flow rates, the heat exchanger heat transfer coefficients are calculated, and the resulting required temperature difference between the external wall temperature and the gas bulk temperature in the heater and cooler determined. These gas bulk temperatures are used for the next iteration of the thermodynamics cycle evaluation.

The gas flow losses in the heat exchangers are also required (section 3.4.3). Often steady flow heat transfer and friction loss correlations have been assumed for Stirling engine analysis, with reasonable results [13, p 132]. The version of SAUCE used here has two possible options which are intended to account for the effects of oscillatory flow on the heater and cooler heat transfer and flow loss coefficients. The Trika method is described by Berchowitz [13, pp 133] and listed in a computer coded form on page 405 of the same reference. The other option, referred to as the 'Sunpower' option has not been published in the open literature, and is therefore not presented, although it was used in the simulations presented here.

The above heat transfer rate required of the heater does not include direct conduction from the heater walls along the external wall of the engine. Any such conduction loss must be added to the above determined value in order to establish the total engine heat source requirement.

3.3 The spring matrix

This matrix deals with those forces acting on the components which can be sensibly expressed as a function of the position of the components of the engine. Thus, a simple linear spring which follows the relationship $f_d = -k(x_d - x_p)$

would contribute terms to the spring matrix [K] as follows:

$$\begin{bmatrix} f_d \\ f_p \\ f_c \end{bmatrix} = - \begin{bmatrix} k & -k & 0 \\ -k & k_p & 0 \\ 0 & 0 & 0 \end{bmatrix} \begin{bmatrix} x_d \\ x_p \\ x_c \end{bmatrix} \tag{3.22}$$

There are three types of elements of the free-cylinder or free-piston class of machines which can be successfully described in terms of the spring matrix. These are: mechanical springs (typically having the characteristics shown above); gas springs, and the principle working space gas pressures. In each case, only those forces which vary during the cycle are taken into consideration, as it is assumed that there are no unbalanced static forces acting on the engine.

3.3.1 Gas springs

In order to obtain the high spring rates required for high frequency operation, many of the free-piston Stirling machines use gas springs for the displacer and/or the piston. In the Sunpower free-cylinder machine shown in figure 2.2 the displacer is sprung to the piston via the displacer bounce space while the piston is sprung to the case via the piston bounce space. By way of example, consider the piston bounce space. Berchowitz [13, pages 216–217] shows that the adiabatic gas law can be applied to the gas spring core.

Thus:

$$pV^\gamma = K \tag{3.23}$$

Differentiating equation (3.23) yields:

$$\frac{\mathrm{d}p}{\mathrm{d}V} = -\frac{\gamma p_m V_m^\gamma}{V^{\gamma+1}} \tag{3.24}$$

Linearizing equation (3.24) about $V = V_m$ yields:

$$\left.\frac{\mathrm{d}p}{\mathrm{d}v}\right|_{V=V_m} = -\frac{\gamma p_m}{V_m} \tag{3.25}$$

Now $\mathrm{d}V = A_p \mathrm{d}x$, and in terms of the matrix equation above, $k_{pp} = -\mathrm{d}f_p/\mathrm{d}x_p$, thus:

$$k_{pp} = -A_p \frac{\mathrm{d}p}{\mathrm{d}x} = \frac{\gamma p_m A_p^2}{V_m} \tag{3.26}$$

Since the gas spring acts on an equal area of the case, $k_{pc} = -k_{pp}$.

Gas spring seen by three components

The model B-10 engine has both the displacer and the piston sprung to the case through a single bounce space. Movement of each component will cause a change in the volume (and hence the bounce-space pressure) proportional to the projected area perpendicular to the axis of motion. The terms of the spring matrix resulting from such a gas space can be determined using the methods shown above, and are as follows (see figure 5.3 for the notation used):

$$\begin{bmatrix} f_d \\ f_p \\ f_c \end{bmatrix} = - \begin{bmatrix} A_r^2 \frac{\gamma p_m}{V_m} & A_r A_p \frac{\gamma p_m}{V_m} & -A_r A_c \frac{\gamma p_m}{V_m} \\ A_p A_r \frac{\gamma p_m}{V_m} & A_p^2 \frac{\gamma p_m}{V_m} & -A_p A_c \frac{\gamma p_m}{V_m} \\ -A_c A_r \frac{\gamma p_m}{V_m} & -A_c A_p \frac{\gamma p_m}{V_m} & A_c^2 \frac{\gamma p_m}{V_m} \end{bmatrix} \begin{bmatrix} x_d \\ x_p \\ x_c \end{bmatrix} \tag{3.27}$$

Work transfer

If one assumes sinusoidal motions, such a spring may transfer work from one component to the other, but there will be no energy dissipation or gain. Assuming motion of the components as in equations (3.12) to (3.20) the cyclic integral of the force acting on the displacer as a result of a linear spring between the piston and displacer would be:

$$\begin{aligned} W_d &= \oint f_d \mathrm{d}x_d = \oint (-k\dot{x}_d + kx_p)\mathrm{d}x_d \\ &= \int_0^T [-kX_d \cos(\omega t + \phi_d) + kX_p \cos(\omega t + \phi_p)]\omega X_d \sin(\omega t + \phi_d)\mathrm{d}t \end{aligned}$$

If ϕ_p is subtracted from the arguments of each of the above trigonometric terms, then the equations are simplified ($\phi = \phi_d - \phi_p$):

$$\begin{aligned} W_d &= \int_0^T -k\omega X_d^2 \cos(\omega t + \phi)\sin(\omega t + \phi)\mathrm{d}t + \int_0^T k\omega X_p X_d \cos(\omega t)\sin(\omega t + \phi)\mathrm{d}t \\ &= \int_0^T k\omega X_p X_d \cos^2(\omega t)\sin\phi \mathrm{d}t \\ &= kX_d X_p \pi \sin\phi \end{aligned} \tag{3.28}$$

Similarly, the work transferred to the piston during a complete cycle would be:

$$W_p = \int_0^T k\omega X_d X_p \cos(\omega t + \phi)\sin(\omega t)\mathrm{d}t - \int_0^T k\omega X_p^2 \cos(\omega t)\sin(\omega t)\mathrm{d}t$$

$$= -\int_0^{\pi} k\omega X_p X_d \sin^2(\omega t)\sin\phi \, dt$$
$$= -kX_d X_p \pi \sin\phi \qquad (3.29)$$

ie, $\oint f_d dx_d = -\oint f_p dx_p$.

The processes which occur in gas springs are not perfectly reversible. Losses do occur, as discussed on page 63.

3.3.2 Work-space gas pressure

The forces which result from the thermodynamic effects in the work space are approximately a function of the position of the components, but do not behave as passive springs. This 'energy converter' transfers thermal energy, into pressure fluctuations which do [illegible] work on the components of the engine. It is not important to consider the details of the thermodynamic cycle here, other authors have done justice to it (see section 3.2 for a short review of the methods used in the SAUCE programme). Suffice to say that if a linear analysis of the machine is to be carried out, then it is necessary to express the thermodynamic effects on the work-space gas pressure as a linearized pressure vector which rotates about the axes at the same frequency as the work-space volume vector. The phase angle of the vector will be different to that of the volume variations. Thus the $\oint p dV \neq 0$. This pressure vector, or rather the force which it exerts on the components can however still be expressed in terms of the spring matrix.

Assume that the pressure in the work space can be adequately represented by the following equation.

$$p(t) = |p_w|\cos(\omega t + \beta_c) + p_m \qquad (3.30)$$

where β_c is the angle by which the pressure wave leads the motion of the case. Again, assuming that there are no unbalanced static forces acting on the engine components, the effects of p_m on the dynamics of the engine can be ignored. It is necessary to express the pressure vector $p(t)$ as the sum of three vectors, each of which is a scalar product of one of the displacement vectors. At first sight it would seem that there is no unique solution. However, one of the three displacement vectors can be eliminated by expressing the other two relative to it. Hence, using equations (3.12) to (3.20):

$$x_{dc} = x_d - x_c \qquad (3.31)$$

$$x_{dc}(t) = X_{dc}\cos(\omega t + \phi_{dc}) \tag{3.32}$$

$$x_{pc} = x_p - x_c \tag{3.33}$$

$$x_{pc}(t) = X_{pc}\cos(\omega t + \phi_{pc}) \tag{3.34}$$

An equation of the form $p_w = k_1 x_{dc} + k_2 x_{pc}$ is required. Substituting equations (3.30) (ignoring p_m), (3.32) and (3.34) into the above:

$$|p_w|\cos(\omega t + \beta_c) = k_1 X_{dc}\cos(\omega t + \phi_{dc}) + k_2 X_{pc}\cos(\omega t + \phi_{pc}) \tag{3.35}$$

Setting $\omega t = \pi/2 - \phi_{pc}$ and noting that $\sin\phi = -\cos(\phi + \pi/2)$,

$$k_1 = \frac{|p_w|\sin(\beta_c - \phi_{pc})}{X_{dc}\sin(\phi_{dc} - \phi_{pc})} \tag{3.36}$$

Setting $\omega t = \pi/2 - \phi_{dc}$,

$$k_2 = \frac{|p_w|\sin(\beta_c - \phi_{dc})}{X_{pc}\sin(\phi_{pc} - \phi_{dc})} \tag{3.37}$$

Using equations (3.31) and (3.33) p can then be expressed as follows:

$$p = k_1(x_d - x_c) + k_2(x_p - x_c) \tag{3.38}$$

$$= k_1 x_d + k_2 x_p - (k_1 + k_2)x_c \tag{3.39}$$

From here, it is not difficult to express the effects of the pressure wave in terms of the spring matrix equation.

$$\begin{bmatrix} f_d \\ f_p \\ f_c \end{bmatrix} = -\begin{bmatrix} A_r k_1 & A_r k_2 & -A_r(k_1+k_2) \\ A_p k_1 & A_p k_2 & -A_p(k_1+k_2) \\ -(A_r+A_p)k_1 & -(A_r+A_p)k_2 & (A_r+A_p)(k_1+k_2) \end{bmatrix}\begin{bmatrix} x_d \\ x_p \\ x_c \end{bmatrix} \tag{3.40}$$

The difference between a conventional spring-mass damper system and the Stirling engine model is shown up by the non-symmetry of the spring matrix. Following the same procedure as shown in equations (3.28) and (3.29), it can be shown that :

$$\oint p\mathrm{d}V = \oint f_d \mathrm{d}x_d + \oint f_p \mathrm{d}x_p + \oint f_c \mathrm{d}x_c \tag{3.41}$$

Although equation (3.40) is non-symmetrical, it does however retain the property mentioned on page 40, that is $f_d + f_p + f_c = 0$ at all times.

3.3.3 Case–ground spring

K_{cg} is the spring which supports the weight of the engine. As the engine can be mounted on a stiff spring, the importance of this force on the dynamics should not be underestimated, particularly as it can be used to increase the natural frequency of the case.

In a complete system design this spring must account for any displacement related interaction between the Stirling engine and the water column within the pump. Such interaction was not considered in the work reported here.

3.4 The damping matrix

The damping matrix is that part of the mathematical model which accounts for interactions which result from the velocities of the components.

$$\begin{bmatrix} f_d \\ f_p \\ f_c \end{bmatrix} = - \begin{bmatrix} D_{11} & D_{12} & D_{13} \\ D_{21} & D_{22} & D_{23} \\ D_{31} & D_{32} & D_{33} \end{bmatrix} \begin{bmatrix} \dot{x}_d \\ \dot{x}_p \\ \dot{x}_c \end{bmatrix} \tag{3.42}$$

In a single dimensional system, the damping matrix is the only system which can account for losses. The principle drawback of the damping matrix in terms of its loss accountancy, is that it is linear. Force is a proportional function of speed. Generally forces due to turbulent gas flow are a function of the square of the velocity. Coulomb friction forces are dependant on direction of motion, but not the velocity, while gas hysteresis losses are a function of the square root of the velocity of the components (see equation (3.44)). This is however not as serious a drawback as it may first appear, as the value of the loss can be determined using any technique, linear or nonlinear, and then an equivalent damping coefficient can be calculated; one which will give, for the same oscillation amplitude and frequency, the same loss. Thus, in an iterative technique such as the one used here, the linear coefficients approximate the nonlinear loss mechanisms fairly closely.

The details of the determination of the loss mechanisms in Stirling engines have not been developed by this author. Use has been made of the extensive work reported by Berchowitz [13]. However, the methods used to incorporate each loss into the damping matrix have been extended for the three-degree-of-freedom system, and some losses have been accounted for in a different manner to that used by Berchowitz.

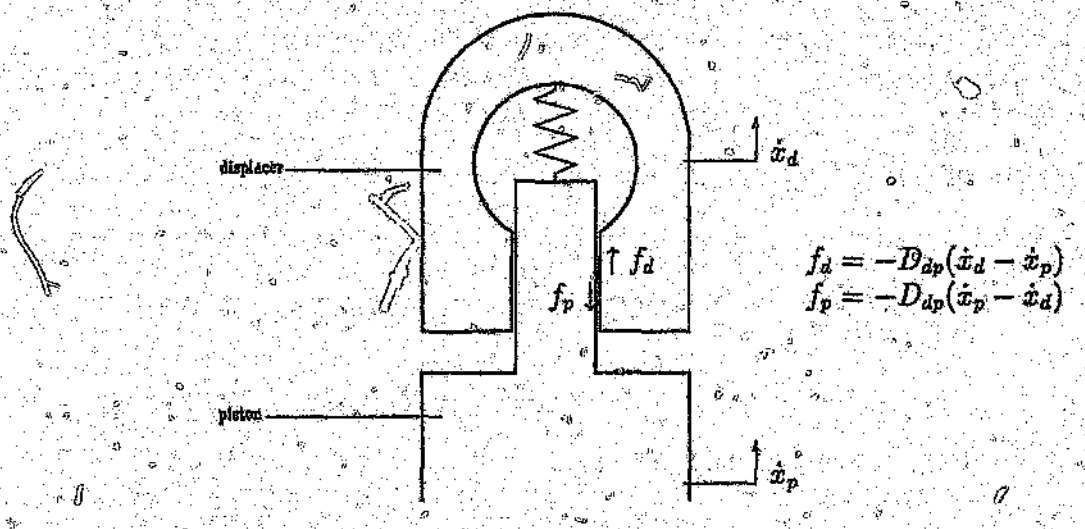

Figure 3.7: The displacer-piston friction loss

3.4.1 Simple friction losses

By a 'simple friction loss' is meant energy which is dissipated as a result of the drag force which occurs between two bodies on account of their relative motion. Thus the sliding friction between the displacer and the piston can be considered such a loss. This friction could be a result of mechanical contact between the two components, or viscous drag of the working fluid in the space between the two components. The magnitude of the force may or may not be simply proportional to the relative velocities. Whatever the nature of that loss, once the decision is made to express it as damping coefficients in the matrix equations, it is necessary to find some way of determining appropriate coefficients for that damping matrix which will match as closely as possible the real loss.

Consider the piston and the displacer and the force interaction which occurs along the seal as an example. A friction loss to the system occurs here. Assume that the energy per cycle which is dissipated as a result of this friction can be determined for given oscillations of the component. Damping coefficients D_{11}, D_{12}, D_{21} and D_{22} are needed in order to model the dynamic consequences of this dissipation.

Any force transmitted across the seal must act equally on both components. Thus $f_d = -D_{dp}(\dot{x}_d - \dot{x}_p) = -f_p$. From equation (3.42), $f_d = -D_{11}\dot{x}_d - D_{12}\dot{x}_p$. Hence $D_{11} = D_{dp}$, $D_{12} = -D_{dp}$, $D_{21} = -D_{dp}$ and $D_{22} = D_{dp}$. The work done

by the displacer to overcome this force during a complete cycle would be:

$$W_d = \oint f_d \, dx_d = \oint D_{dp}(\dot{x}_d - \dot{x}_p) \, dx_d$$

Assuming sinusoidal motion as in equations (3.12) to (3.20) the integral can be expressed as:

$$W_d = \oint D_{dp}[X_d\omega \sin(\omega t + \phi_d) - X_p\omega \sin(\omega t + \phi_p)]X_d\omega \sin(\omega t + \phi_d) \, dt$$

which then becomes:

$$\begin{aligned} W_d &= \int_0^\tau D_{dp}\omega^2 X_d{}^2 \sin^2(\omega t + \phi_d) \, dt - \int_0^\tau D_{dp}\omega^2 X_d X_p \sin(\omega t + \phi_d)\sin(\omega t + \phi_p) \, dt \\ &= D_{dp}\omega^2 X_d{}^2 \frac{\pi}{\omega} - D_{dp}\omega^2 X_d X_p \frac{\pi}{\omega}\cos(\phi_d - \phi_p) \end{aligned}$$

Similarly for the piston:

$$W_p = -D_{dp}\omega^2 X_d X_p \frac{\pi}{\omega}\cos(\phi_d - \phi_p) + D_{dp}\omega^2 X_p{}^2 \frac{\pi}{\omega}$$

The total energy dissipation during a complete cycle is:

$$W = +D_{dp}\omega^2 X_d{}^2 \frac{\pi}{\omega} - 2D_{dp}\omega^2 X_d X_p \frac{\pi}{\omega}\cos(\phi_d - \phi_p) + D_{dp}\omega^2 X_p{}^2 \frac{\pi}{\omega}$$

Since W, X_d, X_p and ϕ are known, D_{dp} can be calculated. The calculation can be simplified by noting that the square of the amplitude of the relative motion of the displacer with respect to the piston can be expressed as follows:

$$X_{dp}{}^2 = X_d{}^2 - 2X_d X_p \cos(\phi_d - \phi_p) + X_p{}^2$$

Hence:

$$D_{dp} = \frac{W}{\omega^2 X_{dp}{}^2}\frac{\omega}{\pi}$$

or, since $\dot{W} = W\frac{\omega}{2\pi}$,

$$D_{dp} = \frac{2\dot{W}}{\omega^2 X_{dp}{}^2} \tag{3.43}$$

This method of calculation of the damping coefficients ensures that for the determined dynamic motions, the losses determined by the damping coefficient have the same magnitude as the actual losses determined by whatever means was chosen. It is important to remember that this work $\dot{W}$ which the components are doing (alternatively called the 'loss') results in heat generation which must be accounted for in the energy balance. Other interactions between the components of the engine will of course add to the damping coefficients already calculated.

3.4.2 Bounce-space hysteresis loss

The 'water-pump' engine piston bounce space, and the displacer bounce space are shown in figure 2.2. Each of these spaces acts as a gas spring, and thus has an important bearing on the operation of the engine. The pressure within each space is principally a function of the volume of the space, (or the position of the components). Thus the effect of pressure variations is accounted for by the 'spring' matrix. Refer to section 3.3.1. However, losses do occur in the gas spaces, the so-called gas spring hysteresis losses. Berchowitz [13, pp 212–226] derives the following equation to determine the loss.

$$\dot{\Phi}_H = \frac{k}{4}\sqrt{\frac{\omega}{2\bar{\alpha}}}\gamma(\gamma-1)T_w A_w \left(\frac{|V|}{V_d}\right)^2 \tag{3.44}$$

Where $\dot{\Phi}_H$ is the dissipation and $\bar{\alpha}$ is the thermal diffusivity of the gas evaluated at the mean pressure and at the wall temperature T_w. A_w is the wetted area of the gas spring, $|V|$ is the amplitude of the volume variations and V_d the mean volume of the gas spring. Other symbols have their usual meanings [13, equation (6.30), p 223]. Berchowitz suggests that a factor of 1 to 2.5 should be applied to the calculated loss, larger factors being applicable when the gas is highly agitated. The equation incorporated in the SAUCE programme uses this factor 2 as a default for the bounce space. A factor of 2 was used as a first approximation for both the engines investigated here. Any fudge factors reported (see appendix C.2 and D.1) are multiplied by this default value of 2.

The dissipation can be accounted for by terms in the damping matrix in a manner similar to that described in section 3.4.1 for a simple friction loss. Berchowitz [13, p 194] treats the gas spring hysteresis losses in this manner, although in his analysis, only one component acts on each gas spring, as he reduced the linearized system to a two-degree-of-freedom system.

Thus, with reference to the 'water-pump' engine: for the displacer gas spring:

$$D_{dp} = \frac{2\dot{\Phi}_H}{\omega^2 X_{dp}^2} \tag{3.45}$$

Since there is negligible pressure gradient across the gas spring, $f_d = -f_p$. Thus the displacer gas spring contributes to the damping matrix as follows:

$$\begin{bmatrix} f_d \\ f_p \\ f_c \end{bmatrix} = - \begin{bmatrix} D_{dp} & -D_{dp} & 0 \\ -D_{dp} & D_{dp} & 0 \\ 0 & 0 & 0 \end{bmatrix} \begin{bmatrix} \dot{x}_d \\ \dot{x}_p \\ \dot{x}_c \end{bmatrix} \tag{3.46}$$

For the piston bounce space the equations are:

$$D_{pc} = \frac{2\dot{\Phi}_H}{\omega^2 X_{pc}^2} \tag{3.47}$$

$$\begin{bmatrix} f_d \\ f_p \\ f_c \end{bmatrix} = - \begin{bmatrix} 0 & 0 & 0 \\ 0 & D_{pc} & -D_{pc} \\ 0 & -D_{pc} & D_{pc} \end{bmatrix} \begin{bmatrix} \dot{x}_d \\ \dot{x}_p \\ \dot{x}_c \end{bmatrix} \tag{3.48}$$

The bounce space of the Model B-10 engine exerts a force on the piston, displacer and case. A simple way to express the hysteresis loss in terms of coefficients in the damping matrix which apply to all three bodies is to think of the dissipative forces acting on the components as resulting from a pressure wave ($\overline{p}_l$) lagging the volume phasor by 90°.

Let the volume of the bounce space be expressed as:

$$\begin{aligned} V_b(t) &= V_{bm} + |V_b| \cos(\omega t + \phi) \\ \dot{V}_b(t) &= -\omega |V_b| \sin(\omega t + \phi) \end{aligned}$$

where $|V_b|$ is the amplitude of the bounce space volume variation. Expressing the dissipative pressure wave in terms of the volume vector:

$$\begin{aligned} p_l(t) &= -d_1 \dot{V}_b(t) \\ &= d_1 \omega |V_b| \sin(\omega t + \phi) \end{aligned}$$

The dissipation resulting from this pressure phasor is:

$$\begin{aligned} \dot{\Phi}_H &= -f \oint p_l \mathrm{d}V_b \\ &= f \oint d_1 \omega |V_b| \sin(\omega t + \phi) \omega |V_b| \sin(\omega t + \phi) \mathrm{d}t \\ &= d_1 \omega^2 |V_b|^2 / 2 \end{aligned} \tag{3.49}$$

Thus

$$d_1 = \frac{2\dot{\Phi}_H}{\omega^2 |V_b|^2} \tag{3.50}$$

Since $\dot{V}_b(t) = -A_r\dot{x}_d + A_p\dot{x}_p - (A_r + A_p)\dot{x}_c$ the terms of the damping matrix follow by inspection.

$$\begin{bmatrix} f_d \\ f_p \\ f_a \end{bmatrix} = -\begin{bmatrix} d_1 A_r^2 & d_1 A_p A_r & -d_1(A_r + A_p)A_r \\ d_1 A_r A_p & d_1 A_p^2 & -d_1(A_r + A_p)A_p \\ -d_1 A_r(A_r + A_p) & -d_1 A_p(A_r + A_p) & d_1(A_r + A_p)^2 \end{bmatrix} \begin{bmatrix} \dot{x}_d \\ \dot{x}_p \\ \dot{x}_a \end{bmatrix} \tag{3.51}$$

3.4.3 Pumping losses

During the operating cycle of the engine, working fluid is forced through the heater, regenerator and cooler by the motion of the displacer, and the changes in volume of the working space caused by the relative motion of the piston with respect to the case. The flow rate through the heat exchangers can be determined as a function of the motion of the components. Various techniques can be used, as assumptions need to be made as to the state of the gas during the cycle, and the temperature of the gas in the expansion and compression spaces. (For example, does one assume isothermal or adiabatic conditions in the expansion and compression space.) Again, the details are not important for this work. The reader is referred to Walker [59], Berchowitz [13, pages 79–84] and to section 3.2 in this work. As a result of the gas flow through the heat exchangers, irreversibilities cause a pressure drop across the heat exchangers. In the iterative procedure used, the pressure drop need not be a simple linear function of mass flow rate. The numerical code developed by Berchowitz [13], on which this work is based, determined the dissipation Φ resulting from the gas flow, and an approximate sinusoidal mass flow rate of amplitude w and phase ϕ for the heater, cooler and regenerator, and their derivation is therefore not discussed further. However Berchowitz assumed that the entire effect of the pressure drop could be applied to the displacer only (as part of D_{dd}). The method below is an attempt to express the effects of the pressure drop on all three components. The pressure drop is not linearized directly. Once calculation of the dissipation has been carried out using any method of choice, an equivalent linear pressure drop which would give the same dissipation is determined. The equivalent linear pressure drop is then used to determine appropriate damping coefficients.

Consider for example the regenerator. Given the already calculated fundamental amplitude w_r and phase ϕ_r of the mass flow rate $\dot{m}_r$ through the regen-

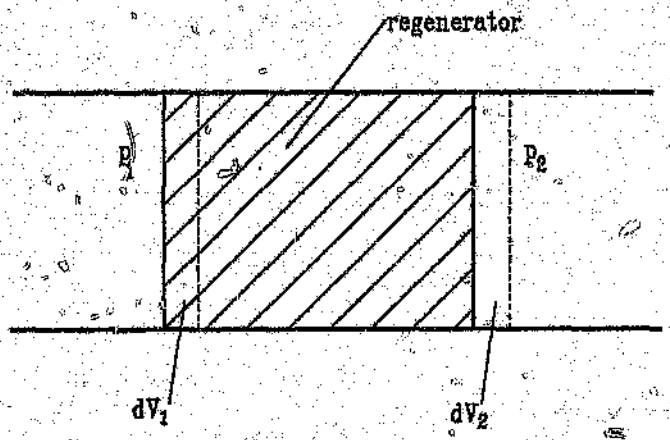

Figure 3.8: Regenerator gas flow losses

erator, and the energy dissipated as a result of flow losses during a complete cycle (Φ_r), the equivalent linear Δp_r can be calculated as follows:

With reference to figure 3.8

$$\Phi_r = \oint p_1 dV_1 - \oint p_2 dV_2$$

Assuming that the pressure drop is proportional to the mass flow rate:

$$\Delta p_r = p_1 - p_2 = k_r \dot{m}_r = k_r w_r \cos(\omega t + \phi_r) \tag{3.52}$$

then $|\Delta p_r| = k_r w_r$, with k_r being a constant of proportionality. If $p_r(t)$ is the pressure at the midpoint of the regenerator, then:

$$p_1 = p_r(t) + \frac{k_r w_r}{2} \cos(\omega t + \phi_r) \tag{3.53}$$

$$p_2 = p_r(t) - \frac{k_r w_r}{2} \cos(\omega t + \phi_r) \tag{3.54}$$

The density of the gas can be considered to be independent of pressure, as pressure variations are only expected to be of the order of 10% during the cycle [13, p 139]. However temperature changes as the gas moves through the regenerator would result in significant density change. For the purposes of this simplified linearization of the gas flow loss effects only a mean density ρ_r is assumed.

Now $dV = \dot{m}_r/\rho_r$. Hence:

$$\begin{aligned}\Phi_r &= \oint [p_r(t) + \frac{k_r w_r}{2}\cos(\omega t + \phi_r)]\frac{w_r \cos(\omega t + \phi_r)}{\rho_r}\mathrm{d}t \\ &- \oint [p_r(t) - \frac{k_r w_r}{2}\cos(\omega t + \phi_r)]\frac{w_r \cos(\omega t + \phi_r)}{\rho_r}\mathrm{d}t \qquad (3.55)\end{aligned}$$

$$\begin{aligned}\Phi_r &= \oint \frac{k_r {w_r}^2 \cos^2(\omega t + \phi_r)}{\rho_r}\mathrm{d}t \\ \Phi_r &= \frac{k_r {w_r}^2 \pi}{\omega p_r} \qquad (3.56)\end{aligned}$$

Hence:

$$k_r w_r = \frac{\Phi_r \omega p_r}{w_r \pi} \qquad (3.57)$$

$$k_r w_r = |\Delta p_r| = \frac{\dot{\Phi}_r 2\rho_r}{w_r} \qquad (3.58)$$

Similarly, for the cooler and heater:

$$|\Delta p_k| = \frac{\dot{\Phi}_k 2\rho_k}{w_k} \qquad (3.59)$$

$$|\Delta p_h| = \frac{\dot{\Phi}_h 2\rho_h}{w_h} \qquad (3.60)$$

Using a similar method to that used for the work-space pressure in section 3.3.2, $|\Delta p_r|$ can be expressed as follows:

$$|\Delta p_r|\cos(\omega t + \phi_r) = -d_1(\dot{x}_d - \dot{x}_c) - d_2(\dot{x}_p - \dot{x}_c)$$

$$d_1 = \frac{|\Delta p_r|\cos(\phi_r - \phi_{pc})}{X_{dc}\omega \sin(\phi_{dc} - \phi_{pc})} \qquad (3.61)$$

$$d_2 = \frac{|\Delta p_r|\cos(\phi_r - \phi_{dc})}{X_{pc}\omega \sin(\phi_{pc} - \phi_{dc})} \qquad (3.62)$$

(3.63)

The effect of the pressure drop on each of the components can then be expressed in the damping matrix as follows:

$$\begin{bmatrix} f_d \\ f_p \\ f_c \end{bmatrix} = -\begin{bmatrix} -\frac{A_p+A_c}{2}d_1 & -\frac{A_p+A_c}{2}d_2 & \frac{A_p+A_c}{2}(d_1+d_2) \\ \frac{A_p}{2}d_1 & \frac{A_p}{2}d_2 & -\frac{A_p}{2}(d_1+d_2) \\ \frac{A_c}{2}d_1 & \frac{A_c}{2}d_2 & -\frac{A_c}{2}(d_1+d_2) \end{bmatrix}\begin{bmatrix} \dot{x}_d \\ \dot{x}_p \\ \dot{x}_c \end{bmatrix} \qquad (3.64)$$

The procedure for the cooler and heater is similar.

3.4.4 Work-space hysteresis loss

Hysteresis losses, such as those which occur in the gas springs, also occur in the working spaces of the engine. Their effect in areas with high velocity and temperature gradients (such as the heat exchangers) are believed to be small [13, p 195 and pp 225–226]. However, for the compression and expansion spaces their effects should be considered. Berchowitz derived the following equation for the hysteresis loss in terms of the pressure variations [*ibid*]:

$$\dot{\Phi}_H = \sqrt{\frac{\omega\bar{\alpha}}{32}} \frac{A_w |p|^2}{\gamma p_m} \tag{3.65}$$

where $|p|$ is the amplitude of the pressure phasor, $\bar{\alpha}$ the thermal diffusivity of the gas evaluated at the mean pressure and wall temperature.

Berchowitz accounted for this loss by modifying the phase of the work-space gas pressure [13, p 196–197]. Thus, re-expressing Berchowitz's work in terms of volume changes rather than motion of the piston:
The available work is $-\oint p dV$. If both p and V are represented by phasors then the available work is proportional to $\sin\beta'$ where β' is the angle by which the pressure phasor leads the volume phasor. Thus if P is the ideal power, and P_a was the actual power with hysteresis losses accounted for, then:

$$\frac{\sin\beta'_a}{\sin\beta'} = \frac{P_a}{P} \tag{3.66}$$

From which

$$\beta'_a = \sin^{-1}\left[\frac{(P - \sum\dot{\Phi}_H)\sin\beta'}{P}\right] \tag{3.67}$$

Figure 3.9 (a) represents this process in terms of a phasor diagram.

The method adopted here is to leave the work-space pressure phasor as represented by the spring matrix unchanged, and then to include a purely dissipative pressure vector at right angles to the volume vector. Hence the dissipation due to hysteresis losses in the working spaces can be expressed in the same manner as that used for the bounce spaces, with coefficients in the damping matrix. This approach was adopted in preference to the phase angle modification, as it allows direct representation of these losses (and others treated in a similar manner below) in the damping matrix, rather than being expressed as part

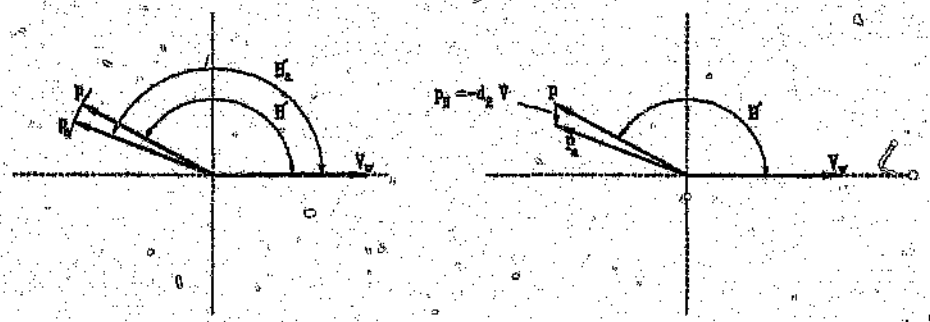

(a) Pressure phase modification (b) Dissipative pressure vector method

Figure 3.9: Effect of work-space gas hysteresis losses on pressure phase

of a composite effect in the spring matrix. Being dissipative forces, it seems more appropriate that they be represented in the matrix usually associated with dissipative elements of a linear model. Furthermore this method has the effect of reducing the amplitude of the effective pressure phasor acting on the components slightly, as shown in figure 3.9 (b).

Following the method used for the Model B-10 bounce-space hysteresis loss (section 3.4.2), the results are:

$$p_H \doteq -d_2 \dot{V}_w(t) \tag{3.68}$$

$$d_2 \doteq \frac{2\dot{\Phi}_H}{\omega^2 |V_w|^2} \tag{3.69}$$

Since $\dot{V}_w(t) = -A_r \dot{x}_d - A_p \dot{x}_p + A_d \dot{x}_c$ the terms of the damping matrix follow by inspection.

$$\begin{vmatrix} f_d \\ f_p \\ f_c \end{vmatrix} = -\begin{bmatrix} d_2 A_r{}^2 & d_2 A_r A_p & -d_2 A_r A_d \\ d_2 A_p A_r & d_2 A_p{}^2 & -d_2 A_p A_d \\ -d_2 A_d A_r & -d_2 A_d A_p & d_2 A_d{}^2 \end{bmatrix} \begin{vmatrix} \dot{x}_d \\ \dot{x}_p \\ \dot{x}_c \end{vmatrix} \tag{3.70}$$

3.4.5 Displacer appendix gap loss

Between the displacer and the cylinder wall and above the displacer seal there is usually a gap containing working fluid. It is often fairly long, in order to keep the seal temperature low. Berchowitz [13, pp 241–264] lists three

identifiable irreversibilities that contribute to the appendix gap loss: shuttle heat transfer; gas enthalpy transfer and hysteresis heat transfer. The first results in a conduction path through the engine, placing a demand on the heat exchangers but having very little effect on the thermodynamic cycle or on the engine dynamics. Berchowitz derives an equation for this loss which is incorporated in the SAUCE programme. However no extension has been necessary for this work, and the loss is incorporated into the heat transfer equations in the original form.

Following the lead given by Berchowitz, the hysteresis loss has been neglected as insignificant for the purposes of the linear analysis model.

The gas enthalpy loss has however been treated differently to that shown by Berchowitz, not in the manner of its calculation, but in the way in which its effects are included in the linear analysis. The gas enthalpy loss into the appendix gap is a transfer of available pV work from the expansion space into heat energy which then flows down the displacer gap. Berchowitz treated both this loss and the expansion space hysteresis loss as direct dissipation to the displacer, in a manner similar to that used for the gas spring hysteresis losses, that is,

$$D_d = \frac{2(\dot{\Phi}_H + \dot{\Phi}_{Gap\ loss})}{\omega^2 X_d^2} \tag{3.71}$$

This places a severe damping load on the displacer, as it assumes that these pV losses impact only on it. Furthermore, Berchowitz uses the pressure wave phase modification equation (3.67) to account for the loss as well. As far as it is understood by this author, the loss is thus accounted for twice. Any pV loss in the working space will have an effect on all the surfaces which interact with the entire working space. Thus the modification of the phase of the pressure wave only, should be considered as sufficient allocation of this loss. Neither of these methods was used in the 3-D SAUCE simulation. The loss was treated as a direct effect on the entire working space and accounted for in the damping matrix, using the same method as described above for the work-space hysteresis losses.

3.4.6 Seal leakage losses

Gas leakage past the seals in Stirling engines can have extremely severe dissipative effects on the cycle. The method of analysis used in the Berchowitz version of SAUCE has not been extended by this author. However, the losses

have been included in the damping matrixes using the same methods as for the work-space hysteresis losses described above, rather than using the pressure phase angle modification suggested by Berchowitz [13, p 232].

3.4.7 A note of caution

It should be noted that neither the phase angle modification suggested by Berchowitz, or the dV/dt form expressed in the damping matrix as suggested by this author reduce the amplitude of the effective work-space (or bounce-space) pressure vector significantly. Where these losses are large (in the case of poor seal surfaces for example) then the amplitude of the pressure vectors will also be significantly effected. It is difficult to incorporate this effect into the analysis, as the basic assumptions used to calculate the amplitude and phase of the work-space pressure vector (isothermal or adiabatic model), and to estimate the pressure wave of the bounce space (ideal adiabatic spring) assume that the seals are perfect. This author has not found a convenient way to extend this limitation, one which may be the cause of serious discrepancies noted in the comparison of experimental and simulation results in the following chapters.

3.4.8 Power delivered to load

Free-cylinder engine

Useful work is extracted from the motion of the cylinder of the free-cylinder Stirling engine. Since this involves the motion of only one component, the case, with respect to ground, the only way of expressing such an energy transfer from the case to the surroundings is through D_{cg}, one of the terms of D_{33} in the damping matrix. The load on the engine is thus considered to be a linear damper. Note: any spring component of the load does not dissipate power, and would be included in the spring matrix coefficient K_{33}. In the discussion of the linear dynamics technique, on page 45, it was indicated that D_{cg} is treated as a variable, the value of which is determined by the iterative process already described. Thus the load damping coefficient is an output from the simulation procedure for a given oscillation amplitude.

The power delivered to the load is:

$$P_{load} = \frac{\omega^2 X_c^2 (D_{cg})}{2} \tag{3.72}$$

where $D_{cg} = D_{33} - D_{cl}$, D_{cl} representing those components of D_{33} which are not part of the useful load.

Free-piston engine

In free-piston Stirling engines the load is normally a linear damper (linear alternator or hydraulic pump) which dissipates energy as a result of the relative motion of the piston and the case. Thus the terms of D_{22}, D_{23}, D_{32} and D_{33} need to be varied until the solution converges as described in section 3.1.

The power delivered by the engine is then:

$$P_{load} = \frac{\omega^2 X_{pc}^{\ 2}(D_{33} - D_{cl})}{2}$$

where D_{cl} again corresponds to those components of the damping coefficient which are not part of the load and were determined according to the various loss mechanisms already discussed.

Caution, and an alternative approach

It is important to note that the calculated power output of the engine, as expressed through D_{cg}, (or the appropriate coefficients above for the free-piston engine) is an integral part of the calculations to determine the dynamic motion of the engine. To achieve satisfactory prediction of the motion of the components all losses (and spring rates) must already have been included in their proper place in the matrixes. One can not, once the simulation is finished, say for example, that the isothermal model overpredicts work-space power by 20%, therefore we should expect an actual output power 20% less than that suggested by equation 3.72. The dynamic consequences of the overprediction will then have been ignored. Such experience based corrections should be applied at their source, ie, in the calculation of the specific coefficients of the spring or damping matrix which they directly affect.

The above technique of calculating the output power can not be used if fixed dynamic motion of the components is assumed. An alternative method has been used in the past to determine the power of the engine (both when fixed or free dynamic motion were assumed). (See Redlich and Berchowitz [44] and Berchowitz [13, pp 175–195]). This was to consider the time averaged product of the work-space pressure force acting on the piston (or the case for a FCSE) and the velocity of the component. From this the losses such

as bounce-space losses were then subtracted to give the final output power. In the method presented by this author the entire matrix is considered, and completely balanced during the solution procedure. This allows the use of the simpler approach described above, the principal advantage being that one only has to ensure that the matrix is correctly set up at the beginning. The losses are then accounted for directly, rather than one having to consider exactly which losses detract from the output power.

3.5 The mass matrix

This matrix takes into account those forces which act on the system as a result of the acceleration of the system components. Although the original version of SAUCE did include terms which represent the effects of gas inertia in the mass matrix, these have not been included in the 3D SAUCE programme. Their omission will not have a significant effect in the simulation of low pressure, low frequency engines such as the Sunpower 'water pump' engine or Model B-10 engine.

The mass matrix is:

$$\begin{bmatrix} f_d \\ f_p \\ f_c \end{bmatrix} = \begin{bmatrix} M_d & 0 & 0 \\ 0 & M_p & 0 \\ 0 & 0 & M_c \end{bmatrix} \begin{bmatrix} \ddot{x}_d \\ \ddot{x}_p \\ \ddot{x}_c \end{bmatrix} \tag{3.73}$$

The masses of the components have a strong influence on the natural frequency of each of the components, and hence on the operating frequency of the engine. In a simple spring–mass, single-degree-of-freedom system, the natural frequency will be: $\omega_n = \sqrt{k/M}$. The natural frequency of each of the components (i) of the three-degree-of-freedom system is defined as $\omega_{ni} = \sqrt{K_{ii}/M_{ii}}$. Thus, altering the mass of individual components is an important means of tuning the engine to obtain optimum resonance and hence operation at the desired frequency. In the free-cylinder engines studied during this research the case mass was relatively high, necessitating a high spring stiffness between the case and ground (K_{cg}) in order to allow either simulation or operation at frequencies compatible with the displacer natural frequency.

There will be some situations in which the load device is rigidly connected to the case of the engine (such as the cable operated pump described in section 2.3.2). Such a linkage adds the mass of the moving components of the pump directly to the case, and its mass should thus be included in the simulation

and engine design process. This will often be inconvenient, as load and engine design is often performed independently. However, since the case motion is essentially sinusoidal, it is possible to decouple the case from the inertial effects of the load by ensuring that any mass added by the load is supported on springs such that its resonant frequency, $\sqrt{K_l/M_l}$ is the same as that of the engine. This will reduce the dynamic effects of the load on the engine to those caused by damping only at that specific frequency. Where operational frequency may vary, such decoupling is not possible, and the load mass and associated springs must be included in the engine simulation.

3.6 Use of the 3-D SAUCE programme as a design tool

An intuitive understanding of free cylinder engines is difficult to grasp. The response of the system to changes of operating conditions, or of particular engine parameters is sometimes quite predictable and orderly, and in other regions may yield sudden dramatic changes in performance or operation mode. Finding a coherent pattern is not easy. The loss of a tractable equation set occasioned by the inclusion of all significant terms in the equations of motion (see section 3.1.1) is unfortunate. Three important design approaches are however still available, as discussed below.

3.6.1 Sensitivity and optimization using the full simulation

The simulation programme can be used in the normal manner to investigate the operation of the engine under different conditions, or to investigate the sensitivity of the engine to changes in particular parameters. This is the approach used to generate most of the simulation curves shown in section 4.3 and chapter 6. It would be a relatively simple matter to include optimisation routines into a linear analysis programme of the type used here. Berchowitz [13, pp 412 – 416] lists the optimization routine applied to the original SAUCE programme.

Such simulation is relatively quick, and processing time could be significantly reduced if the analysis code were rewritten using a language such as 'C' or even a high level package such as *MATLAB*[1]. The important advantage is that the

[1]The MathWorks, Inc. 124 Foxwood Rd., Portola Valley, CA 94025

nonlinear aspects of the system are partially accounted for. This is particularly useful when investigating stability of the system and relationship between the system and load. (See sections 4.4 and 6.3).

Simulation using the full procedure as described in figure 3.5 is akin to carrying out experiments, and thus suffers from one of the major difficulties associated with experimental work on free-cylinder or free-piston engines. One can only run a simulation (or an experiment) on a working engine. If the system has no oscillatory roots, or if the oscillatory root can not be coaxed to lie exactly on the imaginary axis (by variation of the 'relaxed' parameter), then simulation is not possible. The situation is not unlike that of the experimental worker whose engine fails to oscillate, or oscillates so violently that the components are damaged within the first few cycles.

3.6.2 Using the root maps as a design tool

Root locus techniques have been used by Redlich and Berchowitz [44] to investigate the characteristic of free-cylinder Stirling engines. Their maps were deduced from the simplified characteristic equation. The added complexity of the characteristic equation resulting from the approach in this work (see section 3.1) makes such analytical work very difficult. However, as all roots of the characteristic equation are determined using a numerical procedure during the simulation it is still possible, and is very easy, to construct root maps using the 3-D SAUCE programme. As the construction of a root map does not require convergence, or the satisfying of any conditions (such as the presence of a root lying exactly on the imaginary axis) a root map can be obtained for any engine. This allows a rapid investigation of the likely effect of changes to particular parameters, without requiring that the full simulation converges to a complete solution. The method is explained by way of example below.

The simulation is run in the normal manner, with an initial estimate of the engine dynamics being required in order to obtain the coefficients of $[\mathbf{G}(s)]$, and hence the coefficients of the characteristic equation $|[\mathbf{G}(s)]| = 0$. However, instead of then using a search procedure to find the value of the relaxed coefficient of $\mathbf{G}$ which would yield one and only one root pair with a zero real component, the relaxed parameter is simply varied through a user specified range, and the root map determined for each value of the relaxed parameter. The result is a root locus map of the characteristic equation as a function of the relaxed parameter. It is important to remember that for this stage in the analysis, the machine is treated as a perfectly linear device, ie, the coefficients of $[\mathbf{G}(s)]$ are assumed constant (apart from the 'relaxed parameter'). The designer can then study this root map, or a series of such maps, each

corresponding to a slightly different engine configuration, in order to gain an understanding of the behaviour of the machine.

Figure 3.10 shows the upper half of four such root locus maps. Engine data used was as for the 'water pump' engine simulations presented in section 4.4. The same motion estimate was used to produce each map. However the displacer gas spring volume was varied as noted in the figure key. The relaxed parameter chosen was the case-ground damping coefficient (D_{cg}), which was incremented from 0 to 5000 Nm/s in steps of 50 Nm/s. Consider first the curves shown with an $\times$, corresponding to the engine in the form closest to that of the experimental work, the displacer gas spring volume being 5.12×10^{-5} m^3. For low values of D_{cg} there is a single root with a positive real value. The other roots can be ignored, as they all fall into the left hand plane (LHP) for positive values of D_{cg}. The right hand plane (RHP) root indicates instability, and if the engine were perfectly linear, oscillations would increase in an unbounded manner. A close up look at the region of interest is shown in figure 3.11. As D_{cg} is increased the oscillatory root moves into the left hand plane (LHP), indicating that oscillations would die away. The response of the second engine configuration ($\circ$) is similar, except that the root loci crosses the imaginary axis at lower point, indicating an oscillation frequency of about 31 Hz, rather than the 34 Hz of the first configuration. The third and fourth curves (for displacer gas spring volumes of 7×10^{-5} m^3 and 8×10^{-5} m^3 respectively) follow a similar behaviour for low values of D_{cg}. However they recross the imaginary axis again as D_{cg} is increased. The engines corresponding to these curves would thus be unstable for either low values of D_{cg} or high values of D_{cg}. Each crossover point occurs at a different point on the imaginary axis, indicating substantially different frequency of operation for the two different loads. The values of D_{cg} which correspond to stable oscillation (the crossover points) can be easily read from figure 3.12, which shows the real component of the roots plotted against D_{cg}.

An indication of the phase angles and relative amplitudes of oscillation of the components can be gathered from figures 3.13 and 3.14. These were produced by substituting the imaginary component jb of the roots ... est into the Laplace domain equations of motion ($[\mathbf{G}(s)] = 0$) and solving for the relative complex amplitudes. This is the same procedure as used in the full simulation. There are however two important differences which mean that these curves must be treated as a rough indication of the likely effect of changes, rather than as a simulation result. Firstly, the real component of the roots is ignored, the amplitudes and phases calculated are thus only exact solutions of the equations for those values of D_{cg} which resulted in roots with a zero real component (the crossover points in figure 3.12). Secondly, the coefficients of $[\mathbf{G}(s)]$ would in the full simulation be dependant on the motion of the components (the nonlinear

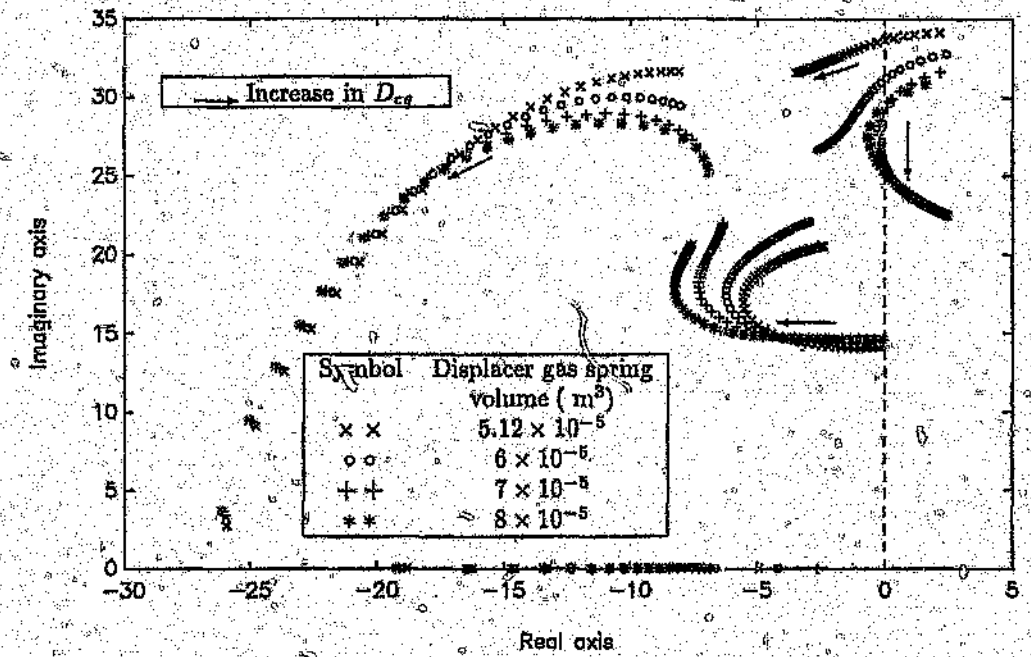

Values have been divided by 2π to yield oscillation frequency in Hz

Figure 3.10: Root map showing effect of increasing displacer gas spring volume

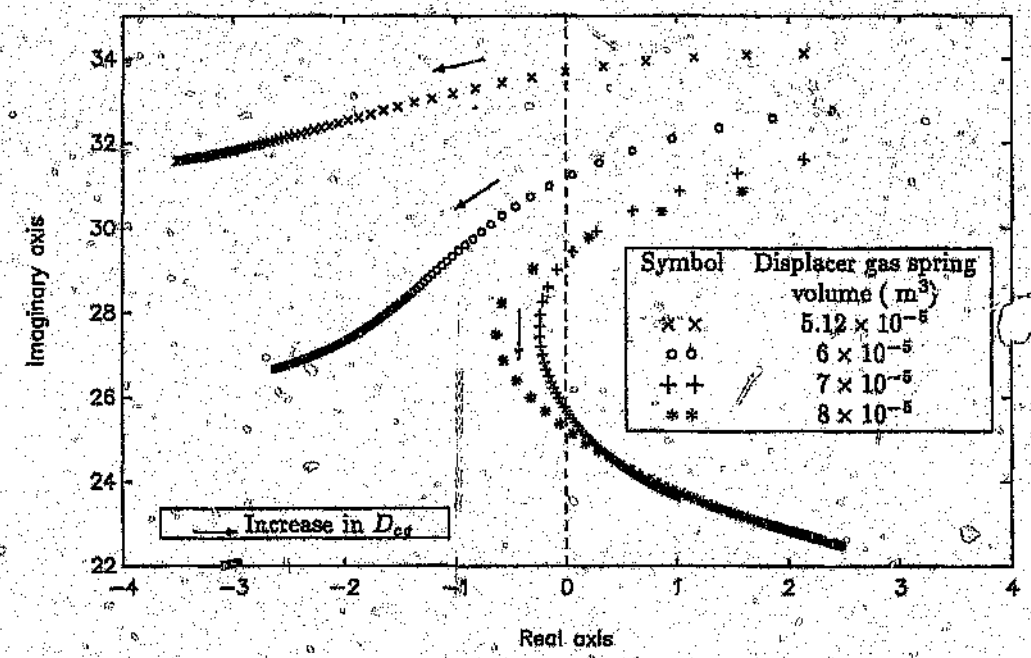

Values have been divided by 2π to yield oscillation frequency in Hz

Figure 3.11: Close up of figure 3.10

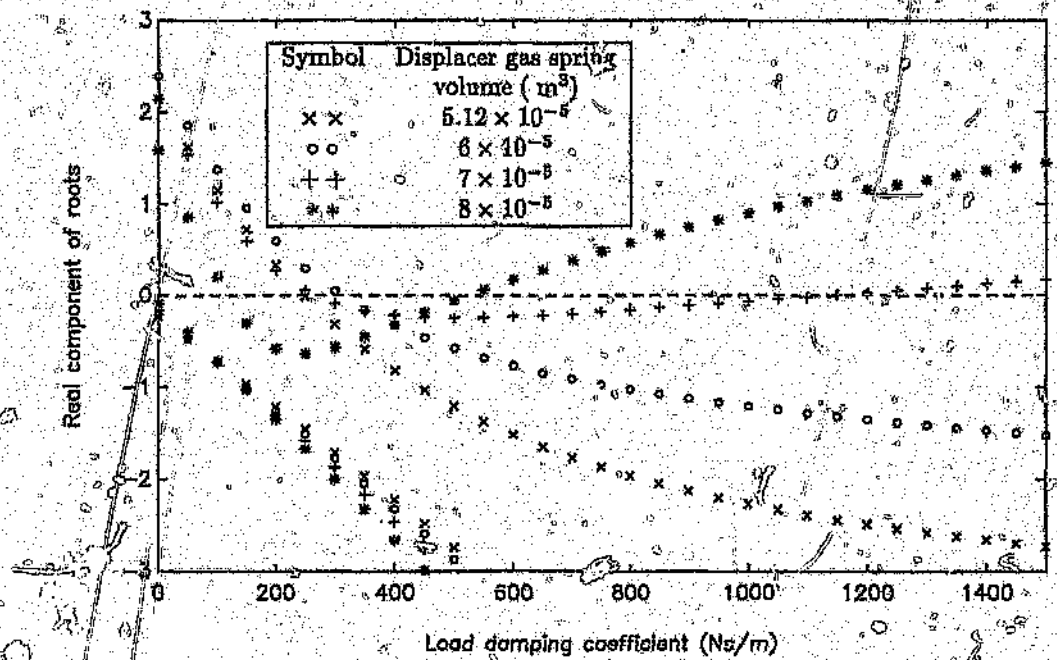

Values have been divided by 2π to yield oscillation frequency in Hz

Figure 3.12: Real component of roots plotted against D_{cg} (region of interest only)

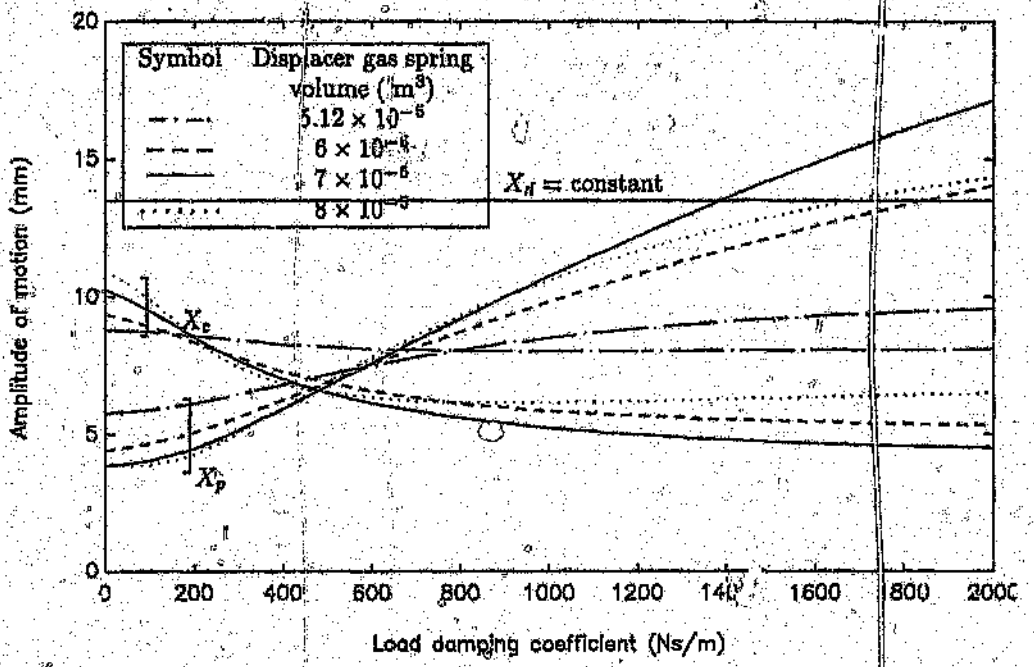

Figure 3.13: Approximate amplitudes of oscillation: root map technique

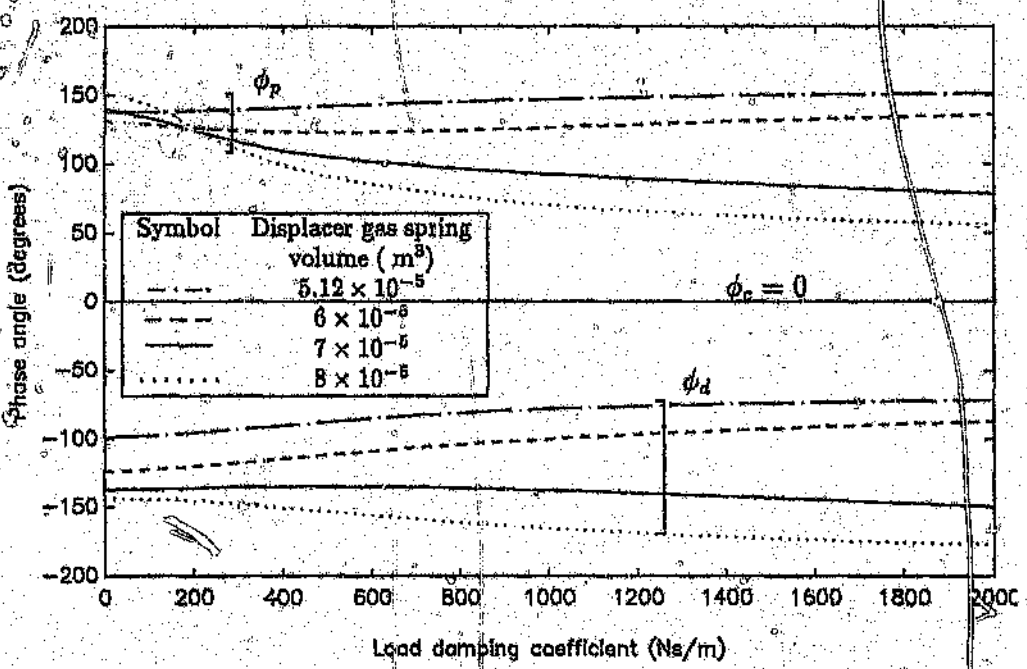

Figure 3.14: Approximate phase angles: root map technique

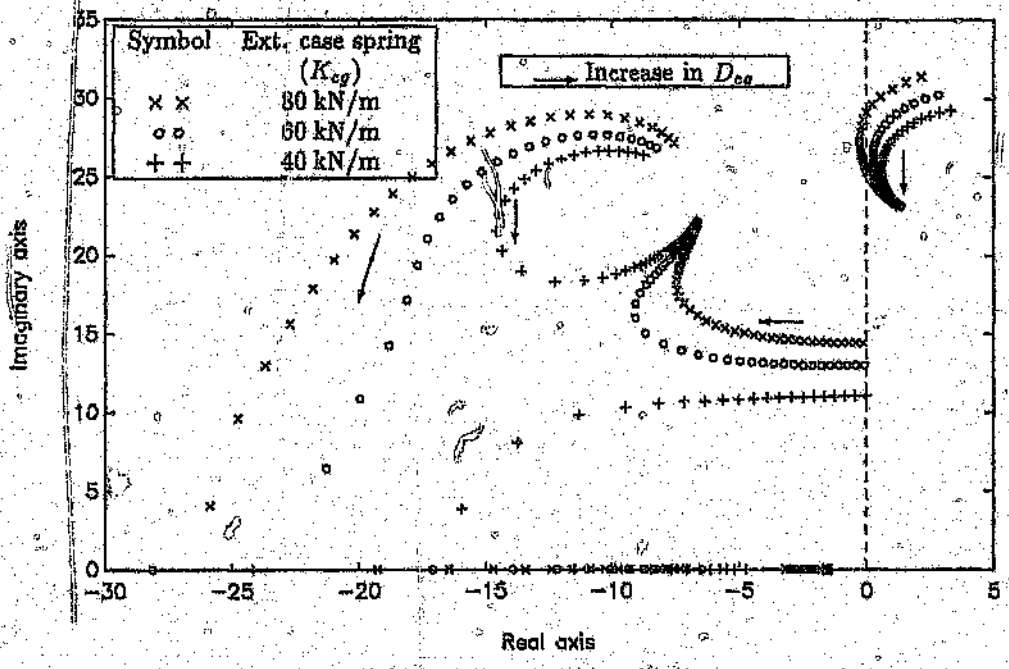

Values have been divided by 2π to yield oscillation frequency in Hz

Figure 3.15: Root locus map showing condition in which engine is unstable for all values of D_{cg}.

components of the system equations). Since no iteration is being carried out here, the implication is that the machine is perfectly linear. (See section 3.1 for a description of how this problem is dealt with in the full simulation). For the purposes of this exercise the displacer amplitude was held constant (at the value used for the motion estimate used to determine the coefficients of the [M], [K] and [D] matrixes).

Note how the pattern of motion changes from that more commonly associated with free-cylinder engines for low values of D_{cg} (case amplitude higher than piston amplitude), to a pattern more typical of free-piston engines for higher values of D_{cg}.

Figure 3.15 shows a series of three root maps. The engine configuration used was the same as for the previous figures, except that the displacer gas spring volume was held at 7×10^{-5} m^3, and the case–ground spring (K_{cg}) was varied as shown in the key. The curve shown with a × uses the same data as the + curve of figure 3.10. Of particular interest in figure 3.15 is that the curves for K_{cg} of 60 kN/m (o) and 40 kN/m (+) indicate that a perfectly linear machine would be unstable at any load.

Often it will be useful to investigate a root map and full simulation results together, as illustrated in section 6.3.

3.6.3 Force vector plots

Force vector plots provide an informative graphical picture of the forces acting on a component. Due to the iterative nature of the solution procedure, the final coefficients of the mass, spring and damping matrixes are calculated using the final simulation amplitudes, phases and frequency of oscillation. The net force acting on each component as a result of these matrixes must of course be zero (this is the solution point of the iterative process). These matrixes can be used in their complete form to construct force vector polygons for each component, where the inertia, spring and damping forces can be separated out. The appropriate displacement, velocity or acceleration vector is simply substituted into the matrix equation of motion. For example the net force acting on the three components as a result of the spring matrix would be as follows:

$$\begin{vmatrix} \overline{F}_d \\ \overline{F}_p \\ \overline{F}_c \end{vmatrix} = - \begin{bmatrix} K_{11} & K_{12} & K_{13} \\ K_{21} & K_{22} & K_{23} \\ K_{31} & K_{32} & K_{33} \end{bmatrix} \begin{vmatrix} \overline{X}_d \\ \overline{X}_p \\ \overline{X}_c \end{vmatrix} \tag{3.74}$$

The motion and force vectors are written in complex phasor form.

It is however more useful to use the available smaller sub-matrixes, each being the description of a particular interaction in the engine (see section 3.3, 3.4 and 3.5 for details on the calculation of these terms). The force vectors can then be plotted in the complex plane, to give a visual picture of the magnitude and phase of the forces acting on each component. Figures 3.16, 3.17 and 3.18 show the force polygons for the 'water pump' engine, using engine data as described in section 4.4. Some of the forces have been grouped together in order to simplify the diagrams.

Such diagrams may help the designer to understand relationships within the engine better. For example, the case force diagram (figure 3.18) highlights the large inertia force resulting from the mass of the case. Hence a stiff external spring is required to balance this force.

In figure 3.16 note that a large rod force is required to counteract the effect of the gas pumping and spring hysteresis losses on the displacer.

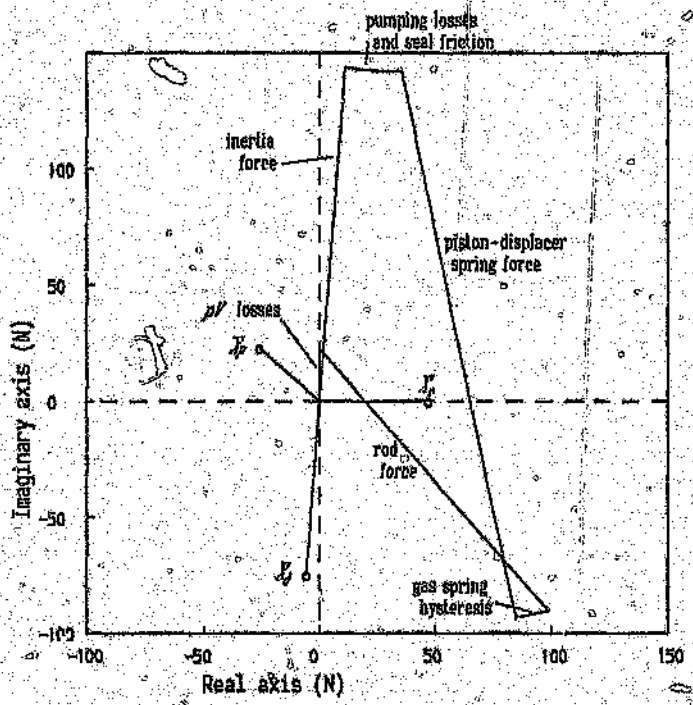

Figure 3.16: Displacer force polygon

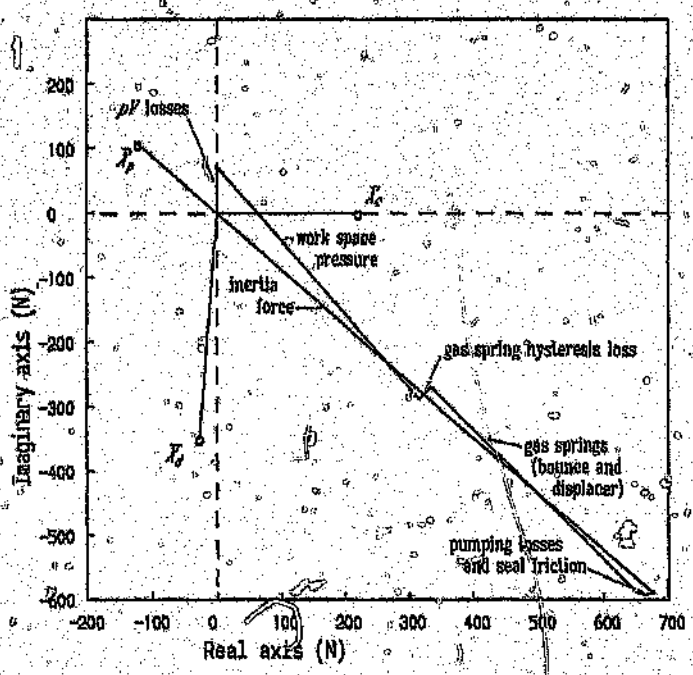

Figure 3.17: Piston force polygon

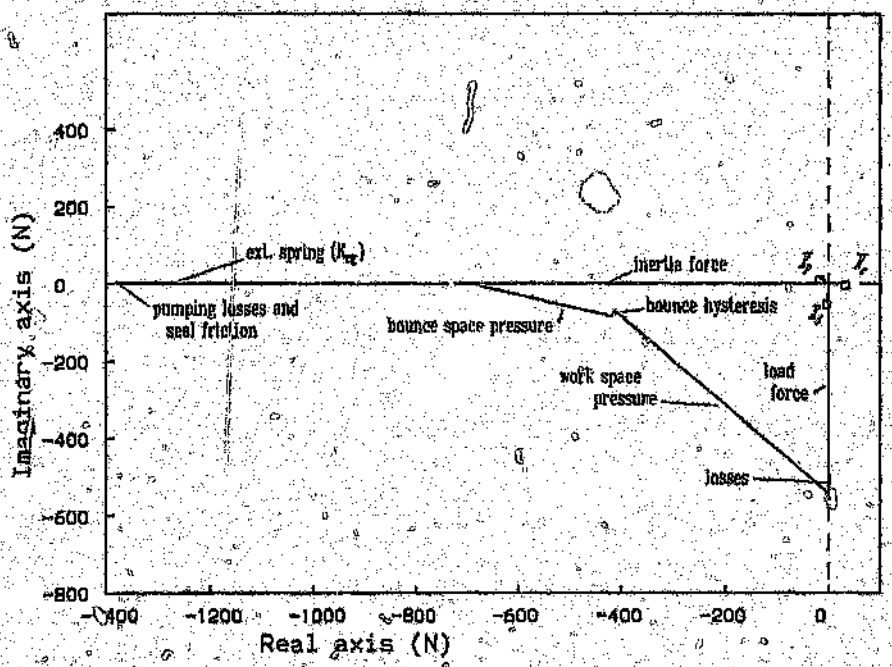

Figure 3.18: Case force polygon

From figure 3.17 we see that as far as the piston is concerned the dissipative forces are relatively insignificant compared to the inertia, gas spring and work-space pressure force vectors.

Chapter 4

Experimental results: 'water pump' engine

Two groups of experimental work were carried out during this study. The first was during the period 1988 to 1989, using the free-cylinder engine donated by Sunpower Inc, as described in section 2.1 (the 'water pump' engine). The second set of experimental work was carried out using a modified Model B-10 Demonstrator. This later work was carried out in order to gain a better understanding of free-cylinder Stirling engine operation, and as a further check on the computer simulation package. As the two engines are significantly different, the discussion of the experimental equipment and results is divided into separate chapters, the 'water pump engine' being described first, and then the smaller Model B-10 engine'.

4.1 Apparatus

4.1.1 Drive unit and supporting frame

Actuator

Early on in the programme it was realised that the engine would not run in an unmodified form. This author lacked the expertise or experience to delve directly into the art of redesigning and building the engine, without at least gaining some idea of its operating characteristics. It was not immediately apparent where the fault lay in the original engine. Testing the engine was impossible without some means of causing the engine components to oscil-

late. Thus a rig was designed so that the engine could be mounted on a hydraulic ram. The ram was driven by a feedback control system so that a range of frequencies and oscillation amplitudes could be attained. A load cell was mounted between the ram and the engine, and the position of the ram (and thus of the engine case) was measured using a linear variable differential transformer (LVDT). Thus it was possible to monitor the interaction between ram and engine directly. The results reported in the remainder of this chapter were obtained using this rig.

As of May of 1989, the hydraulic ram was required for other experimental work in the School of Mechanical Engineering. Since no similar actuator of sufficient power was available, a simple crank-driven actuator was designed and built. This incorporated a variable speed DC drive, with a connecting rod between a variable length crank arm and a yoke on the engine. Other small modifications were made. The rig was used for a final year BSc (Eng) project with moderate success. After this a decision was made not to use the engine for further work as it was felt that the model B-10 engine would provide a quicker and more varied insight into the characteristics of free-cylinder Stirling engines.

Engine supporting frame

The 'water pump' engine was mounted between two stationary steel channel sections as shown in figure 4.1, supported in the vertical plane by light roller bearings. A variable stiffness spring (K_{cg}) (visible at the base of the engine in the figure) served two purposes. The first and most important was to keep the rigid linkage between engine and ram in tension at all times, so as to avoid impact loads due to free play in the linkages. (The spring was not strong enough to perform this task as well as had been anticipated.) The second was to serve as an adjustable spring to ground in the hopeful event that the engine could be disconnected from the actuator and run on its own. Note, as discussed on page 47, it is the incorporation of this spring which made the direct application of the Redlich and Berchowitz [44] analysis inapplicable.

Gas burner

Heat sources for free-cylinder Stirling engine water pumps have been discussed in section 2.2. The burner used for the experimental work was designed by CB Broadwell and this author. Propane gas was selected as the most suitable fuel, as the pressure at ambient temperatures is sufficient to draw in combustion air using a simple jet-mixing chamber.

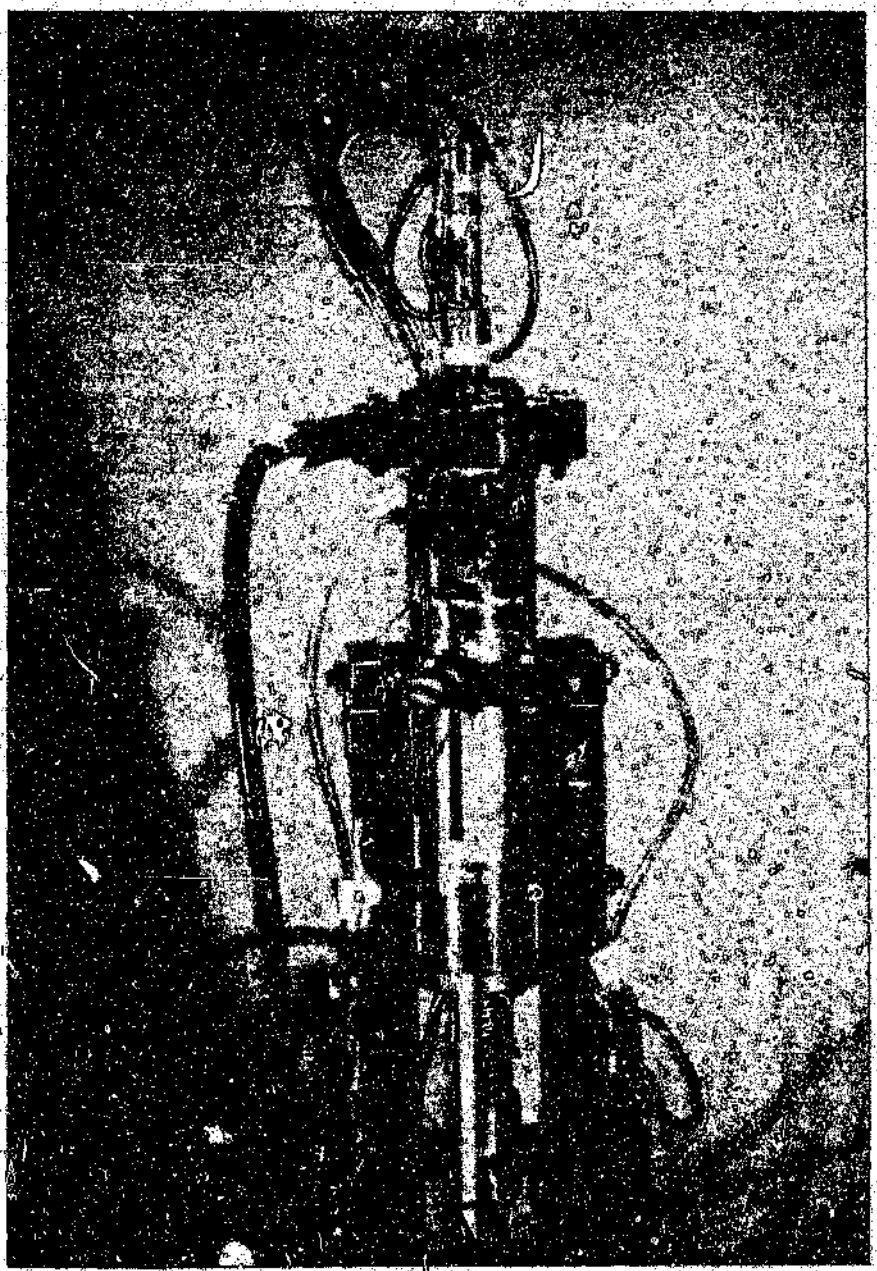

Figure 4.1: 'Water pump' engine, with instrumentation and burner, mounted on the hydraulic shaker.

The fuel was premixed before entering the chamber which surrounds the flame front. Thus care had to be taken to ensure that flashback did not occur. A stainless steel mesh with an aperture size of 420 micron served as a reliable flame arrestor. The mesh withstood the high temperatures remarkably well. It was not necessary to replace the screen during the entire experimental period.

The flame was exhausted from the bottom of the burner. The prime reason for this was to keep hot exhaust gases away from the pressure transducers and displacement transducers at the top of the engine. There was no efficient recuperation of the exhaust gas thermal energy, although it would be possible to encase the burner in a larger can, thereby forcing the exhaust gases to flow over the outer surface of the burner and then through an exhaust nearer the top of the engine. The burner was thus not an efficient heat source for the engine. It simply provided sufficient heat to allow investigation of the engine operating characteristics.

4.1.2 Instrumentation

A brief description of the instruments used is given below. Calibration procedures, correlation coefficients and specifications can be found in appendix A.1

Displacement transducers

The LVDT displacement transducer on the hydraulic ram has already been noted above. This measured the position of the case during the cycle.

The position of the piston and the displacer was measured using FASTAR [1] transducers, mounted as shown in figure 4.2. Thus the displacer position was measured through the hot end of the engine. This technique worked reasonably well. There were two drawbacks which should be noted. The first is that the friction losses of the carbon bush when at high temperature may have had a degrading effect on the performance. However, as far as can be established this loss was small. Secondly, the cooling required so close to the hot end had a severe effect on the hot-space gas temperature, making investigation of heater effectiveness impossible, and impairing the performance of the engine. The cooling system did however keep the transducer temperature well below 100°C. The piston transducer was attached to the bottom of the engine, using a similar method to that shown for the displacer. Cooling was of course not

[1] Trade name: Instrument supplied by Data Instruments Inc. 100 Discovery Way, Acton, MA01720 (Sunpower Inc. design)

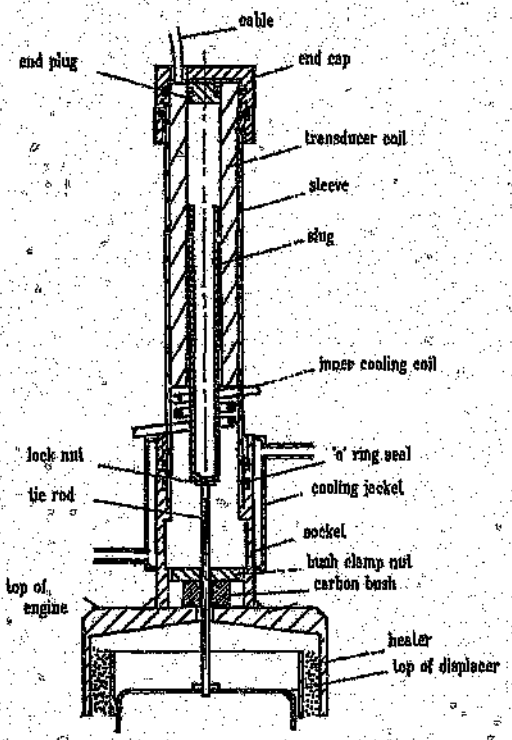

Figure 4.2: Displacer displacement transducer mounting

required. Both the displacer and the piston transducer sealing systems worked extremely well, with no observed leakage.

Pressure transducers

The pressures in both the bounce and the work spaces of the engine were monitored using piezoelectric pressure transducers. The bounce-space pressure transducer was a Kistler high frequency transducer. Resolution was of the order of 1 kPa. The work-space pressure was measured through the top end of the engine using a water cooled pressure transducer. The PCB [2] transducer that was used proved extremely difficult to calibrate as the instrument had a high signal decay rate (a short time constant). The Budenberg type dead weight tester used was therefore unsuitable for dynamic calibration purposes. For this reason the suppliers calibration curve [3] was used.

A further consideration in the selection of pressure transducers for this applica-

[2]PCB Piezotronics Inc. 3425 Walden Avenue, Depew, New York 14043-2495

[3]Calibration of instrumentation used to certify sensor traceable to NBS. PCB Piezotronics' calibration procedure is in compliance with MIL-STD-45662.

tion was that the transducers had a low response to acceleration, as they were mounted on an oscillating structure. Both the Kistler and PCB transducers had a sensitivity to acceleration of less than 15 Pa/G. At a case oscillation amplitude of 5 mm at 35 Hz, this yields an acceptable maximum error due to acceleration of 0.340 kPa.

The pressure transducers used could not measure absolute pressures, as the output signal decays with time. A bourdon tube pressure gauge was connected to the line used to charge the engine. This gauge pressure was then added to atmospheric pressure and the result taken as the average pressure of both the work space and bounce space.

Force transducers

The coupling force between the engine and the hydraulic ram was measured using a strain guage load cell, which was supplied with the hydraulic ram system (see section A.2).

Temperature measurement

Type K thermocouples were used to monitor temperature at various locations on the rig. These have a response of approximately 4.28 mV per 100 °C. The important locations were the heater external wall and the top and the bottom of the cooler (the cooler external wall temperature was taken as the mean of the latter two measurements. Other temperatures were measured to monitor instrument environments during operation. Thermocouples were either read using a dedicated data logger or using digital multimeters (in the latter case the cold junction temperature was measured using a mercury thermometer to allow for later cold junction compensation).

4.1.3 Data capture

Each of the transducers described above had its own associated signal conditioning equipment, so that all output signals were in the range $-10\ V$ to $+10\ V$. The transient data (displacement, pressure and force transducers) was measured using a computer-scope card which fitted into a slot in an IBM-compatible computer. This is a twelve-bit analogue to digital device which has a minimum sampling time of 8 μs. Typically just more than one complete engine cycle was recorded at a time. Each channel was usually sampled 4 000

times during the cycle. The resolution of the instrument was ±5 mV. The data was recorded on floppy disks for later processing.

4.1.4 Routine data processing

A computer programme entitled 'WPUMP' was used to process the raw data. The primary operations are detailed below.

Determination of cycle length

Generally piston motion was chosen as the reference for the determination of the cycle length and for the determination of phase angles. The data was first smoothed fairly severely, using the routine described below, and then divided up into cycles by looking for those regions of the curve which had the same value and the same sense as the starting region of the curve. Each such point was then considered as the end point of a cycle.

Data compression and smoothing

Each set of data was first compressed by taking the average of every eight points of the source data and storing these in a shorter working array. If necessary the data was further smoothed. This involved taking the average of a number of points on either side of the point of interest, with those points closer to the point of interest (and the point itself) having a higher weighting than those further away. Smoothing was only undertaken where necessary, and the degree of smoothing was a user determinable variable which could be set for each channel.

Conversion to standard units

All the transducers used for this work had a linear relationship between measured property and signal output. Thus translation of the recorded voltages to measured properties was relatively simple. The displacement and force transducers delivered an output proportional to the absolute value of the measured parameter, thus offset corrections could easily be applied. The pressure transducer data was normalized with respect to the average work-space pressure by first calculating the mean of the raw data, and then subtracting this mean

from each data point, thus setting the mean to zero. The average pressure, as determined by the bourdon tube gauge, was then added to each data point.

Plotting of transient data

Plots of the transient data were made, either to screen or plotter. Of importance in regard to the interpretation of these plots is that two conventions were used when considering the displacement of the components. The piston and displacer transducers measure the relative motion of these components with respect to the case. Furthermore it is the relative motion of these components which is of importance when considering the engine as a thermodynamic engine, and when comparing the engine to a free-piston machine (where case motion is often very small). Thus the Lissajous trace shown is of the relative motions. However, when considering the dynamics of the machine, the absolute motion of all three components is important. The convention used in the data presentation is that absolute motions are subscripted by a letter corresponding to the component in question only, eg, x_d means the absolute displacer displacement. Relative motions are subscripted, first by the letter of the component in question, and then by the letter corresponding to the component relative to which the motion is represented (eg, $x_{dc} = x_d - x_c$ is the displacer motion relative to the case motion).

Determination of phase angles

The phase angle by which the expansion space volume variations lead the work-space volume variations is an important means by which various Stirling engines can be compared. So too is the angle by which the pressure fluctuations in the work spaces lead the volume variations. However, this term 'phase angle' is somewhat ill defined when one is not dealing with perfectly sinusoidal motion or waves. For the 'water pump' engine tests the phase angle has been defined as follows: The complete cycle as determined above is considered as 360°. Each degree thus corresponds to 1/360 of the period of oscillation. The position of the maximum of the reference wave (usually x_{pc}) is determined, and so is the position of the minimum, in degrees, with 0° considered as the start of the cycle. The positions of the maximum and minimum of the wave of interest are then determined in a similar manner. The amount by which the maxima lead each other is called the 'peak lead angle', while the 'trough lead angle' is the number of degrees by which the minimum of the wave of interest leads the minimum of the reference wave. The 'average lead' is the mean of these two. Where only one phase angle or lead angle is reported then this is the 'average

lead'.

Calculation of pV work flow integrals

The last series of routine data processing on each test was to determine various integrals in order to gain some insight into the work flow patterns through the engine. Within the engine there are three gas spaces. The pressure of the work space and the bounce space were measured, and it was possible to estimate the pressure of the displacer gas spring by assuming it to behave as an ideal adiabatic spring. Each of the components of the engine presents specific known faces or areas to these gas spaces, and the motion of the components was known. Thus it was possible to calculate the pV work transfer from each such surface to its associated gas space during the cycle. The sum of all the work transferred into a gas space is $\oint p dV$ for that space, or expressed as a rate of energy flow, $f \oint p dV$, where f is the frequency of oscillation.

4.2 Typical engine performance

Very few 'positive output power' tests were achieved. In the discussion below, much emphasis is placed on only one run. It may seem strange to devote a major section of this work to a mere 0.035 seconds of data. However, it yielded a considerable amount of information. This is the best run of the engine obtained to date. Problems which can be rectified are identified, and it would seem pointless to discuss the myriad of tests which were performed while preliminary problems were being ironed out.

This particular test was reported by Banks [1]. A copy of the paper is appended to this dissertation. This paper contains some minor errors which could not be rectified before publication. These are noted in the appended copy. Furthermore the account given was very brief. The following presentation uses the same data, but explains the results in more detail. For the test the charge was helium at a pressure of 16 bar. The external wall hot-end temperature was 624° C (897 K) while the external cooler wall temperature was $\simeq$ 75° C (348 K). The case was oscillated at 32.7 Hz at an amplitude of 3.4 mm.

During the discussion, reference is made to the results obtained from a simulation using the 3-D SAUCE programme. A complete listing of the data input for this simulation can be found in appendix C.1. For the simulation the external wall temperatures, charge pressure and case amplitude were set equal to the measured values. The adiabatic working space model was used (see

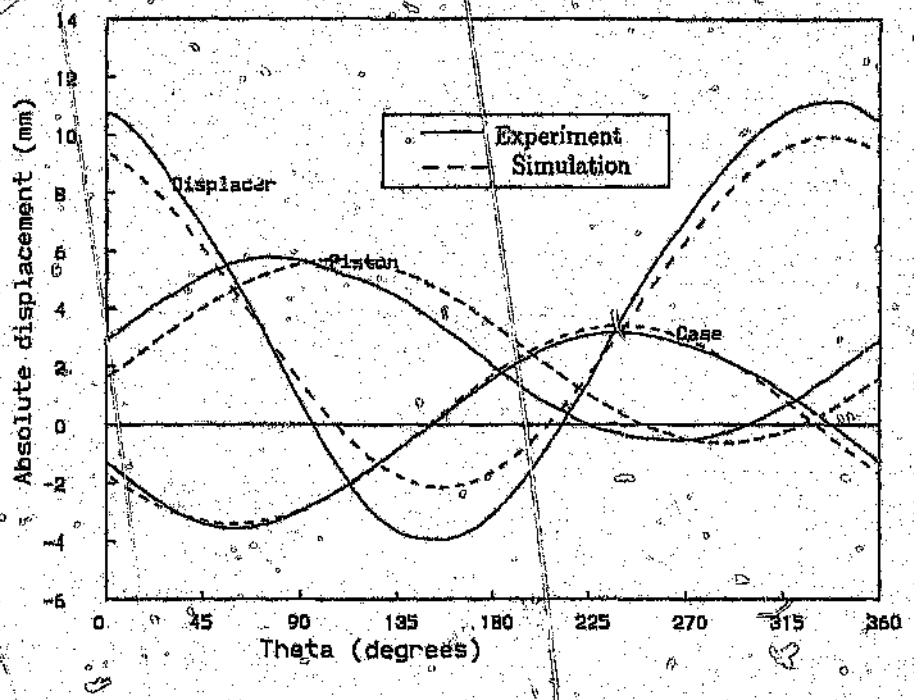

Figure 4.3: Absolute motion of 'water pump' engine components

section 3.2.2). The external mechanical spring constant K_{cg} was adjusted so that the simulation engine frequency agreed with the experimental oscillation frequency.

4.2.1 Absolute motion of the engine components

Figure 4.3 shows the absolute motion of the components as a function of θ, where θ is a time based division of the period of oscillation. Both the piston and the displacer mean positions do not correspond with the mean position expected (2.5 mm and 3.9 mm above mean respectively). In a well designed engine with good seal surfaces one would expect the displacer mean position to correspond to that position when the centering ports are lined up. The implication is that the centering ports are not large enough, or alternatively the seal leakage is too great for correct centering to occur. When the engine was dismantled after these tests it was found that the displacer gas spring seal had been severely damaged for reasons given below. Furthermore, the displacer is located by the piston, thus the offset of 3.9 mm is the sum of the piston–case and the displacer–piston offsets.

The magnitude of oscillation of both the piston and case firmly excludes the possibility of ignoring the motion of one of them in order to simplify the analysis of the engine. However the waves do have a predominantly sinusoidal pattern. The dotted curves were plotted using the amplitude and phase given by the simulation (assuming the same component mean positions as recorded experimentally). Correlation is reasonable, although the piston–case phase angle is under-predicted.

The phasor representation of the motion of the components in figure 4.4 allows easy visual comparison of the experimental and simulation data. As described earlier, the experimental phase angle is derived from the maxima and minima of the curves of figure 4.3.

4.4.2 Relative motion of components

If the displacer and piston motion are shown relative to the case motion (as measured by the transducers) it becomes much easier to compare the free-cylinder Stirling engine with other Stirling engines of the beta configuration. Such direct comparison is only relevant to thermodynamic and gas flow effects. The engine types are *not* directly comparable in a dynamic sense.

Figure 4.5 shows both simulation and experimental phasors for the piston and displacer. The displacer phase angle of 67° (experimental), 78.5° (simulation) is not unusual for a free-piston engine. Also shown in the same figure are the bounce- and work-space volume and pressure phasors.

Figure 4.6 is a plot of the relative motion of the displacer with respect to the case along the y-axis and the relative motion of the piston with respect to the case along the abscissa. The dotted curve is that produced by the simulation. The sides of the graph frame, the top, and the diagonal line on the lower right hand side represent the mechanical limits to the motion of the piston and displacer relative to the case.[4] The amplitude of oscillation of both piston and displacer were thus far short of that possible for this engine. The simulation results indicate that performance would have improved considerably at larger amplitudes (see section 4.4). However, steady state operation at large amplitudes could not be attained as the heat supply to the engine was not sufficient. Furthermore, the forces required to oscillate the case (and the hydraulic ram) at large amplitudes became dangerously high.

At frequencies lower than 32 Hz the displacer amplitude was reduced and the phase lead decreased, resulting in inferior thermodynamic performance

[4] This method of representation taken from Berchowitz[13].

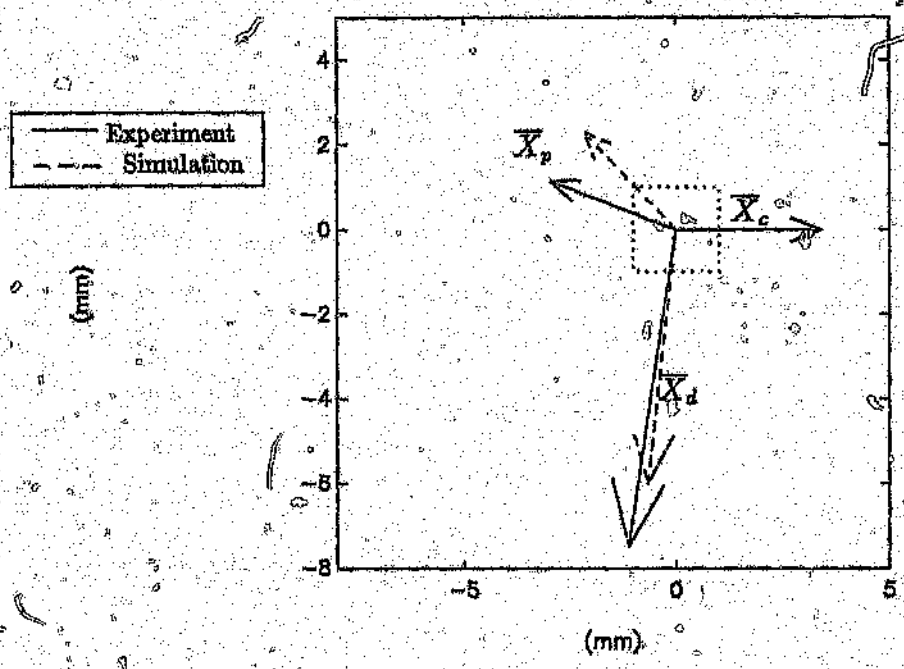

Figure 4.4: Phasor representation of experimental and simulation results.

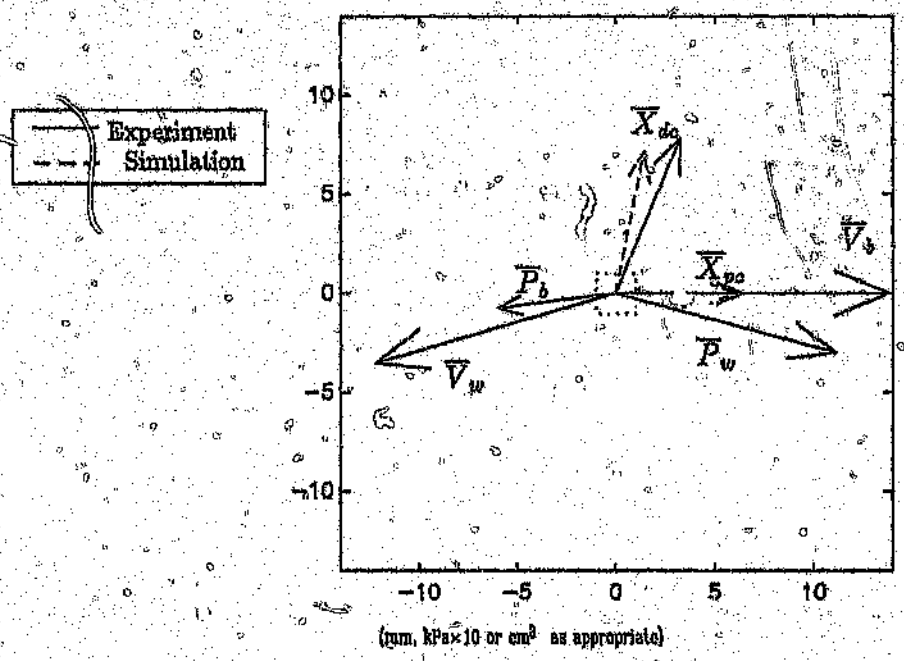

Figure 4.5: Phasor representation of relative motion, volumes and pressures

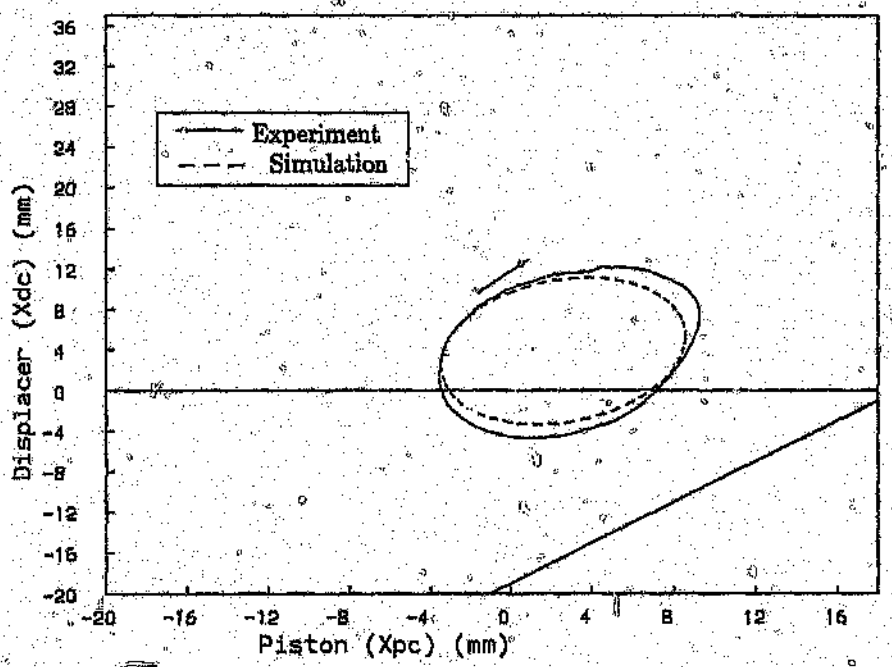

Figure 4.6: Motion of piston and displacer relative to the case

(see figures 4.12 and 4.13). Since the thermodynamic performance affects the displacer amplitude, a negative feedback system quickly reduces any 'free' engine to an inert lump of metal.

When the engine was dismantled after the tests it was found that the dome of the displacer had been rubbing against the inner cylinder wall. This resulted in a severe friction loss. Furthermore, since both the dome and the cylinder wall were at high temperatures, friction welding occurred, causing particles of metal to be broken off. These worked their way through the displacer centering ports and damaged the displacer rod seal. The above defects must have been at least partially responsible for the low displacer amplitude.

4.2.3 Force between case and ram

Figure 4.7 shows the force applied by the ram to the case versus the case displacement. Slight free play in the linkages between the ram and the engine was the primary cause of the somewhat unusual shape of this curve. The area of this curve is the work per cycle delivered by the engine. For this test the integral $\oint F_c dx_c$ yields an output of 1.23 Joules per cycle (40 Watts). The power

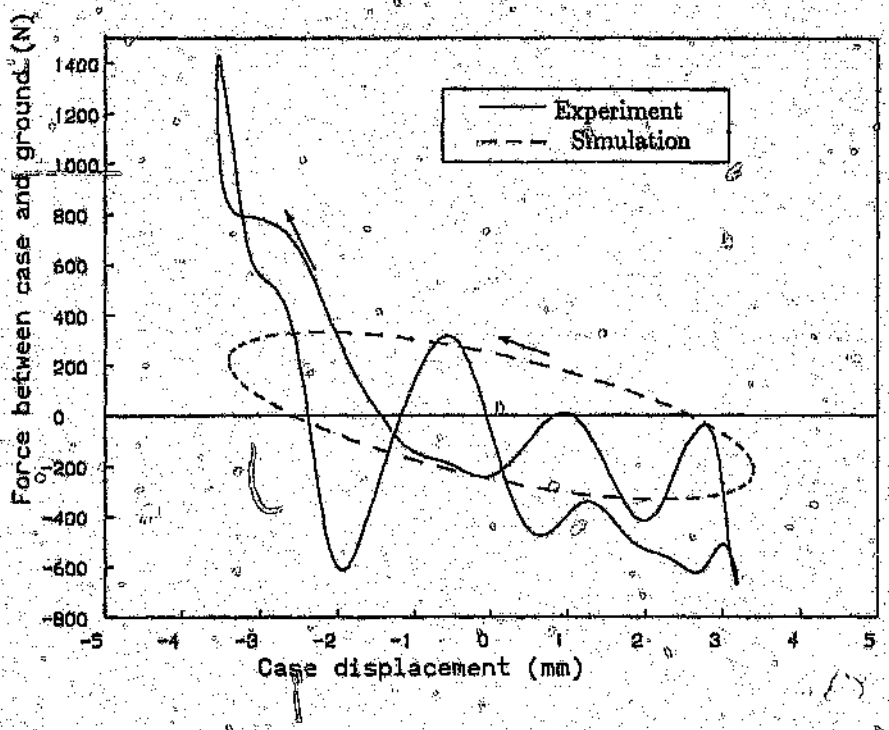

Figure 4.7: Case force versus case motion

predicted by the simulation was 88 W. Although there was a net transfer of energy from the engine to the ram during this cycle, the forces required to maintain oscillation at the correct frequency were extremely high (> 1.2 kN). The case was obviously not oscillating at its natural frequency. For stand-alone operation it would be necessary to tune the engine, so that the displacer and case motions are better matched without the need for a sophisticated loading device. The dotted curve shown in the figure is that force which would occur between the case and ground as determined by the simulation (a combination of the effects of the case–ground spring ($K_{cg} = 64$ kN/m) and the case–ground damping solved for by the simulation ($D_{cg} = 359$ Ns/m). The combined calculated force is: $F_c = D_{cg}\dot{x}_c + K_{cg}x_c$.

4.2.4 Pressure–volume diagrams

The pV diagrams for both the bounce- and work-space volumes are shown in Figure 4.8. Clockwise rotation about the diagram indicates positive work. Thus the bounce space is absorbing work. The sum of the cyclic area of the two curves is the total energy per cycle available both to drive the components and to deliver power. The waviness near the ends of the pV diagrams is assumed

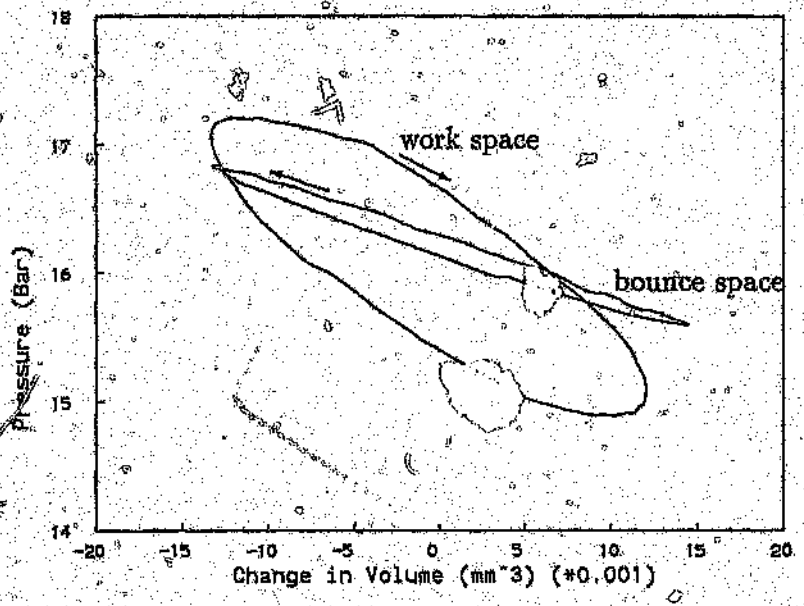

Figure 4.8: Pressure-v diagram

to be the result of the extremely high accelerations imparted to the case as a result of the linkage free play.

This diagram highlights one of the other problems of the test free-cylinder engine. The area of the bounce-space curve indicates a net loss of 9.81 Watts. This is a significant fraction of the work delivered by the engine. There are three mechanisms which cause this loss, the bounce-space hysteresis loss, seal and centering port losses, and gas flow dissipation (the last two not included in the simulation). The simulation indicates a bounce-space hysteresis loss of 4.3 W, and a piston seal loss of 2.8 W. The simulation thus underpredicts the bounce-space losses.

A series of tests was performed on the piston rings. Tests were performed with a nominal pressure of 200 kPa across the seals, the low pressure side open to atmosphere. Leakage rates varied from 0.12 l/s to 0.24 l/s. Although the working fluid would be more dense at the working pressure of 16 bar, it is clear that the seals did not perform very well. Misalignment of the engine components, and slight imperfections on the seal surfaces are assumed to be the principal cause of this.

4.2.5 Phase angles

Table 4.1 shows pertinent phase angles and amplitudes for the above test. Data from a similar test for which nitrogen was used as the working fluid is also presented. The left hand figure in each column is the experimental result, while the right hand figure is that predicted by the 3-D SAUCE analysis.[5]

The helium experimental and simulation results agree reasonably well. However, for the nitrogen test the simulation was not very successful, particularly as it indicates that the engine should have produced a positive net power output, whereas the experimental results show that the engine was being driven by the ram for this test. Displacer amplitude and piston phase are also not well simulated.

4.2.6 Work flow paths

A method was described on page 92 whereby an indication of the work flow paths through the engine can be obtained by analyzing the cyclic integrals of the terms which comprise the equation for $\int \oint p dV$ of each gas space. Table 4.2 shows the value of these integrals. (Note: For the purposes of this table, the displacer gas spring was assumed to be an ideal adiabatic gas spring with no losses).

The indicated power available for transmission through the case to the load is $\int \oint F_{pc} dx_c$. Mechanical friction losses which result from the case movement, both with respect to the internal components and the external case supports would have to be subtracted from this in order to obtain the actual output power of the engine. The actual output power was however measured, $\int \oint F_{ec} dx_c$. Since $\int \oint F_{ac} dx_c$ is the higher value, it must be inferred that there is significant error in one or both of the readings. This could not be located and eliminated during the time available. However, the most likely cause is the free play in the linkage from the case to the hydraulic actuator. This caused shock loads which distorted both the pressure and load cell dynamic traces.

The indicated power at the working space, $\int \oint p_w dV_w$ is significantly higher than the power available externally. An important loss is that required to drive the displacer, $\int \oint F_{pd} dx_d = 12.2$ W, or 15% of the indicated power. As mentioned above there was evidence to suggest that the friction losses on the displacer were abnormally high, accounting in part for this. There are other

[5] Although the properties of 'air' were used for simulation of the 'nitrogen' test the difference in gas properites is insignificant for the purposes of this exercise.

Table 4.1: Data summary

		Test	Simulation	Test	Simulation
Charge	1600 kPa	Helium		N_2	Air
Frequency	Hz	32.7	32.7	30.7	30.7
$f \oint F_{ec} dx_c$	J	40.2	88.9	-24.7	69.2
Heater ext. wall temp	K	897	897	889	889
Cooler ext. wall temp	K	348	348	345	345
Piston amplitude	mm*	6.4	6.02	6.2	6.59
Displacer amplitude	mm*	8.5	7.25	4.1	7.67
Displacer/piston phase	deg.*	67.4	78.5	65.5	82.2
Work space					
Maximum pressure	kPa	1720	1732	1710	1728
Minimum pressure	kPa	1490	1467	1500	1472
Pressure/piston phase	deg.*	-15.1	-26.4	4.0	-18.5
Bounce space					
Maximum pressure	kPa	1656	1657	1647	1652
Minimum pressure	kPa	1543	1543	1552	1448
Pressure/piston phase	deg.*	187	183	192	181
Absolute Motion					
Case amplitude	mm	3.4	3.4	3.6	3.6
Piston amplitude	mm	3.1	3.16	2.7	3.41
Piston/case phase	deg.	159	133	200	140.2
Displacer amplitude	mm	7.3	6.04	4.6	6.8
Displacer/case phase	deg.	262	264	302.3	270.9

Values marked with an * refer to piston and displacer motions relative to the case motion, ie, $(x_p - x_c)$ for the piston and $(x_d - x_c)$ for the displacer.
Phase is calculated as the average of the number of degrees (where 360 degrees corresponds to a complete cycle) by which the peak of one signal precedes the peak of the reference signal and by which the trough of one signal precedes the trough of the reference signal.
F_{ec} refers to the external force (excluding the mechanical spring) acting on the case, ie, between engine and load. Thus $f \oint F_{ec} dx_c$ is the power output.

Table 4.2: Work flow paths, helium test

—	Piston	Displacer	Case	Sum
Work space	$-f\oint p_w A_p \mathrm{d}x_p$	$f\oint p_w A_r \mathrm{d}x_d$	$-f\oint p_w A_c \mathrm{d}x_c$	$f\oint p_w \mathrm{d}V_w$
Work space	4.71	43.2	33.7	81.4
Displacer gas spring	$-f\oint p_{ds} A_r \mathrm{d}x_p$	$f\oint p_{ds} A_r \mathrm{d}x_d$	—	$f\oint p_{ds} \mathrm{d}V_{ds}$
Displacer gas spring	30.9	0.9	—	0
Bounce space	$f\oint p_b A_s \mathrm{d}x_p$	—	$-f\oint p_b A_c \mathrm{d}x_c$	$f\oint p_b \mathrm{d}V_b$
Bounce space	-11.2	—	1.4	-9.8
Sum	$f\oint F_{pp} \mathrm{d}x_p$	$f\oint F_{pd} \mathrm{d}x_d$	$f\oint F_{pc} \mathrm{d}x_c$	
Sum	24.4	12.2	35.0	71.6
Load cell $f\oint F_{ec} \mathrm{d}x_c$	—	—	40.2	—

Notation:
f: Frequency of oscillation (Hz)
F_{pp}: Force due to gas pressure acting on piston
F_{pd}: Force due to gas pressure acting on displacer
F_{pc}: Force due to gas pressure acting on case
F_{ec}: Force between case and hydraulic actuator (load)

losses which have an effect on the displacer. The displacer gas spring has a high ratio of $\Delta V/V$, resulting in a simulation hysteresis loss of 5.8 W, of which 4.0 W is a direct load on the displacer. The simulation estimated loss due to ring seal friction is 0.5 W, while that due to leakage of the gas spring clearance seal was estimated at 2.1 W by the simulation. (A clearance gap of 25 μm was assumed. The displacer rod seal was found to be in poor condition after the tests, thus the simulation probably underestimated the leakage losses.) The effect of the gas-pumping losses on the displacer was an estimated dissipation of 4.5 W. The net work required to drive the displacer is thus similar to that predicted by the simulation.

From the above experimental results the work required to drive the piston is 24 W, or 30% of the work-space output. The simulation however predicts a loss of only 9.8 W, made up as follows:

piston seal leakage	2.8 W
piston friction loss	0.5 W
a portion of the gas flow losses	0.7 W
the displacer gas spring	5.8 W.

The bounce-space hysteresis loss does not form part of the above loss as it

is accounted for separately in table 4.2. Thus the simulation results do not match well. However, it should be noted that for the integral $f \oint p_w A_p \mathrm{d}x_p$ the pressure was measured at the top of the engine, thus any pressure drop across the heat exchangers (and hence reduction in the available pV work to drive the piston) would not have been reflected in the experimental results.

Two routes exist whereby work from the work space is transferred to the outside world (the case of the engine). The first is obviously through the differential area of the case acting on the work space, $-f \oint p_w A_c \mathrm{d}x_c$. However, both the displacer and the piston absorb work from the work space, some of which is transferred through the bounce space, acting on the case as $-f \oint p_b A_c \mathrm{d}x_c$. The displacer path involves transmission through both the displacer gas spring and the piston into the bounce space. This second transmission path is important, as a reduction in bounce-space, seal leakage and friction losses would allow a considerable portion of the work extracted from the work space by the piston and displacer to reach the case.

Note: The condition and exact dimensions of the heat exchanger surfaces in the engine are not known. It would be necessary to irreversibly damage the engine to gain access to these surfaces. Although care was taken in deducing their geometry (using engineering drawings of a very similar Sunpower macine), the data may be incorrect. This would have an effect on the simulation heat exchanger flow loss predictions.

4.3 Performance curves

Detailed performance curves for the engine were not obtained. However, the data collected during the various engine trials does show a remarkable degree of conformity, and serves to give an indication of trends and expectations. Unless labelled 'cold', the data points shown are for tests where the hot-end temperature was within the range of 820 K and 970 K. The majority of tests were conducted at a hot-end temperature of above 870 K. The only tests which reflect a positive engine output power are some of those clustered around 33 Hz with helium as the working fluid.

Where appropriate, performance trends from the 3-D SAUCE simulation are included. The simulation operating frequency was controlled by varying the spring constant between the case and ground (K_{cg}). In order to obtain simulation results for the lower frequencies it was necessary to assume values for $K_{cg} \leq 0$. This resulted in a non-oscillatory unstable root (positive real component, zero imaginary component) of the characteristic equation. An engine

mounted on such a spring would either move up or down to the nearest mechanical end stop. The data shown was obtained by ignoring this root, and allowing convergence to take place around the usual oscillatory root. It does therefore represent a hypothetical situation, and is only included because it serves to illustrate the trends effectively. The hot-end temperature was set at 890 K, and that of the cold end at 345 K. Case amplitude was fixed at 3.5 mm. All other input data for the simulation is as for the helium and nitrogen simulations described in table 4.1. For all the simulation runs, the power output was positive ($D_{eg} > 0$).

4.3.1 Amplitude ratios

Piston amplitude ratio

Figures 4.9 and 4.10 show how the ratio of piston amplitude to case amplitude increased around the piston resonant frequency of 22 Hz. The similarity between the 'hot' and 'cold' data points might lead one to assume that the thermodynamic effects on the engine are of minor importance. This is not the case, as the amplitude ratio for the operating engine was significantly higher (the upper points on the helium curve near 33 Hz.) The simulation results indicate general conformity with those from the tests.

Displacer amplitude ratio

The displacer has a resonant frequency which is in the region of 32 Hz, as shown by figures 4.11 and 4.12. The first figure also highlights the distinction between absolute and relative motion of the piston and displacer. At the higher frequencies, the displacer responds far more than the piston, although the relative motions, (and therefore the work-space volume variations) do not undergo as significant a change. The dip in the curves at 22 Hz corresponds to the resonant frequency of the piston.

In figure 4.12 the absolute and relative displacer amplitude is normalised with respect to the case amplitude. The lower curve, that of X_d/X_c is remarkably flat. This is not because the displacer shows no clear resonant frequency, but is rather a reflection of the source of the driving force to the displacer. As the displacer gas spring is coupled directly to the piston, the reduction in piston amplitude with an increase in frequency reduces the displacer excitation. Thus the approach to the natural frequency of the displacer yields less of an increase in displacer amplitude than may be expected. The upper curve, which

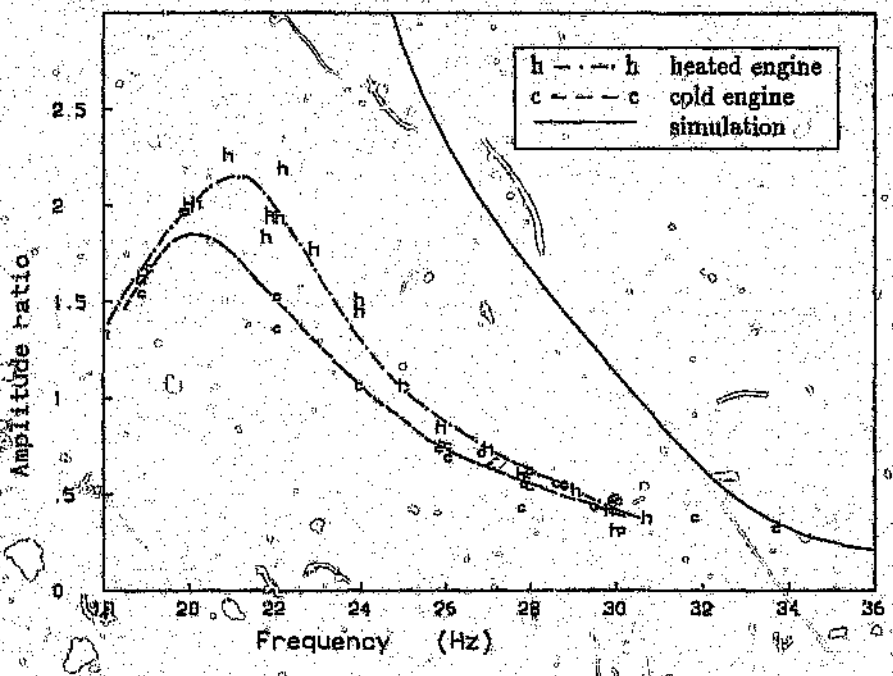

Figure 4.9: Piston amplitude/case amplitude versus frequency: nitrogen

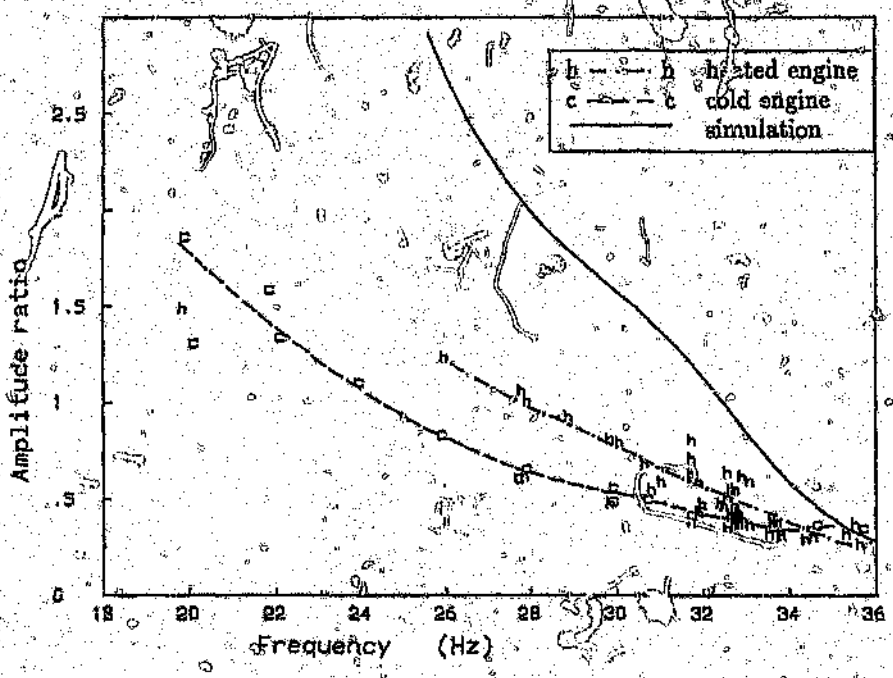

Figure 4.10: Piston amplitude/case amplitude versus frequency: helium

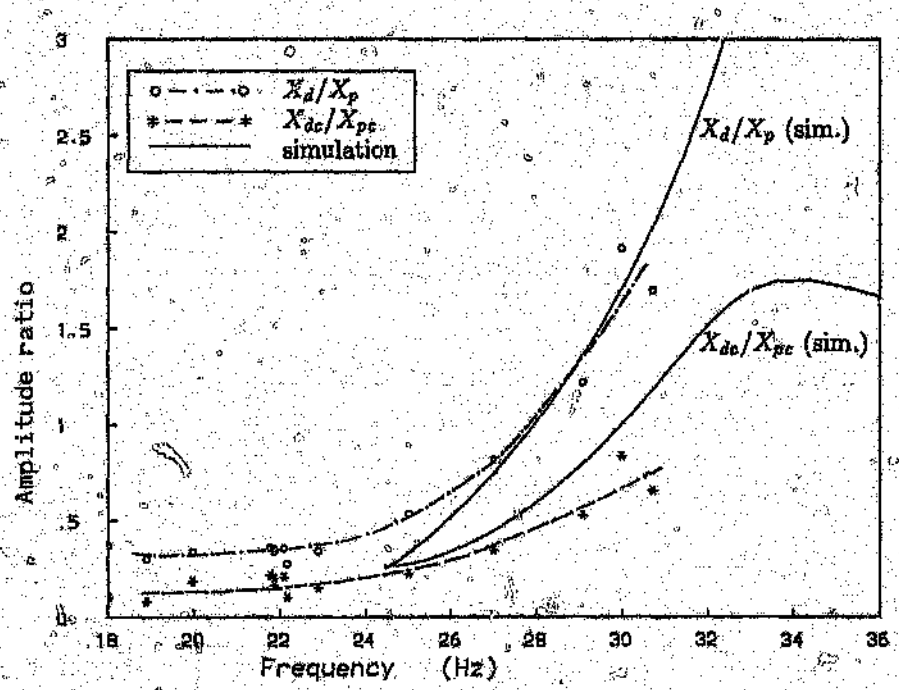

Figure 4.11: Displacer amplitude/piston amplitude versus frequency: nitrogen

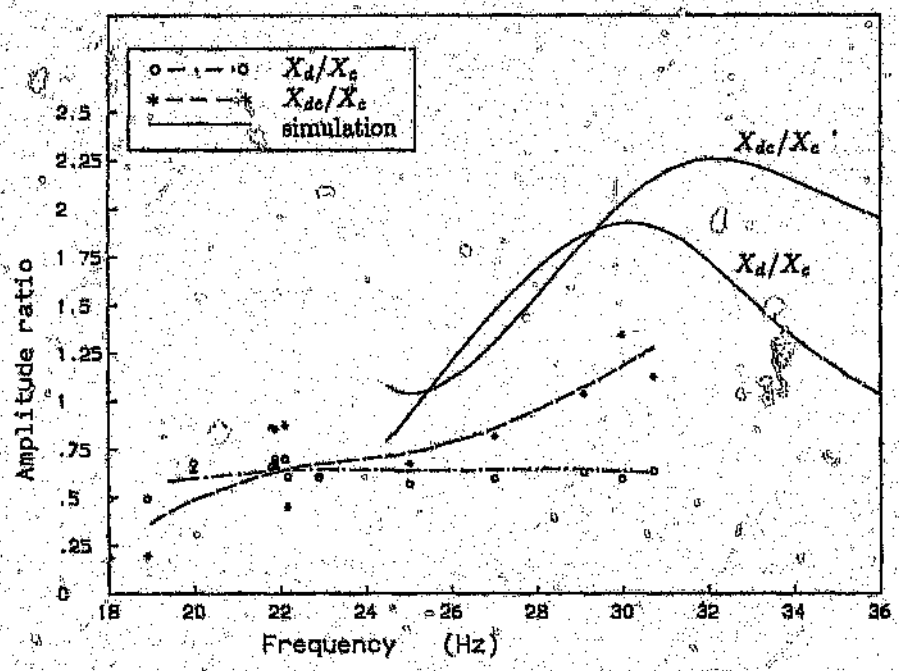

Figure 4.12: Displacer amplitude/case amplitude versus frequency: nitrogen

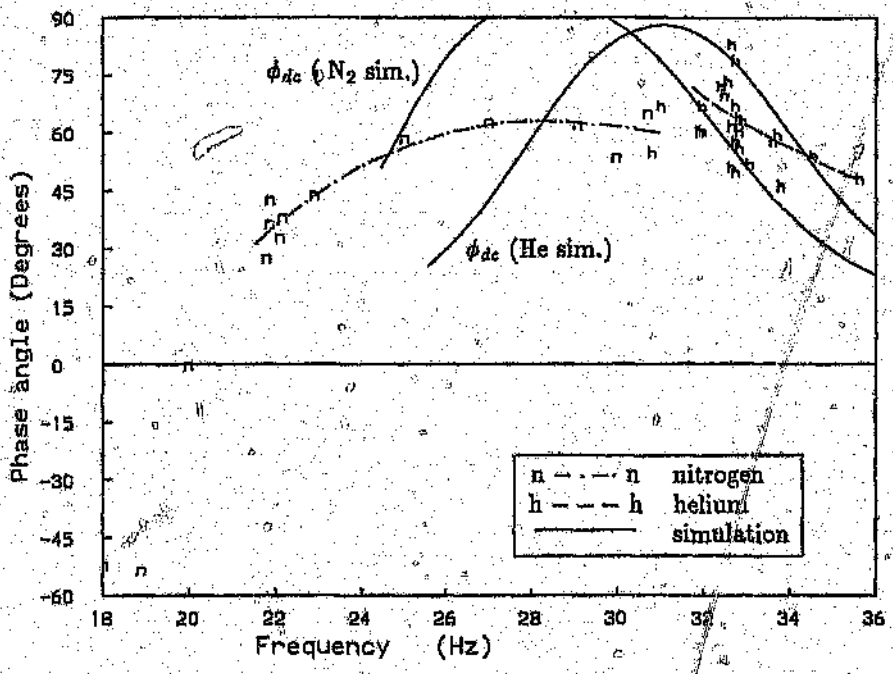

Figure 4.13: Displacer–piston relative motion phase angle versus frequency

represents the ratio of expansion space volume variations to case amplitude, indicates a clear increase as the frequency approaches 31 Hz. Since the thermodynamic performance of the engine is highly dependent on expansion and compression space volume variations, this further explains the restriction of engine operation to frequencies near 31 Hz (nitrogen) and 33 Hz (helium).

4.3.2 Phase angles

Figure 4.13 shows the number of degrees by which the relative motion of the displacer with respect to the case leads the relative motion of the piston with respect to the case. This is equivalent to the usual displacer–piston phase angle reported in the general literature, and allows direct comparison with free-piston or kinematic engines of the beta configuration. The considerable scatter in the 'operating regime' indicates the significant changes in the dynamic operation of the engine as it produces net positive output power. There is a fairly broad band over which the displacer phase angle is within acceptable limits for successful operation (24 to 34 Hz, nitrogen experimental results), which would seem to indicate a tolerance to frequency variation. However, reference to figure 4.11 shows that the displacer amplitude is strongly dependant

on frequency, thus limiting the operating regime. The simulation curves for both helium and nitrogen agree closely with the experimental results over the operating region (near 31 Hz for nitrogen and 33 Hz for helium). However, they show more sensitivity to frequency than noted experimentally.

Figure 4.14 shows the phase angles by which the absolute motion of the piston and the displacer lead that of the case. The upper curve illustrates the approach of the displacer to its resonant frequency, where its motion lags that of the case and leads that of the piston by approximately 90°. The transition of the piston phase through a typical resonance phase angle of 270° at 22 Hz to a phase angle close to 180° near the engine operating frequency is also clear. The simulation results, which predict positive output power, have a significantly lower phase angle for the piston. (No nitrogen experiments yielded positive output power). However, figure 4.15 (helium), which includes some tests with a positive output power indicates considerable variation of the piston phase angle within the region where the engine produced positive power. Some of the data points fall close to the range given by the simulation. This apparent random scatter becomes markedly clearer when one compares the piston phase angle to the output work ratio.[6] Figure 4.16 shows only those helium tests within the frequency range 32.4 – 33 Hz. This is the region contained between the vertical lines in figure 4.15. Tests with a higher output work ratio have a lower piston–case phase angle. The simulation, which predicts that the engine should produce even higher output work, predicted an even lower piston–case phase angle (the bottom curve of figure 4.15).

4.3.3 Indicated work

Figures 4.17 and 4.18 show the bounce-space indicated work $(\oint p_b \mathrm{d}V_b)/X_c$, the work-space indicated work $(\oint p_w \mathrm{d}V_w)/X_c$, and the work transferred from the engine to the ram $(-\oint F_{cc}\mathrm{d}x_c)/X_c$. Each quantity is divided by the engine case amplitude to reduce the effects of amplitude variation.

4.4 Possible engine performance

The results presented in this section are based on the simulation of the 'water pump' engine, and serve to illustrate the potential performance of such an engine. No effort has been made to optimize the design of the engine, although

[6] Defined as the quotient of the work delivered to the ram by the engine and the amplitude of oscillation of the case in millimetres.

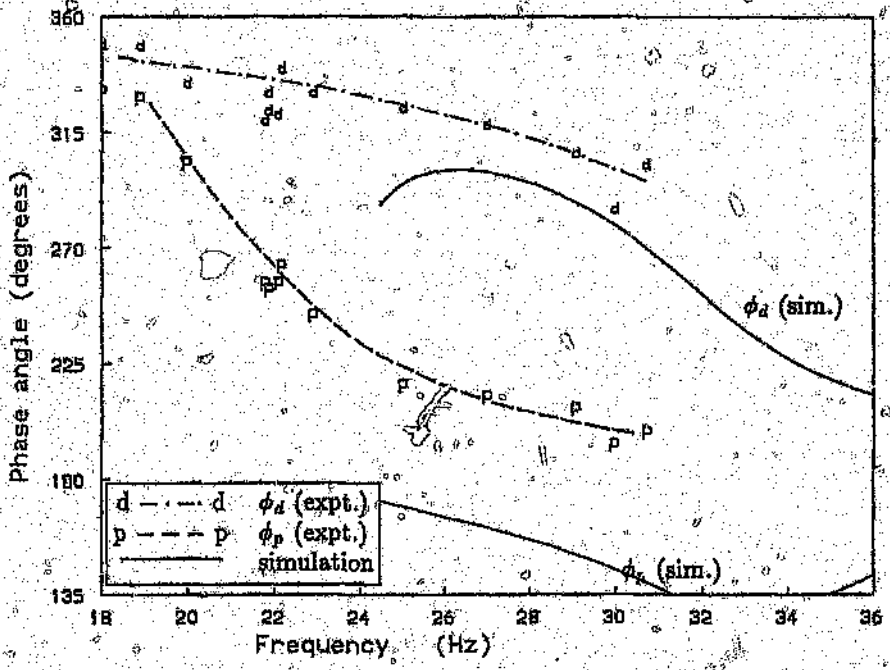

Figure 4.14: Displacer (d) and piston (p) absolute motion phase versus frequency: nitrogen

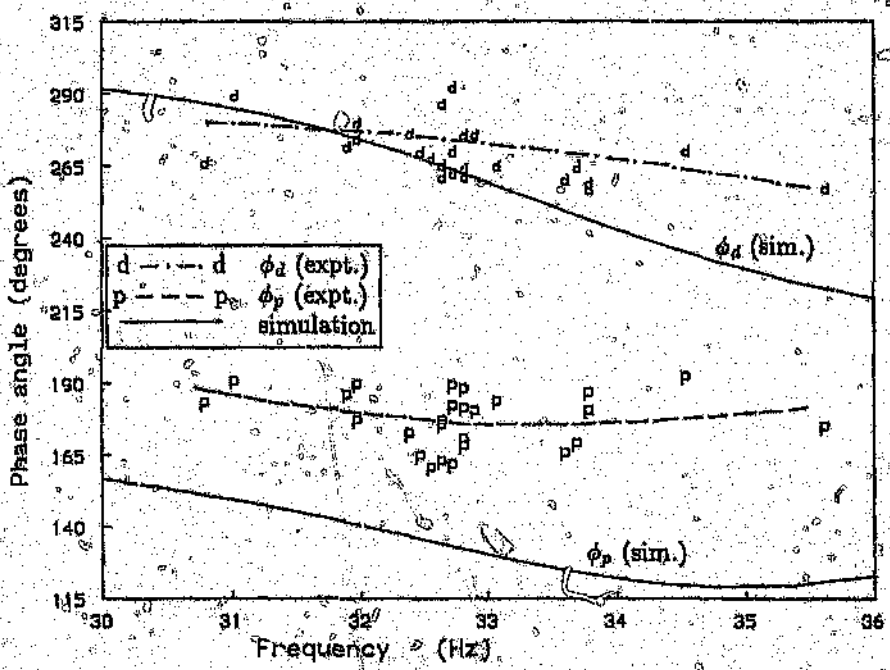

Figure 4.15: Displacer (d) and piston (p) absolute motion phase versus frequency: helium

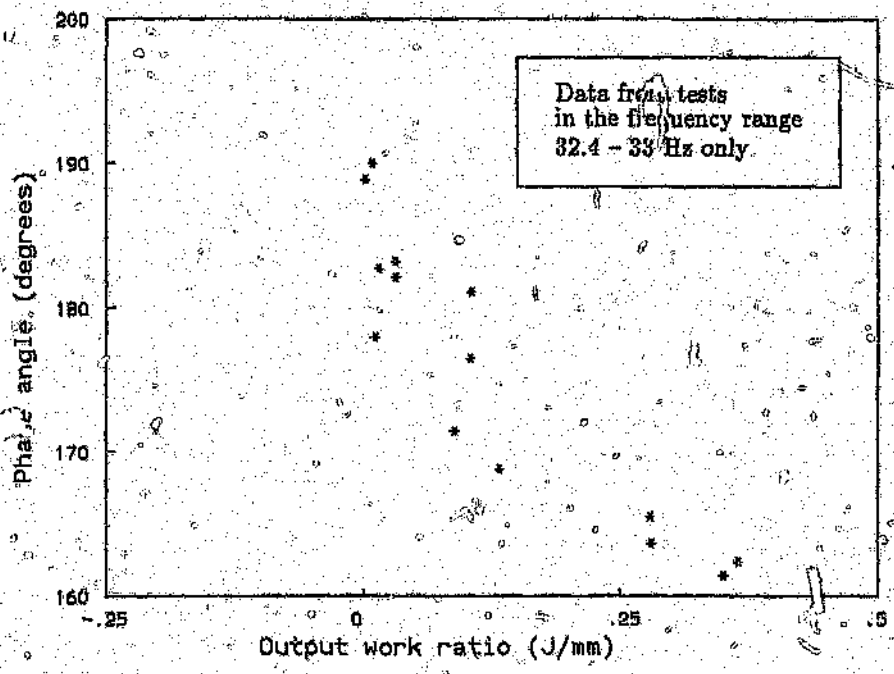

Figure 4.16: Output work ratio $((-\oint f_{ec} dx_c)/X_c)$ versus piston phase: helium

the manner in which the simulation could be used to assist in engine design is illustrated in section 3.6.

The geometrical data for the engine is identical to that used for the comparisons presented in section 4.3. The hot-end external wall temperature was set at 973 K (unless otherwise stated) while the cold-end wall temperature was set at 333 K. The thermodynamic analysis assumes adiabatic work spaces. The working fluid is helium. The displacer mean position was raised, so that the clearance between piston and the bottom of the displacer, and that between the top of the displacer and the hot end were approximately equal.

Figure 4.19 shows the relationship between the power delivered by the engine, the engine efficiency (power out/heat input to engine), and the amplitude of oscillation of the case. It can be seen that the experimental work was conducted at amplitudes far lower than the optimum. Experimental work was not conducted at these amplitudes for the following reasons. The forces required to oscillate the hydraulic ram at such amplitudes were beyond the capabilities of the hydraulic systems. Free play in the linkages connecting ram to engine induced very severe shock loads. Lastly, but perhaps most importantly in terms of future development of the engine, the heat transfer

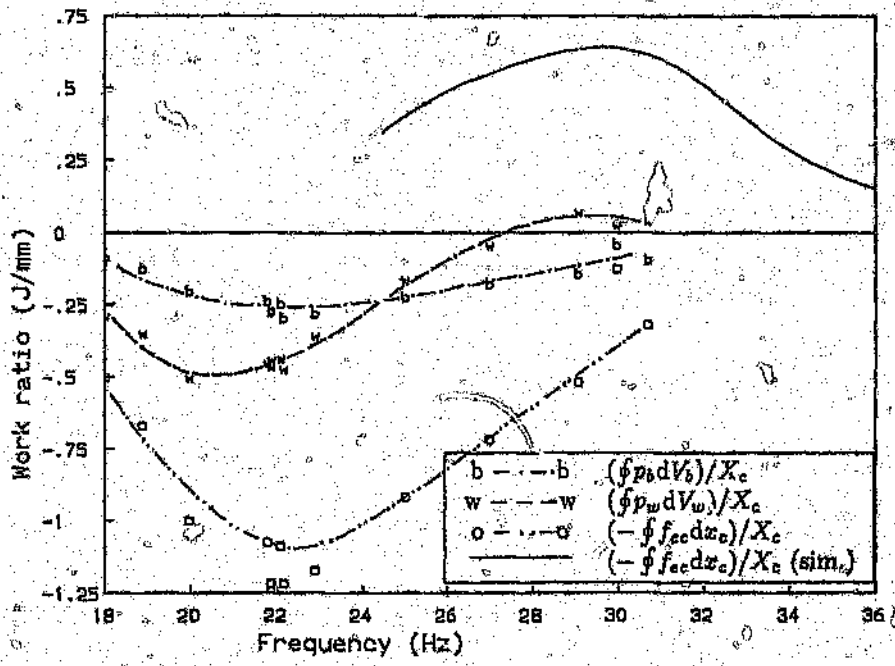

Figure 4.17: Indicated and measured works versus frequency: nitrogen

rate from the burner to the external walls of the engine was insufficient. As noted earlier, the heat transfer model used in the analysis does not examine the heat transfer from heat source to engine external wall, although heat transfer from this wall to the working gases is analyzed (section 3.2.3). If future work is to be considered then these factors will clearly have to be addressed.

The free-cylinder Stirling engine can only interact with its load via those components of the matrix equations which link the case to the ground, ie: D_{cg}, a component of D_{33}, and K_{cg}, a component of K_{33}. Two other important variables as far as the load is concerned are obviously the amplitude and the frequency of oscillation. The power delivered from the engine to the load is: (From equation (3.72), $D_{cg} = D_{33} - D_{cl}$)

$$P_{load} = \frac{\omega^2 X_c{}^2 D_{cg}}{2}$$

In the simulation procedure used the case amplitude of oscillation was fixed and the frequency and the power are determined through an iterative process. Thus figure 4.19 was produced by simulating the engine over the indicated range of amplitudes. The spring constant K_{cg} was kept constant at 80 kN/m.

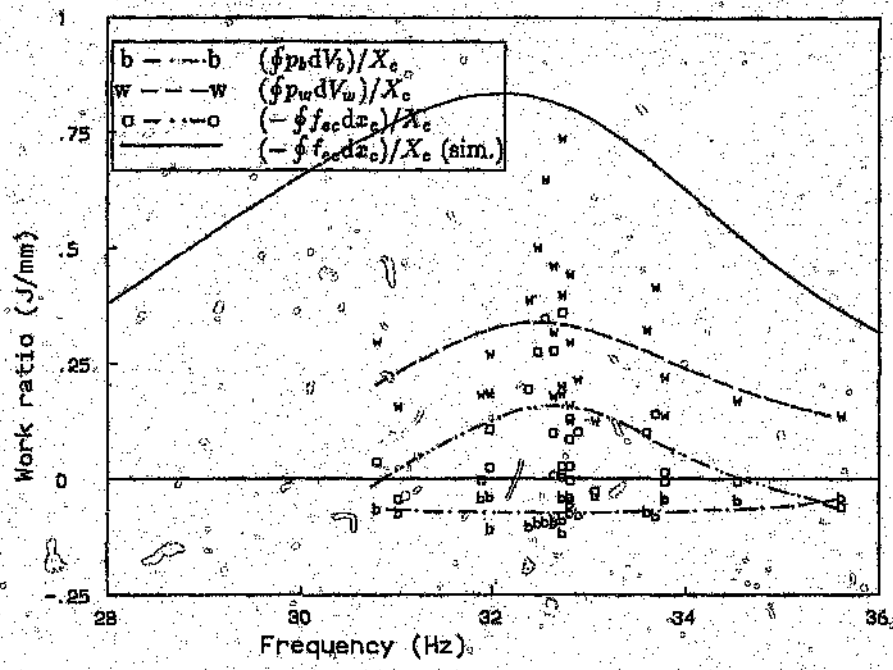

Figure 4.18: Indicated and measured works versus frequency: helium

The curves in figure 4.20 indicate the changes in the required values of D_{cg} over the same operating range as for figure 4,19. Thus, if the load device was such that it had a constant damping coefficient D_{cg} then the engine would operate along line **ab**, depending on the hot-end temperature. Often a load such as a water pump will have a damping coefficient which increases with increasing amplitude. Such a situation may be advantageous as shown by curve **cb** in figure 4.20. This allows oscillation at larger amplitudes and higher power over a range of hot-end temperatures. The angle λ at which the load damping coefficient curve intersects the engine operating curves should be as large as possible. A shallow curve, such as **eb** will result in a larger variation of amplitude and hence power delivered to load for a given temperature variation. A steep curve such as **cb** will result in less variation of the operating parameters.

Figure 4.21 shows the frequency variation through the same amplitude range. Frequency remains relatively constant. The frequency of oscillation of the engine is principally a function of the mass and spring constants applicable to each component. Given a particular free-cylinder Stirling engine, the only way in which the frequency of oscillation can be materially affected by the load is by variation of K_{cg}. The effect of different values of K_{cg} is discussed in section 3.6 and 4.3 and is therefore not considered further here. See section 3.5 for a

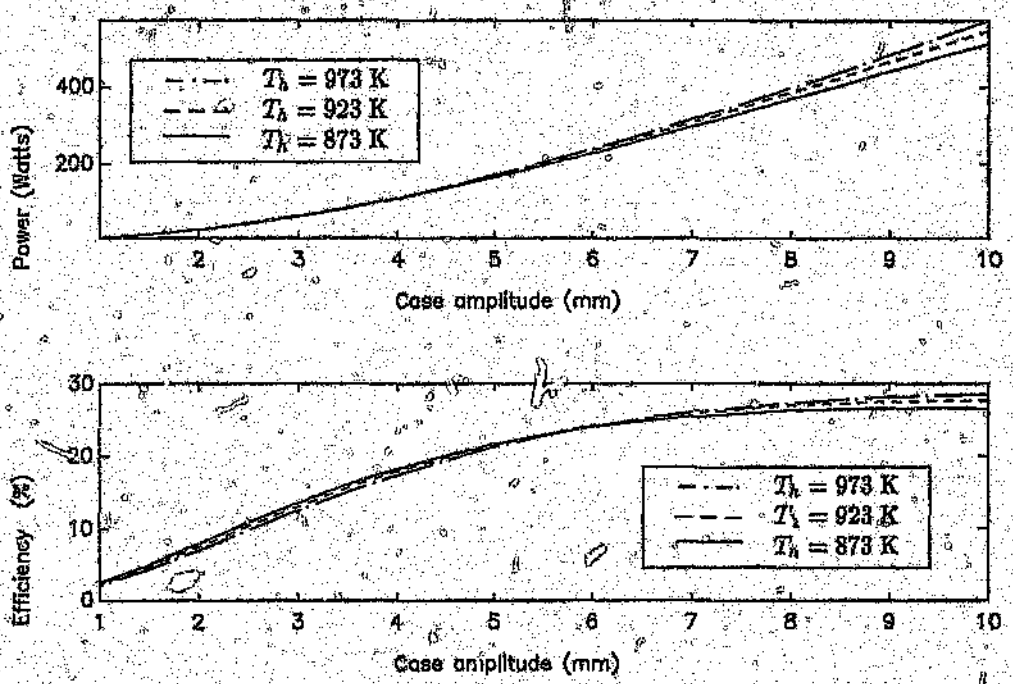

Figure 4.19: Engine power and efficiency as a function of case amplitude

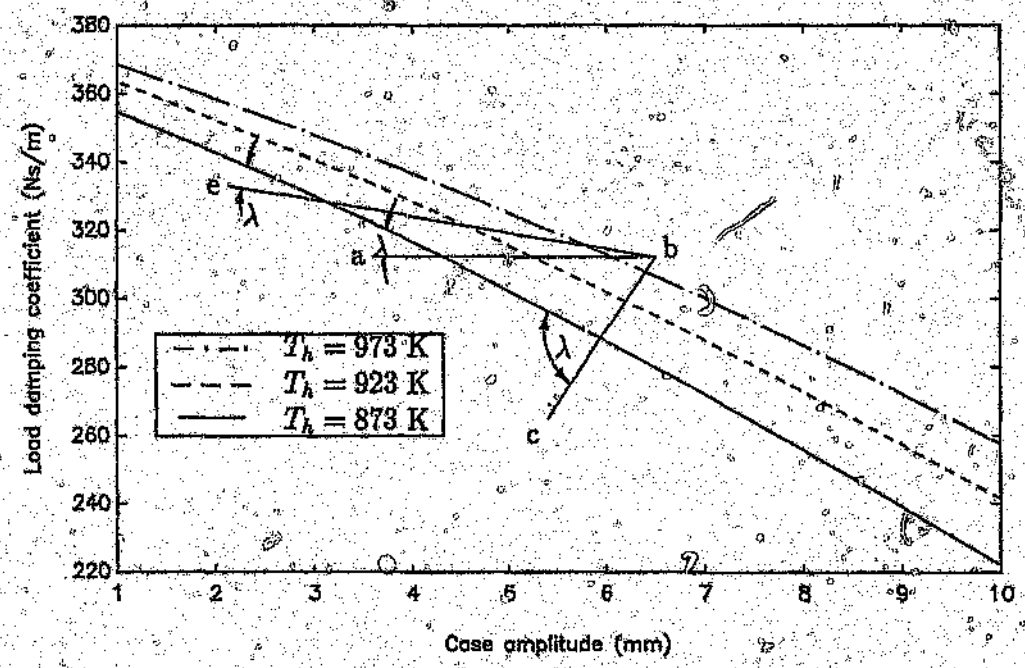

Figure 4.20: Load damping coefficient versus case amplitude

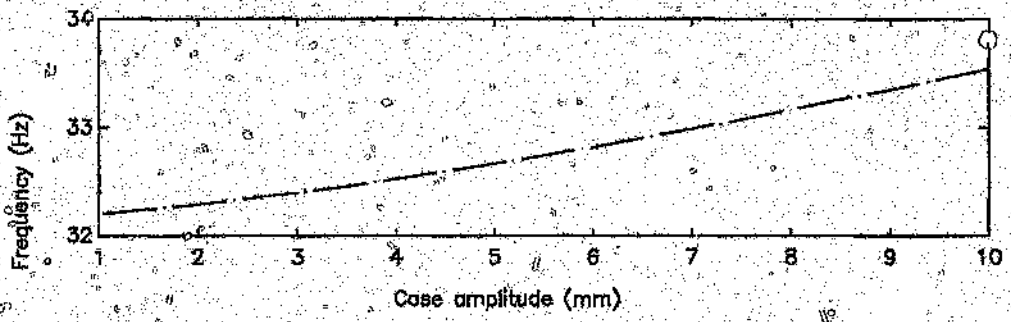

Figure 4.21: Engine frequency versus case amplitude

discussion of how any mass which is part of the load, but rigidly connected to the case could be treated.

4.5 Summary: 'Water pump' engine experimental and simulation results

The comparison of the experimental and simulation results presented in the preceding sections indicates that the 3-D SAUCE programme is a reasonable tool for the prediction of the behaviour of free-cylinder Stirling engines. While the simulation constantly overpredicts the performance of the engine, the basic dynamic motion of the engine is modelled reasonably well. General trends in amplitude and phase angle are similar in experimental and simulation results. It is unfortunate that a better understanding of the heat transfer in the engine, as well as of the seal leakage was not obtained, as the uncertainty of these parameters makes further refinement of the dynamic model very difficult. It is however felt that the results do illustrate that the analysis model as developed in chapter 3 provides an acceptable framework for the analysis of free-cylinder engines similar to the 'water pump engine'.

Chapter 5

Experimental results: Model B-10 engine

5.1 Introduction

The engine used for the experimental work described below was the well known Model B-10 Demonstrator, produced by Sunpower Inc. As slightly different versions of this engine have been produced over the years, a drawing of the original engine is shown in figure 5.1. The engine is very simple, and easy to run. It has a wide tolerance to variations of the operating pressure, springs and masses of the components. Various fourth year engineering projects have been carried out, partially under this authors supervision, in which the engine was tested in the free-piston mode. This author subsequently designed an experimental rig such that the engine could operate in the free-cylinder mode. Greig [26] used this rig for his final year BSc (Eng) project. Further modifications were made and the work reported here was then carried out in the latter part of 1992.

The instrumentation developed and used allowed testing for fairly long periods over a wide range of operating conditions. The important parameters which were varied, were: charge pressure and working fluid, hot-end temperature, case mass and case-ground spring stiffness, displacer mechanical spring stiffness and engine load. It would have been fairly simple to vary other parameters, however this was unnecessary for the purposes of this study.

Tests were usually run for either 10 or 40 seconds. The shorter tests were used to evaluate the engine under steady state conditions, and the longer for evaluation of the response to sudden changes in load.

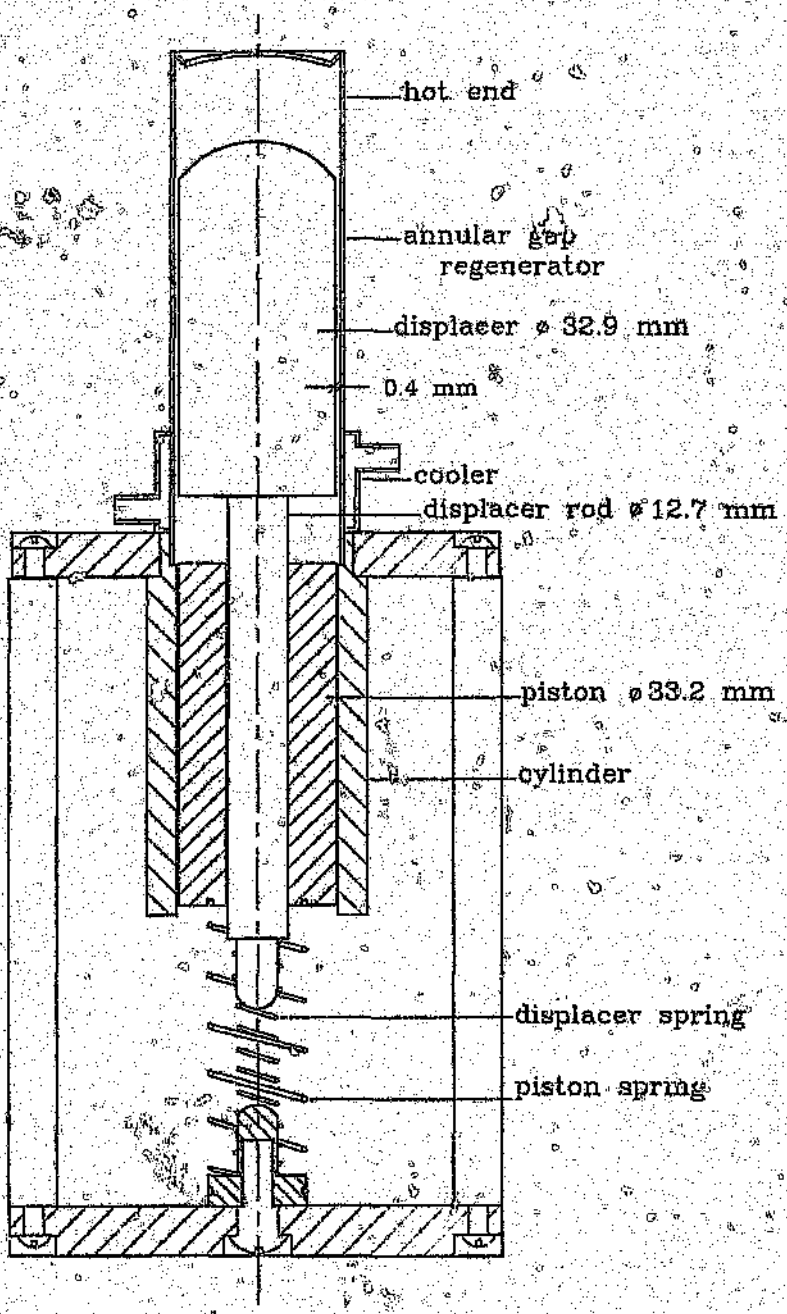

Figure 5.1: Drawing of B-10 engine before modification

5.1.1 B-10 engine

Figures 5.3 and 5.2 show the engine, mounted within a frame, so that the case of the engine could oscillate. The case, with its mass significantly reduced by the removal of metal from the wall and flange, was supported on a spring, and could drive a load device through the force transducer. The clear perspex tube around the bottom half of the engine allowed pressurization of the engine. Black and white markers were attached to the piston, displacer and case. Thus the motion of the components could be recorded using a video camera.

The engine was heated using an electrical resistance heater. A thermocouple and control circuit allowed constant temperature control. Cooling was achieved using circulated water. The load device shown comprised a 20 Watt loudspeaker attached to a negative impedance circuit (see section B.1.4). The load on the engine could thus be varied during tests.

During the course of the experimental work the engine was modified by changing the length of the case spring, and thereby changing its stiffness. Four different displacer mechanical springs were used, while the piston spring stiffness remained essentially constant. Spring stiffness was measured at various points during the testing by means of static measurements of displacement for a known applied force.

The case mass was varied by clamping large C-type clamps onto it.

5.1.2 Instrumentation

Figure 5.4 shows the instrumentation system in a block diagram format. The instrumentation and routine data processing is described in more detail in Appendix B.2. Motion data was recorded using a video camera, while pressure, force and temperature data was recorded using two computer-scope cards linked directly to personal computers. Synchronization of the recording media was achieved using a strobe light trigger-pulse output from the video camera. As the motion measurement system is non-intrusive, and requires only that clearly visible markers be attached to the engine components it has clear advantages over the more traditional techniques. However the slow sampling rate (200 Hz) did require that engine operation be steady, to enable a composite picture of engine motion to be developed over a number of cycles. Furthermore, synchronization of the video data and the computer-sco data was difficult. As discussed in section B.4.1, the image processing required to obtain numerical rather than visual information also proved difficult and time consuming.

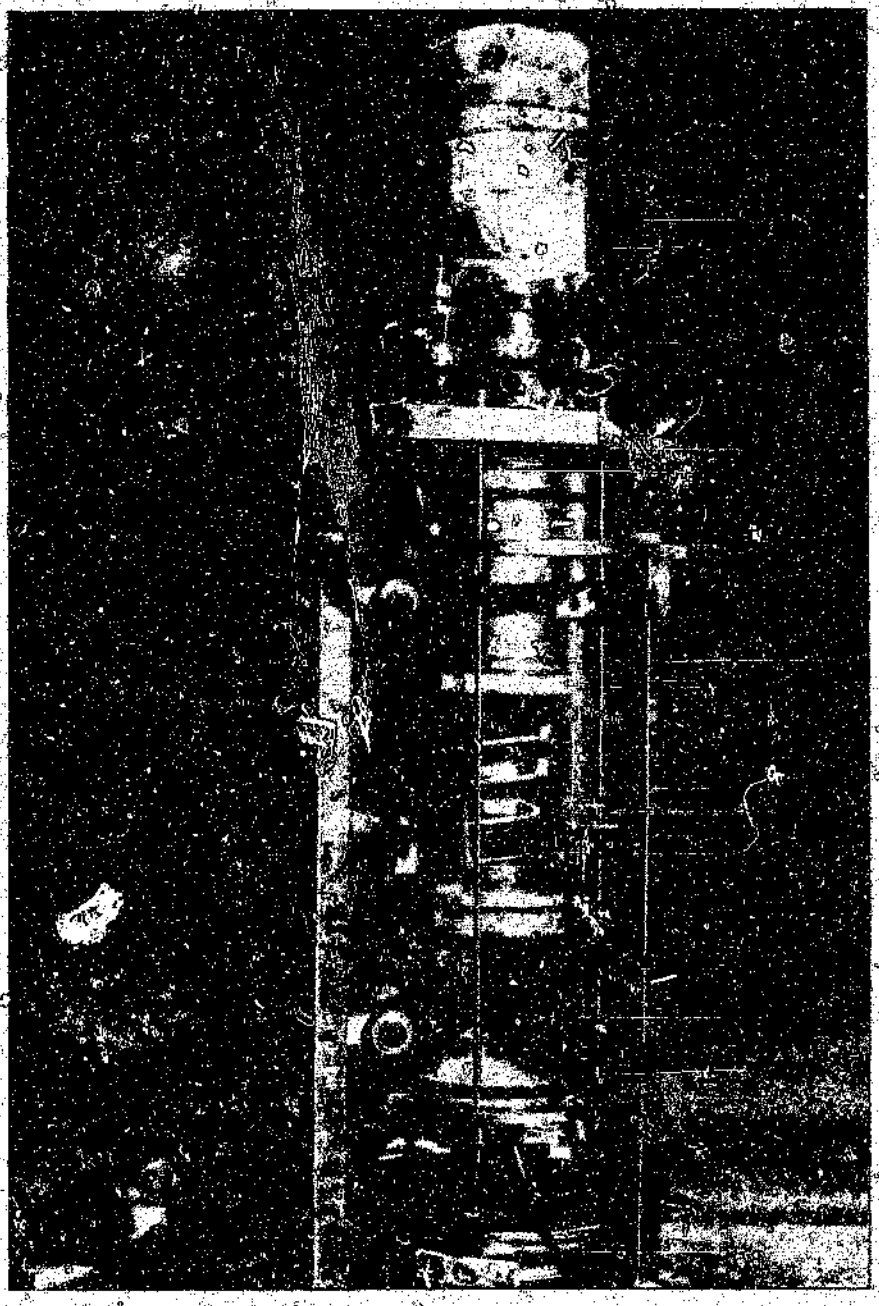

Figure 5.2: Photograph of Model B-10 free-cylinder rig

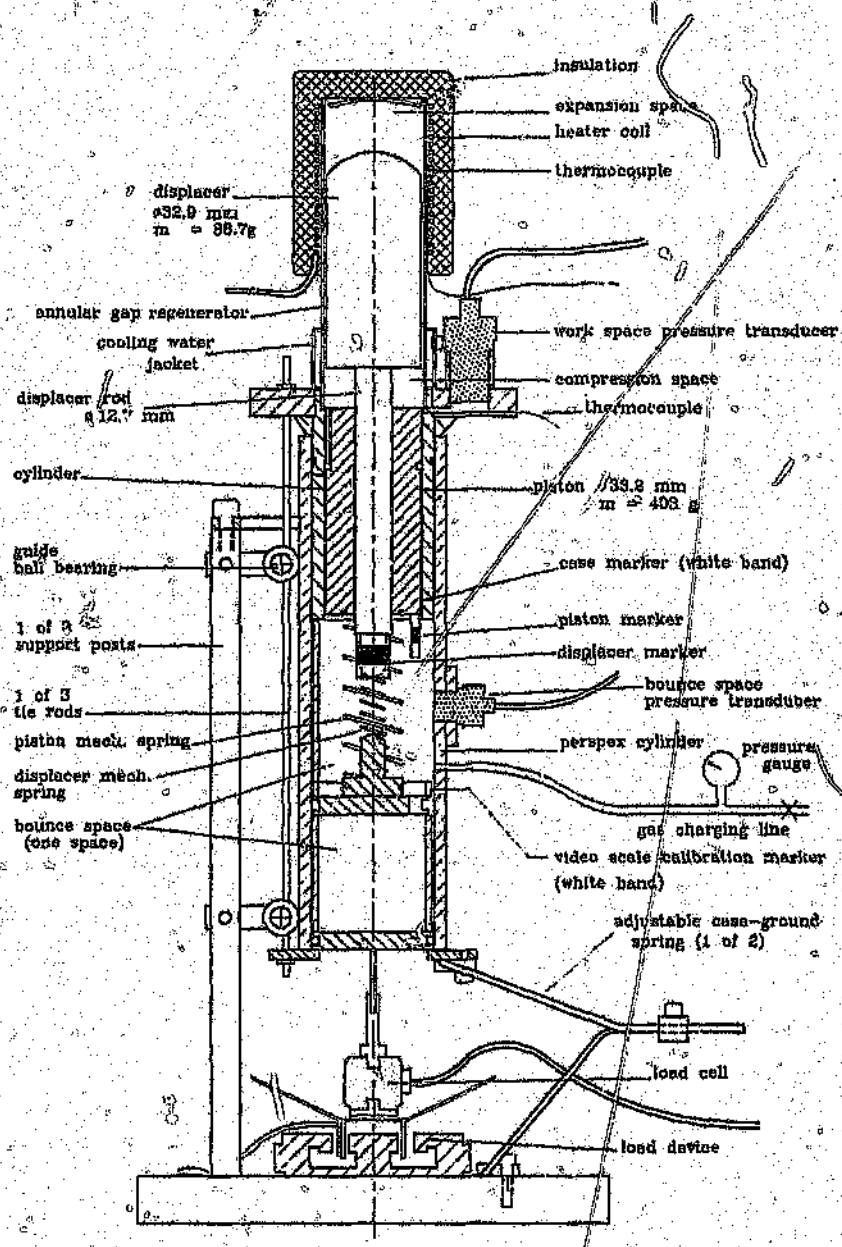

Figure 5.3: B-10 engine mounted such that free-cylinder motion is possible

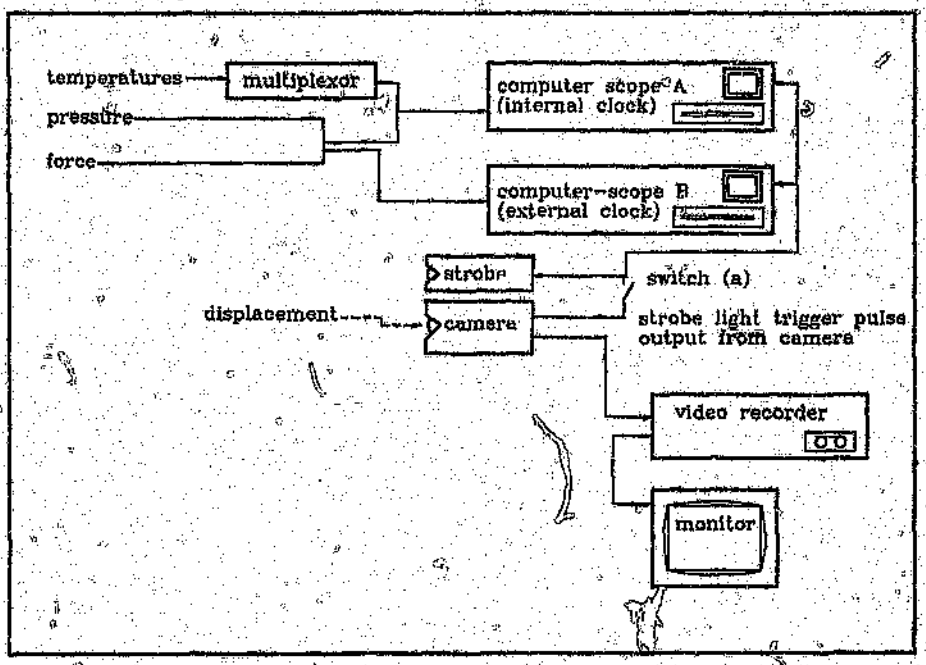

Figure 5.4: Instrumentation block diagram

Table 5.1: Instrumentation resolution

Instrument	Resolution		Calibration variance
Work-space pressure	0.48	kPa	1%
Bounce-space pressure	0.50	kPa	0.6%
Load cell	0.03	N	3%
Motion data	0.25	mm	1%

The pressure and force measurements were calibrated using quasi-static measurements as discussed in sections B.2.2 and B.2.3, while the motion data was calibrated using the fixed distance between two markers on the case. Typical values for the resolution and accuracy of the instruments are given in table 5.1.

5.1.3 Data processing methods

The video information was converted to numerical data using a video frame grabber and custom written tracking routines running on an 286 (AT) com-

puter. Image quality was not always excellent, and tracking errors did sometimes occur (see sections B.2.1, B.4.1, and B.4.3).

Routine data processing involved the synchronization of the pressure, force and motion data, and the collection of temperature and charge pressure data. (See sections B.4.3 and B.2.4). A time base for the data set was created using the measured information regarding the camera strobe trigger pulses (section B.4.4). For the purposes of evaluation, the data was divided into segments, usually of one second duration. These segments therefore contained 200 data samples, taken over a number of engine cycles. (Engine frequency ranged between 12 and 24 Hz). The work-space pressure wave was then approximated by fitting a sinusoidal curve to the data from each segment. The constants A, $\omega = 2\pi f$, ϕ and C were determined such that ϵ of equation (5.2) was a minimum, (the 'least squares approach', see section B.4.5 for more detail).

$$\Sigma\Delta^2 = \sum_{i=1}^{n}[x_i - A\cos(\omega t_i + \phi) - C]^2 \tag{5.1}$$

$$\epsilon = \sqrt{\frac{\Sigma\Delta^2}{n-1}} \tag{5.2}$$

For the other measurements only A, ϕ and C were determined, as each component, pressure or force measurement must oscillate at the same frequency for stable operation. If the engine motion varied significantly during the segment length, or if the assumption of sinusoidal oscillation was invalid, this was reflected by higher than normal values for the variance given by equation 5.2. If the test was of sufficient interest, the segment length could be reduced in order to allow changes in operating condition to be investigated.

It was possible to use the approximation to carry out quite rigorous screening of the video data (section B.4.5). The data was then re-analyzed, excluding data points regarded as erroneous.

Even if the data could not be accurately represented using the sinusoidal approximation, the frequency information from the least squares analysis did allow data from all cycles within a segment to be superimposed to form a composite picture of the cycle, yielding a much higher virtual sampling rate than the 200 Hz limitation of the camera.

It should be noted that a fast-Fourier transform (FFT) analysis was not utilized for two reasons. Firstly, the frequency resolution of FFT analysis is limited to:

$$\frac{\text{sampling rate}}{\text{number of samples}}$$

which for a segment length of one second yields a resolution of only 1 Hz. Secondly, as discussed in section B.2.1, the camera sampling rate was not exactly regular, comprising a 50 Hz base cycle with 4 subframes taken at unequal intervals within each base cycle. As an accurate time base could be determined, this did not affect the least squares approach used above, but would have affected a Fourier analysis. Lastly, it is not easy to ignore known data errors in a FFT analysis, whereas this was possible using the least squares approach.

5.1.4 Data presentation

As the linear dynamics approach to free-cylinder Stirling engine analysis also assumes sinusoidal motion of the engine components and sinusoidal variation of the forces acting on those components, the majority of the results of the experimental work are presented using the sinusoidal approximation described above. Where appropriate, the more detailed representation using the superimposition of many cycles onto one cycle is presented.

5.2 A detailed look at one test

A single test, which highlights some of the characteristics of the engine, and the techniques used to analyze and present the data, is discussed in some detail below. The test was carried out over a period of 40 seconds, during which the load drawn from the engine was altered. This load variation was achieved by holding the base of the force transducer (ie, between the transducer and the usual load device) with a pair of pliers. The engine thus delivered power to my hand by shaking it. This delivery of power was however still measured by the force transducer. No other factors were altered.

Figures 5.5 and 5.6 show typical segments of the data sets and the sinusoidal approximations. The data presented represents a segment length of 1 second. It has been condensed onto one cycle using the frequency information from the sinusoidal approximation. The amplitudes and mean values for the data sets were multiplied by the appropriate calibration factors and offsets to yield the calibrated data as presented.

As the displacer amplitude of this test was quite large, severe tracking errors occurred near the points of maximum displacement from the mean, where the displacer marker was obscured by the piston. An extra screening process was required in order to eliminate these wrong data points. Those points not

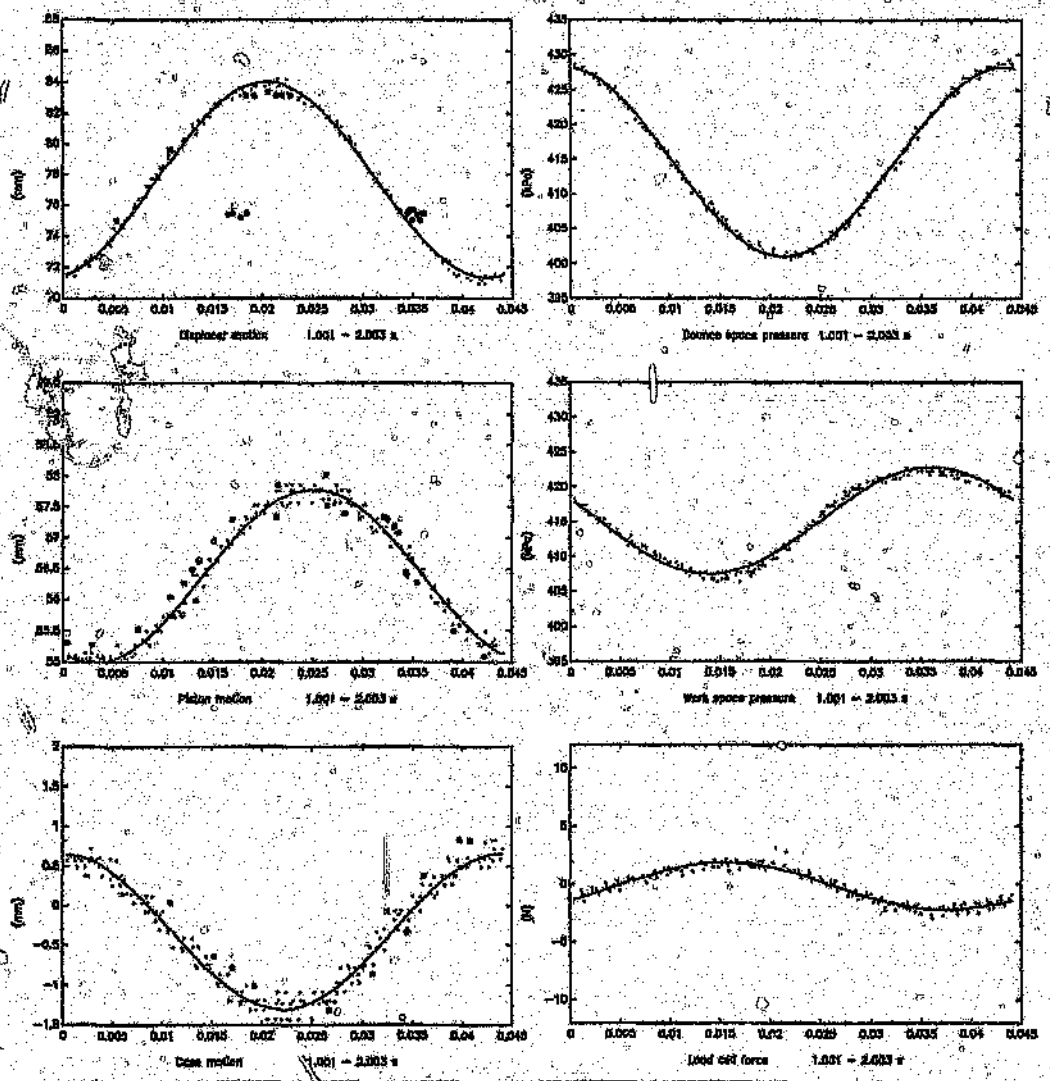

"·" accepted data, * rejected data, — sinusoidal approximation

Test no. BE16N27			Test condition and base data		
Segment: 1 – 2 seconds			Case mass:		1.529 kg
Charge pressure:	415 kPa		Hot-end ext. wall temp.:		723 K
Mechanical springs:	K_d		K_p		K_c
	1225	N/m	827	N/m	9098 N/m
Frequency:	22.69	Hz			
Load condition:	Low load				
Variable	Amplitude		Variance		Phase lead
X_d	6.4	mm	0.22	mm	-167°
X_p	1.4	mm	0.10	mm	155°
X_c	1.0	mm	0.11	mm	0°
P_b	13.7	kPa	0.45	kPa	6°
P_w	7.7	kPa	0.65	kPa	66°
F_{cl}	2.1	N	0.34	N	-127°

Figure 5.5: Calibrated data and sine wave approximation: low load condition

considered in the analysis are however still plotted, but with a plus sign, rather than the usual point. It will be noted that many of the excluded points lie closer to the mean position, and within approximately 60° of the waveform peak or trough. They were identified as being incorrect because they fell within this region.

The variance ϵ of the motion data from the assumed curve is smaller than the resolution of the video recording device (1 pixel corresponds to approximately 0.23 mm). For this test it is thus a reasonable approximation to assume sinusoidal motion. Similarly, for the bounce-space pressure the variance is of the same order as the resolution of the measuring instrument, and the curve does match the approximation well. The variance of the work-space measurements is slightly higher than the resolution of the instrument, and it can be seen from the trace of the data points that they do follow a slightly different pattern to that of the sinusoidal approximation. In percentage terms, the variance of the work-space reading is 8% of the amplitude. The resolution of the instrument was 0.48 kPa (6% of the amplitude) — thus the difference is barely significant when compared to the instrument accuracy. The case force measurements have a considerably greater variance, both with respect to the resolution of the instrument (0.0288 N ±3%), and expressed as a percentage of the case force amplitude. However, the data points are scattered fairly evenly around the approximation, and it is thus impossible to draw any meaningful conclusion with respect to the validity or not of the sinusoidal approximation based on the variance alone.

Figure 5.6 shows the engine during the same test, but 18 seconds later, when the loading on the engine had been increased. It will be seen from the ϵ values and visual examination of the curves that the sinusoidal approximation is still a reasonable assumption. The engine has adjusted the amplitudes of oscillation, and more importantly the relative phase angles, so that it is able to deliver the increased power being demanded of it. In this configuration, the free-cylinder engine therefore not only maintained a reasonably constant frequency (1.1% variation), but also maintained a relatively constant amplitude of oscillation of the case (12.7%) under two very different load conditions.

5.2.1 Derived data

The above amplitude and phase lead information can be conveniently represented in the form of a phasor diagram, either using polar co-ordinates (r, θ), or by representing the amplitude and phase of a waveform using complex numbers, $(\overline{X} = A\cos\phi + iA\sin\phi)$, and plotting these on the complex plane (see equation 3.11). It is easier to manipulate the waveform information using the

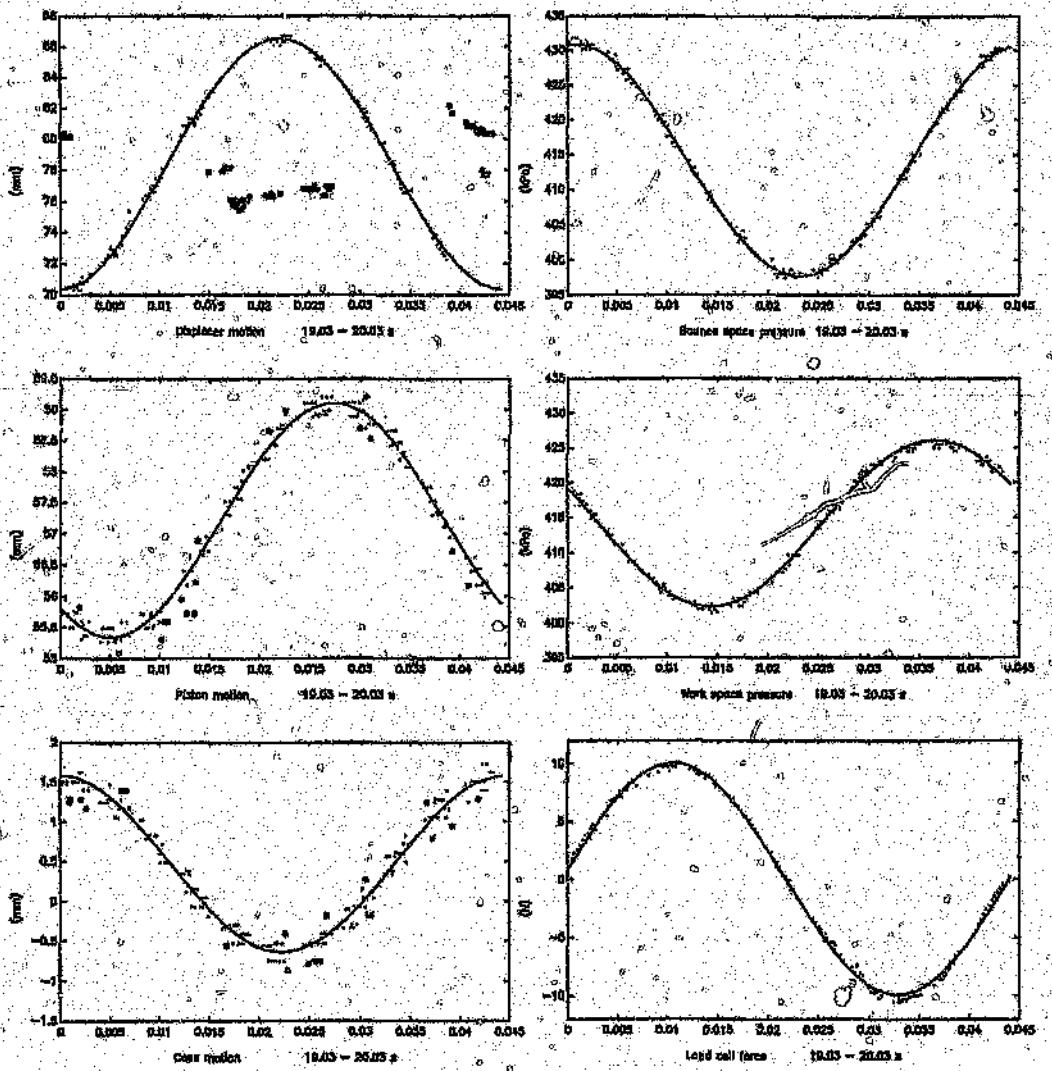

· accepted data, * rejected data, — sinusoidal approximation

Test no. BE16N27			Test condition and base data		
Segment: 19 – 20 seconds			Case mass:		1.529 kg
Charge pressure:	415 kPa		Hot-end ext. wall temp.		723 K
Mechanical springs:	K_d		K_p		K_n
	1225	N/m	827	N/m	9098 N/m
Frequency:	22.44 Hz				
Load condition	High load (held manually)				
Variable	Amplitude		Variance		Phase lead
X_d	8.1	mm	0.28	mm	-178°
X_p	1.9	mm	0.13	mm	139°
X_c	1.1	mm	0.10	mm	0°
P_b	16.6	kPa	0.49	kPa	-7°
P_w	11.9	kPa	0.51	kPa	65°
F_{cl}	10.0	N	0.31	N	-86°

Figure 5.6: Calibrated data and sinusoidal approximation: high load condition

complex number notation, and this is therefore used to explain the derivation of various important parameters such as the volume variations, the determination of the output power, damping coefficients and external spring coefficients.

Figures 5.7 and 5.8 show the above two test conditions represented as a phasor diagram. In all cases the high load test yielded phasors of greater magnitude.

For the second figure the motion of the piston and displacer relative to that of the case is shown, allowing easier comparison with other Stirling engines of the beta configuration. The small displacer phase angle of 28°, and the high amplitude of the displacer relative to that of the piston were disappointing and result in a large phase difference between the expansion space and the compression space volume variations (see figure 5.9 below).

Volume variations

From figure 5.3 the volume variations are:

$$\overline{V}_e = -\overline{X}_{dc} A_d \tag{5.3}$$

$$\overline{V}_c = \overline{X}_{dc}(A_d - A_r) - \overline{X}_{pc} A_p \tag{5.4}$$

$$\overline{V}_w = \overline{V}_e + \overline{V}_c \tag{5.5}$$

$$\overline{V}_b = -\overline{V}_w \tag{5.6}$$

Figure 5.9 shows the volume phasors. As for the motion data, the larger amplitudes apply to the high load test condition. The angle by which the expansion space phasor leads the compression space phasor does not fall within the range of 60 to 120° given by Walker and Senft [61, p 18], indicating poor optimisation of the engine dynamics.

Figure 5.10, which shows the accepted data and the sinusoidal approximation of the volumes and work-space pressure in the form of a pV diagram, illustrates very clearly the increase in available work as a result of the increase in pressure and volume amplitudes, and a fattening of the curves as a result of slightly changed phase angles.

A check on the forces between the case and ground

As noted in section 3.1 the force exerted between the case and ground is the only connection of the engine to ground. Therefore, the product of the acceleration of all components and their masses must equal the force between

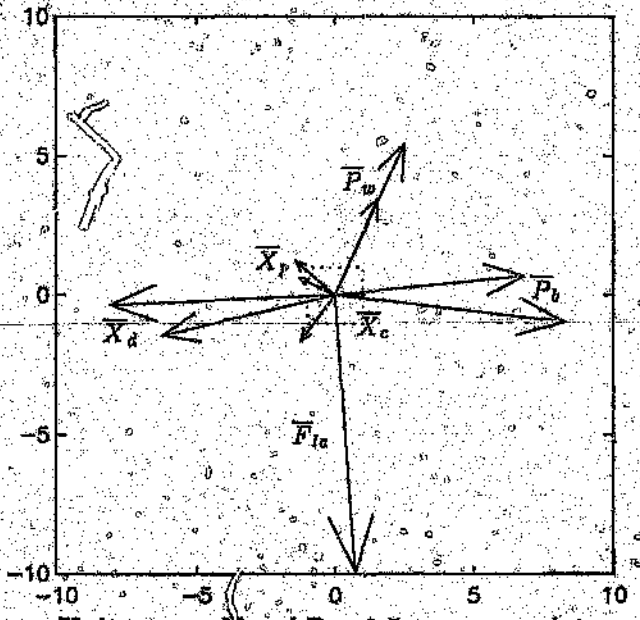

Units: mm, N or kPa×0.5 as appropriate

Figure 5.7: Absolute motion phasors, low and high load condition

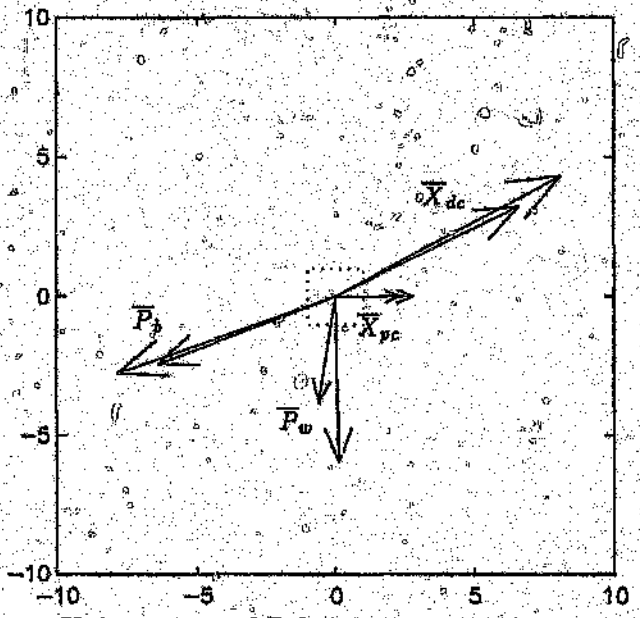

Units: mm or kPa×0.5 as appropriate

Figure 5.8: Relative motion phasors, low and high load condition

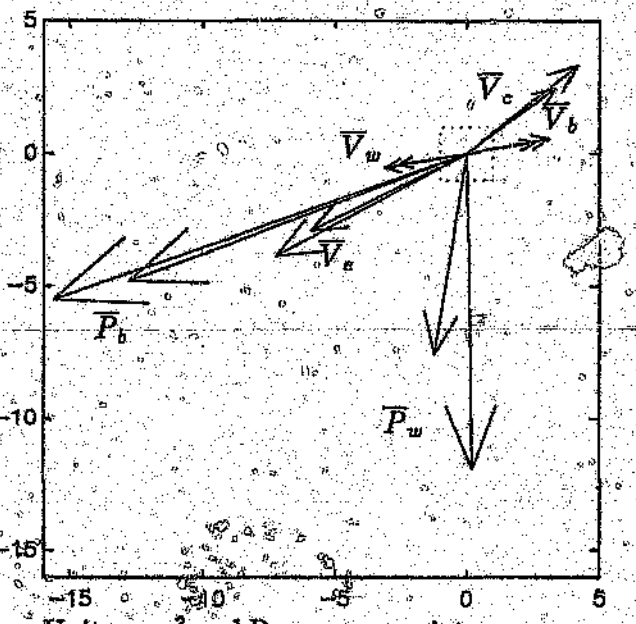

Figure 5.9: Volume and pressure phasors, low and high load condition

the case and ground.

$$m_d\ddot{\bar{x}}_d + m_p\ddot{\bar{x}}_p + m_c\ddot{\bar{x}}_c = f_{lc} + f_{cg} \tag{5.7}$$

The force measured by the load cell is represented by f_{lc}. The balance of external forces acting on the case is represented by f_{cg}. The major component of this force is exerted by the mounting springs, although it also includes friction losses through the movement of connecting hoses and in the engine support bearings. Any mass attached to the engine, but not included in m_c, will also exert a force on the engine, which would be reflected in f_{cg}. All parameters except f_{cg} were measured in the experiments. It is thus possible to calculate f_{cg}. Using the complex phasor representation:

$$\overline{F}_{cg} = m_d\omega^2\overline{X}_d + m_p\omega^2\overline{X}_p + m_c\omega^2\overline{X}_c - \overline{F}_{lc} \tag{5.8}$$

By far the largest component of $\overline{F}_{cg}$ is that force exerted on the case as a result of the case–ground springs. This force can be reduced to equivalent

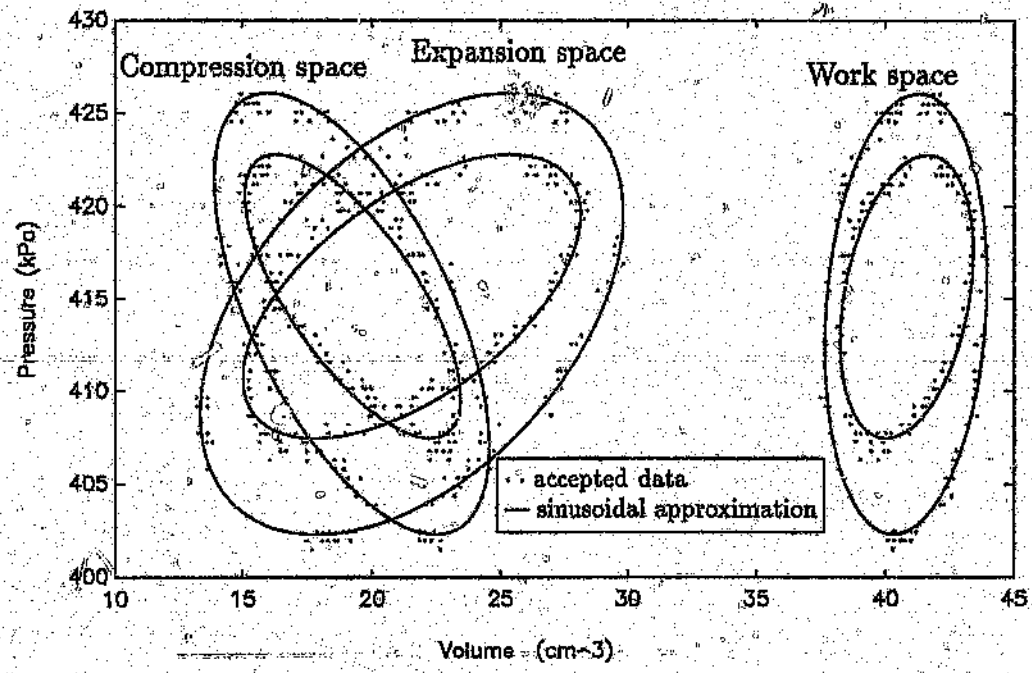

Figure 5.10: pV diagram for low and high load conditions: Test BE16N27

linear spring and damping coefficients as follows:

$$K_{cg} = \Re\left(\frac{\overline{F}_{cg}}{\overline{X}_c}\right) \tag{5.9}$$

$$D_{cg} = \Im\left(\frac{\overline{F}_{cg}}{\overline{X}_c\omega}\right) \tag{5.10}$$

K_{cg} should be approximately equal to the spring coefficient of the mechanical case–ground springs. (Note: any additional mass moving with the same velocity as the case, but not included in m_c will tend to reduce the value of K_{cg}). In table 5.2, the values for the two test points under discussion are presented. The spring constants of the mechanical case spring as measured during static tests are also shown. Considering that the force balance result for K_{cg} is derived from an expression which uses the sinusoidally approximated accelerations of all three components, and the load cell measurements, the difference of 14% between this value and the static measurement is acceptable. D_{cg} represents that work required to overcome the friction between the case and its supports. However, as these damping forces were very small relative to the magnitude of the spring forces, measurement error and the assumption of sinusoidal motion limited the value of the results obtained.

Table 5.2: Measured and calculated external forces

	Phasor rep. Amp. (N)	Phase	Coeff. rep. K (N/m)	D (Ns/m)
Low load condition				
Measured case force ($\overline{F}_{lc}$)	2.1	-127 °	1261	11.7
Force balance result ($\overline{F}_{cg}$)	7.8	4.6°	7883	4.4
High load condition				
Measured case force ($\overline{F}_{lc}$)	10.0	-86 °	-675	63.8
Force balance result ($\overline{F}_{cg}$)	8.8	-4.6°	7926	-4.5
Static measurement of K_{cg}			9098	

The force measured by the load cell, $\overline{F}_{lc}$ can also be expressed as if it comprised a linear spring and damper. Equivalent coefficients are presented in table 5.2.

Balancing the internal forces

The force balance concept can be taken further to yield information on some of the internal interactions within the engine. The method, and some results are presented in the appendixes (section D.3). Sensitivity of the results to errors in the primary measurements is such that the results were not considered useable. The reader may however find the force polygon figures presented in the appendix useful to assist in the visualization of the forces acting on the components.

Work flow through the engine

It is the volume variations within the engine that determine the thermodynamic interactions, and hence the power available for useful work. The available work per cycle is $\oint p_w \mathrm{d}V_w = \oint p_w \mathrm{d}V_e + \oint p_w \mathrm{d}V_c$. If this is multiplied by the frequency of operation, this is the power available to overcome mechanical losses in the system, and to provide useful engine output. In a manner similar to that used for the 'water pump' engine (see section 4.1.4), tables 5.3 and 5.4 show the flow of this work throughout the system.

Each integral represents the rate of energy transfer across a boundary as the result of a force being applied to a moving object. Rigid objects, such as the case, displacer and piston will not gain energy, as implied by the positive values of the integrals $f\oint f_d \mathrm{d}x_d$, $f\oint f_p \mathrm{d}x_p$ and $f\oint f_c \mathrm{d}x_c$ shown in the table.

Table 5.3: Work flow paths: Test BE16N27, segment 1–2 seconds

—	Displacer	Piston	Case	Sum
Work space (Watts)	$-f\oint p_w A_r \mathrm{d}x_c$ 0.3518	$-f\oint p_w A_p \mathrm{d}x_p$ 0.5634	$f\oint p_w A_c \mathrm{d}x_c$ 0.4238	$f\oint p_w \mathrm{d}V_w$ -1.3390
Bounce space (Watts)	$f\oint p_b A_r \mathrm{d}x_d$ 0.0977	$f\oint p_b A_p \mathrm{d}x_p$ -0.5169	$-f\oint p_b A_c \mathrm{d}x_c$ -0.0847	$\oint p_b \mathrm{d}V_b$ -0.5039
Mech K_{dc} (Watts)	$f\oint K_{dc}(x_c - x_d)\mathrm{d}x_d$ 0.1230	— —	$f\oint K_{dc}(x_d - x_c)\mathrm{d}x_c$ -0.1230	0 0
Mech K_{pc} (Watts)	— —	$f\oint K_{pc}(x_c - x_p)\mathrm{d}x_p$ -0.0342	$f\oint K_{pc}(x_p - x_c)\mathrm{d}x_c$ 0.0342	0 0
Load cell (Watts)	— —	— —	$f\oint f_{lc}\mathrm{d}x_c$ -0.1149	-0.1149
Balance force F_{cg} (Watts)	— —	— —	$-f\oint f_{cg}\mathrm{d}x_c$ -0.0432	-0.0432
Sum (Watts)	$f\oint f_d \mathrm{d}x_d$ 0.5725	$f\oint f_p \mathrm{d}x_p$ 0.0123	$f\oint f_c \mathrm{d}x_c$ 0.0923	0.6771

Table 5.4: Work flow paths: Test BE16N27, segment 19–20 seconds

—	Displacer	Piston	Case	Sum
Work space (Watts)	$-f\oint p_w A_r \mathrm{d}x_c$ 0.7631	$-f\oint p_w A_p \mathrm{d}x_p$ 1.1202	$+f\oint p_w A_c \mathrm{d}x_c$ 0.7288	$f\oint p_w \mathrm{d}V_w$ 2.6121
Bounce space (Watts)	$f\oint p_b A_r \mathrm{d}x_d$ 0.1853	$f\oint p_b A_p \mathrm{d}x_p$ -0.9155	$-f\oint p_b A_c \mathrm{d}x_c$ 0.1270	$\oint p_b \mathrm{d}V_b$ -0.6032
Mech K_{dc} (Watts)	$f\oint K_{dc}(x_c - x_d)\mathrm{d}x_d$ 0.0323	— —	$f\oint K_{dc}(x_d - x_c)\mathrm{d}x_c$ -0.0323	0 0
Mech K_{pc} (Watts)	— —	$f\oint K_{pc}(x_c - x_p)\mathrm{d}x_p$ -0.0792	$f\oint K_{pc}(x_p - x_c)\mathrm{d}x_c$ 0.0792	0 0
Load cell (Watts)	— —	— —	$f\oint f_{lc}\mathrm{d}x_c$ -0.7747	-0.7747
Balance force F_{cg} (Watts)	— —	— —	$-f\oint f_{cg}\mathrm{d}x_c$ 0.0547	0.0547
Sum (Watts)	$f\oint f_d \mathrm{d}x_d$ 0.9807	$f\oint f_p \mathrm{d}x_p$ 0.1255	$f\oint f_c \mathrm{d}x_c$ 0.1827	1.2889

There are other forces such as friction losses acting between the components, and the pressure difference between the hot and the cold space which dissipate the implied energy gain of each component. The values thus show the work required simply to keep the engine components moving. The high values for the displacer indicate that the work required to move the gases between the hot and cold spaces is considerable. The case and piston have a significantly lower amplitude of oscillation, and are not responsible for such significant unmeasured gas flow, thus the dissipation required to keep them moving is much lower. It must however be remembered that the bounce-space loss, which was measured, is a similar sort of loss to the above loss described for the displacer. It can be seen from the tables that it represents a very significant portion of the total available power.

5.2.2 Profile of the complete test

The above discussion centred around data extracted from two segments of one test. Figures 5.11 and 5.12 show the data collected for the complete test. Note that each segment represents the average for one second of engine operation. The response of the engine to the increased load (at segment 5), and its subsequent return to the low load condition at segment 23 is quite clear. Also notable is the relative stability of engine operation. The variance values, plotted as a percentage of the variable amplitude in figure 5.13, give a good indication of the reliability of the data, indicating problems with the displacer tracking at segments 13 and 18, and with the load cell measurements at the transition points. Engine frequency remained remarkably consistent, decreasing by only 0.3 Hz during the period of high load, and then rising again once the load on the engine had been reduced. The remarkable and rapid increase in engine power is clearly shown in the bottom curve of 5.12. In the same figure, the calculated damping and spring coefficients derived from equation 5.7 are shown. While K_{lc} and D_{lc} are derived from the case motion and the measured load cell forces only, and are therefore relatively reliable, the curves for K_{cg} and D_{cg} are derived using four independently measured parameters and thus should be treated with some caution. It is however pleasing to note that K_{cg} is approximately equal to the statically calibrated case-ground spring stiffness coefficient $K_{cg\,(static)}$ as expected.

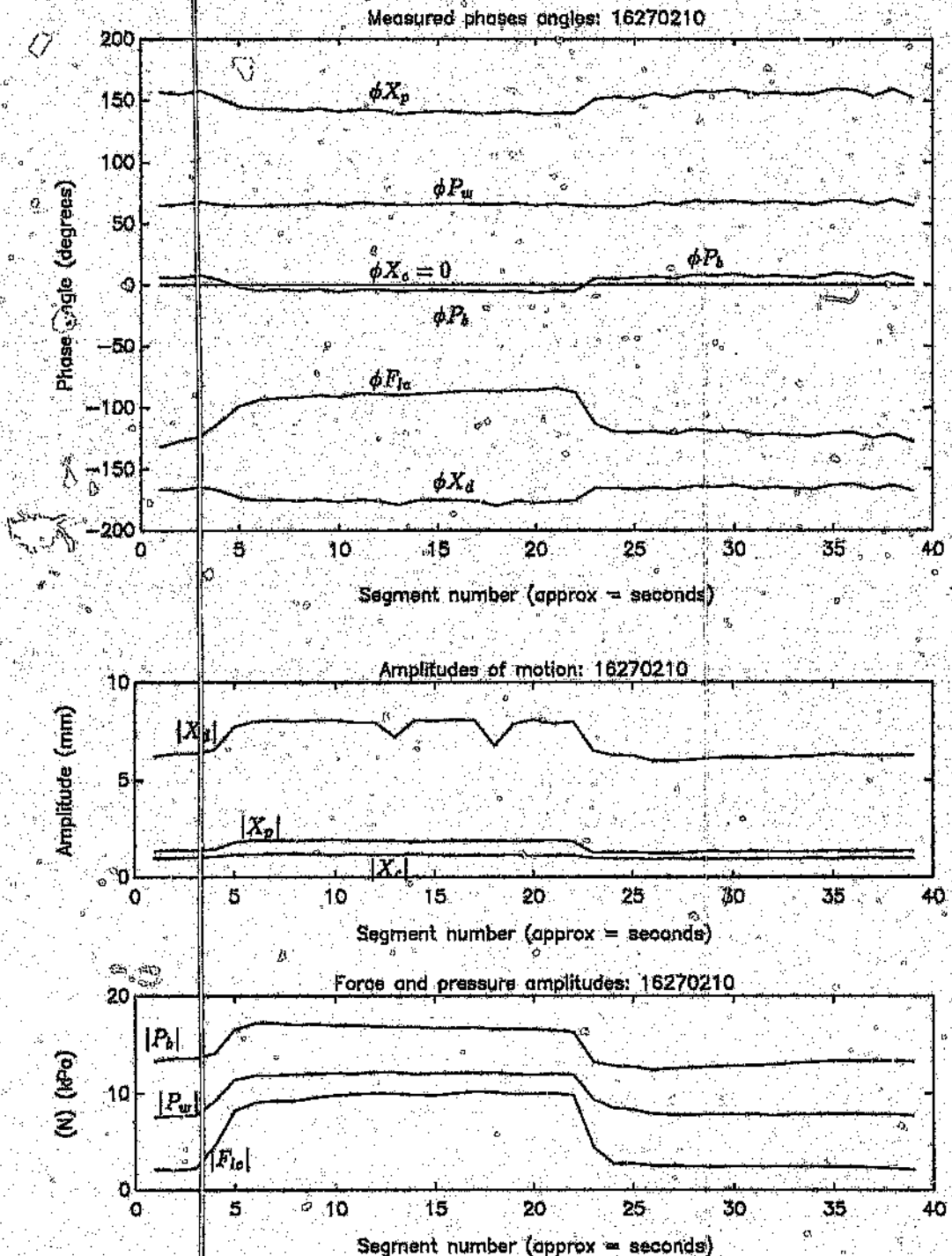

Figure 5.11: Measured data for complete test BE16N27

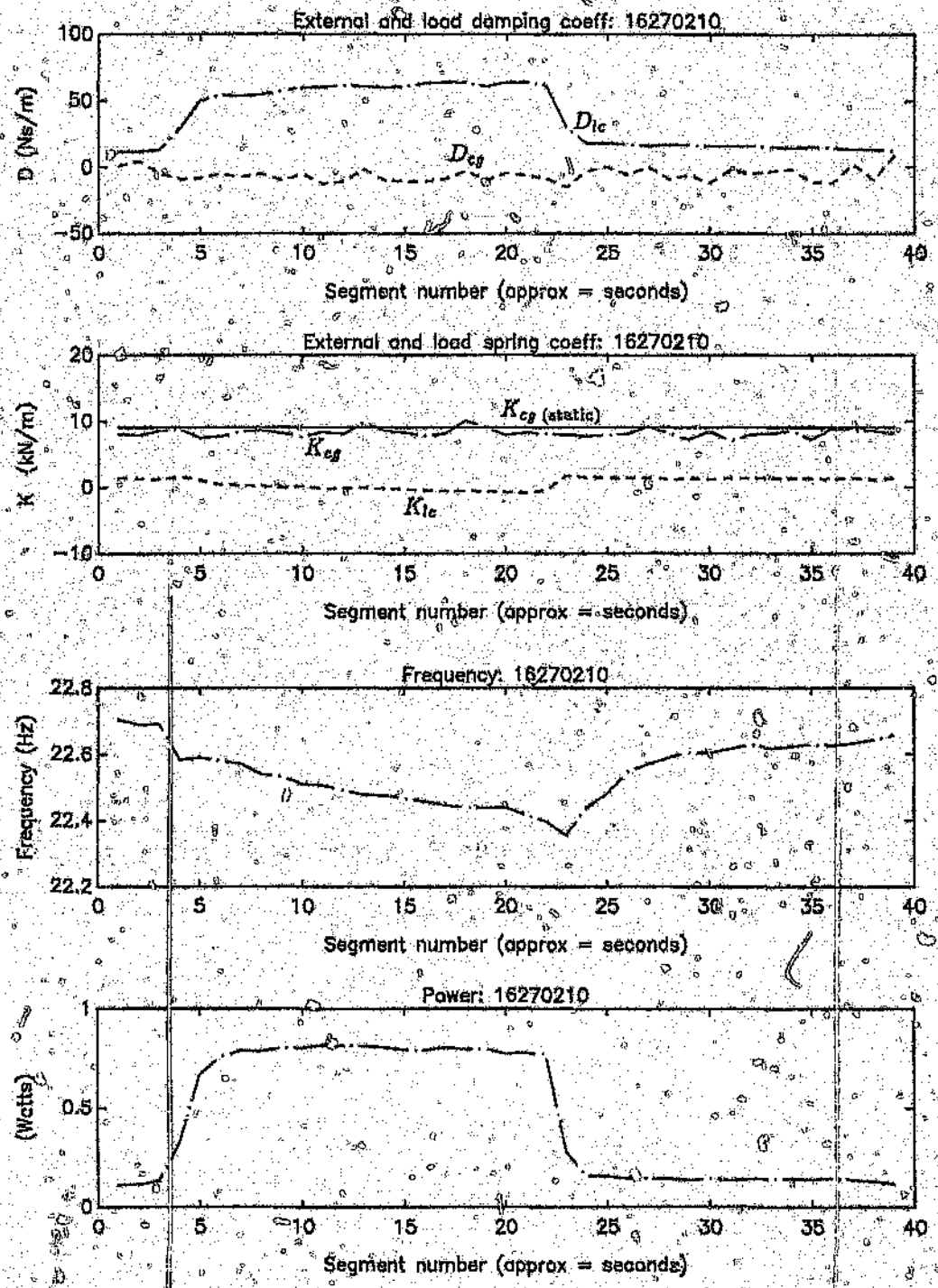

Figure 5.12: Further results for test BE16N27

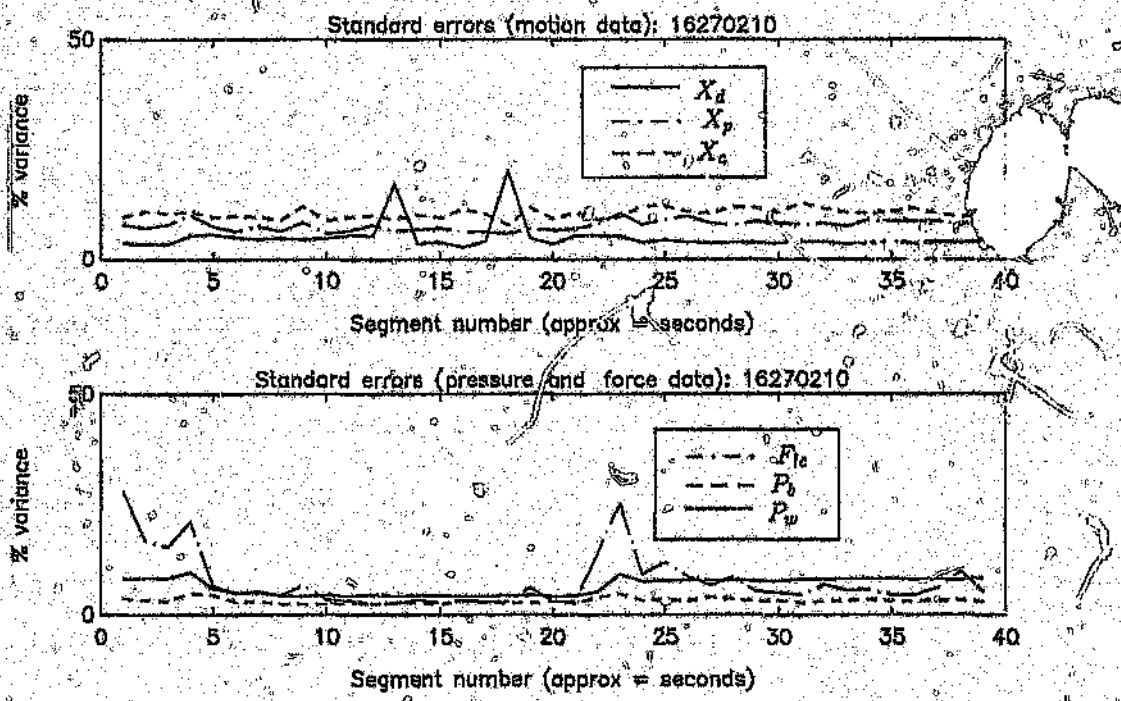

Figure 5.13: Variance expressed as a percentage of the relevant amplitude ($\frac{\epsilon \times 100}{|X|}$) for test BE16N27

5.3 Presentation and discussion of general results

The engine was operated under a variety of conditions. Modified parameters included: Case spring, displacer spring, charge pressure, case mass. Such factors can be considered as design parameters, unlikely to change once a unit is in the field. The working fluid was also changed, with nitrogen being used for the earlier tests, and helium for the later test series. Operational parameters were also varied. These were the damping coefficient of the load device, and the heater temperature.

5.3.1 Variation of hot-end temperature and charge pressure

The first series of tests investigated engine operation as a function of the temperature difference between the external wall temperature of the heater and the cooler temperature, and as a function of the charge pressure. Figure 5.14 shows the engine output power as a function of these two parameters. The four sets of curves correspond to different working fluid mean pressures as shown in the key. The lower curve represents that measured by the load cell only. The upper curve is the sum of the power to the load cell and the power required to overcome the indirectly measured damping D_{cg}, derived from the external system force balance [equations (5.7—5.10)].

The engine spring, mass and load parameters were as shown in table 5.5 for all the tests shown. The displacer spring failed due to fatigue during a demonstration run once the tests were completed, but before its stiffness constant could be checked. Thus only the pre-test value is presented. The constant may have been lower than the given figure near the end of the test series (when the engine was tested at higher pressures). The values for the piston mechanical spring are from measurements before and after the tests, as are the values for the case–ground external spring. Unfortunately the case–ground mechanical spring stiffness increased gradually during the tests. The above uncertainty with respect to the spring values detracts from the utility of the results. However, the trends discussed are quite clear and it is felt that they were primarily caused by the temperature and pressure variations rather than variation of the mechanical spring stiffnesses.

The engine performance, as expected, improved with increase in the temperature difference for all the conditions shown. However, the performance was

Table 5.5: Series BE09N spring and mass parameters

	Displacer	Piston	Case
Mass (g)	89	403	979
Mechanical spring N/m	654	768–794	17218–23763
Load condition	As constant as possible		

negatively affected by an increase in charge pressure. The engine would only start at higher temperatures, and in each case the output power at a given temperature difference decreased with increase in charge pressure. (If the combined power to the load cell and the indirectly measured D_{cp} is taken as the available power then the best performance was for the second pressure range of 156 kPa).

The stiffness of gas springs increases as the charge pressure is increased. One would therefore expect the engine frequency to increase as the charge pressure is increased. However figure 5.15 illustrates that this was not the case for the B-10 engine in this configuration. Although the engine frequency increased significantly with an increase from 82 kPa to 156 kPa, the frequency dropped again when the charge pressure was increased to 232 kPa. For higher temperatures the frequency increased again, with the 233 kPa curve crossing the 156 kPa curve at a ΔT of between 350 and 400 K. The 304 kPa curve remains below the 232 kPa curve for all temperatures tested. Such anomalous behaviour may have been due to weakening of the displacer spring towards the end of the test period, although the consistency of the two high pressure series indicates that this is unlikely.

The decrease in engine performance as the pressure was increased is explained in part by figures 5.16 and 5.17 which show the amplitude and phase (w.r.t the case) of the component motion phasors. Although the displacer amplitude for the 156 kPa tests is higher than for the 82 kPa tests, the phase angle is significantly lower. For the higher pressures, although the displacer phase angle remains within the 30° to 50° band, the amplitude steadily decreases as the pressure increases.

5.3.2 High pressure tests

The second series of tests run were at constant engine configuration, and charge pressure, as shown in table 5.6. The response of the engine to the load was then investigated for three temperature ranges. Figure 5.18 shows the output

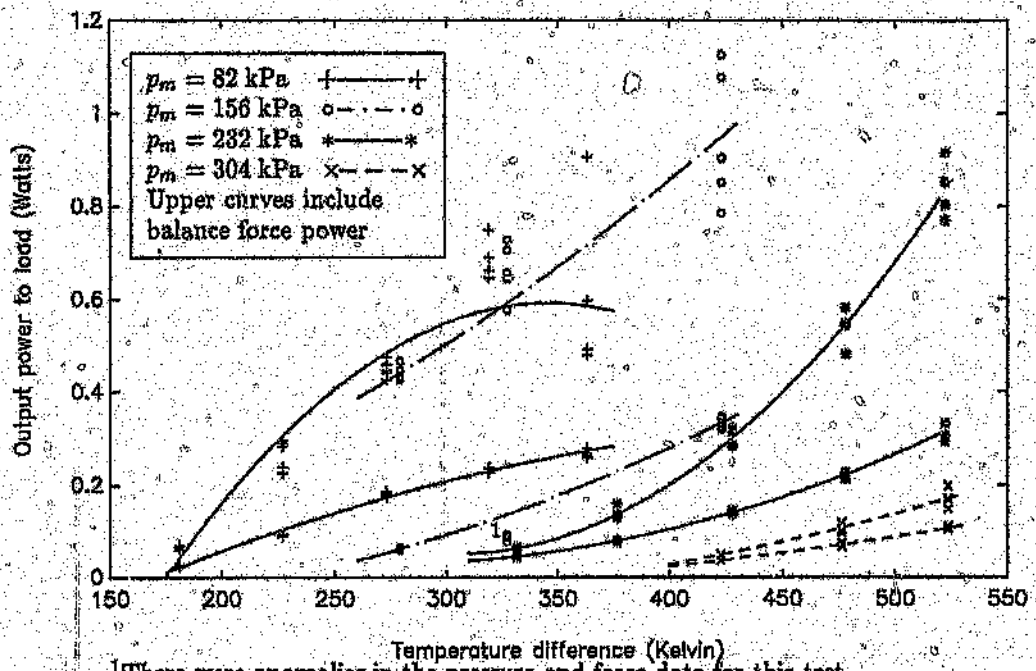

[1]There were anomalies in the pressure and force data for this test.

Figure 5.14: Engine power as a function of temperature difference and charge pressure.

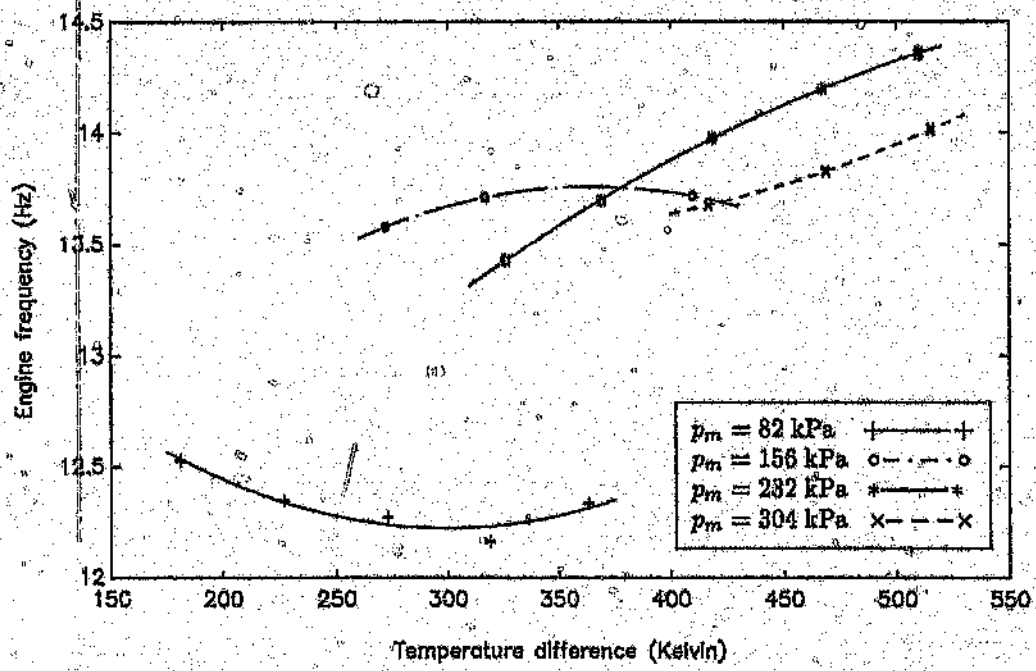

Figure 5.15: Engine frequency as a function of temperature difference and charge pressure

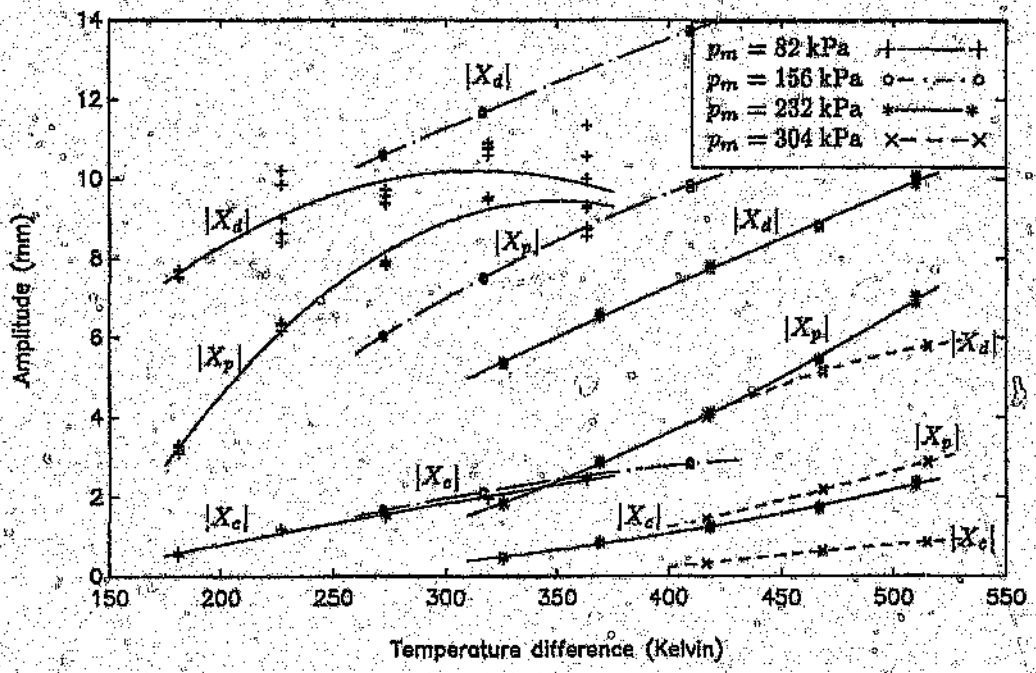

Figure 5.16: Amplitudes of motion as a function of temperature difference and charge pressure

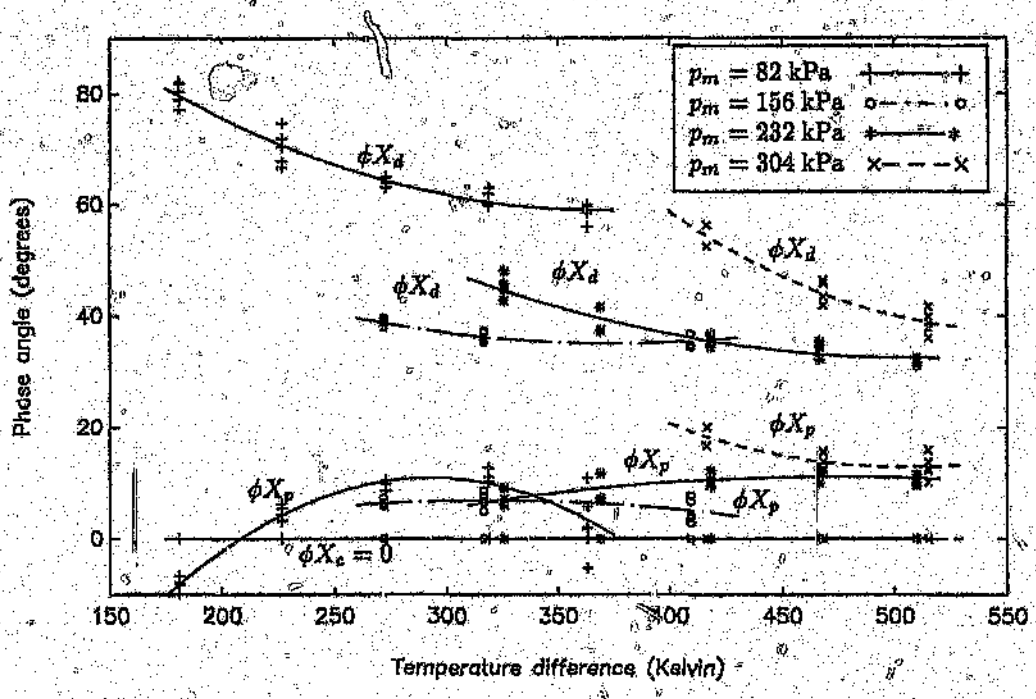

Figure 5.17: Motion phase angles as a function of temperature difference and charge pressure

Table 5.6: Series BE14N spring and mass parameters

	Displacer	Piston	Case
Mass (g)	89	403	979
Mechanical spring N/m	1513	827	19078
Mean pressure	374 – 379 kPa		

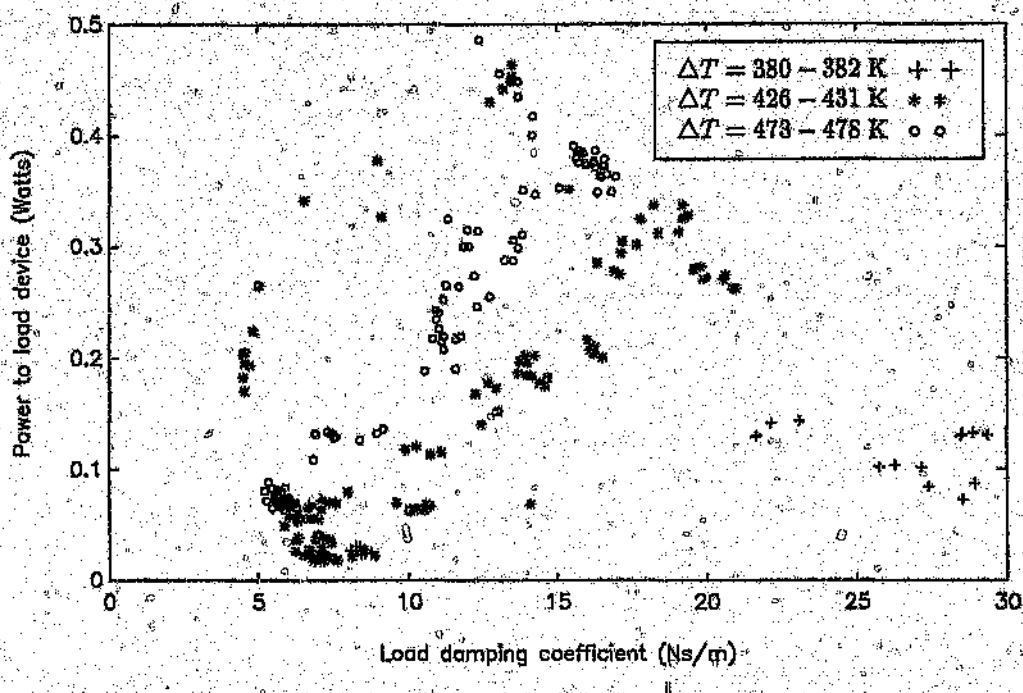

Figure 5.18: Output power versus load damping coefficient

power as a function of the load damping coefficient for the three different temperature ranges. For each range there is a clear increase in output power as the load damping coefficient was increased. Under these conditions the engine response to load was therefore similar to those shown for the single test discussed in section 5.2. As for the BE09N series, the power for a given load condition increases as the temperature increases. (The data on the far left of the figure are from a single medium temperature test during which the load damping coefficient was decreased. Their deviation from the norm is unexplained.)

The high temperature tests were investigated further in an attempt to determine why the engine output power increased as the load damping coefficient was increased. Figure 5.19 shows the motion and load force phasors for the tests. As shown by the arrows, for each component, the amplitude of oscillation increased as the load damping coefficient was increased. The increase in case amplitude with increase in load is somewhat unexpected as it indicates potentially unstable behaviour. This situation is reconsidered in section 6.3, where the use of root maps and the 3-D SAUCE programme help to explain this behaviour.

5.3.3 Series BE16N tests

The main objective of this test series was to investigate the relationship between engine operation, and the case mass and case external spring constants. Tests were therefore conducted for three different case masses, and three different spring constants. The damping on the engine was also varied for each of the nine conditions. The charge pressure was held essentially constant, in the range of 410 to 420 kPa. The hot-end temperature was maintained between 700 and 750 K. The piston and displacer mechanical springs were left as for the series BE14N tests at 827 N/m and 1 513 N/m respectively. However, at the end of the test period, the displacer spring stiffness was measured again, and found to be 938 N/m. This reduction in stiffness was partly due to metal fatigue, and also due to gradual failure of the bonding between the spring and its mountings. A stiffness of 1 225 N/m was assumed for the analysis presented here.

The engine operation was found to be quite unstable during those tests for which a high case external spring stiffness of (K_{cg} = 18646 N/m) was used. Under certain loads the engine had two distinct modes of operation, each at a different frequency (page 146), and in the test with a high case mass the engine cycled between two modes at a frequency of about 1 Hz (page 146). The operation was thus significantly different to that of the other two spring con-

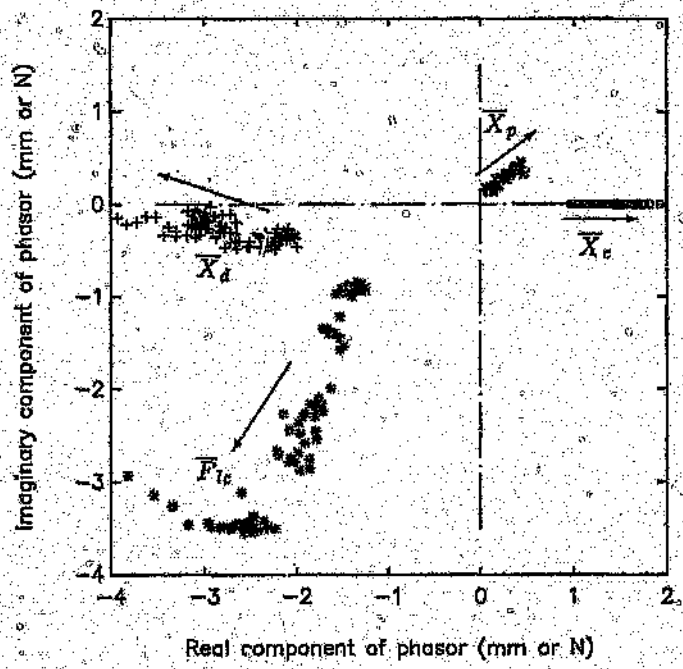

Figure 5.19: Motion and force phasors, magnitude increases with increased D_{lc}

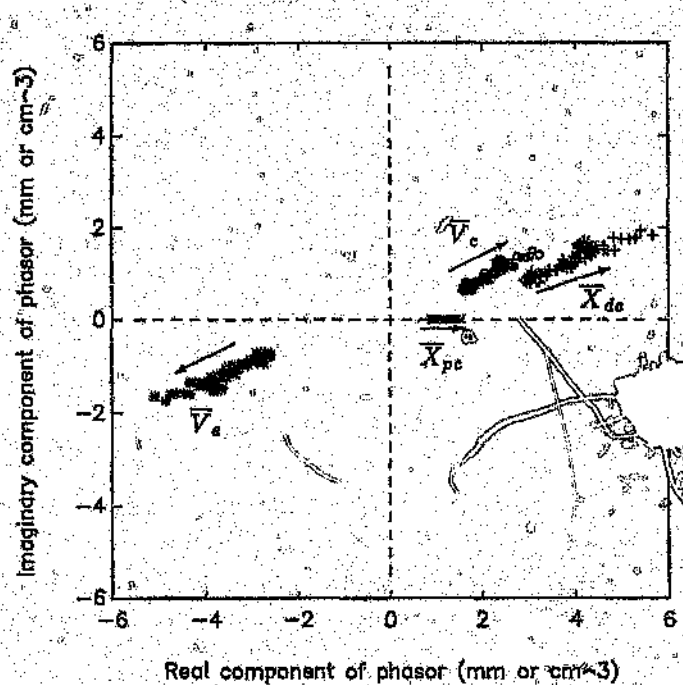

Figure 5.20: Relative motion and expansion and compression space phasors, magnitude increases with increased D_{lc}

ditions, making comparative analysis difficult. At the medium spring setting (9 097 N/m) engine operation was stable and followed a set pattern, while for the lowest spring setting stable operation was only recorded for the medium and high mass situations. A short investigation of the engine response to changes in case mass and external spring constants is presented in the next section, while the following two sections look at the two interesting unstable cases referred to above. The test BE16N27 discussed at the beginning of this chapter was also from this test series.

Response of the engine to changes in case mass and external spring stiffness

Figure 5.21 shows seven tests, the first two conducted with an external case spring stiffness constant of 7 147 N/m (low K_{cg}), the next three with a spring stiffness of 9 097 N/m (medium K_{cg}), and the last two with a spring stiffness of 18 646 N/m (high K_{cg}). Although the load was varied slightly between the different tests, changes due to variation in load were less significant than those resulting from changes in case mass.

In all tests, the case amplitude remained surprisingly constant. However, both the piston and the displacer show an increase in amplitude as the case mass was increased (right to left within each subseries), and as the case external spring stiffness was reduced (right to left from subseries to subseries). Although the displacer–case phase remained essentially constant for all the tests, the piston-case phase angle increased with increased case mass and with reduced external spring stiffness.

In an attempt to express these trends using a single domain comprising a composite of the case mass and the case external spring stiffness, the curves in figure 5.22 are presented. These show the case, piston and displacer motions plotted against the undamped natural frequency of the case $\omega_c = 2\pi\sqrt{K_{cc}/M_c}$ (Hz) where $K_{cc} = K_{cg} + K_{\text{int springs and gas springs}}$. The internal mechanical springs remained constant throughout the series. Both the bounce space and the work space were treated as gas springs using equation (3.26). The mean volume of the spaces and the charge pressure remained approximately constant for the series. Therefore the value of K_{cc} was only affected by changes in the external spring. These curves illustrate quite clearly that for the engine in this configuration, the effect of adding mass to the engine can be reduced by simultaneously increasing the external spring stiffness, thereby keeping ω_c approximately constant. It is important to note that the simply calculated term ω_c is not quite appropriate, as it is derived assuming that the piston and displacer remain stationary. Their motion is indeed significant. Due to the interactions within

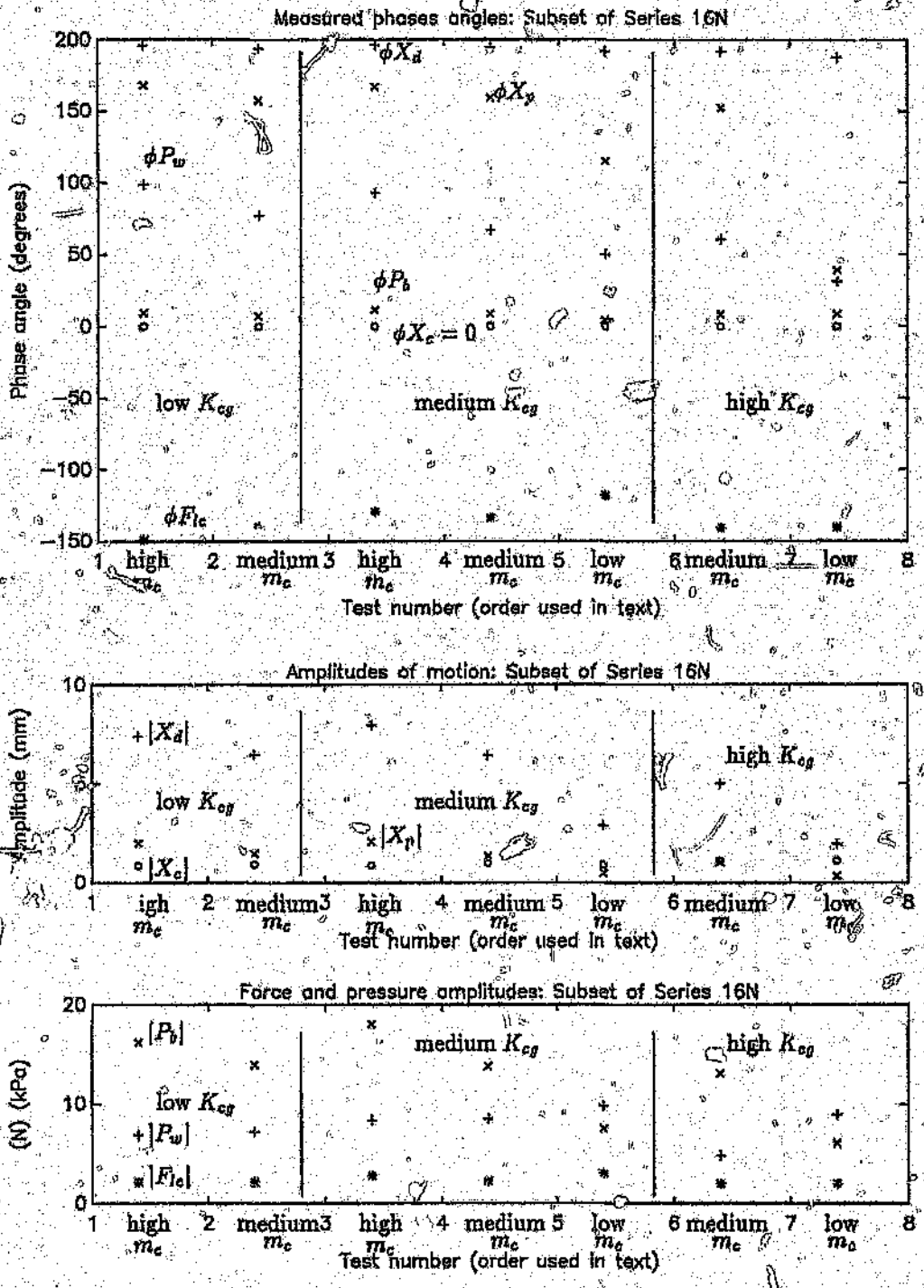

Figure 5.21: Motion data for case external spring and case mass investigation

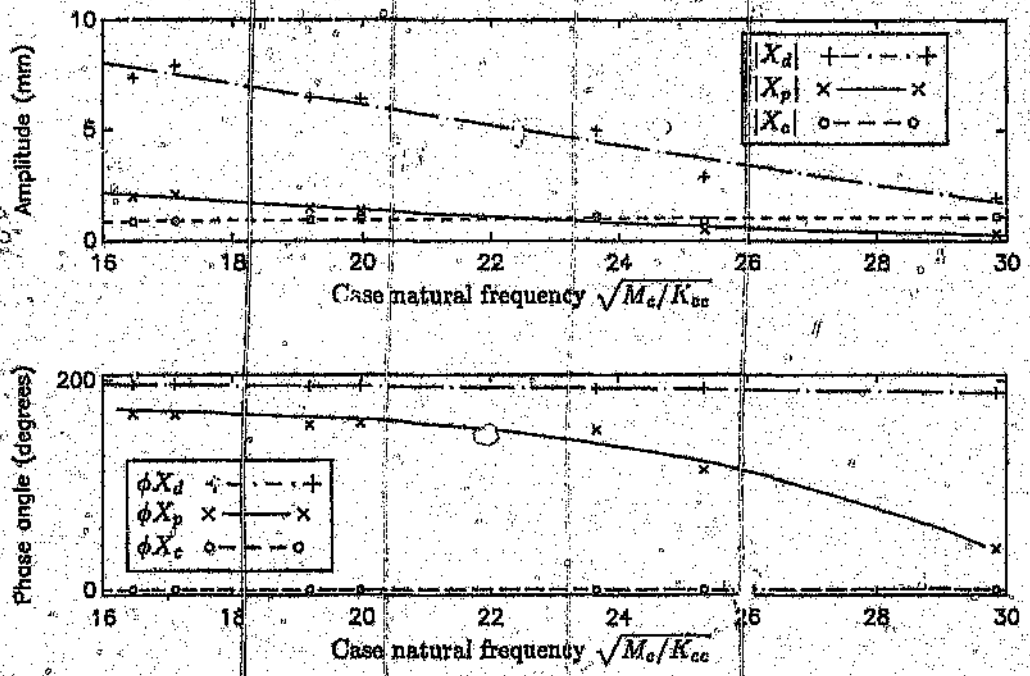

Figure 5.22: Case, piston and displacer motion versus w_n

the engine a full dynamic simulation is necessary to predict the response of the engine to changes in springs or masses. Figure 5.23 shows up the difficulties that may be encountered using the above simplification. The frequency curve, when plotted against the same x-axis shows that such a simplification would not be appropriate. For the high and medium spring stiffness condition the engine frequency increases with increase in mass, and for the low spring stiffness test the frequency drops. The use of w_n as the domain does not order the results along a smooth curve. Thus although there appear to be some simple trends, they are not reliable.

In conclusion, the above tests show that in general the addition of mass to the case, or the reduction of the external spring stiffness tend to increase the displacer and piston amplitude, and increase the piston phase. However, the effects on frequency are not as consistent. In section 6.4 similar slightly erratic frequency behaviour is noted in the simulation of the engine under these conditions.

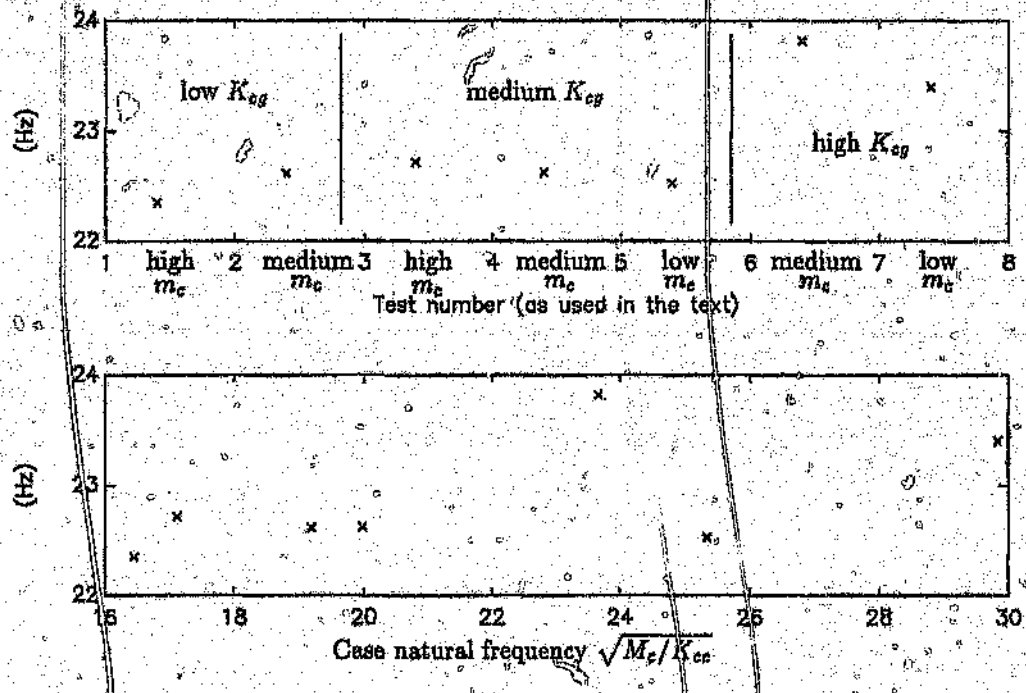

Figure 5.23: Frequency response to changes in case mass and external spring stiffness

Unstable engine operation

Walker [61, p 69] indicates the possibility of a quasi-stable state in which the engine may operate, until disturbed by some random perturbation, after which it will be dislodged from this path, and begin to vibrate in its preferred stable mode. Figures 5.24 and 5.25 show just this occurring. For this test the external case spring was at the 'high' level ($K_{cg} = 18646$ N/m), and the case mass was at its normal 0.979 kg. Engine parameters and the load setting were not changed. The change in operational mode occurred spontaneously. Note the large change in frequency of operation. It is clear from the phases of the piston and displacer, that the engine, in the low frequency mode, is essentially operating as a single large mass (rigid body) oscillating on the external case spring. Indeed the frequency of 17.9 Hz is the same as the undamped natural frequency given by equation 5.11 below.

$$\omega_{rb} = 2\pi\sqrt{\frac{K_{cg}}{M_c + M_p + M_d}} \qquad (5.11)$$

The high value for the damping forces deduced from the force balance (D_{cg} of figure 5.25) during the low frequency part of the test should not be granted undue attention. At the very low case amplitude recorded for this part of the test, any small error, or small forces resulting from coulomb friction would yield a high equivalent damping coefficient as X_c is the denominator in equation 5.10.

Cyclic instability

Figures 5.26 and 5.27 show an even more unusual mode of operation. For this test the external spring stiffness was still 18 646 N/m, but the case mass had been increased to 2.083 kg. In order to investigate the observed cyclic changes in operation the analysis segment length was reduced to $\frac{1}{10}$ second. Thus each data point on the curves corresponds to approximately 2 cycles. This results in poor frequency resolution, but does allow investigation of changes in engine operation. The motion data shows a cyclic variation, with the absolute motion amplitudes of the piston and displacer gradually decreasing, reaching a minimum, and then increasing again. The case amplitude increases and decreases in the same manner, but reaches a minimum when the other two are at a maximum. One would expect to see similar cycles reflected in the pressure and case force measurements. The lower graph in figure 5.26 indicates that this is not so. The case force, as measured by the load cell should be a function of the case motion, and thus the consistency of this measurement indicates some

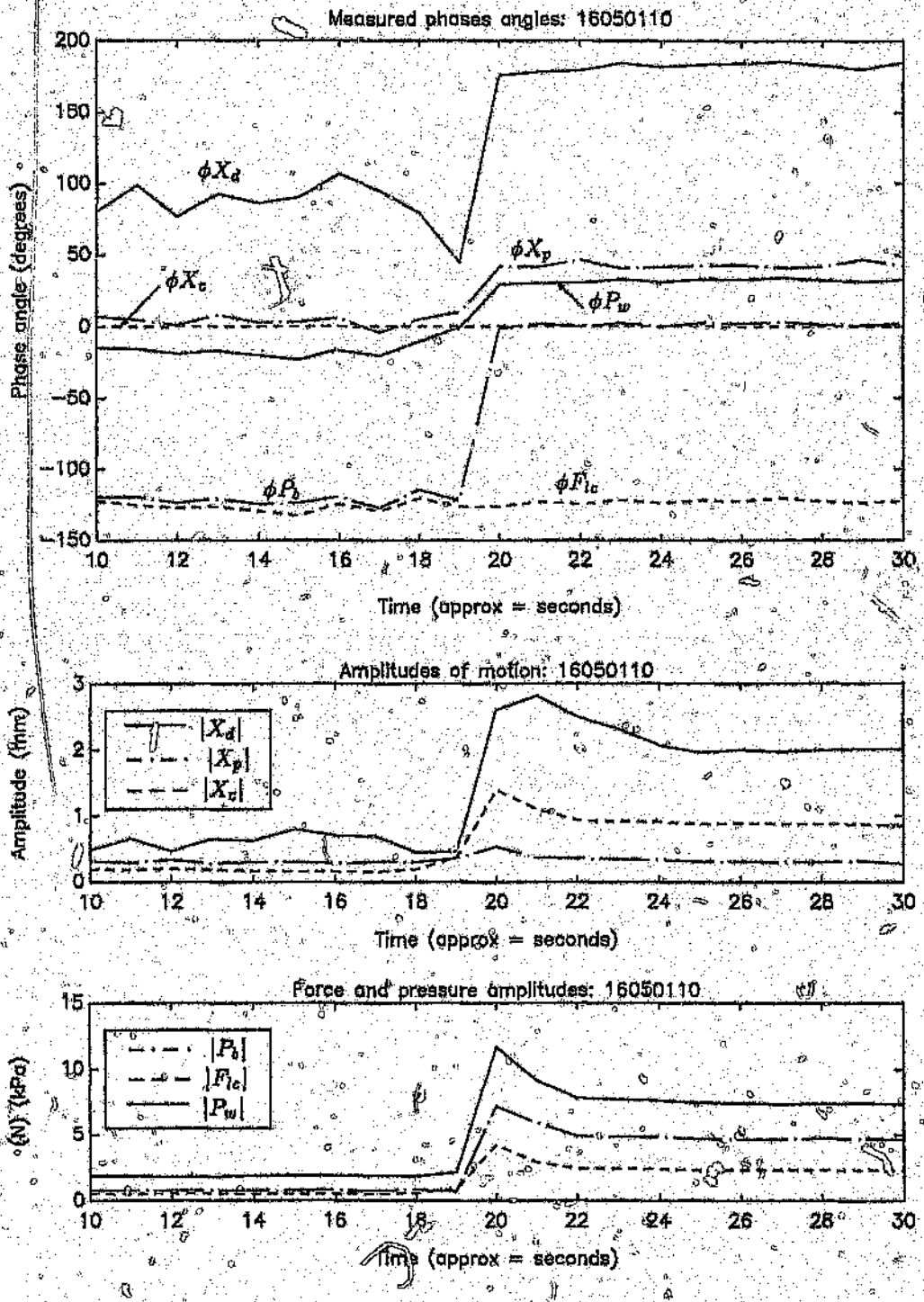

Figure 5.24: Quasi-stable engine operation: Phases and amplitudes

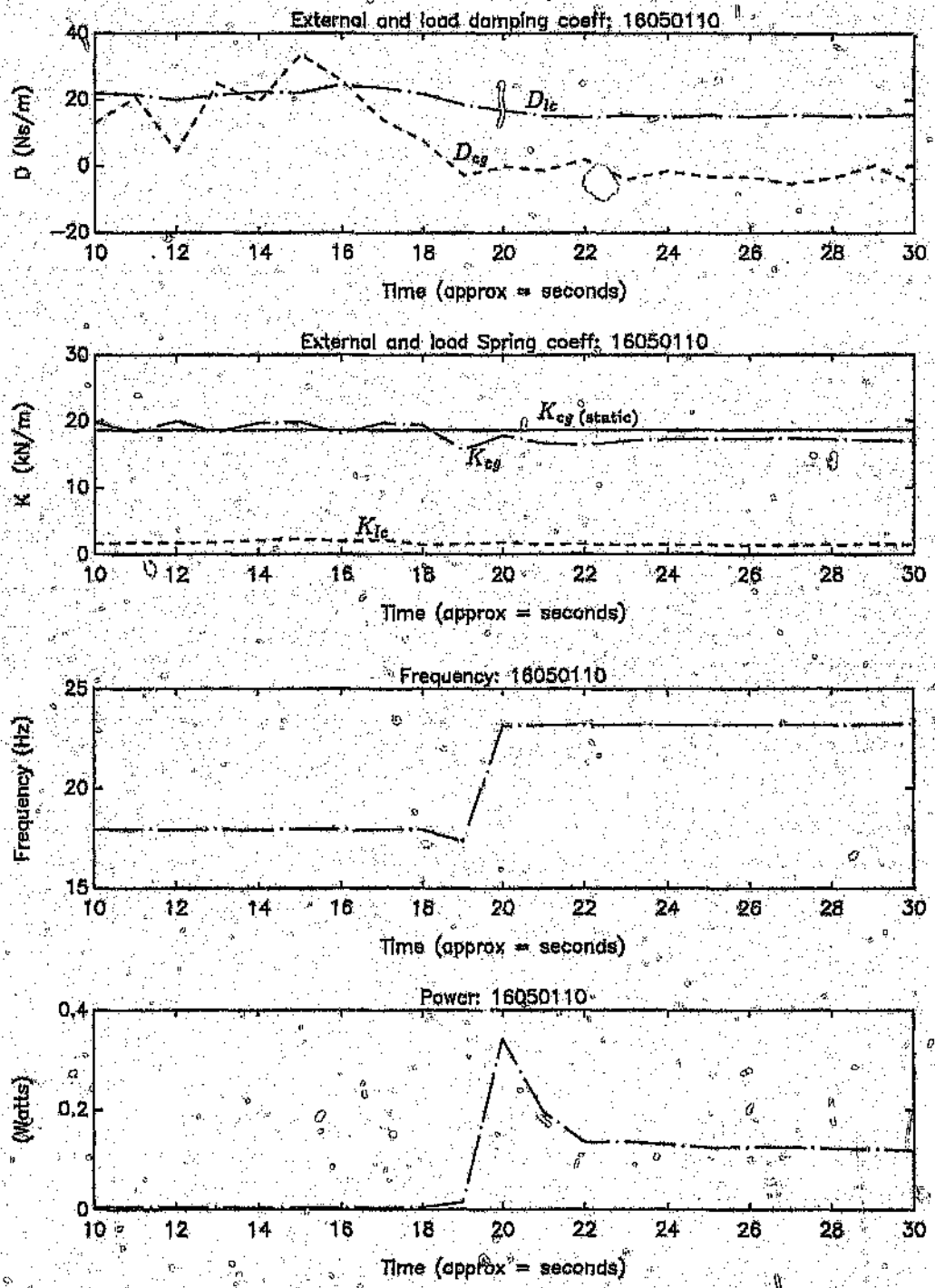

Figure 5.25: Quasi-stable engine operation: Frequency, output power and spring and damping coefficients

instrumentation problem. The measurements were checked quite carefully, and no explanation found. The pressure wave amplitude should be approximately proportional to the amplitude of the work-space volume variations, which are in turn a function of the relative motions of the components with respect to the case. Figure 5.28 shows that the relative motion amplitudes, and phases remain reasonably constant, despite the above noted changes in the absolute motion of the components. Thus the constant bounce- and work-space pressure amplitudes do seem reasonable.

5.3.4 Series BE19N tests

The final series of tests conducted used helium instead of nitrogen as the working fluid. The intention was to compare the operation of the engine under similar conditions to the earlier series BE09N tests. Tests were conducted at two charge pressure ranges (125 – 135 kPa and 155–163 kPa). The tests reported were carried out with ΔT in the range 236 – 381 K, although the majority were conducted using a ΔT of 330 K. The piston and displacer mechanical spring stiffnesses were similar to those for the BE09N series tests, being 841 N/m and 648 N/m respectively. (Series BE09N values were 778 N/m and 653 N/m). The external case spring stiffness ranged from 12 550 N/m to 19 520 N/m. For most of the tests the case mass was at 1.02 kg, although some runs at a case mass of 1.57 kg were done. The engine response to changes in the load damping coefficient was also investigated.

As noted above, small changes in parameters may have large effects on the operation of the FCSE. The helium tests were conducted at the end of the test process, and the similar nitrogen tests were conducted at the beginning of the process. Thus inevitable small variations in mechanical spring stiffness and of the friction losses due to wear of rubbing surfaces makes direct comparison of the data difficult.

Generally the mode of operation of the engine was similar to that of the series BE09N tests, principle characteristics being that the piston amplitude was higher than that of the case, with the displacer amplitude being higher still. The phase angles were also quite similar. Data from two similar tests is shown in table 5.7. Temperature difference, charge pressure, and case external spring stiffness were similar for the two tests.

The data shown in figures 5.29 and 5.30 shows the recorded data, and the sinusoidal approximation for a high amplitude test. It is quite clear that the engine, operating under these conditions cannot be well represented by assuming sinusoidal motion of the components. The load device was obviously

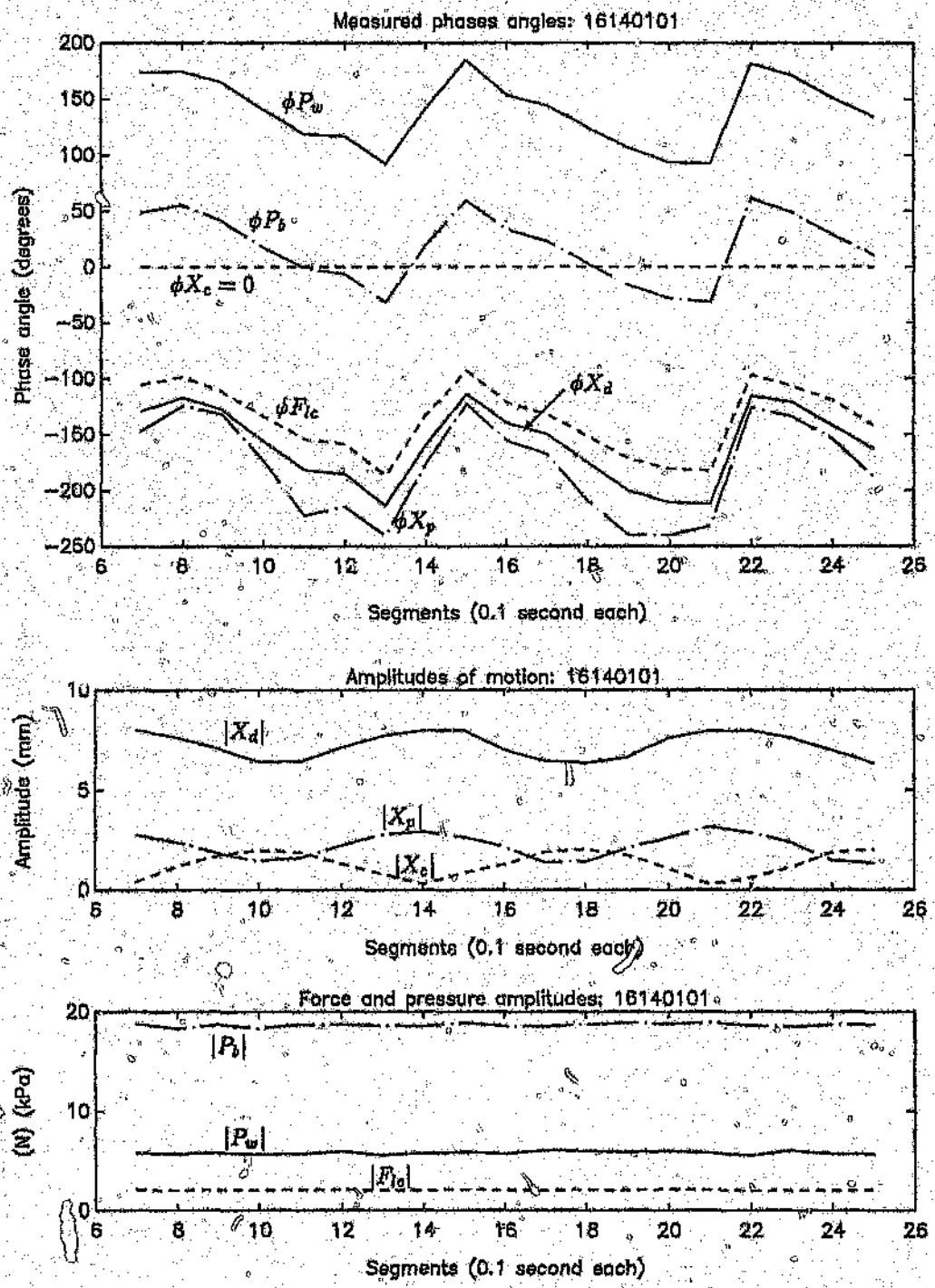

Figure 5.26: Cyclic variation in operation: Phase and amplitude data

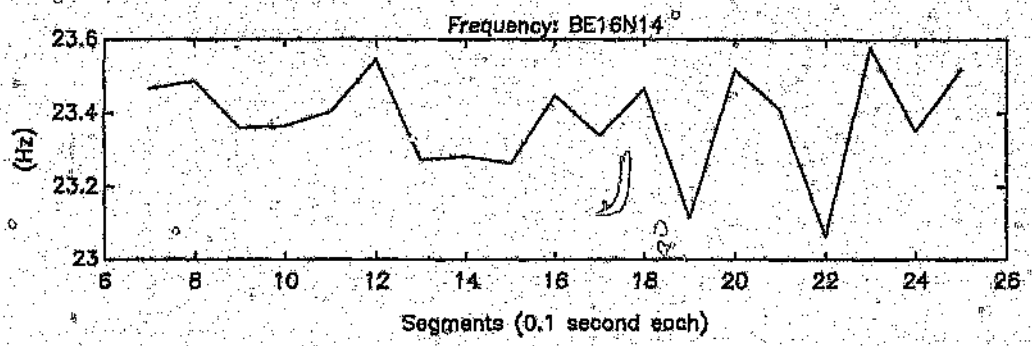

Figure 5.27: Cyclic variation in operation: Frequency data

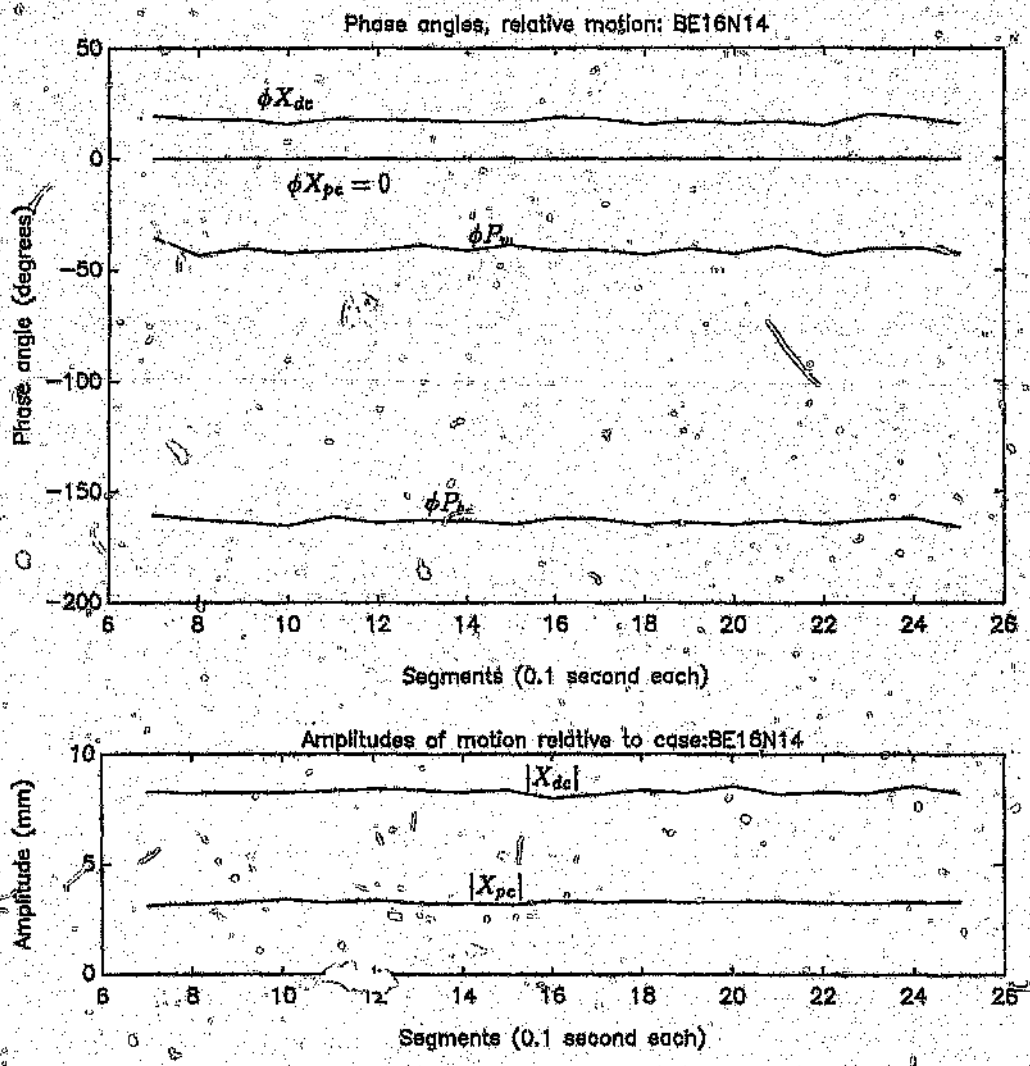

Figure 5.28: Cyclic variation in operation: Phase and amplitude data (relative motion)

Table 5.7: Comparison of motion data: selected helium and nitrogen test

	Nitrogen test		Helium test	
Frequency	13.71		13.26	
Motion:	Amplitude	Phase	Amplitude	Phase
Case	2.1 mm	0°	3.2 mm	0°
Piston	7.5 mm	5.4°	8.4 mm	5°
Displacer	11.7 mm	35.6°	10.1 mm	30°

highly nonlinear at these amplitudes, the peak in the curve corresponding to the bottom of the case stroke. The load cell was hitting an end stop. This affected the case motion significantly, and, although it did not directly affect the piston and displacer motion, had a significant effect on the bounce- and work-space volume variations. There are corresponding flat spots on the pressure curves, and as can be seen in the pV diagrams, the volume stayed approximately constant for a short part of the cycle, (right-hand edge of both pV curves). The lower amplitude tests deviated less from the linear curve, although nonlinearities were still apparent (see figure 5.31 as an example).

The engine in this mode was therefore not expected to be a good candidate for simulation using linear analysis, although as a first off design tool linear analysis may still be applicable.

Despite significant changes to the charge pressure, case mass, and case-ground spring (K_{cg}) carried out during the test series, the engine frequency, phase of oscillation of the components, and general mode of operation were largely unaffected. The small but consistent variation of frequency noted is discussed below. Figure 5.33 shows the engine frequency plotted against the rigid body natural frequency ($\omega_{rb} = \sqrt{K_{cg}/(m_c + m_p + m_d)}$). As ω_{rb} is not affected by the charge pressure the data is separated into two sets, the high pressure tests on the upper left-hand side of line a–b, and the low pressure tests on the lower right-hand side of this curve. Within each set there is reasonable relationship between frequency and the rigid body natural frequency. Thus, for this mode of operation an increase in external spring stiffness, or a reduction in the case mass resulted in a small increase in engine frequency. The separation of the data into two clear sets indicates that higher charge pressure resulted in a higher engine frequency. High and low pressure tests carried out at similar values of ω_{rb} yield a vertical movement on the figure.

As a rough indication of the motion for the test series, see figure 5.34 which shows the ratio of piston and displacer amplitude to that of the case. It should however be noted that this data is the result of fitting a sinusoidal curve to the original data, and is thus only an approximation of the nonlinear curves,

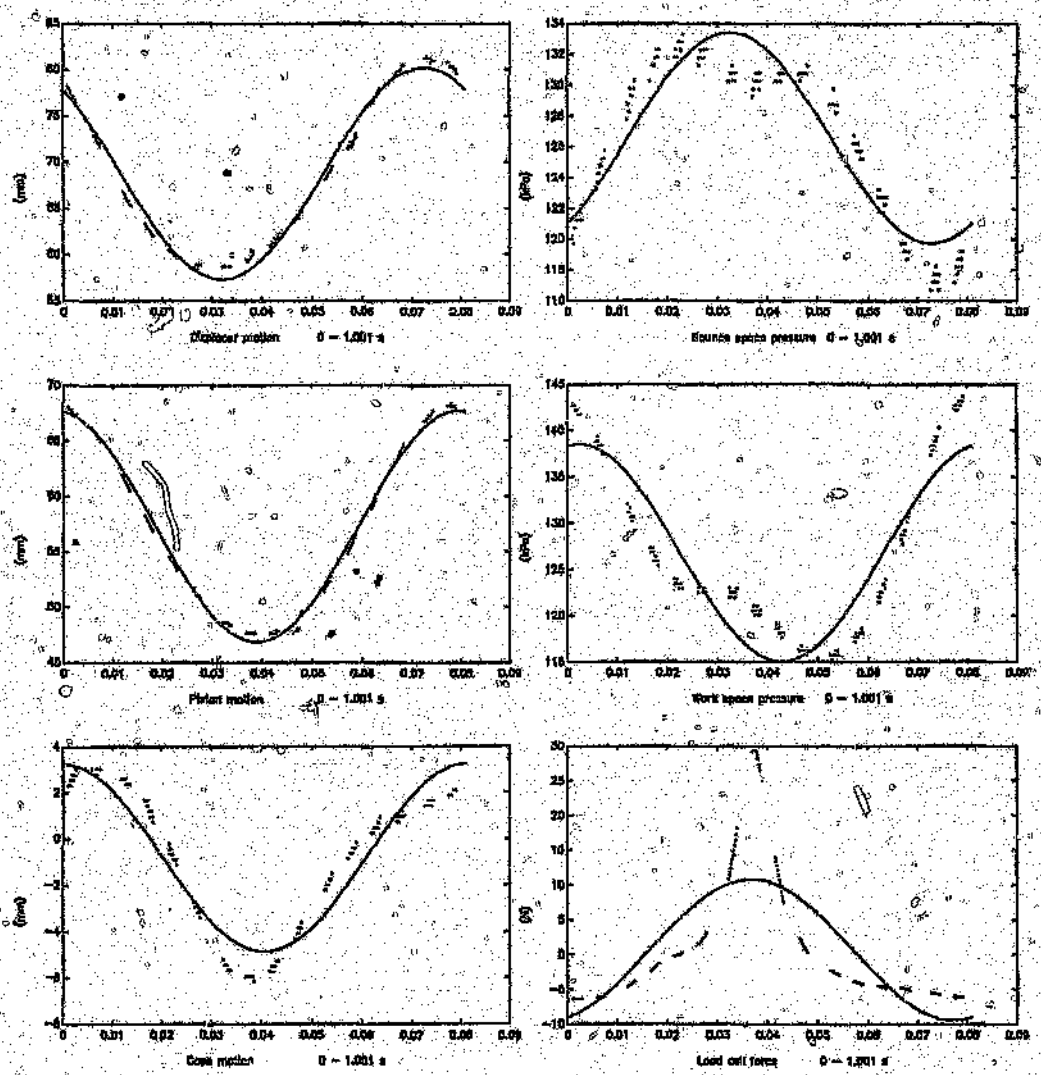

" accepted data, * rejected data, — sinusoidal approximation

Test no. BE19N24			Test condition and base data		
Segment: 0 – 1 seconds			Case mass:		1.02 kg
Charge pressure:	126.5	kPa	Hot-end temperature:		512 K
Mechanical springs:	K_dc		K_pc		K_cg
	648	N/m	840	N/m	14100 N/m
Frequency:	12.33	Hz			

	Sinusoidal approximation of waveform				
Variable	Amplitude		Variance		Phase lead
X_d	11.5	mm	1.0	mm	38°
X_p	10.4	mm	0.5	mm	7°
X_c	4.1	mm	0.9	mm	0°
P_b	6.8	kPa	1.9	kPa	-144°
P_w	11.8	kPa	3.6	kPa	-10°
F_{cl}	10.1	N	5.8	N	-163°

Figure 5.29: Calibrated data and sine wave approximation: high amplitude helium test (BE19N24)

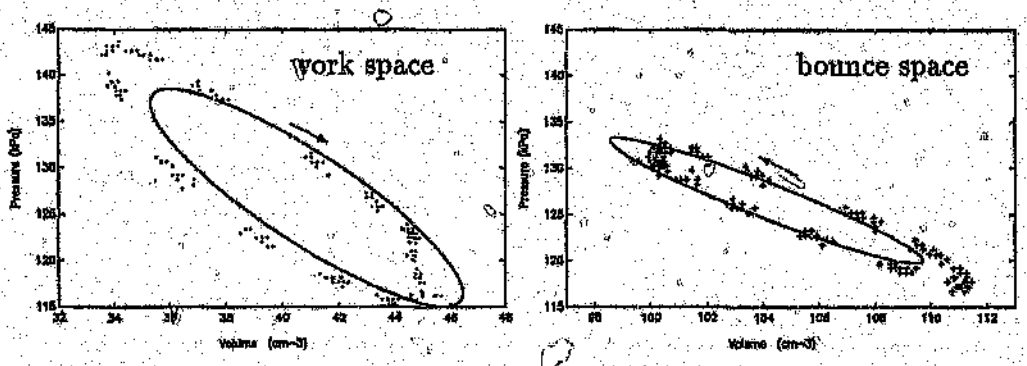

Figure 5.30: Pressure–volume diagram: high amplitude helium test (BE19N24)

as shown in figures 5.29 and 5.31. Figure 5.35 shows the phase with which the piston and displacer motion leads that of the case. The same x-axis, namely the rigid body natural frequency is used, as this will later be shown to give some measure of order to the simulation data (section 6.5).

In the previous tests when response to load was discussed, it was noted that the performance of the engine improved as the load damping coefficient was increased (see figures 5.11, 5.12 and 5.18. This was not however always the case. Figures 5.36 and 5.37 show how the helium charged engine adjusted to a small increase in load, but then stalled as the load was increased further.

5.4 Summary

The primary purpose of the experimental work was to provide a set of data which could be compared with calculations carried out using the 3-D SAUCE programme. Salient points will thus be picked up for further discussion in the next chapter. Important trends which run throughout are:

- All three components of the engine have significant amplitude of oscillation.
- The engine oscillated in a stable condition without requiring external control of the dynamics (two exceptions reported).
- The load on the engine modified the dynamics, usually improving the engine performance (some exceptions reported).
- The parameters varied (temperature, pressure, load, spring rates and case mass) all had significant effect on the engine dynamics and perfor-

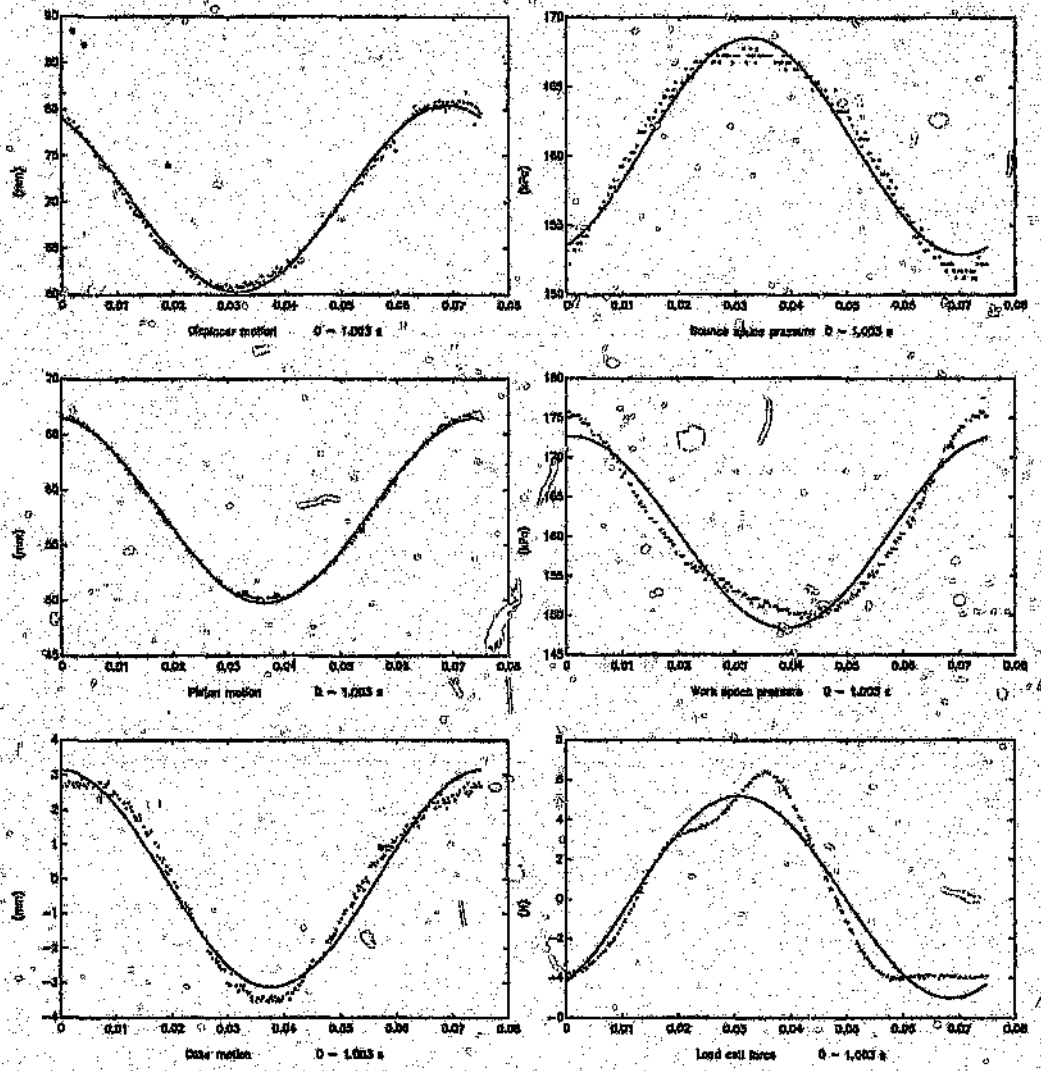

· accepted data, * rejected data, — sinusoidal approximation

Test no. BE19N15			Test condition and base data		
Segment: 0 – 1 seconds			Case mass:		1.02 kg
Charge pressure:	160.4	kPa	Hot-end temperature:		617 K
Mechanical springs:	$K_d c$		$K_p c$		$K_c g$
	648	N/m	840	N/m	17242 N/m
Frequency:	13.26	Hz			

	Sinusoidal approximation of waveform				
Variable	Amplitude		Variance		Phase lead
X_d	10.1	mm	0.6	mm	30°
X_p	8.4	mm	0.3	mm	5.4°
X_c	3.1	mm	0.4	mm	0°
P_b	7.8	kPa	0.9	kPa	-157°
P_w	12.1	kPa	2.1	kPa	-5.3°
F_{cl}	5.1	N	0.8	N	-147°

Figure 5.31: Calibrated data and sine wave approximation: lower amplitude helium test (BE19N15)

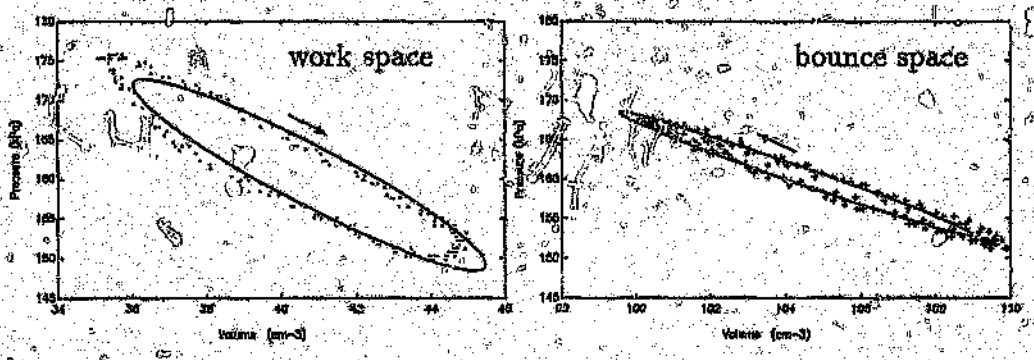

Figure 5.32: pV diagrams: lower amplitude helium test (BE19N15)

mance.

- Motion of the components is generally sinusoidal.

The various tests reported in the previous sections illustrate the wide variability in the operation of the Model B-10 engine. Although clear trends under particular circumstances were discernable, there were other situations in which the behaviour of the engine did not follow a readily recognisable pattern of behaviour.

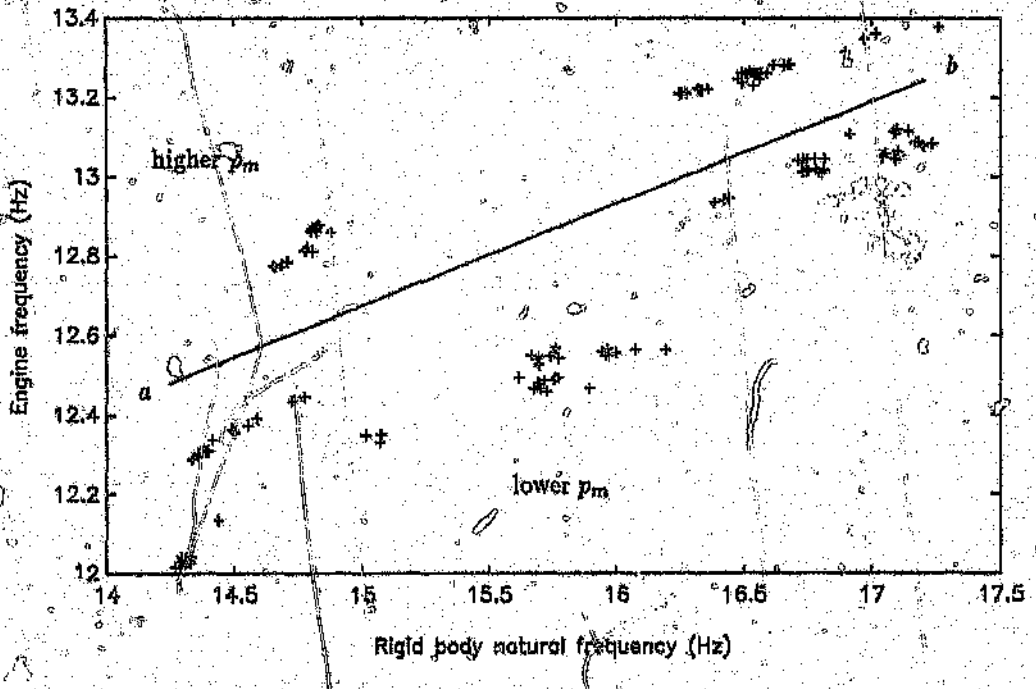

Figure 5.33: Series BE19N: Engine frequency versus rigid body natural frequency

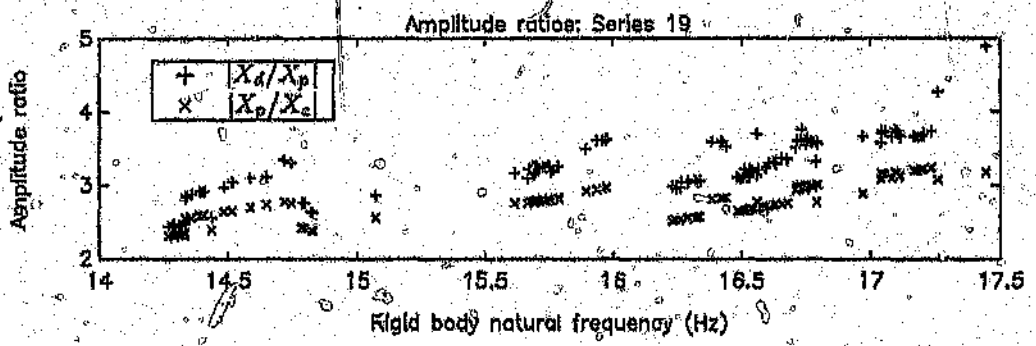

Figure 5.34: Series BE19N: Amplitude ratios ($|X_p/X_s|, |X_d/X_c|$) versus rigid body natural frequency

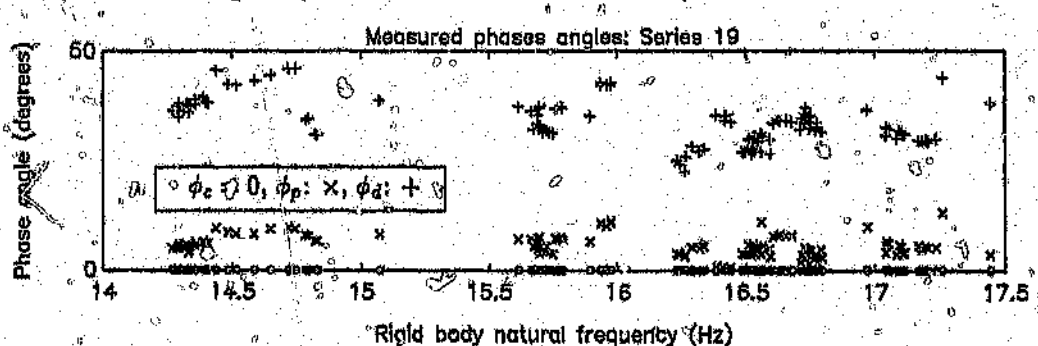

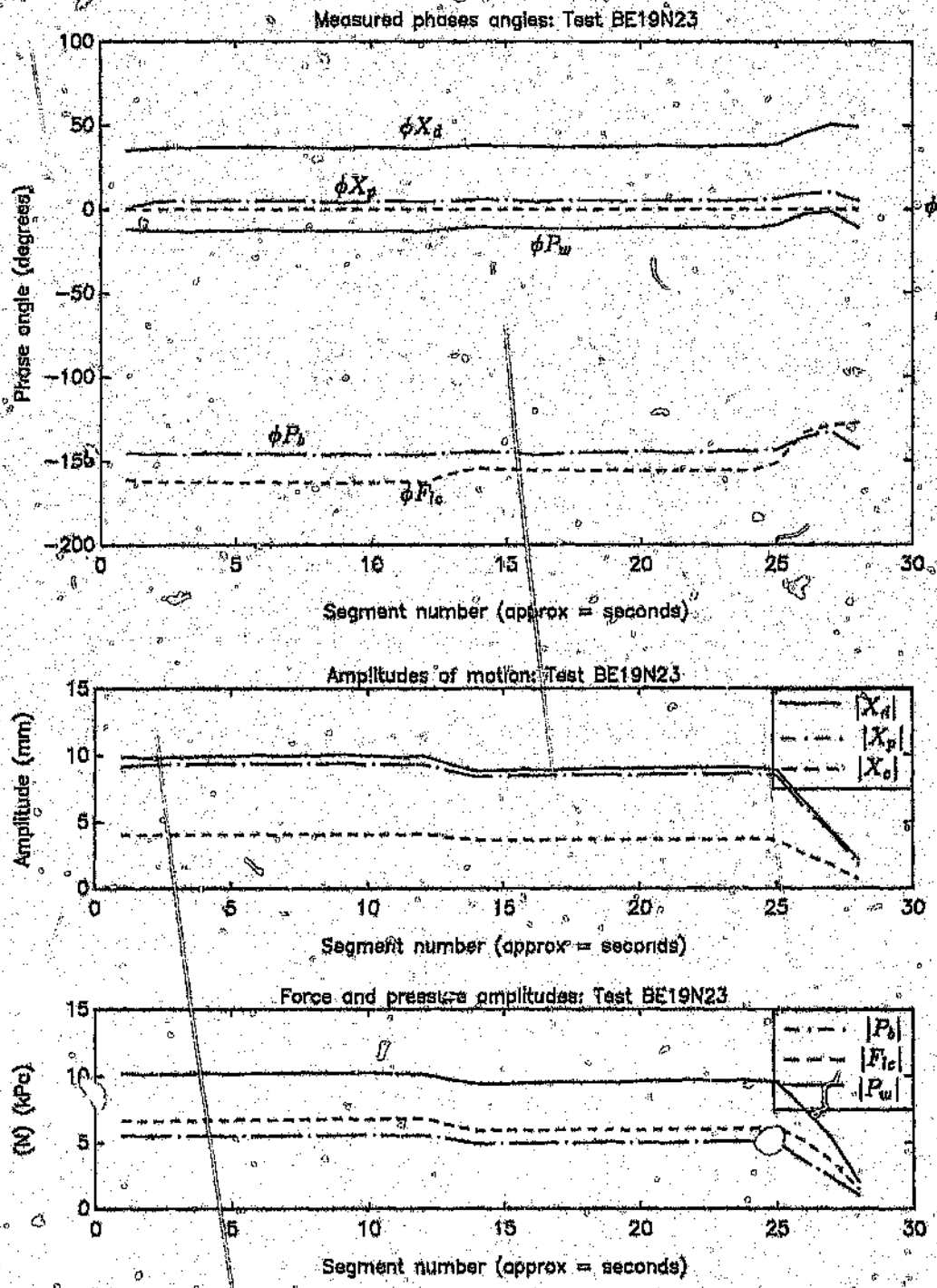

Figure 5.36: Response of engine to increase in load: motion data

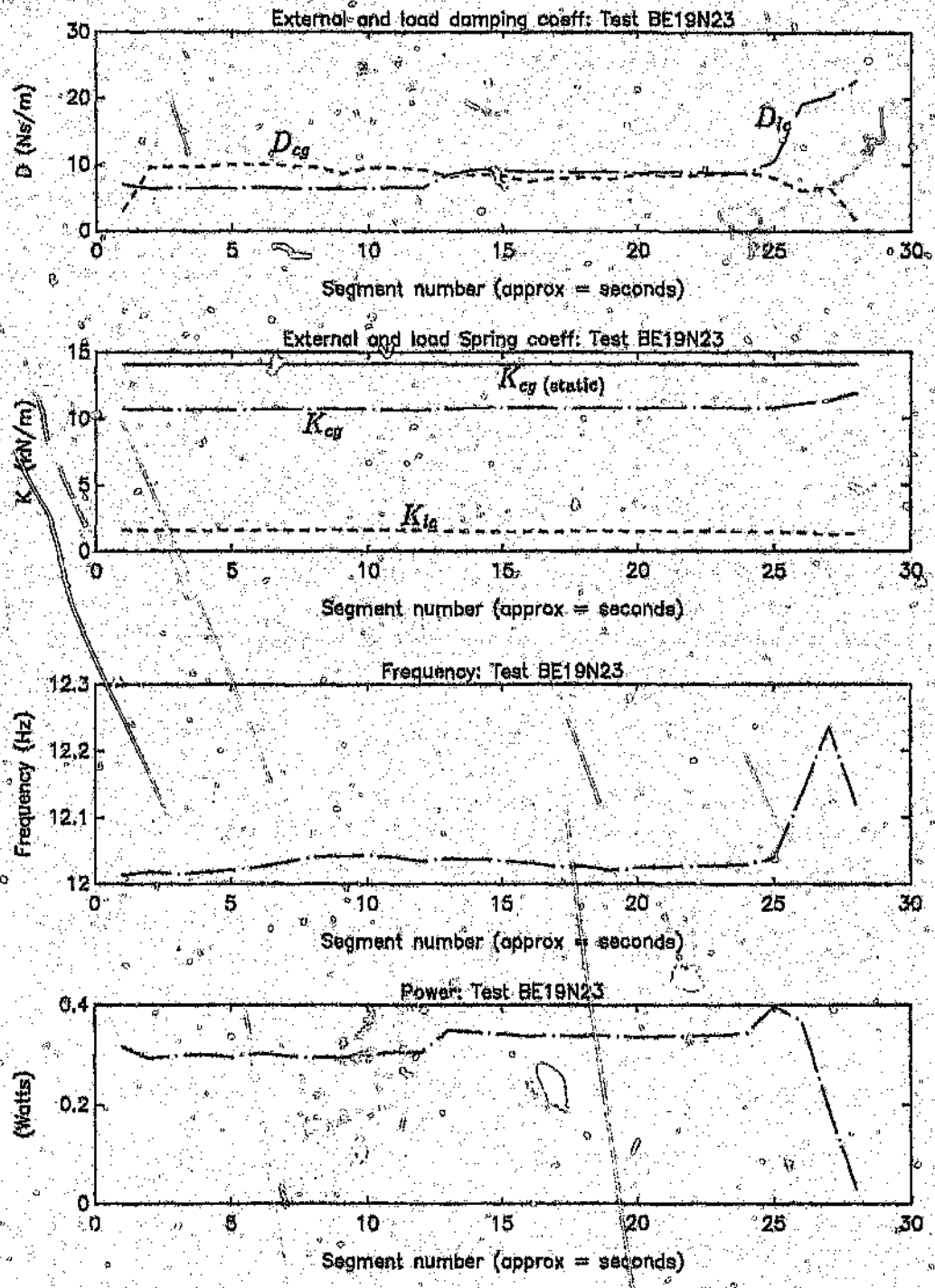

Figure 5.37: Response of engine to increase in load

Chapter 6

Simulation of the B-10 engine

6.1 Introduction

For this section of the work an attempt was made to simulate the engine under the range of operating conditions reported in the previous chapter. Use was made of the same 3-D SAUCE computer programme as used for the 'water pump' engine analysis.

Comparisons are drawn between the experimental and the simulation results. Areas of difference or similarity are pointed out. In an effort to avoid endless reams of data, and to save on space and time not all data are presented, only key areas representative of particular modes or characteristics. Emphasis is on amplitudes, phase, and frequency of the component dynamics.

Table C.3 (page 213) shows the basic data input to the simulation programme. For the various simulations described below factors varied in the input data followed those varied in the experimental work (eg: case mass, hot- and cold-end temperatures, mean pressure, mechanical spring constants). The mean position of the piston and the displacer was not always constant from test to test. The appropriate parameters were changed in the simulation input so that the mean expansion and compression space volumes matched those measured in the experiments. The working spaces were assumed to be adiabatic (see section 3.2.2).

6.1.1 Approximations and assumptions

As the thermodynamic and heat exchanger routines have not been further developed by this author, they are not discussed in detail. Due to the significant interactions between the thermodynamics and the dynamics of the engine, errors in the thermodynamic and heat transfer calculations obviously have significant impact on the linear analysis results. By using the analysis programme in the fixed dynamics mode, the dynamic operation of the engine could be set to that recorded in the experiments, and the thermodynamic, and friction losses so calculated compared directly with those parameters recorded or calculated from the experimental work. Areas of significant difference could then be reduced by the use of fudge factors on the thermodynamic and friction loss calculations. A useful comparison in this regard is the pressure acting on the top face of the piston. This was directly measured in the experiments, and could be calculated from the spring and damping matrixes in the simulation. The use of such fudge factors was kept to a minimum, and the simulations were therefore not always matched as closely to the experimental work as possible. Matching of simulation to experimental results can almost always be achieved if sufficient time is spent modifying fudge factors. However in a real design situation, experimental results will not be available. Thus fiddling with fudge factors does to a certain extent negate the purposes of running a comparison between the simulation and the experimental work. Where such manipulation of the simulation has been carried out, possible causes of the discrepancy are given, as well as pointers to areas for further work.

Seal leakage and centering port losses

The piston clearance seal on the model B-10 engine used had been recoated twice (as a result of wear) before the tests reported in the previous chapter were undertaken. The piston was fitted to the cylinder bore by hand, very fine sandpaper being used to remove coating until the piston fitted neatly. Although this procedure worked reasonably well, it did mean that the clearance gap was not constant along the entire seal. The displacer seal had not been replaced, although it was quite old. No attempt was therefore made to simulate the seal losses accurately. A reasonably small gap (for such a low pressure engine) of 25 μm was assumed. The seal losses are assumed to be catered for in the bounce-space loss fudge factor estimated in section D.1. The gas transfer resulting from the centering ports was not simulated.

Emphasis has not been placed on achieving similar output power for the experimental and simulation results as the losses in the engine are so large in comparison with the output power that small errors in their calculation would

lead to large changes in the output power determined.

6.2 Simulation of series BE09N tests

As reported in section 5.3.1 the first series of tests was conducted at four different charge pressures, with the hot-end temperature being varied for each charge pressure. Figure 6.1 shows the amplitude and phase data from both the experimental work and engine simulation for the lowest pressure condition. The simulation data are joined by straight lines, while the experimental results are simply shown by their appropriate symbols. The only inputs to the simulation which were changed for each of the different points were the hot- and cold-end temperatures and the case amplitude, the latter being used as the fixed amplitude required by the simulation process. The experimental amplitudes and phases of motion were used as initial estimates for the simulation procedure. The simulation predicted the piston amplitude and phase reasonably well. At the lower temperatures the displacer amplitude was underpredicted by the simulation, while at the highest temperature the simulation displacer amplitude was slightly higher. The simulation displacer phase angle is approximately correct, although the gradual decrease in phase angle noted in the experimental results is not mirrored in the simulation work.

In contrast with the experimental results, where the frequency ranged between 12.53 Hz and 12.17 Hz (figure 5.15) the simulation frequency remained relatively constant, (12.60±0.03 Hz). The simulation yielded higher output powers at higher temperature differences, as shown by figure 6.2, although if the case force determined by the force balance equation (5.10) was also considered as part of the load for the experimental results, the power comparison is much better.

In order to achieve the simulation results above, two fudge factors were required as modifications to the damping calculations. In appendix D.1 it is shown that for the most part the equation suggested by Berchowitz for determining the bounce-space hysteresis losses underpredicted the losses noted in the experimental work. For this series of tests a factor of 1.5 approximately corrects the difference. This is perhaps the first quite simple and yet serious difficulty experienced as a result of working on such a small rig, where losses such as seal leakage could not be adequately controlled. As explained in the appendix, the B-10 engine as configured for this work does not provide a suitable rig for the detailed investigation of bounce-space losses, and thus the fudge factors calculated in the appendix are used without further comment. The second fudge factor required was an additional damping coefficient represent-

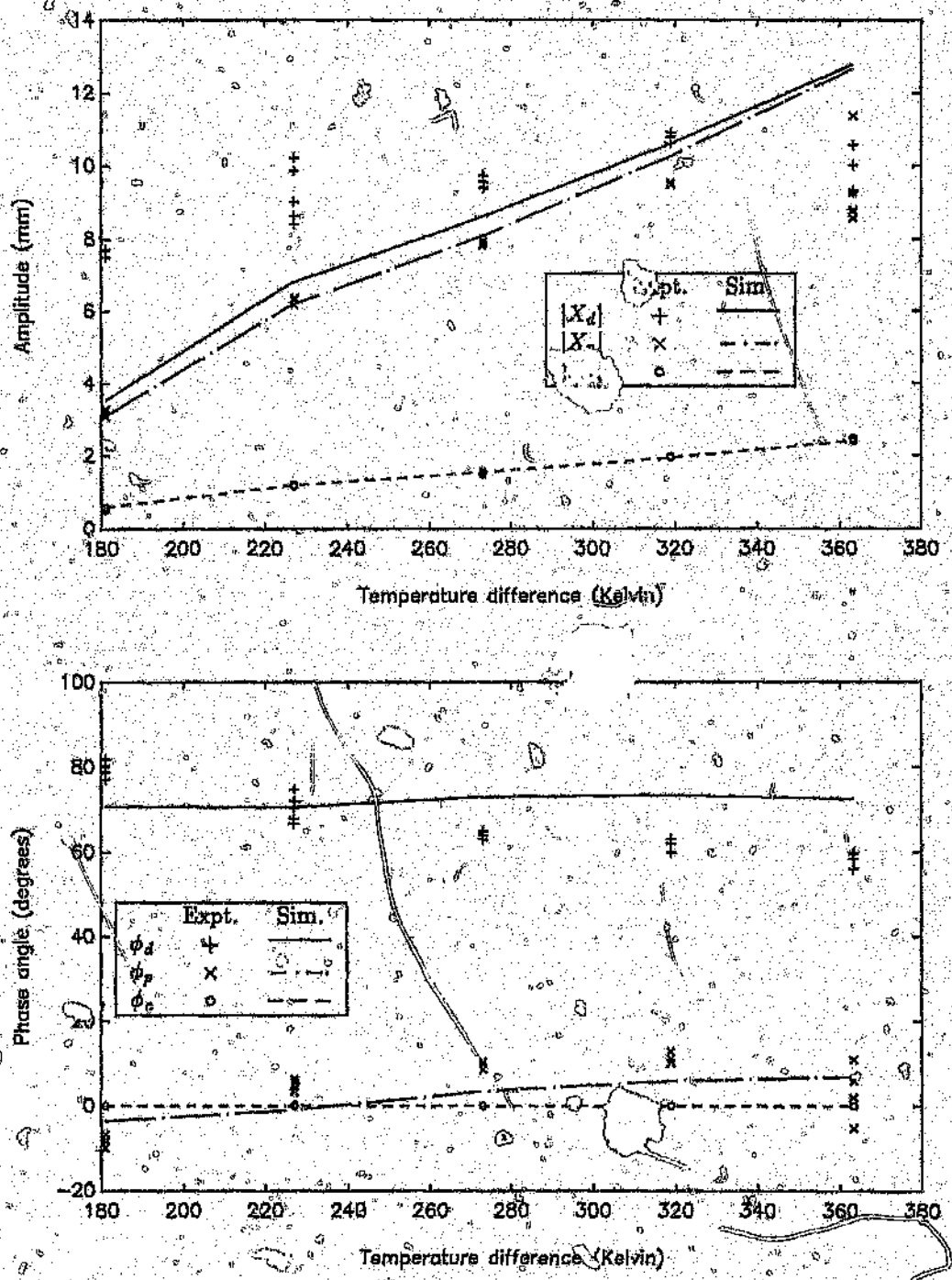

Figure 6.1: Simulation and experimental results; low pressure range of test series BE09N

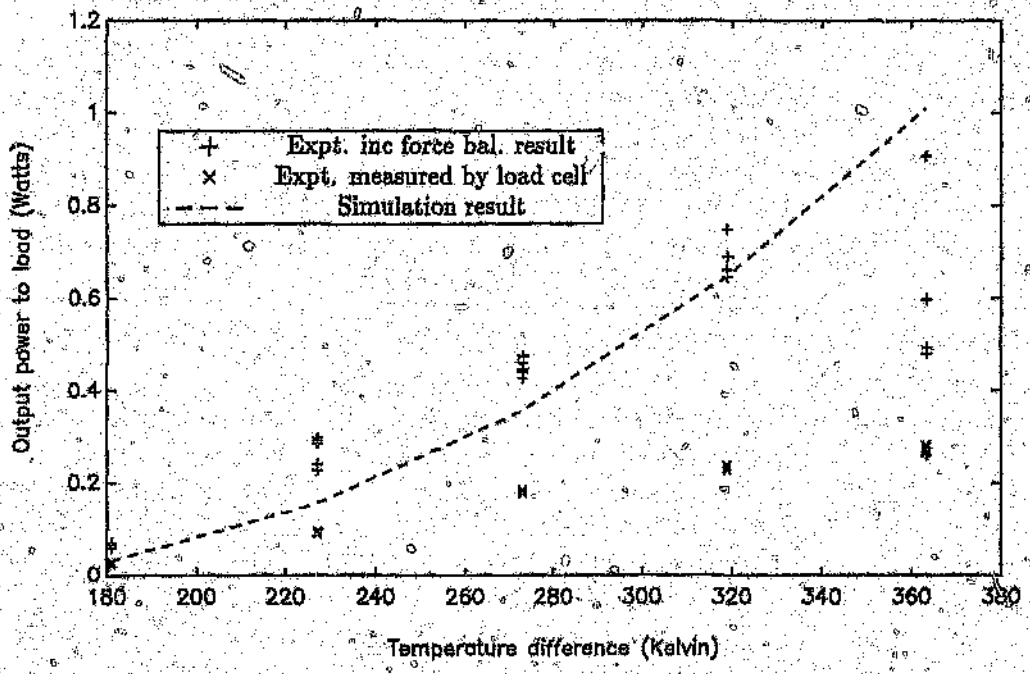

Figure 6.2: Simulation and experimental results: Output power, low pressure range of test series BE09N

ing damping between the piston and case. This was set to a value of 1 N/m. This is a significant damping at quite a fundamental point of interaction in the engine. It is however difficult to use this information as a pointer to specific deficiencies in the model. Force transfer between the case and piston could take place through the bounce-space gas pressure, the work-space pressure, as a result of friction losses in the clearance seal, and as a result of hysteresis losses in the mechanical spring. In appendix D.3 an attempt was made to isolate the gas pressure force transmission from the spring and clearance seal friction damping. The damping coefficients calculated from the experimental results using the methods of appendix D.3 showed such sensitivity to the bounce- and work-space pressures that it was not considered practical to use the method for the B-10 work. From this it can be deduced that relatively small errors in the simulation calculation of the work- or bounce-space pressure variation, as seen by the piston, would result in the need for quite significant 'unknown' damping between the piston and case in order to achieve adequate simulation.

The model B-10 engine used for this work was a number of years old, and the clearance seal coating had been replaced twice. Matching of the seal surfaces was therefore not ideal, and may have resulted in significant leakage losses, or sliding friction, which would be alternative contributors to the 'unknown'

damping between the piston and case.

The simulation curves for all four pressure ranges are shown, on the same axes in figures 6.3 to 6.6. The simulation is far less variable than the experimental data. However there are some more serious departures. Although the piston amplitude is reasonably well predicted, the displacer amplitude is significantly underpredicted for most of the tests (compare with figure 5.16). The displacer phase decreases steadily with increase in charge pressure, an effect not as clearly shown in the experimental results (figure 5.17).

The power curves (figure 6.3) are in some respects similar to the experimental data, in that power increases with increase in temperature, and for the most part decreases with increase in charge pressure. The simulation output power should be compared with the upper experimental data curves, as they include all external damping on the case (no external damping apart from the load was assumed in the simulation). Both simulation and experimental results show better performance for the 156 kPa curves. The experimental results showed a variation of engine frequency with temperature difference for each of the four pressure ranges (see figure 5.15), although no clear trend common to all the ranges was established. The simulation results were more consistent, with little change resulting from temperature difference, but a significant increase as a result of increase in charge pressure (figure 6.4).

6.3 High pressure tests

This series of tests proved difficult to simulate adequately. At first no roots of the characteristic equation with zero real parts could be found. When running the simulation in the fixed dynamic mode, using the results from test BEI4N14, it was noted that the calculated pressure drop across the displacer was very significant, leading to suspicion that the heat exchanger friction losses were being overpredicted by the simulation programme. Berchowitz, in his original form of the SAUCE software provided a fudge factor for the friction losses. Setting this at 0.3 (i.e. 30 % of the calculated pressure drop across the heat exchangers) improved the situation markedly. The heat exchangers in the B-10 engine simply comprise the annular gap between the displacer dome wall and the case. The resistance to gas flow is thus very sensitive to the exact dimension of the gap, and to any eccentricity in the alignment between displacer and case. In section D.2 some calculations using the fixed dynamics mode are presented in order to illustrate this. An experimental estimate of the pressure drop across the heat exchangers is presented in section D.3. This, although very approximate, does lend some support to the fudge factor of 0.3

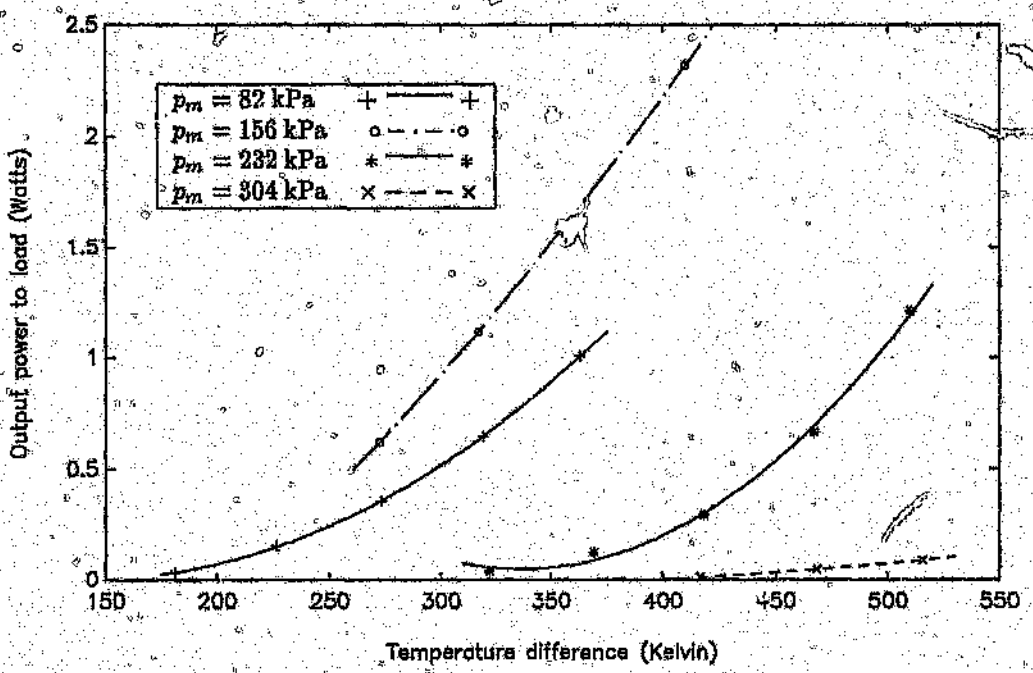

Figure 6.3: Engine power as a function of temperature difference and charge pressure (simulation results).

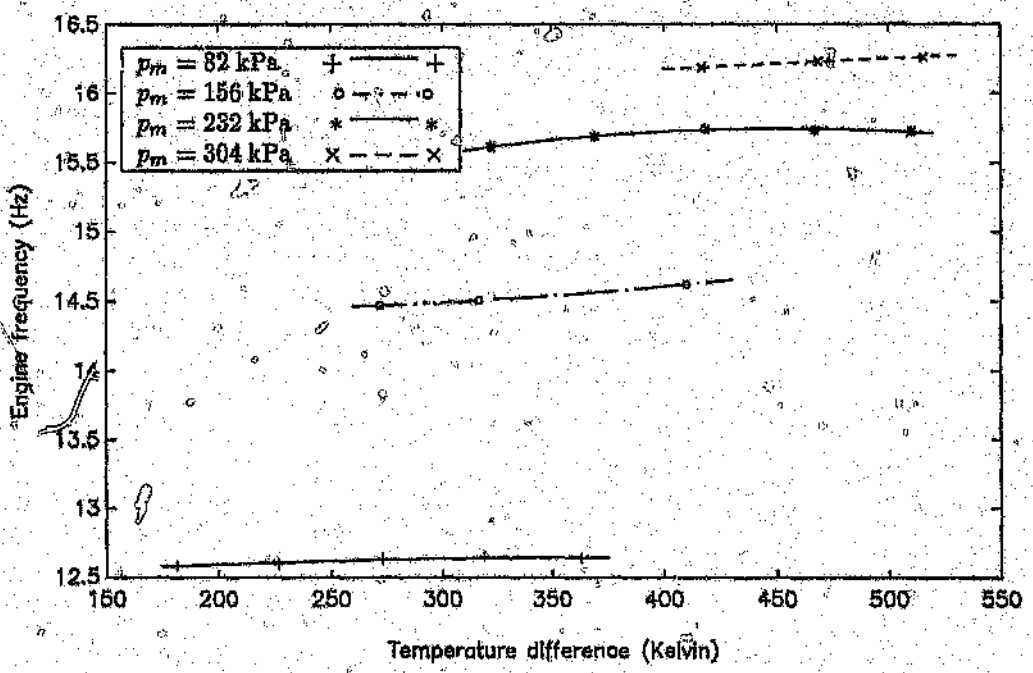

Figure 6.4: Engine frequency as a function of temperature difference and charge pressure (simulation results).

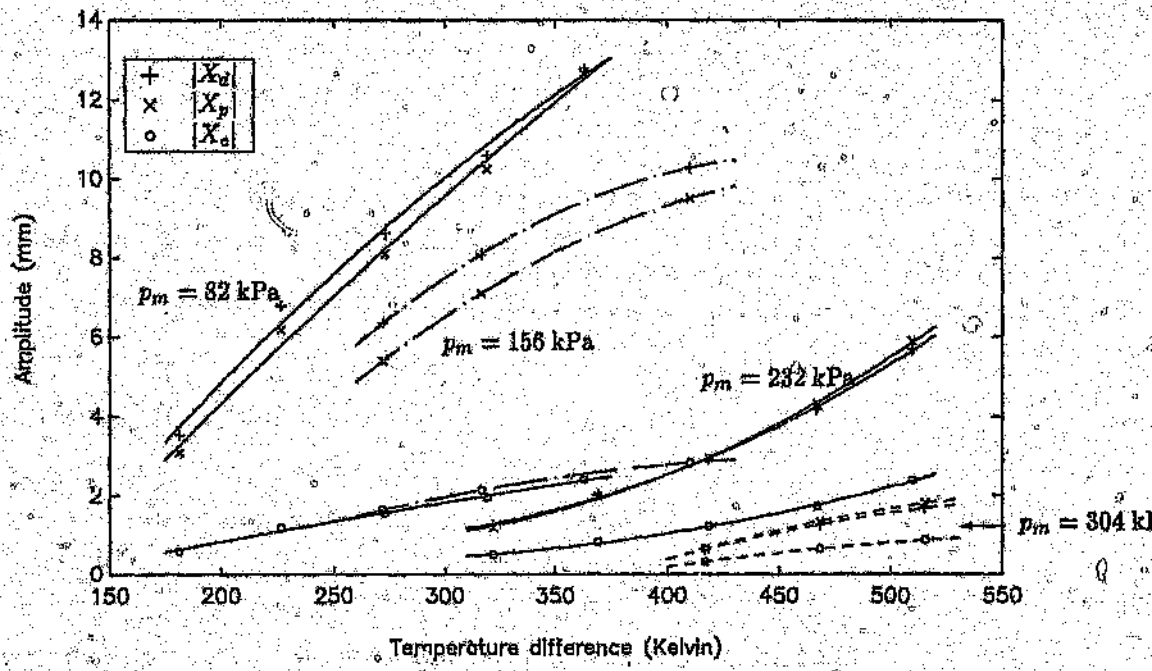

Figure 6.5: Amplitudes of motion as a function of temperature difference and charge pressure (simulation results).

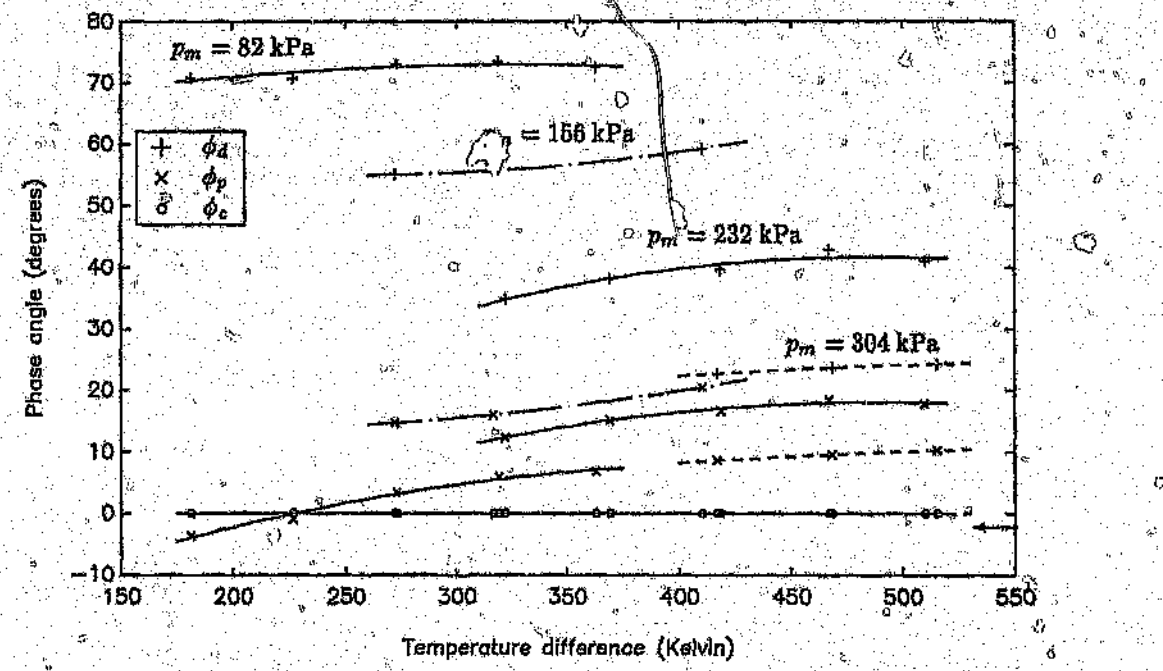

Figure 6.6: Motion phase angles as a function of temperature difference and charge pressure (simulation results).

used.

The heat exchanger performance calculations seemed to underpredict the heat transfer significantly, the calculated temperature drop between the external wall temperature and the gas being of the order of 60° C. This resulted in a poor comparison of the work-space gas pressure, as seen by the piston (13.89 kPa, $\phi = 24.9°$ for the experimental results versus 8.25 kPa, $\phi = 30°$ for the simulation results). The heat-transfer fudge factors, also provided in the original implementation of Berchowitz's programme were therefore set to 2, yielding a simulation compression space pressure phasor of 14.23 kPa, $\phi = 22.76°$.

The bounce-space hysteresis losses fudge factor, estimated from figure D.4 was 4, much higher than expected.

In order to maintain conformity between this set and the previous simulation, the 'unknown' damping coefficient D_{pd} was held at 1 Ns/m, although its effect was quite small.

Once these fudge factors had been chosen it was possible to coax the programme to predict a similar mode of operation to that noted in the experimental work.

Consider the simulation procedure as described in section 3.1. A given estimated set of motion vectors is used to determine the damping and spring coefficients of the equations of motion as represented by equation (3.1). The Laplace transform of the matrix equation yields a single matrix of the form $[s^2\mathbf{M}+s\mathbf{D}+\mathbf{K}]$. The determinant of this matrix yields the characteristic equation, the roots of which define the dynamic operation for the next cycle. The asterisks (*) in figure 6.7 show the roots determined from the initial conditions for test BE14N14 (i.e. after a number of iterations in the fixed mode using the motion data as recorded in the test). For this root pattern, the damping coefficient D_{cg} was estimated using the power available from the thermodynamic cycle as a guide. The roots have been multiplied by $1/2\pi$ so that the imaginary component represents the frequency of oscillation (in Hz) associated with a particular root. The transient response of the engine is a function of all three roots. However for steady state motion one of the root pairs must have a zero real component, with the other two pairs having a negative real component. Oscillations associated with the latter two would then die away. Conversely, if one of the root pairs had a positive real part then its associated oscillations would increase with time, obviously an untenable situation. The next stage in the solution procedure is to determine an appropriate value for D_{cg} such that one pair of the roots in figure 6.7 lie on the imaginary axis, while the others all remain in the left half of the plane. The lines in figure 6.7 show the root loci for values of D_{cg} from -10 to 50. Note that the roots corresponding to oscillations

of 17 and 31 Hz move from right to left as D_{cg} is increased, while the 24 Hz root paradoxically moves from left to right as D_{cg} is increased. Note that in this configuration the root loci are all approximately horizontal, implying that the frequency of each mode of oscillation is not significantly affected by the damping coefficient.

In figure 6.8 only the real component of the conjugate pairs are plotted as a function of D_{cg}. There are thus two values of D_{cg}, D_1 and D_2 for which the equations of motion with coefficients determined from the initial conditions indicate stable operation. Values of D_{cg} between D_1 and D_2 would result in decaying oscillations, while values to the left of D_1 or to the right of D_2 would yield a root with a positive real component, and hence increasing amplitudes of oscillation.

Either of these values can be chosen for subsequent iterations. Following from the selection of an appropriate value for D_{cg} the associated value of ω (the imaginary part of the root having a zero real component) is substituted back into the Laplace equation of motion matrix, and the amplitude ratios and phase relationship of the component oscillation determined. The iteration procedure is then repeated using the new dynamics to work out new values of the spring and damping matrix coefficients.

In each subsequent iteration a similar choice of D_{cg} and hence of the root pair, will have to be made. Provided the choice is consistent either route could lead to a mode of operation. If the engine was a perfectly linear system (then the coefficients of the spring and damping matrixes would not vary under slightly different conditions), then iteration would not be necessary, and it would be clear from the root locus map that two modes of operation are possible, depending on the value of the load damping.

In the case under discussion, the solution procedure did not converge if the lower value D_1 was chosen.

Consistent selection of the higher value lead to the results shown in figures 6.9 and 6.10, which compare favourably in form if not magnitude with the experimental results (figures 5.18 and 5.19). The range of data points plotted represent simulation of the engine at a series of operating points, all with the same conditions except for the case amplitude, which was varied from 1.18 to 1.82 mm. This was the same range of case amplitudes measured in the experimental work. The simulation and experimental results yielded similar frequency ranges (23.3 — 24.60 Hz and 23.11 — 23.45 Hz respectively). The discontinuities in the curves result from changes in the flow regimes (and hence use of different equations) in the heat exchanger analysis. The simulation piston phase angle and amplitude is generally higher than that recorded in the

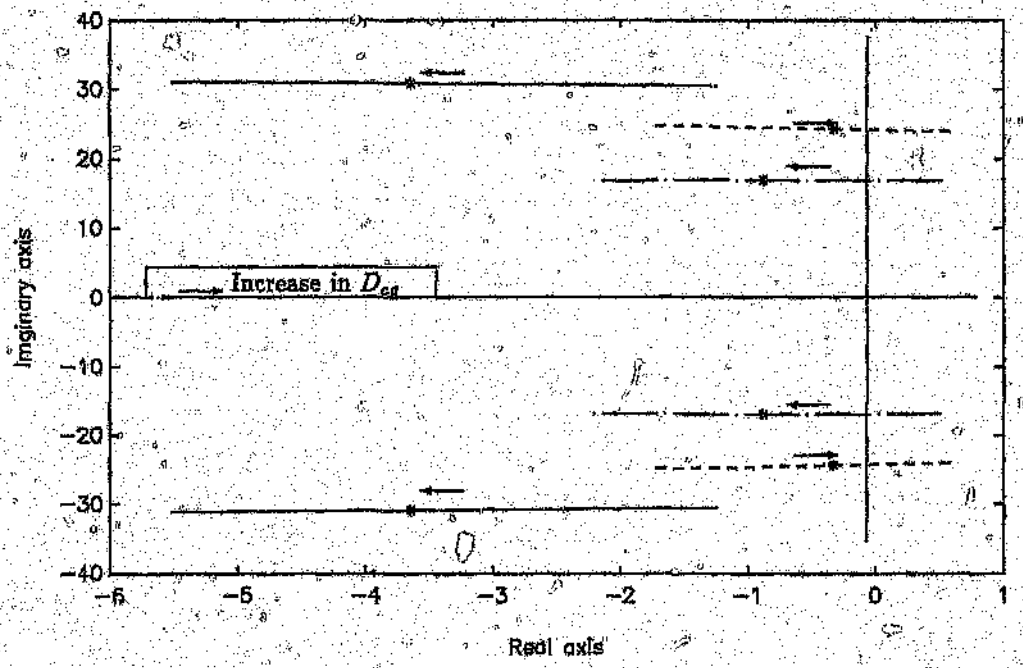

Values have been divided by 2π to yield oscillation frequency in Hz

Figure 6.7: Root locus diagram, test BE14N14 at initial conditions

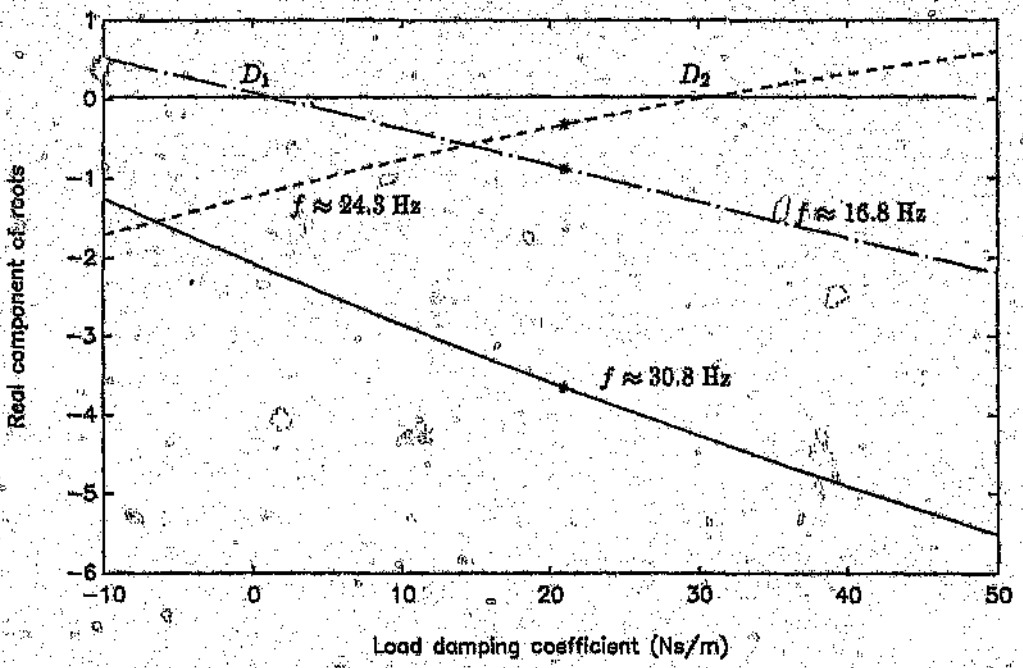

Values have been divided by 2π to yield oscillation frequency in Hz

Figure 6.8: Real component of roots versus load damping coefficient, conditions as for above figure.

experimental work, indication that the damping between the piston and case was underestimated. The simulation displacer phase is less than 180°, whereas the experimental results indicated that it was close to or greater than 180°.

In section 5.3.2 it was noted that for the BE14N series the output power and the case amplitude increased with increase in load damping. This was somewhat unexpected as it seemed to indicate unstable engine operation, and could not be readily explained. The simulation indicates similar results, as shown by figures 6.9 and 6.10. The engine load damping coefficients required by the simulation for a series of different amplitudes are shown in figure 6.11. (This curve uses the same data as that of figure 6.9). From knowledge of the root locus map (figure 6.7) and the definition of a solution (section 3.1), (X_c, D_{cg}) pairs lying on this curve yield a complex conjugate pair with a zero real part. Consider a small deviation below this line, say at the point (X'_c, D'_{cg}). D'_{cg} is less than the required value for stable operation at X'_c. This would result in the oscillatory root moving away from the imaginary axis towards the left hand half of the complex plane in figure 6.7. As a result of this the oscillation amplitude would gradually decrease. Provided D'_{cg} remained constant the oscillation amplitude would decay along the dotted line shown until a new operating point (X^1_c, D'_{cg}) was reached. Alternatively, should the engine as a result of some perturbation or change in load find itself operating at some point (X^2_c, D^2_{cg}), above line a—a, this would result in the oscillatory roots being located in the positive half of the complex plane. Oscillations would thus increase until stable operation was reached at point (X^3_c, D^2_{cg}). In the above discussion it as been assumed that D_{cg} is not primarily a function of amplitude, remaining constant except when adjusted by some external condition. (e.g. change in head of a water pump). This is not a necessary condition, for example a load curve of the form b—b would also result in a stable operation point at the crossover point of this line and the engine curve a—a. However a load curve of the form d—d, where the load damping increased with a steeper slope than that of the engine curve a—a would not yield stable operation. It would be intriguing to see whether an engine could be designed to operate efficiently in the mode described above, as it would provide an elegant solution to problems of engine control under fluctuating loads. For example if the engine were driving a linear alternator, as the power taken from the system was increased, so the damping on the alternator would increase, resulting in increased case (alternator) oscillation and hence increased power available. Should the power requirement suddenly be reduced, the alternator damping would be reduced and the engine oscillations would quietly die away until stable operation was reached at the lower power point, without any control system being necessary. It should be possible to match the alternator characteristics such that the engine would deliver nearly constant voltage over the power range.

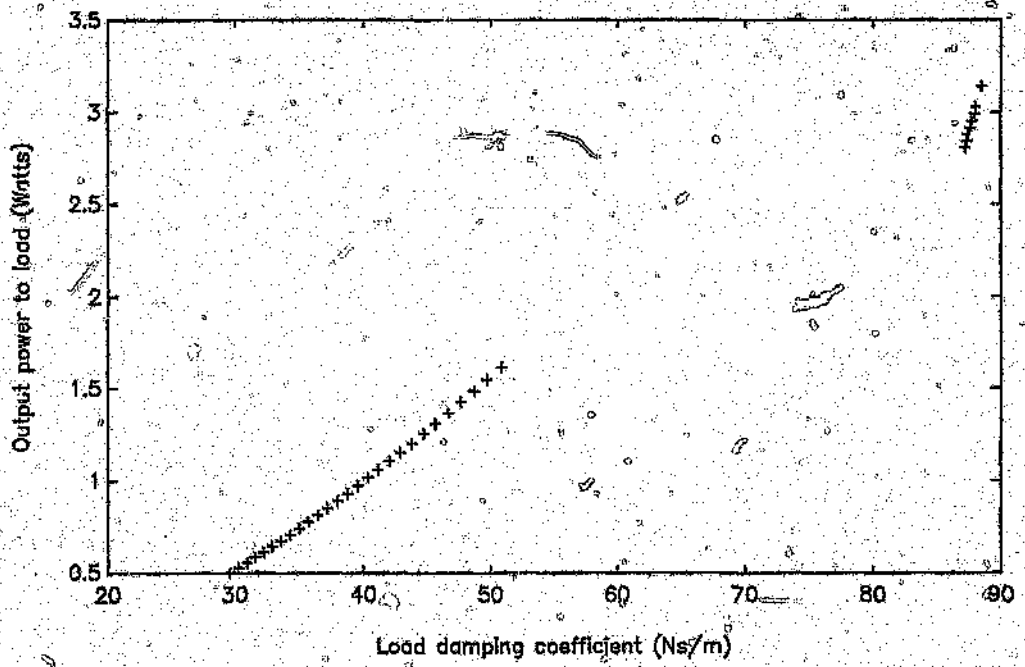

Figure 6.9: Output power versus load damping coefficient

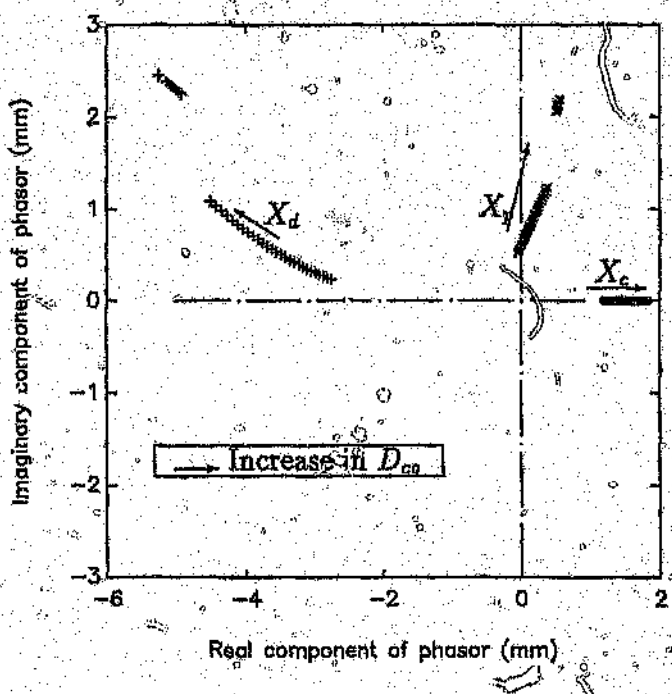

Figure 6.10: Motion phasors, magnitude increases with increased D_{eq}

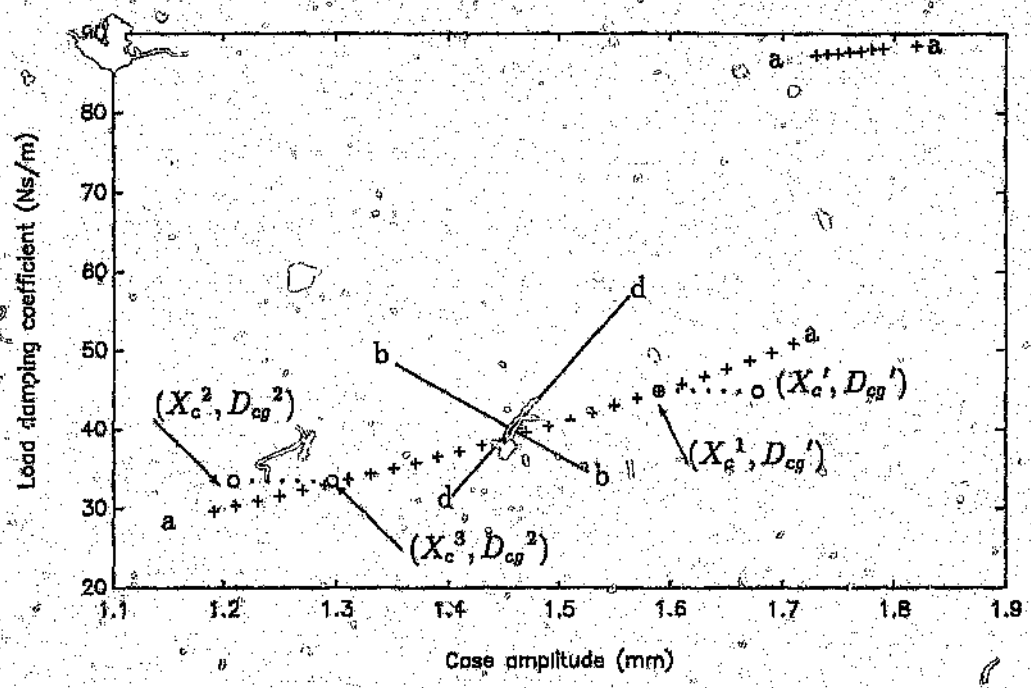

Figure 6.11: Load versus case amplitude curve

6.4 Simulation of the series BE16N tests

As noted in the account of the experimental work, the parameters varied during this series of tests were the case mass and the case spring stiffness coefficient. Simulation of the group as a whole proved difficult. However, once the basic method of simulation had been finalised, it was found that the engine behaved similarly across the range.

At first, no reasonable simulation could be achieved. Following from the lead given by the previous test series for which the charge pressure and amplitudes of oscillation were similar, the same fudge factors of 2 for the heat transfer, and 0.3 for the heat exchanger friction losses were applied. The bounce-space hysteresis losses fudge factor was estimated from figure D.6 (section D.1). The figure was again much higher than expected, at 4.

Convergence to a solution was however only possible if an unknown damping mechanism was assumed to interact between the case and the piston. The engine was simulated as if it were a free-piston, with an unknown linear damper acting between the case and piston (see section 3.4.8). An appropriate value for the actual load (damping between case and ground) was entered as a fixed, user

determined input to the simulation. The iterative procedure then determined an appropriate damping factor for the unknown piston-case damping force. This procedure, although quite empirical, did work consistently across the stable tests reported, and yielded results that agreed in form and magnitude with those yielded by the experimental work.

Following the method given by Berchowitz [13, pg 269] the dissipation from a constant frictional force is as follows:

$$\Phi_{sc} = \oint |F_{sc}\frac{dx}{d\theta}|d\theta \tag{6.1}$$

$$= 4F_{sc}X_{pc} \tag{6.2}$$

Using the methods of section 3.4.1 and an equation of the form (3.43) it is possible to determine a constant frictional force which would yield the damping between the piston and case demanded by the simulation method described above. It was hoped that once this constant friction force had been determined using one of the tests, applying the same factor to the other tests would yield satisfactory results. However, the simulation was very sensitive to the exact value of the piston-case damping coefficient so calculated. Hence no single value applicable to all the tests could be determined. It was therefore decided to simply treat the piston–case damping as an unknown, and to allow the simulation procedure to determine an appropriate value for each test. The utility of the simulation as a tool to investigate the change in operation of the engine as the case mass and case external spring were varied could thus still be investigated. Figure 6.12 shows the key simulation data, corresponding to figures 5.21 and 5.23. The case amplitude was held constant at 0.95 mm, and the case–ground damping was set at 10 Ns/m. Four values of case–ground spring stiffness were investigated, the values being 8.18 kN/m, 12 kN/m, 15 kN/m and 18 kN/m. Within each range the engine was simulated for a range of case masses from 2.08 kg to 0.83 kg. No other parameters were varied (except of course the piston–case damping which was solved for during the simulation procedure).

As for the experimental results, the displacer and piston amplitudes generally increased as the case mass was increased (right to left within each subseries) and as the case external spring stiffness was reduced (right to-left from subseries to subseries). The displacer phase showed a slight decrease from right to left within each subseries, as did the piston phase. The latter was however slightly more erratic, with a jolt in the curve for each subseries. This jolt corresponded to a sudden change in the frequency trends, as shown in the lower figure. Their curves show a similar decrease from right to left, with a sudden increase occurring at increasing values of the case mass (right to left from subseries to subseries). The extreme right hand set of data shows a much lower frequency, and significantly different phase angles. The engine operation has changed

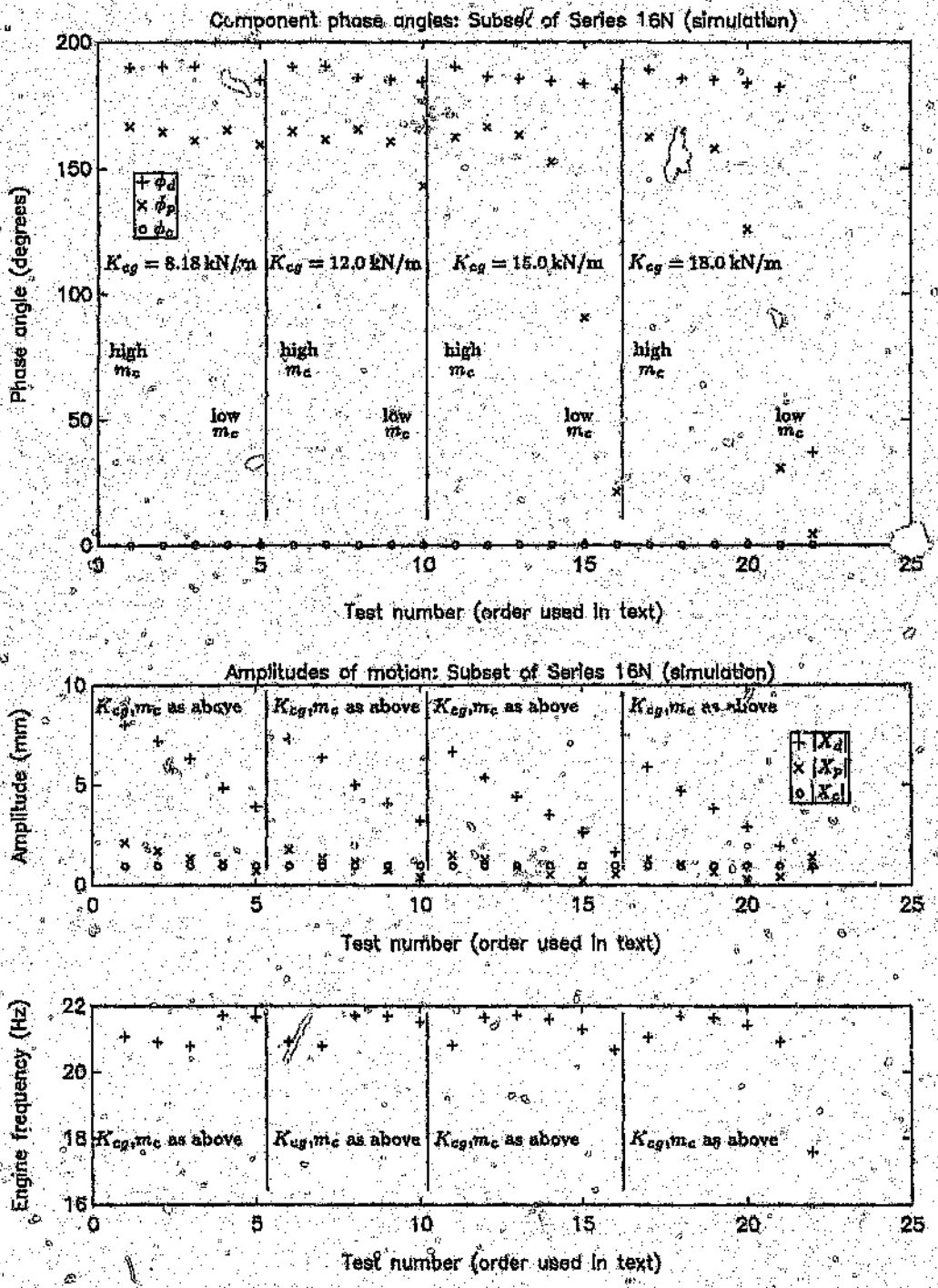

Figure 6.12: Motion data for series BE16N simulation: K_{cg} and M_c varied

Table 6.1: Comparison of motion data: unstable operation, experimental and simulation results

	Low frequency mode				High frequency mode			
	Experiment		Simulation		Experiment		Simulation	
Frequency	17.91 Hz		17.22 Hz		23.19 Hz		21.95 Hz	
Motion:	Amplitude	Phase	Amplitude	Phase	Amplitude	Phase	Amplitude	Phase
Case	0.16 mm	0°	0.85 mm	0°	0.67 mm	0°	0.85 mm	0°
Piston	0.29 mm	2.8°	1.32 mm	-0.1°	0.30 mm	41°	0.58 mm	22°
Displacer	0.62 mm	86°	0.62 mm	11.7°	1.97 mm	186°	1.97 mm	184.6°

modes. It was noted in the experimental work that the engine operation was unstable for low case masses at a high value of K_{cg}. The simulation frequencies are all slightly lower than the experimental results.

6.4.1 Unstable engine operation

Section 5.3.3 discussed a test in which the engine suddenly changed from one mode of operation to another, without any change in operating parameters. The same conditions were simulated with only moderate success. The high frequency, higher amplitude mode was simulated fairly easily, the engine operating in much the same manner as for the high K_{cg} tests discussed in the above section. However, although a low frequency , low amplitude mode could be simulated after adjusting the case–ground damping coefficient by about 10%, the phase angles were quite different from the experimental results. Furthermore, the required damping between case and piston was significantly different for the two conditions. The experimental data for this low frequency, low amplitude condition were unfortunately not very accurate (as a result of the very small amplitudes), thus it was not possible to use these results as a guide to improve the simulation. Table 6.1 lists the key experimental and simulation results. (Note, the displacer amplitude was chosen as the fixed amplitude for these simulations, refer to section 3.1).

The conditions for which the cyclically unsteady behaviour occurred, as reported in section 5.3.3, correspond approximately to those yielding the extreme right hand data point of figure 6.12. The simulation is clearly unstable in this region (note the sudden change in frequency for only a small change in case mass). Unfortunately little further insight into this regime could be gained from the simulation. However, the fact that the simulation does show sudden changes at or near the operating conditions is helpful, as this would indicate areas to avoid when designing an engine.

Table 6.2: Comparison of key data: Test BE16N27, experimental and simulation results

	Low load				High load			
	Experiment		Simulation		Experiment		Simulation	
Frequency	22.69 Hz		20.71 Hz		22.44 Hz		20.45 Hz	
Motion:	Amplitude	Phase	Amplitude	Phase	Amplitude	Phase	Amplitude	Phase
Case	1.0 mm	0°	1.0 mm	0°	1.1 mm	0°	1.1 mm	0°
Piston	1.4 mm	155°	1.21 mm	156°	1.9 mm	139°	1.61 mm	131°
Displacer	6.4 mm	193°	6.17 mm	189°	8.1 mm	182°	7.31 mm	175.5°
Power to load	0.115 W		0.127 W		0.775 W		0.629 W	
$f_e \oint p_b dV_b$	0.504 W		0.384 W		0.603 W		0.502 W	
Power to 'unknown' D_{pc}	—		0.699 W		—		0.878 W	

6.4.2 Test BE16N27

This test whose parameters fell within the range of figure 6.12, was discussed in some detail in section 5.2, the purpose being to illustrate the techniques used in the experimental analysis, rather than for the sake of the specific test. As the test falls within the somewhat atypical group requiring the 'unknown' damping between the case and piston, it has not been selected for similar special treatment in this chapter. However, it was simulated reasonably successfully, using the same approach as described to generate the data in figure 6.12. Some of the key results are therefore compared with the experimental results in table 6.2.

6.5 Simulation of series BE19N tests

These tests were conducted using helium as the working fluid, and with the engine spring and mass parameters being similar to those for the series BE09N air tests. Significant non-sinusoidal motion of the case, and the work- and bounce-space pressure waves was noted in the experimental work. The engine was thus operating in a manner which would not be suitable for analysis using the linear analysis technique. However, as a test to see whether the simulation programme could at least give some idea of the expected motion of the engine under these conditions, a series of simulations were carried out at a constant case amplitude, but under the range of conditions used in the experimental work: namely with the case–ground spring (K_{cg}) being varied from 12 000 N/m to 20 000 N/m for the four different conditions presented by the combinations of two different case masses (1.02 kg and 1.57 kg) and two different mean pressures (126 kPa and 162 kPa).

Figure 6.13 shows the engine frequency, plotted as a function of the rigid body natural frequency. As for the experimental data, the frequency of oscillation

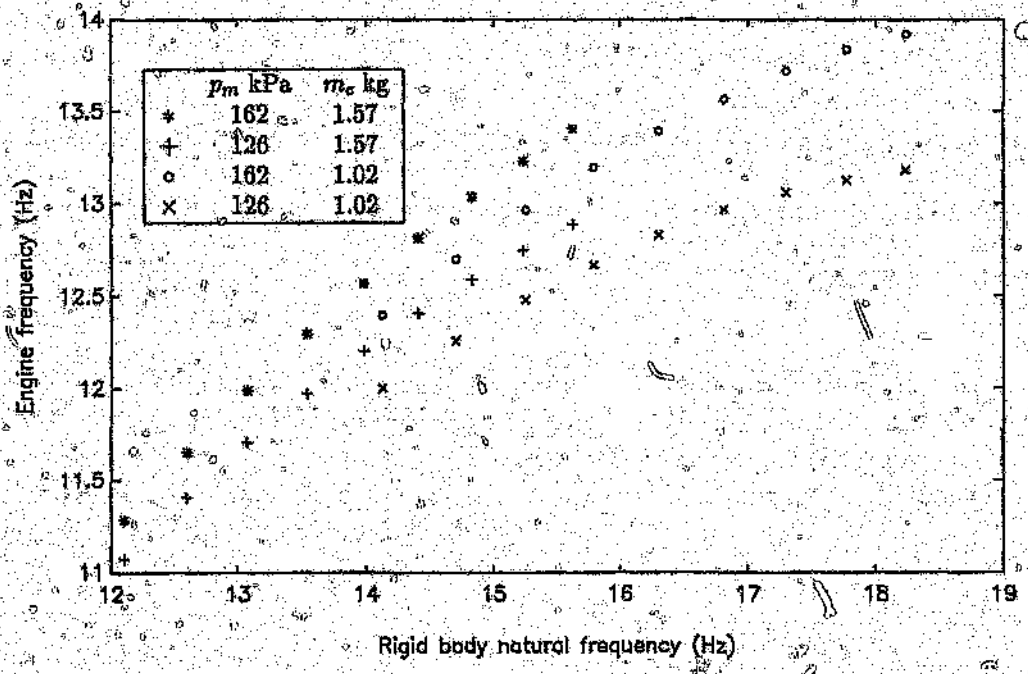

Figure 6.13: Series BE19N simulation: Engine frequency versus rigid body natural frequency

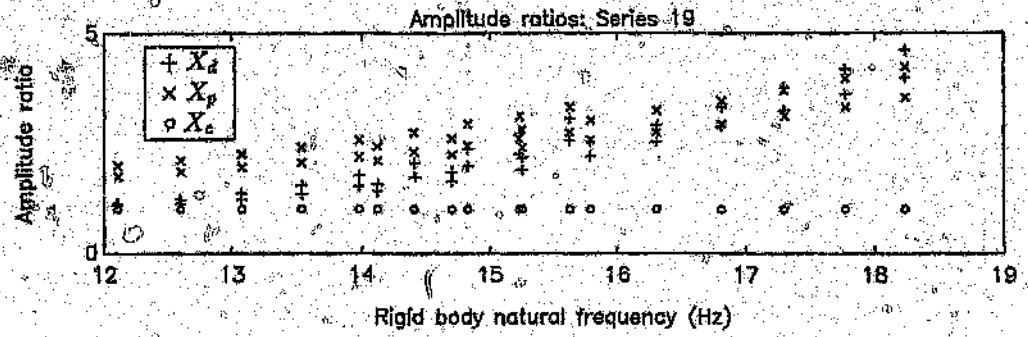

Figure 6.14: Amplitude ratios ($|X_d/X_c|$), ($|X_p/X_c|$) versus rigid body natural frequency

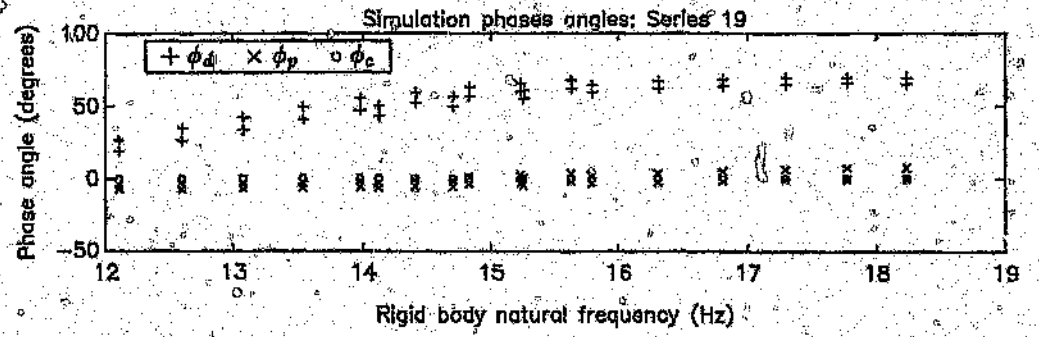

Figure 6.15: Series BE19N simulation: Phase angles

of the engine increases gradually with increase in K_{cg}. An increase in charge pressure also results in an increase in oscillation frequency, as does a reduction of the case mass. Figure 6.14 shows the piston, case and displacer amplitudes as a function of the rigid body natural frequency. Note the significant rise in displacer amplitude as the engine frequency is increased, indicating that the frequency of oscillation is approaching the natural frequency of the displacer. A corresponding rise in the displacer phase angle is evident from figure 6.15. This behaviour was not as apparent in the experimental work, (see figures 5.34 and 5.35), although within the clumps of data corresponding to each test the data did show a similar rise towards the right.

Nevertheless, the simulation results do give a rough indication of the operating mode of the engine, the phases, and frequency of operation of the simulation and experimental data being in the same region. Thus, even if there are significant nonlinearities in the behaviour of the engine, the simulation would still be a useful tool for design analysis.

6.6 Summary

The 3-D SAUCE programme, as applied to the Model B-10 engine, predicts the general behaviour of the engine quite well. Response to variation of the major parameters (charge pressure, hot end temperature, displacer and case spring stiffness, case mass and load) are similar to those noted in the experimental work. This was particularly encouraging when one considers the considerable ranges over which the parameters and operating conditions were investigated. However, the required fudge factors imply that there are severe problems, particularly with respect to the estimation of dissipation in the bounce space, and flow loss through the regenerator. As discussed in appendix D the small size, and inadequate refinement of the experimental rig and instrumentation made detailed investigation of these losses impractical.

Chapter 7

Closure

7.1 Conclusions

7.1.1 3-D linear dynamics simulation of free-cylinder Stirling engines (3-D SAUCE)

The linear dynamics portion of the SAUCE computer programme to simulate Stirling engines has been successfully expanded to allow the analysis of free-cylinder Stirling engines. The linearized equations of motion are utilized in a general form, without requiring the assumptions of either negligible piston motion [57], or of negligible case-ground spring stiffness [44]. The resulting programme produces results which compare moderately well with a wide range of experimental results, collected from two quite different free-cylinder Stirling engines.

The modified computer programme proved to be well behaved, in that convergence usually occurred within twenty iterations of the modelling cycle, the entire process to simulate the engine at a particular operating point taking between 20 and 60 seconds on a 486 DX class IBM compatible computer (the programme running in an interpreted BASIC environment).

The approach adopted for the linear analysis allows one to use the full set of linearized coefficients of the equations of motion, thus facilitating the generation of complete, balanced force vector diagrams for each component (section 3.6.3). Furthermore, although tractable equations yielding oscillation criteria could not be obtained, the roots of the characteristic equation for a particular configuration are available during the simulation process. This allows the quick

development of root maps, from which stability, frequency and behaviour under varying conditions can be deduced (section 3.6.2 and 6.3).

7.1.2 Sunpower prototype free-cylinder Stirling engine

Performance of this engine was disappointing. This was due in part to the condition of the seal surfaces, difficulties experienced in aligning the engine, the adverse effects of the instrumentation on heat transfer and friction losses in the engine, and limitations of the experimental equipment used to test the engine. However the motion, pressure and load force data gathered, provided a useful insight into the behaviour of free-cylinder Stirling engines. The results also provided an important reference against which the 3-D SAUCE simulation could be compared.

The predicted performance of the engine at higher amplitudes than those tested is promising, with a estimated power output of over 300 W and efficiency (excluding the burner) of better than 20%. This indicates that the engine does have considerable potential, if the difficulties mentioned above can be overcome.

7.1.3 Model B-10 Demonstrator engine as a free-cylinder Stirling engine

Although the experimental rig developed using this engine had some severe drawbacks (particularly with respect to reliability and accuracy of measurements and in the determination of friction losses), the engine did provide a wealth of data over a wide range of operating conditions. This was important as it allowed validation of the computer simulation technique over the same broad range of conditions. The engine demonstrated some unusual operating modes, highlighting the potential instability of free-cylinder Stirling engines (section 5.3.3). However, under most conditions the engine ran at a steady frequency, and with a well behaved response to changes in load. The ability of free-cylinder engines to naturally increase power output as the load requirement is increased, while maintaining or even increasing the amplitude of oscillation and holding a relatively constant frequency, was demonstrated both experimentally and in the simulations of this engine.

7.1.4 Free-cylinder Stirling engine as a power source for a rural water pump

Based on the experimental data, no firm conclusion can be reached regarding the suitability of the free-cylinder Stirling engine as the power source for a water pump in rural areas. The computer simulation work does however indicate that the engine may be a feasible power source. Although no attempt was made to develop and simulate an optimum design, the predicted performance of the Sunpower 'water pump' engine is reasonable, and the 3-D linear dynamics approach presented in this work should provide a powerful tool for the development of improved free-cylinder Stirling engine designs.

Some of the system components of a rural water pump have been considered. Other researchers have demonstrated the feasibility of biogas production, gas burners, and the induced flow type of water pump. Thus a system comprising a biogas digester, gas burner, free-cylinder Stirling engine and one of the water pump concepts seems practical. Self-starting of the engine has not been adequately explored, and it is thus unclear whether solar heating will be a practical option.

7.2 Recommendations for further work

7.2.1 3-D linear dynamics approach

A severe weakness in the work carried out here has been the lack of attention, both in the experimental work, and in the simulation, to the specific application of the flow, friction and leakage loss calculations to the engines studied. Existing material was simply applied in an attempt to obtain a broad validation of the linear dynamics technique. While that validation has been obtained, it has been limited. More complete validation will require that more rigorous investigation of the above loss mechanisms be carried out. This is unfortunately one of the difficulties inherent in work on a simple, low cost machine. Such machines will invariably have non-ideal seals and gas flow passages which are not exactly shaped (and perhaps not identical from machine to machine). This makes exact experimental and analytical work difficult, if not impossible.

As with almost any computer programme, there is room for continuous improvement of the 3-D SAUCE code. If the SAUCE system is to be developed further, it is strongly recommended that a more suitable language be chosen, as

the current implementation of 3-D SAUCE is approaching the size limitations of the QuickBasic environment. A significant reduction in the time required for a simulation could also be achieved by using a language such as 'C'.

The generalized treatment of the matrix equations of motion presented here should facilitate the application of the coupled linear analysis – second order thermodynamic, heat transfer and flow loss simulation to other free-piston Stirling systems which have more than two moving masses (such as the duplex Stirling machine [40]).

7.2.2 Free-cylinder Stirling engines

The logical continuation of this work would be to design and evaluate a new free-cylinder engine. Recent developments in free-piston Stirling engine technology should be easily transferable to free-cylinder engines, allowing the mechanical difficulties experienced with the 'water pump' engine to be overcome at a reasonable cost.

An updated system design and costing exercise on the free-cylinder engine as part of a complete water pumping installation is also required.

These steps at least are necessary before the free-cylinder Stirling engine may be relegated to the long list of promising Stirling ideas that have not quite achieved commercial realisation.

Appendix A

Instrumentation: 'water pump' engine

A.1 Displacement transducers

A.1.1 Case motion

Transducer type:	Linear Variable Differential Transformer (LVDT)
Manufacturer:	Instron Ltd., England

Calibration procedure

The position of the case was measured using a vernier calliper at various points over its range of motion. These measurements were correlated with voltage measurements from the computer-scope. The LVDT was calibrated once near the beginning of the series of tests reported, and once near the end. The calibration factor used was the mean of both these figures.

	mm/V	Correlation coefficient
First calibration:	1.586	0.999891
Second calibration:	1.556	0.999652
Factor used:	1.571	

A.1.2 Displacer and piston motion

Transducer type:	FASTAR FS1000 with SP100 signal processor (fast linear displacement transducer)
Manufacturer:	Sunpower Inc., later items manufactured by Data Instruments Inc. (Instrument design unchanged)
Range:	60 mm
Calibration factor used:	10mm/V

Calibration procedure

These instruments deliver a DC signal proportional to the position of a slug within an inductance coil. Calibration was performed with the transducer installed in the engine. The position of the piston or displacer relative to the case was measured using a vernier calliper, and this correlated with the voltage as recorded by the computer-scope card. Repeated calibration at various times during the test procedure yielded a calibration factor within 1.5% of that quoted by the manufactures, and a correlation factor better than 0.9998. The manufacturers data indicate a flat response at frequencies for 0 to 12 kHz. Thus the nominal calibration factor of 10 mm/V, coupled with the resolution of the computer-scope card (section A.4), yielded a resolution better than 0.1 mm. Due to minor variations in the length of the coupling rod between the transducer and the component, the absolute value of the displacement for any given voltage varied as the engine was assembled and re-assembled many times during the test period. Thus the offset value as determined by the above mentioned calibration procedure was changed when appropriate.

A.2 Force between case and ram

Transducer type:	Strain-gauge dynamic load cell
Manufacturer:	Instron Ltd., England
Range:	± 5 kN
Calibration factor used:	603.6 N/V

Calibration procedure

The load cell was calibrated using mass pieces placed on the transducer such that the load cell was placed into compression by the mass pieces. The results obtained were not very satisfactory, as the output from the transducer fluctuated due to a vibration from the hydraulic ram. The calibration factor obtained was 630 N/V. A previous undergraduate research project yielded a figure of 584 N/V. Due to the uncertainty of this author's procedure, a compromise calibration factor, the mean of the above two, was used throughout the tests. This is within 5% of the above two factors, and thus the error in the force measurements is of this order. However, it was felt that this was satisfactory, as the primary objective of the experimental work was to determine trends rather than absolute values.

A.3 Pressure transducers

A.3.1 Bounce-space pressure

Transducer type:	Kistler 603B piezoelectric pressure transducer
Manufacturer:	Kistler Instrumente AG
Range:	0–150 $\times 10^5$ Pa
Calibration factor used:	Varied through test series: Approx 1 $\times 10^5$ Pa/V

Calibration procedure

The Kistler transducer could be mounted in a dead weight tester. The crystal charge decay time was sufficiently slow to allow static calibration of the transducer, amplifier and computer-scope card as a complete unit. The amplifier has a vernier scale setting which was sometimes varied if the instrument was used for other experimental work. Thus the system was calibrated at various stages during the experimental work, and different calibration factors used accordingly. Typically an extremely linear curve with a correlation coefficient of 0.9994 or better was obtained.

A.3.2 Work-space pressure

Transducer type:	PCB Model 113A26 piezoelectric pressure transducer
Manufacturer:	PCB Piezotronics Inc.
Range	0–500psi [0 – 34.5×10^5 Pa]
Calibration factor used:	6.813 $\times10^6$ Pa/V

Calibration procedure

The transducer could not be calibrated satisfactorily as the crystal charge decay time was too rapid for the above described static calibration method. A dynamic pressure transducer calibration system was not available. However, the calibration curve supplied with the instrument was deemed satisfactory for the purposes of this work (see section 4.1.2).

A.4 Computer-scope card

Type:	ISC-16 Computerscope card
Manufacturer:	RC Electronics Inc.
Range:	$\pm$ 10 V
Resolution:	5 mV
Maximum sampling rate:	125 kHz (8 channels)

A.5 Temperature measurement

During the 'water pump' engine tests reported, the thermocouples were read directly using either digital multimeters, or using a Fluke data logger. An ice-point cold junction was not used as the Fluke data logger was equipped with temperature compensated inputs for thermocouples. When digital multimeters were used then the temperature of the cold junction was measured with a mercury thermometer so that the readings could be compensated accordingly.

Appendix B

Apparatus and methods: Model B-10

B.1 Apparatus

B.1.1 Model B-10 engine

Please refer to figure B.1 and section 5.1.

B.1.2 Engine heat source

The engine was heated using an electrical resistance heater, manufactured by winding nichrome wire around the top portion of the case. A thin layer of 'fiberfax', a ceramic wool, was used between the wire and the engine to electrically insulate the heater from the engine. A thicker layer of the same material was used on the outside for thermal insulation of the heater. Two thermocouples were bound between the heater coil and the engine, thereby allowing measurement of the wall temperature. The output from one of the thermocouples was used as the feedback to a set-point controller, which rapidly turned the heater element on and off as required (using a triac semi-conductor switch). Thus the external wall of the heater could be held at any desired temperature under variable load conditions.

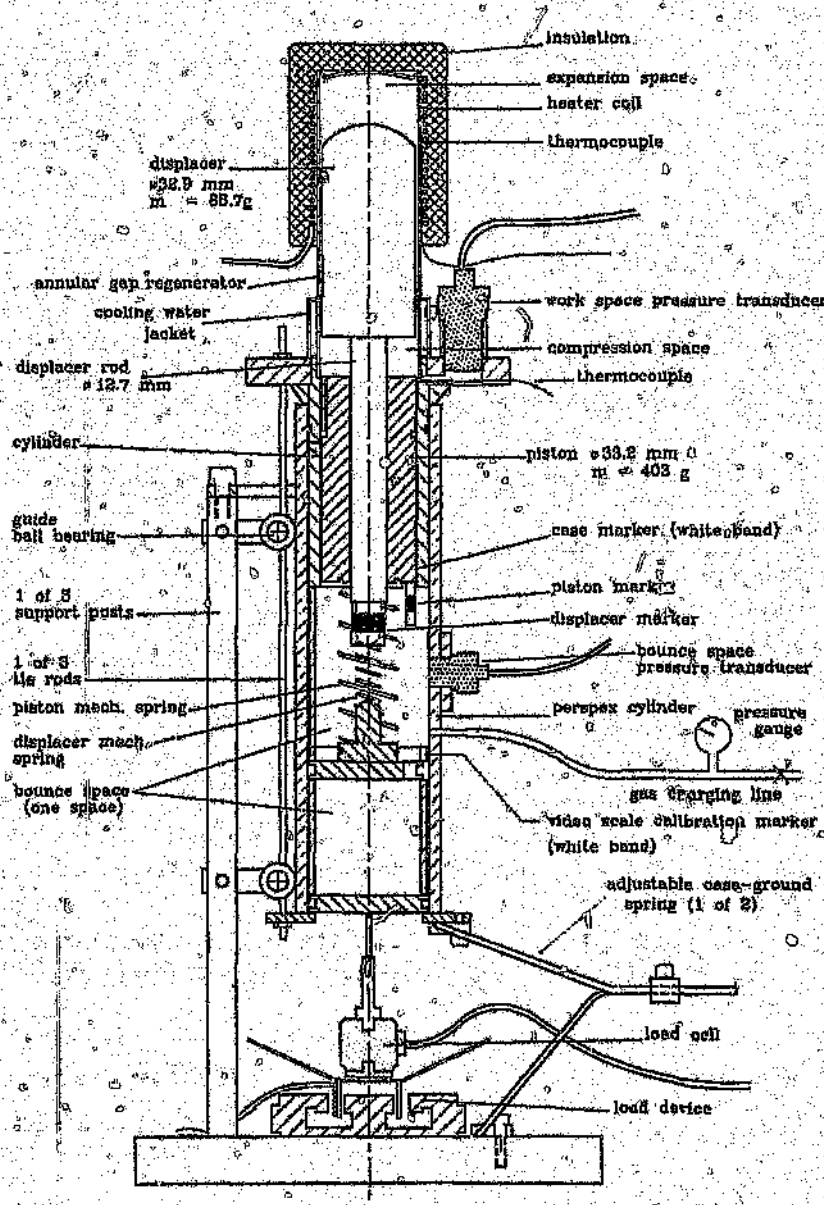

Figure B.1: Engine and instrumentation

B.1.3 Cooling

The Model B-10 was supplied with a small brass water jacket around the cooler portion of the cylinder. Water was circulated through this to achieve the necessary cooling of the engine.

B.1.4 Load device

A simple load device was constructed by using a 20 W automobile loud speaker connected to a negative impedance circuit. This allowed electronic variation of the load. Unfortunately, the capacity of the system was lower than the maximum power output of the engine. Thus, at times the engine was manually loaded, as described in section 5.2.

B.1.5 Mechanical springs

The Model B-10 engine has a mechanical spring between the case and displacer, between the case and piston, and in the modified version used here between the case and ground. The spring stiffness of all three was checked at various stages during the test period, the stiffness being reported in chapter 5. The case spring was calibrated 'in situ', by resting objects of known mass on top of the engine, and measuring the resulting displacement using a vernier calliper. The piston and displacer springs were calibrated separately from the case. The spring support was set directly onto an electronic scale, and then either the piston or the displacer (depending on which spring was being checked) was clamped in a retort stand, thereby compressing the spring. By varying the clamp position a table of displacement versus apparent mass could be drawn up, from which the spring stiffness could be calculated.

The stiffness of all three springs could be easily varied, although for the work carried out here, only the displacer and the case–ground springs were changed. The piston spring stiffness did vary slightly, but this was due to changes in attachment details rather than by design.

Typical curves of the spring stiffness checks are shown in figures B.2, B.3 and B.4.

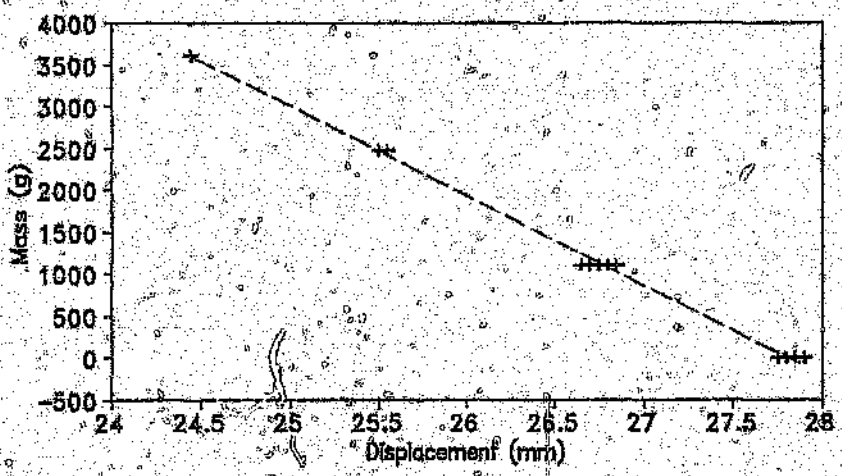

Regression Output:		
Constant	29819.57	g
Std Err of Y Est	62.06285	
R Squared	0.997976	
No. of Observations	18	
X Coefficient	-1072.37	g/mm
Std Err of Coef.	12.07211	
Spring stiffness	10500	N/m

Figure B.2: An example of the data from a case-ground spring stiffness check

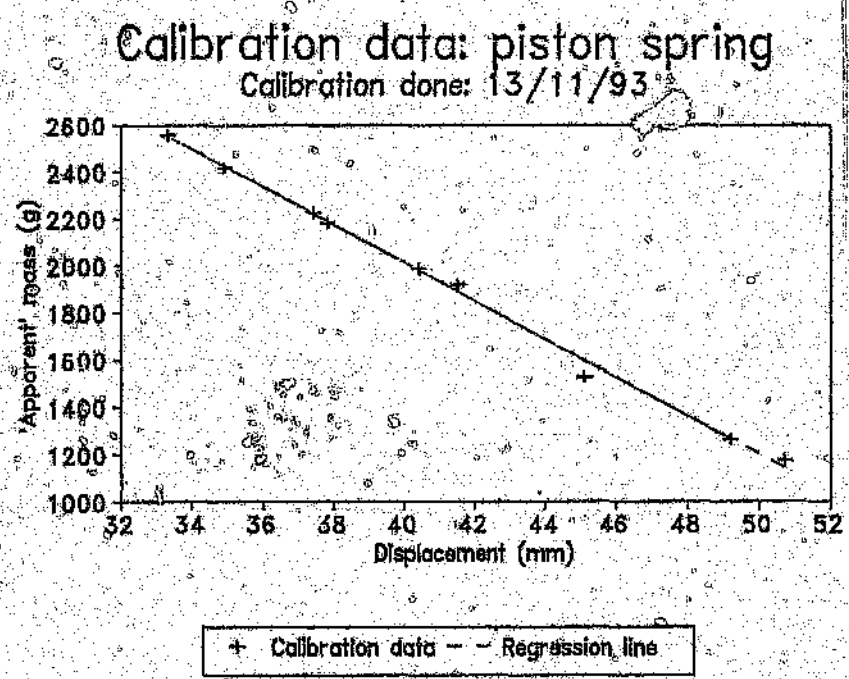

Regression Output:		
Constant	5253.676	g
Std Err of Y Est	31.9841	
R Squared	0.996355	
No. of Observations	9	
X Coefficient	-81.1122	g/mm
Std Err of Coef.	1.854408	
Spring stiffness	794	N/m

Figure B.3: An example of the data from a piston-case spring stiffness check

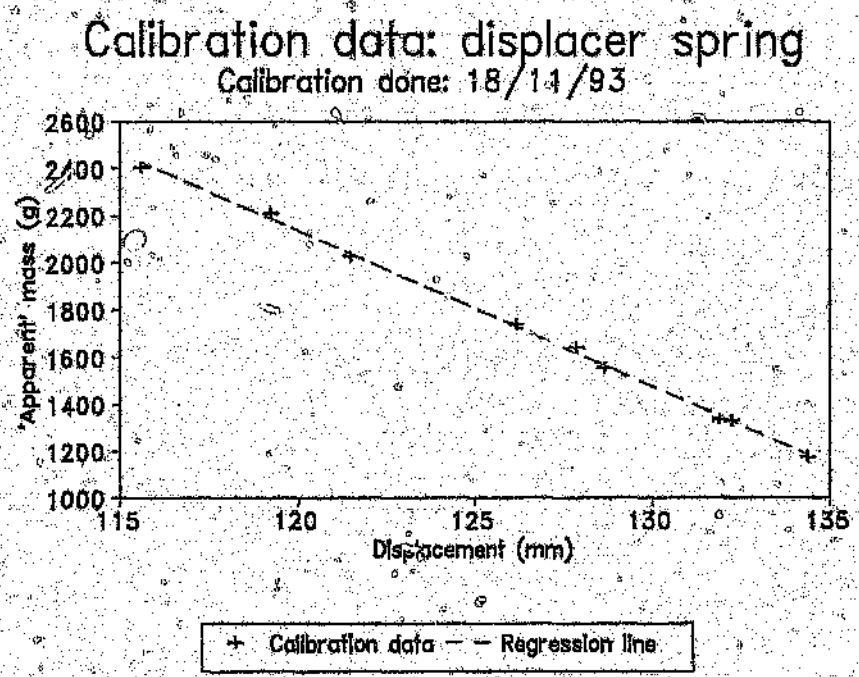

Regression Output:		
Constant	10077.53	g
Std Err of Y Est	17.78833	
R Squared	0.99846	
No. of Observations	9	
X Coefficient	-66.1785	g/mm
Std Err of Coef.	0.98246	
Spring stiffness	648	N/m

Figure B.4: An example of the data from a displacer-case spring stiffness check

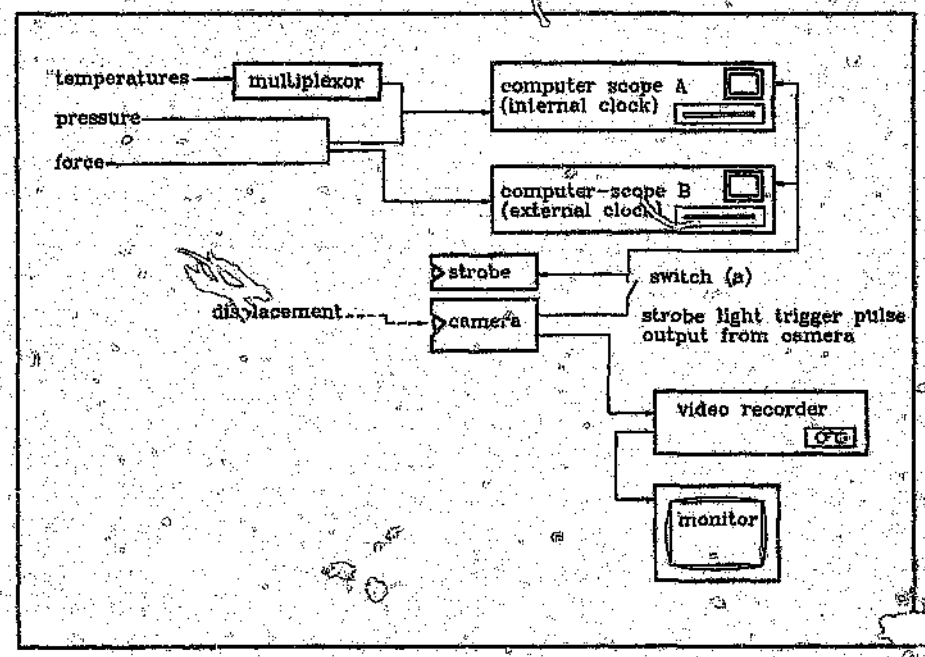

Figure B.5: Instrumentation block diagram

B.2 Instrumentation

Figure B.5 shows the instrumentation layout in a block diagram form. Sub units are described below.

B.2.1 Motion data

In previous Stirling engine work at the University a variety of instruments have been used to record the motion of engine components. These have included linear variable differential transformers (LVDT) and capacitance transducers, as well as the Fastar transducers used on the 'water pump' engine. Both the LVDT and the Fastar transducers require that a slug be attached to the moving components, such that it passes through a pickup coil. Although a Fastar transducer has been successfully attached to the B-10 engine displacer in the past [33, 56, 17], the mass of the transducer and friction losses between the slug and the coil housing did result in impaired engine performance. For these undergraduate student projects the piston motion of the B-10 engine was recorded by surrounding the piston with a thin metal sleeve, attached to,

but insulated from the case, and then measuring the capacitance between the piston and the sleeve. This also worked satisfactorily, although it did involve the addition of mass to the case. Measurement of case motion was not required for the above work. In 1991 a new method was tried, that of ensuring that all components of the engine were visible, and then recording the engine motion during operation using a video camera and recorder. Subsequently image processing was used to obtain numerical information on the engine operation. Greig [26], using a 50 Hz video camera and a Panasonic time lapse cassette recorder, demonstrated the potential of the system during his final year BSc (Eng) project. As the system is non-intrusive, and requires only that clearly visible markers be attached to the engine components, it has clear advantages over the more traditional techniques. However the slow sampling rate does require that engine operation be steady, to enable a composite picture of engine motion to be developed over a number of cycles. Furthermore, precise synchronization of the video data, and the other parameters such as pressure, which were recorded using conventional means, is difficult. As will be discussed below, the image processing required to obtain numerical rather than visual information also proved difficult and time consuming.

For the work presented here a specially modified camera was hired from the CSIR[1]. The camera – time lapse cassette recorder combination records 50 frames a second. However, each frame is divided into four approximately equal subframes (referred to here as fields, see figure B.6). Timing and data storage circuits within the camera allow the recording of information for each field to be sequential, and to cover the same field of vision. There are thus approximately 200 fields per second, an effective sampling rate of 200 Hz. Higher sampling rates were possible, however the image size and quality deteriorated as the sampling rate was increased. The camera shutter speed was fixed, and relatively slow. It was therefore necessary to freeze the engine motion using a strobe light. The camera was equipped with a strobe trigger pulse output, which was used to drive a gas discharge strobe. Thus the motion data was recorded at intervals defined by the camera strobe trigger output. This output was used to synchronize and control the entire data recording, as described below.

It will be noted from figure B.6 that the engine appears to be on its side. This is because the camera was rotated through 90° in order to fit the important engine components into the narrow rectangular fields. The engine operated in the vertical position at all times.

[1] CSIR, P O Box 395, Pretoria, 001

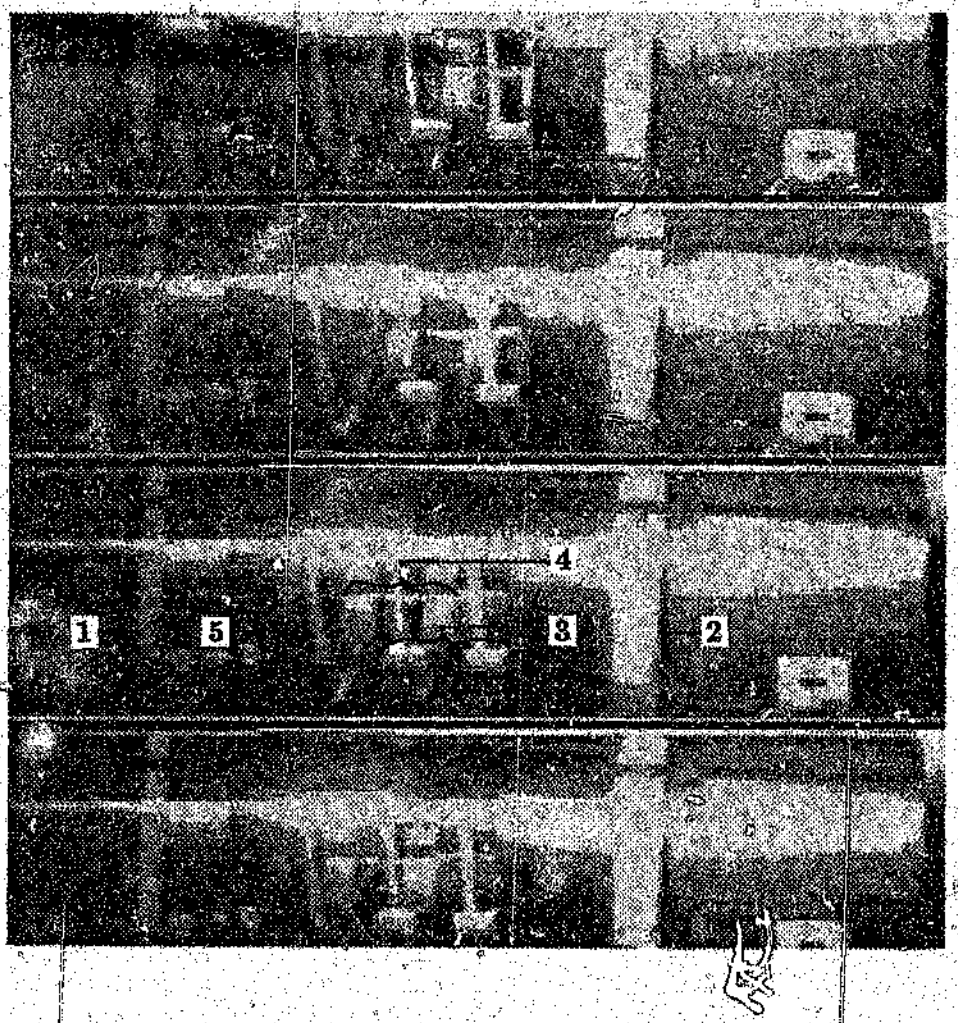

Figure B.6: A typical video frame, showing the composite image produced during $\frac{1}{50}$ of a second

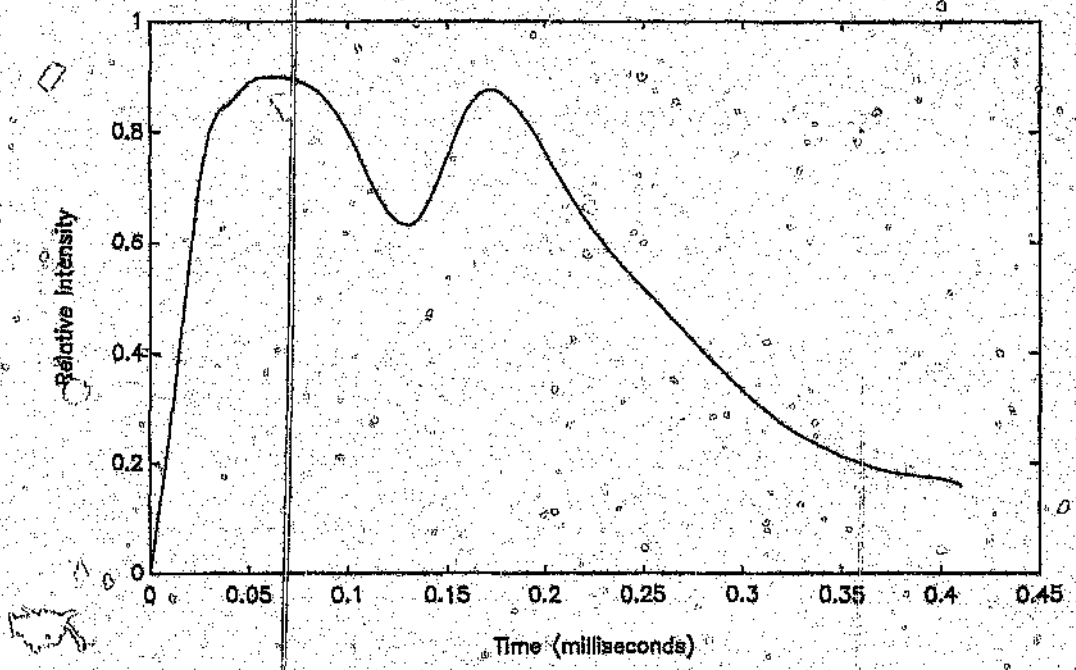

Figure B.7: The strobe light pulse intensity as a function of time

Image quality

The video camera and associated gas strobe light had some limitations. Firstly, the time delay between consecutive strobe trigger pulses was not even. The interval between the first two trigger pulses (1 – 2) of each frame was longer than that between pulses (2 – 3, 3 – 4 and 4 –1). This complicated analysis of the final data set as discussed below. Secondly, the light pulse emitted from the strobe was not of sufficiently short duration to freeze the engine motion during tests when high component velocities were reached. This resulted in ghost images being produced, making reliable tracking of the markers difficult. A trace of the strobe output was produced using a light sensitive transistor, coupled to a digital storage scope. A hand tracing of the signal so produced is shown in figure B.7. From this it can be seen that maximum light intensity was only reached at some time after the initiation of the strobe trigger. The net result was that the component position was recorded approximately 0.1 ms after the leading edge of the strobe trigger pulse.

B.2.2 Pressure transducers

Both work- and bounce-space pressure transducers were of the Kistler piezoelectric type 603B. See section section A.3.1 for a description of the calibration procedure used.

B.2.3 Force transducer

The force between the engine and load was measured using a piezoelectric load cell, manufactured by PCB Piezotronics Inc. Although the signal from these instruments decays with time, the rate of signal decay was sufficiently slow that a simple calibration of the entire system could be carried out. Mass pieces were placed on the transducer, and then rapidly lifted, the resulting step in the output corresponding to the force exerted by the mass.

B.2.4 Temperature measurement

Temperature measurement was carried out using type K thermocouples. As described earlier, the heater temperature was monitored using two thermocouples, sandwiched between the heater coils and the wall of the engine. A third thermocouple was placed immediately above the cooling water jacket, while the fourth was inserted into the work-space volume, so that it lay within the work-space pressure measurement port. Each thermocouple signal was individually amplified using a dedicated integrated circuit (chip) with on-board cold junction compensation. The output from these chips, at a nominal value of 10 mV/°C was then multiplexed, such that it could be read as a single stream of data by computer-scope A.

B.3 Data capture

Three different recording devices were used simultaneously in order to record engine operation, as shown in figure B.5. A VHS video recorder stored the video camera output onto video tape, for subsequent translation as described below. A computer-scope card (A) of the type described in section A.4 was used to record the following information:

Channel No.	Measured value
1	Force transmitted to load
2	Bounce-space pressure
3	Work-space pressure
4	Multiplexor (temperatures of hot end, compression space, top of cooler)
5	Strobe trigger pulses (for synchronization and timing)
6	Load device voltage (not used)
7	Video signal (helps to check on synchronization)

The card was configured so that it would record at least one full period of oscillation of the engine. A typical sampling rate was 50 kHz.

A second computer-scope card (B) was used to record the case force, bounce-space pressure and work-space pressure. The card was configured in the external clock mode, with the strobe trigger pulse being used to drive the sampling. Thus measurements of the pressure and force data were taken at almost exactly the same time as the motion data was recorded. (As noted above there was approximately 0.1 ms time difference between the two sets of readings.) The buffer length was usually set to allow either 10 or 40 seconds of engine operation to be recorded.

B.3.1 Synchronization of the recording devices

See figure B.5. Switch (a) on the strobe trigger output from the camera was used to initiate data capture. The switch was initially set to the open position. The computer-scopes were then set to the ready mode, waiting for a trigger pulse. The video camera and video recorder were set in motion, although no image was recorded as there was insufficient light. The start of data recording was then initiated by closing switch (a). This allowed the strobe trigger pulse to reach the strobe light, the recording initiation trigger input of computer-scope A, and the external clock input of computer-scope card B. The first such pulse therefore provided the first clear image on the video recorder, and initiated data recording by both computer-scope cards. Subsequent strobe trigger pulses synchronized image freezing and recording by the video camera and data capture by the computer-scope card B. Unfortunately switch closure sometimes occurred during a strobe trigger pulse, rather than between a pulse. The first pulse to reach the strobe and computer-scopes was therefore sometimes incomplete. Furthermore switch bounce sometimes resulted in the leading edge of the first pulse being very noisy. This resulted in added complication of the data synchronization process which will be discussed in section B.4.4 below. If a similar system is to be used in the future it would

be advisable to use a logic circuit to ensure that switch closure is clean, and occurs in the lull between two trigger pulses. This would ensure that all three devices initiate data recording clearly and in synchronization.

B.4 Routine data processing

B.4.1 Translation of the video data

Before the motion data could be analyzed it was necessary to translate the visual information into a digital form which could be integrated with the other data and analyzed numerically.

The video cassette was mounted in a time lapse video cassette recorder/player. This was equipped with a remote frame advance control, so that the images could be analyzed on a frame by frame basis. The signal for each frame was stabilized using a time base corrector and then fed to a Data Translation DT2853 low cost frame grabber card mounted in a 286 (AT) computer. The software supplied with the card allowed the digitization of each video frame. A 512 by 512 pixel array was used to represent the video image, with a pixel value between 1 and 256 being assigned to each element of the array. The pixel value gave an indication of the intensity of the image (0 being black, 256 being bright white) at each point. This digital information was then analyzed numerically to locate the piston, case and displacer markers.

Figure B.6 shows a typical image as grabbed by the card. The contrast between different elements of the image was not very high, and the markers attached to the objects of interest could not always be easily isolated from other visual images. For both the piston and the case, the search procedure was relatively simple. A search band was specified within the video frame, and then groups of pixels were examined within this region, as shown in figure B.8. Pixel values were averaged across the width of the search band to yield an image brightness value β_i as a function of pixel position i in the x plane only. A search direction was specified (ie, left to right or right to left). A required change Δ in the mean pixel brightness was then specified, as well as the sense of this change, ie, from white to black ($\lambda = 1$), or black to white ($\lambda = -1$). The average pixel values were examined, and the first occurrence of a contrast greater than or equal to that specified was taken as the location of the object marker. In order to avoid picking out objects of only one or two pixel width the average pixel brightness values were compared in sets of six or more. For example, if a left to right search were in progress, then the following criterion had to be met in

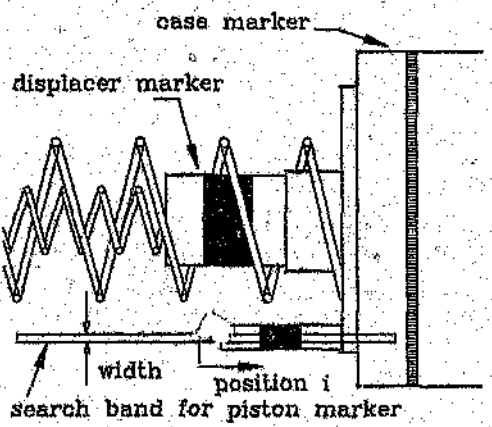

Figure B.8: Piston search band on the video image

order to locate the edge of an object marker.

$$[\Delta < \lambda(\beta_{i+1} - \beta_{i-2})] \cap [\Delta < \lambda(\beta_{i+2} - \beta_{i-1})] \cap [\Delta < \lambda(\beta_{i+3} - \beta_i)] \quad \text{(B.1)}$$

The value of i which first satisfied the above criterion was then recorded as the assumed position of the object marker edge. If no suitable value was found then the search was repeated, with a lower value of Δ. However, if after the second search no edge was found, then a recognisable error value was assigned to the marker position for that reading.

The displacer tracking was more difficult as the displacer marker was inside the piston spring coils. These showed up as bright white lines, obscuring the edge of the displacer marker at times. The displacer marker comprised two white bands, separated by a black band. This allowed comparison of the entire marker with a known predetermined map of the displacer marker, a form of object recognition. The speed of the available computer made full image comparison techniques impractical, thus the following search procedure was developed. All transitions from black to white, and from white to black within a search band were located in a manner similar to that described above for the piston and case. In figure B.9 the points marked a to j would have been located. These points then formed possible keys onto which a map of the known displacer marker could be superimposed, saving the time which would have been required if the map had been superimposed using each point i as a key. The best fit of the map onto the video image was then determined by using the map as a filter. All pixel values of the video image falling within the area of the white bands of the map were summed yielding a total brightness for each possible key position. The position yielding the maximum brightness was then selected as the assumed displacer marker position. In the case of

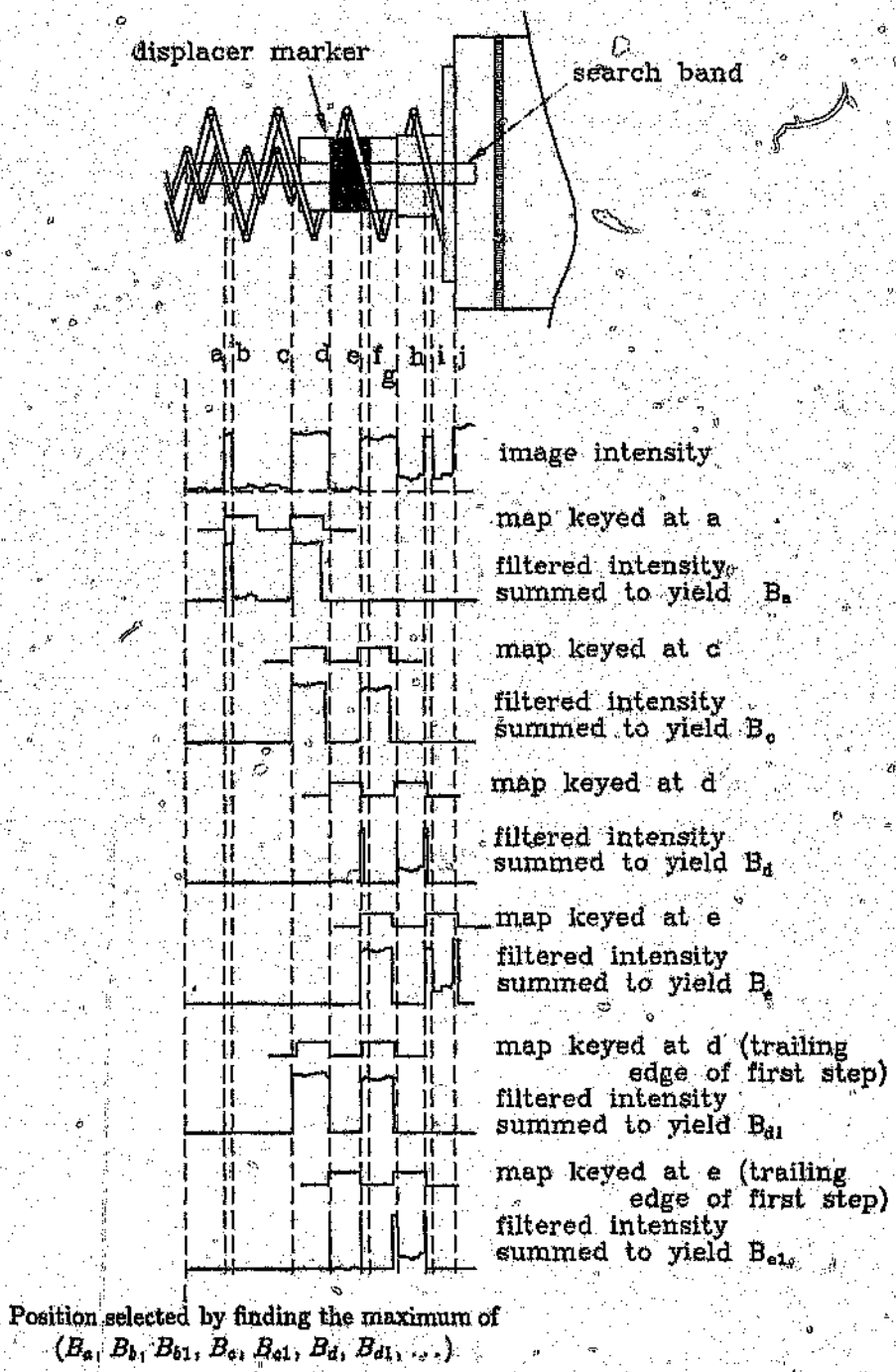

Figure B.9: Displacer search algorithm (examples of possible keys)

reasonably clear images it was not necessary to test all possible positions. If a particular key yielded a brightness which exceeded a predetermined threshold then further tests of the other possible key positions were not considered necessary.

Once all four fields of the video frame had been tracked the video recorder was advanced by one frame (using a relay switch driven by the processing computer) and the next frame could then be processed. The data for each test was stored as an ASCII file, allowing integration into the data processing software. Tracking time was approximately one minute for each second of recorded data. The system worked reasonably well. Tracking errors were variable, depending on the quality of the video image, and the velocity of the engine components.

Scale factors

The above tracking yielded a relative position for each of the component markers in pixels. It was therefore necessary to obtain a conversion factor from pixels to millimetres for each test. To do this video-calibration data was translated for each test. The positions of both a white band just above the piston and displacer spring support (ie, fixed to the case - see 'video scale calibration marker' in figure B.1) and that of the normal case marker were tracked and recorded for each field of one video frame of each test. As the distance between these two markers was constant, and known for all the tests, it allowed direct calibration. The engine mounting and the camera positions did not vary during each of the five tests series. Thus, particularly as in some tests video-calibration data was difficult to obtain, average conversion factors for each test series were obtained using the calibration data from all possible tests within the series. A typical value for the resolution was 0.258 mm/pixel, and in the worst case the standard deviation was 0.75 mm over the calibration distance of 63.4 mm. It should be noted that the accuracy for all motion measurements was not as good as the above figures indicate. Image clarity and hence tracking success were not constant, and even depended on the particular position of the components during the oscillation cycle (See equation (B.3)).

B.4.2 Translation of the computer-scope data

The computer-scope data, stored in a non-ASCII format, was converted to the ASCII format. The same programme analyzed the multiplexor data (stored by computer-scope A), and extracted the voltage output of each thermocou-

ple amplifier. As high accuracy in the temperature measurements was not required, these were simply converted to degrees Celsius using the conversion factors supplied by the thermocouple amplifier manufacturers. The charge pressure, as read off the pressure gauge during the test, was also entered to the computer and stored with the temperatures as a secondary data file.

The above programmes were written in a variety of languages. However, once in an ASCII format the data was integrated and analyzed using programmes written in the *MATLAB* [2] environment.

B.4.3 Motion data conditioning

A variety of steps were necessary to achieve suitable data conditioning.

Location of the start of the data set, and determination of the field number at which this occurred

In order to ensure that the first strobe pulse (ie, the first clear image of the engine) in a test was included in the data set a few blank fields were tracked prior to the first lit field of the video recording of each test. The starting point of the test then had to be located, as well as the field number at which this start took place. The start was relatively easy to find, as the tracking programme yielded a default 'wrong' value for the position of the components when the strobe was off, (ie, insufficient light). The next field after the start field was taken as the new 'first data point', or synchronization point, just in case the switch was flicked halfway through a strobe pulse resulting in poorly defined data for the first pulse. The field number (1–4) in which this 'first data point' was recorded was noted for later use when synchronizing the computer-scope data.

Isolation of known tracking errors

Specific motion data values which were obviously out of kilter with the bulk of the data set could sometimes be identified. These indicated erroneous tracking, and various techniques were used to isolate the incorrect data and nullify its effects.

The most easily identified erroneous data points were those with a value of 512,

[2] The MathWorks, Inc. 124 Foxwood Rd., Portola Valley, CA 94025

signalling that the tracking routines had been unable to locate any suitable component marker position. However in many cases the routines did pick up an area of the image which satisfied the search criteria, but which did not represent the actual position of the component marker. Often these points fell beyond a 'reasonable amplitude' from the mean, and could thus be thrown out on that basis (This 'reasonable amplitude' was determined by trial and error). The indexes of these points were noted, and their values were substituted by that of the data point immediately preceding each erroneous data point. This substitution was only used for the next routine discussed. Erroneous data points were omitted by all other routines.

Normalization of field means

Due to differences in image quality in the four different fields of the video frame, the tracking criteria for each field were not necessarily identical. Thus, even when the engine was stationary, the tracking routine determined slightly different positions for each component in each of the different fields. However, the differences were reasonably constant from frame to frame. For example, if $x_{k,1}$ refers to a measurement taken from frame k, field 1, and $x_{k,2}$ refers to a measurement from field 2 of the same frame, then $x_{k,1} - x_{k,2} \approx x_{k+i,1} - x_{k+i,2}$. As the number of data points collected was quite large (2000 for the shortest tests, representing approximately 140 cycles at the slowest frequency of engine operation) it was possible to account for these consistent differences between the four fields by normalizing all values from each of the four fields with respect to the mean value for the entire data set. Thus if $\bar{x}$ is the mean value for the entire data set and $\bar{x}_j$ the mean of all data collected from field j in each frame, then each data point $x_{k,j}$ was corrected as follows:

$$x_{k,j} = x_{k,j} - \bar{x}_j + \bar{x}$$

B.4.4 Synchronization

It now remained to determine the data points in the computer-scope data sets which corresponded to the above synchronization point in the motion data. As described above, the time delay between consecutive strobe trigger pulses supplied by the camera was not even. Examination of the delays between trigger pulses as recorded by the high sampling rate computer-scope card A therefore allowed one to assign field (not frame) indices to these trigger pulses. It was then a relatively simple matter to find the first trigger pulse in the computer-scope A data set which had the same field number as the motion data starting

field number (see section B.4.3 above). Furthermore, the times between the trigger pulses were noted, allowing the calculation of a time base for the entire data set. Thus the computer-scope A data, recorded at a high, fixed sampling rate, was used to measure the cyclic irregularities of the sampling rate used for the motion data and the computer-scope B data sets.

Computer-scope A and computer-scope B both monitored the same transducers on their channels 1 to 3. Thus, by comparing the values recorded by A at the data synchronization point, with those recorded by B near the start of the B data set, it was possible to locate the synchronization point for the computer-scope B data. For added security, the comparison between scope A and B was carried out over sets of three scope B samples.

All data sets were then stripped of data preceding the synchronization point, resulting in three new data sets, each with the same starting point. The motion data and that collected by computer-scope card B could be combined, as they now both contained data collected in synchronization. Further reference to 'the data set' implies this combined data set. A time base for the data set was then generated using the computer-scope A information about the strobe trigger pulse timing.

B.4.5 Least squares analysis

The net result of the above processes was a single data set for each test, containing information collected at approximately 200 Hz. This could be treated as an array $(7 \times n)$, where n referred to the number of samples taken, and the columns 1 to 7 contained the following information:

1. piston position
2. case position
3. displacer position
4. force measured between the case and load
5. bounce-space pressure
6. work-space pressure
7. time base for the data set.

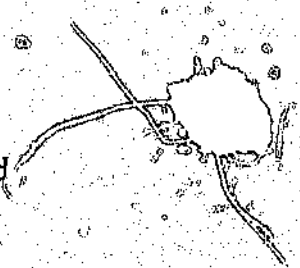

For the purposes of the general analysis the data set was broken up into segments of 1 second each. (Minimum test duration was 10 seconds, many tests

were run over 40 seconds). Thus each segment contained 200 data points for each variable. The work-space pressure measurements were then used to determine the frequency f of the engine during a segment. This was achieved by determining the constants A, $\omega = 2\pi f$, ϕ and C of equation B.2 which yielded the minimum variance ϵ (the 'least squares approach'). An iterative method was used to determine ω and ϕ, while the amplitude A and the constant C could be calculated using equations B.4 and B.5. Note, in the equations below x_i refers to the i'th measurement in the data set, while t_i refers to the time at which this measurement was taken ($t_1 = 0$).

$$\Sigma\Delta^2 = \sum_{i=1}^{n}[x_i - A\cos(\omega t_i + \phi) - C]^2 \tag{B.2}$$

$$\epsilon = \sqrt{\frac{\Sigma\Delta^2}{n-1}} \tag{B.3}$$

$$\Sigma\lambda = \sum_{i=1}^{n}\cos(\omega t_i + \phi)$$

$$\Sigma\lambda^2 = \sum_{i=1}^{n}\cos^2(\omega t_i + \phi)$$

$$\Sigma x = \sum_{i=1}^{n} x_i$$

$$\Sigma\lambda x = \sum_{i=1}^{n} x_i\cos(\omega t_i + \phi)$$

$$A = \frac{\Sigma\lambda\Sigma x - n\Sigma\lambda x}{(\Sigma\lambda)^2 - n\Sigma\lambda^2} \tag{B.4}$$

$$C = \frac{\Sigma x - A\Sigma\lambda}{n} \tag{B.5}$$

The frequency was then held constant and the amplitudes A, phases ϕ and mean values C of the remaining 5 measured parameters were calculated using the same least squares method. It is important to note that the above method of analysis is not affected by irregularities in the time base, as long as these irregularities are recorded in the time base vector t. This would not have been the case with a fast-Fourier transform analysis. It was also possible to exclude data points determined as being erroneous from the analysis, simply by removing them from both the data set x and the time base t before passing to the least squares analysis subroutine.

The motion data set was then screened once more, this time using the above determined coefficients to predict x_i values for each t_i value. Any data points

further than a specified limit from the predicted value were regarded as erroneous values. The data was then reanalysed using the least squares analysis routine. Thus the data set used in the final analysis was relatively free of errors caused by poor tracking.

If the variance ϵ was low, relative to the amplitude of oscillation this indicated that the engine operation was reasonably constant over the segment period, and that the assumption of sinusoidal motion was fair. If the engine motion was not sinusoidal, or if changes in operating condition took place during a segment, then a high value of the variance was recorded. If the test was of sufficient interest, the segment length could be reduced in order to allow changes in operating condition to be investigated.

The routine data processing therefore provided a sinusoidal approximation of the collected data, as well as an estimate (the variance ϵ) of the validity of this approximation. As the linear dynamics approach to free-cylinder Stirling engine analysis also assumes sinusoidal motion of the engine components and sinusoidal variation of the forces acting on those components, the majority of the results of the experimental work are presented in this form. However, the frequency information alone allowed superimposition of original data from a number of cycles onto one cycle. This facilitated either graphical or numerical analysis of the data, without requiring the assumption of sinusoidal motion.

Appendix C

Computer simulations

C.1 Engine data

Note: The data presented below is in the format of a matrix as used in the computer programme. The data matrix is an extended and slightly modified version of that used by Berchowitz [13, pg 396]. Units are as follows:

Description	Units
Linear dimensions	m
Area	m^2
Volume	m^3
Temperature	Kelvin
Frequency	Hz
Angles	degree
Thermal conductivity	W/mK
Friction coefficient	Dimensionless
Damping coefficient	Ns/m
Spring stiffness	N/m

C.2 'Water pump' engine

This engine was simulated using the 3-D SAUCE programme, Version DB94.1. Table C.2 lists the input data to the programme. The cell labels are given in table C.1. The engine was simulated assuming adiabatic compression and expansion spaces, using the appropriate subroutine developed by Berchowitz (see section 3.2.2 for some further detail). Heat transfer and gas flow losses was modelled using the 'Sunpower' option, (see section 3.2.3). Fudge factors of 1

Table C.1: Matrix of input variables for computer code

–	1	2	3	4	5
1	charge pressure	cooler wall temperature	heater wall temperature	frequency	X_{pc} (initial value)
2	displacer mass	piston mass	case mass	displacer diameter	displacer rod area
3	compression space length	expansion space length	bounce space volume	bounce space wetted area	piston diameter
4	gas type	cooler type, 0 = tubes 1 = fins 2 = lanced fins	heater type (as for cooler)	X_{dc} (initial value)	ϕ_{dp} (initial value)
5	cooler tube diameter	cooler length	number of cooler tubes	cooler plenum volume	displacer mechanical spring constant
6	heater tube diameter	heater length	number of heater tubes	heater plenum volume	dynamics model 0 = fixed 1 = free
7	cooler fin height	cooler passage width	number of cooler fins	cooler entrance/exit loss	cooler wall thickness
8	heater fin height	heater passage width	number heater fins	heater entrance/exit loss	heater wall thickness
9	regenerator type 0 = random wire 1 = screens 2 = annuli	regenerator can Area	regenerator length	regenerator porosity	regenerator wire diameter
10	–	inner displacer gas spring volume	outer displacer gas spring volume	inner displacer gas spring area	outer displacer gas spring area
11	displacer sprung to: 0 = case 1 = piston	cooler port diameter	displacer area seen by bounce space	piston area seen by bounce space	ϕ_{dc} (initial value)
12	displacer seal friction factor	piston seal friction factor	rod seal friction factor	displacer seal type 0 = clearance seal 1 = ring seal	piston seal type 0 = clearance seal 1 = ring seal 2 = both
13	rod seal type 0 = clearance seal 1 = ring seal	displacer clearance seal gap	piston clearance seal gap	rod clearance seal gap	displacer clearance seal length
14	piston clearance seal length	rod clearance seal length	displacer clearance seal eccentricity	piston clearance seal eccentricity	rod clearance seal eccentricity
15	displacer seal extra damping coeff.	piston seal extra damping coeff.	rod seal extra damping coeff.	displacer ring seal width	displacer ring seal material
16	piston ring seal width	displacer spring seal type	displacer spring clearance seal gap	displacer spring clearance seal length	displacer spring clearance seal eccentricity
17	displacer spring seal extra damping coeff.	piston ring seal material	displacer spring ring seal friction factor	regenerator wall thickness	regenerator wall internal diameter
18	number of regenerators	regenerator wall material	regenerator wall thermal conductivity	displacer dome thickness	displacer dome material
19	displacer dome thermal conductivity	displacer type 0 = extended rod 1 = posted rod 2 = split displacer	appendix gap	stuffer outer diameter thickness	stuffer outer diameter
20	stuffer internal diameter thickness	stuffer internal diameter	stuffer insulation material	stuffer can material	displacer out stop
21	piston out stop	piston in stop	stuffer insulation thermal conductivity	stuffer can thermal conductivity	cooler fin thickness
22	cooler fin material	heater fin thickness	heater fin material	cooler fin thermal conductivity	heater fin thermal conductivity
23	cooler wall thermal conductivity	heater wall thermal conductivity	cooler tube thickness	heater tube thickness	cooler port width
24	number of cooler tube bends	number of heater tube bends	cooler wall or tube material	heater wall or tube material	cooler port offset
25	regenerator annular gap	regenerator foil thickness	regenerator internal diameter	regenerator matrix thermal conductivity	regenerator matrix material
26	–	piston spring centering port diameter	number of regenerator screens	regenerator screen pitch	regenerator screen wire diameter
27	inner piston gas spring volume	outer piston spring volume	inner piston spring puck area	outer piston spring puck	mechanical piston spring constant
28	rod ring seal width	rod ring seal material	number of displacer ring seals	number of piston ring seals	number of rod ring seals
29	displacer spring ring seal width	number of displacer spring ring seals	displacer spring ring seal material	X_{pa} (initial value)	X_{da} (initial value)
30	simulation type 1 = 3-D free-piston, 2 = 3-D free-cylinder	X_{ca}	case-ground mechanical spring stiffness	case-ground damping coeff. (excluding load)	ϕ_{pa} (initial value)
31	–	secondary piston clearance seal diameter	–	–	–

were used for heat transfer and flow loss. See appendix D.1 for a discussion of bounce-space fudge factors. A value of 1 was used for all the 'water pump' engine simulations.

Although the materials used for critical components are listed using a code, the relevant information required (eg, thermal conductivity or friction factor) is also listed in the table. For the sake of clarity these components and the properties used are as follows: Piston and displacer rings seals were manufactured from Rulon J, a coefficient of friction of 0.02 was assumed for the ring-cylinder wall contact. A thermal conductivity of 19 W/mK (stainless steel) was assumed for all other components except the heater fins (aluminium, $k = 160$ W/mK), and the cooler fins (copper, $k = 350$ W/mK). The use of aluminium for the heater fins was an error, only noticed during the final stages of preparing this document. A re-run of the simulation however indicated the effect to be negligible (a 1 K difference in the temperature drop across the heat exchanger for the test data reported here).

C.3 Model B-10 engine

The data in table C.3 is that used to simulate the series BE09N low pressure test conducted at a temperature difference of 363 K. Please refer to section 6.2 for information concerning fudge factors used for this specific set of tests. The data is representative of that used to simulate all the Model B-10 operating points. Items which were varied from series to series are noted in the first few pages of chapter 6 and in the discussion of each test series simulation.

Table C.2: Matrix of input data for 3-D SAUCE: File FCHELBAS.DAT

–	1	2	3	4	5
1	1600000	348	897	33	.006
2	.238	3.2	3.596	.052	.0005074
3	.019	.036	.0006119	.104565	.052
4	1	1	1	.0084	67
5	0	.052	0	2.29E-06	0
6	0	.047	0	.0000153	1
7	.008	.001	68	1.7	.0012
8	.008	.001	68	1.7	.0012
9	0	.0020339	.03	.8	.00005
10	1	1	5.1232E-05	0	.0005067
11	1	.001	0	.002156	-101.805
12	.02	.02	0	1	2
13	0	0	.000025	0	0
14	.03	0	0	0	0
15	0	0	0	.0018	5
16	.002	0	.000025	.04	0
17	0	5	0	.001	.077
18	1	1	19	.0005	1
19	19	1	.0005	0	.0524
20	.0008	.0524	1	1	.037
21	.018	.025	19	19	.062
22	3	.002	2	350	.160
23	19	19	0	0	.6015
24	0	0	1	1	.021
25	.0001	.00005	.036	19	1
26	3	.001	0	0	0
27	1	1	0	0	1000
28	0	0	2	2	0
29	0	0	0	.0031545	.01
30	2	.0034	64000	0	155.05
31	0	.029	0	0	0

Table C.3: Matrix of input data for 3-D SAUCE: File 09N09BE.DAT

1	82000	304	667	12.34	.003
2	.08866	.4026	.97904	.033	1.2668E-04
3	.01423	.0296	1.0495E-04	.0182	.0332
4	3	1	1	.00469	0
5	0	.03	0	0	653.51
6	0	.03	0	0	1
7	4.0705E-04	.104637	1	1.7	.00085
8	4.0705E-04	.104637	1	1.7	.00085
9	2	4.25925E-05	.0645	0	0
10	1	1	1	0	0
11	0	0	.000127	7.3902E-04	59.5
12	0	0	0	1	0
13	0	.00055	.000025	.000025	.0645
14	.0702	.0702	0	0	0
15	0	.1	0	.001	6
16	0	1	.000025	.0702	0
17	0	0	0	.000775	.03395
18	1	1	19	.0005	1
19	19	0	.000525	0	.0329
20	0	.0329	3	1	.03
21	.022	.022	.12	19	.0001
22	1	0	1	19	19
23	19	19	0	0	0
24	0	0	1	1	0
25	4.0705E-04	0	.0329	19	1
26	3	0	0	0	0
27	1	1	0	0	778.43
28	0	0	1	0	0
29	.001	1	6	.00878	.01001
30	2	.0024	20388	0	1.9
31	0	0	0	0	0

Appendix D

Model B-10 simulation: equation modifiers

Although the main emphasis in this work has been on the linear analysis technique, and its suitability as an analysis tool for FCSE design work, effective simulation is dependant on adequate calculation of interactions in the engine, given specific dynamic operation. Various fudge factors were used in chapter 6 in order to achieve adequate correlation between the simulation and the experimental results. These are investigated in a little more detail below.

D.1 Bounce-space spring and damping coefficient calculation

The equations developed by Berchowitz, (referred to in section 3.4.2, and section 3.3.1) were used to estimate the gas spring hysteresis losses and the gas spring stiffness coefficient for both the B-10 engine and the larger 'water pump' engine simulations. Berchowitz suggested that a factor of 1 to 2.5 should be applied to the calculated loss, larger factors being applicable when the gas is highly agitated. Both the B-10 engine and the 'water pump' engine have bounce spaces in which the degree of agitation is quite severe, thus a factor of 2 was used as a first approximation.

Data from the first three B-10 series of tests reported are compared with the calculated values in the figures below. The working fluid for all these tests was nitrogen (treated as 'air' in the simulation equations). The simulation amplitudes are based on equation (3.26), the experimental results are the sinusoidal

approximations of the measured data. The hysteresis losses as calculated using equation (3.44) (multiplied by the factor of 2 noted above) are compared with the measured $\oint p_b dV_b$ (the sinusoidal approximation of the measured data being used in all cases).

The amplitudes of the measured data and the amplitudes estimated by equation (3.26) are remarkably close. However, the bounce-space dissipation resulting from the hysteresis loss equation alone is much lower than that measured for all three series of tests. The data collected from the small B-10 rig was not suitable for a thorough investigation of the above discrepancies for a number of reasons including:

- the presence of a small bore charge line of approx 1 m in length, diameter 2.5 mm, with a pin hole opening to the bounce space and a pressure gauge at the other end (to measure the mean pressure),
- uncertainty regarding the exact dimensions of the clearance seal gaps and centering ports,
- the limited accuracy of the motion and pressure recording instrumentation,
- the pr ence of markers and a thin sheet of black paper (a backdrop for the markers) within the bounce space.

Appropriate fudge factors (in addition to the factor of 2 noted above) were therefore applied to the existing simulation loss equations for the purposes of the Model B-10 simulation work. The fudge factors were determined graphically from the hysteresis loss figures shown, and are the inverse of the slopes of the straight lines drawn through the data.

D.2 Heat exchanger friction losses: sensitivity to gap dimension and eccentricity

In section 6.3 it was noted that the flow losses in the heat exchangers were overestimated by the equations used in the simulation. That particular set of tests was sensitive to these flow losses, and a fudge factor of 0.3 was therefore applied to the flow loss calculations in order to allow adequate simulation of engine performance. Using the fixed dynamics mode of the simulation programme it is possible to investigate the sensitivity of the calculated flow dissipation

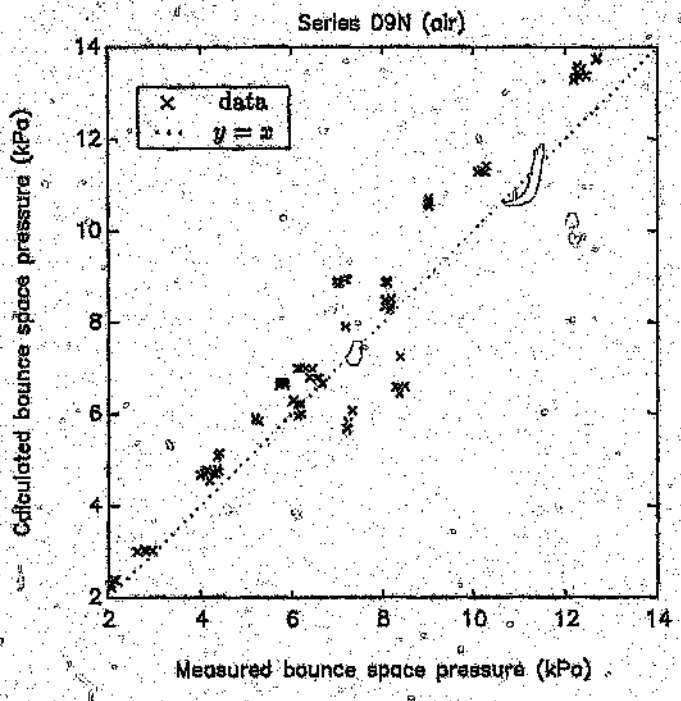

Figure D.1: Comparison of linearized adiabatic simulation and measured bounce-space pressure amplitude (Series BE09N).

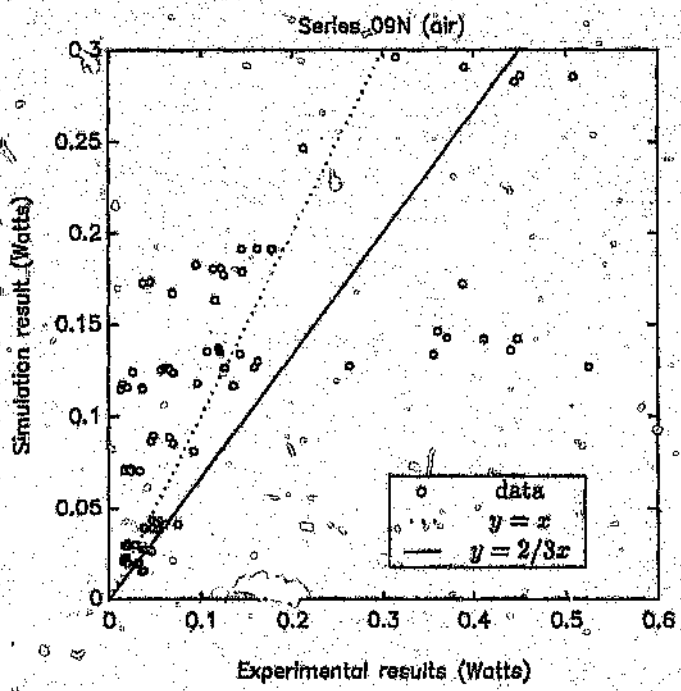

Figure D.2: Comparison of bounce-space hysteresis loss: simulation and experimental data (Series BE09N).

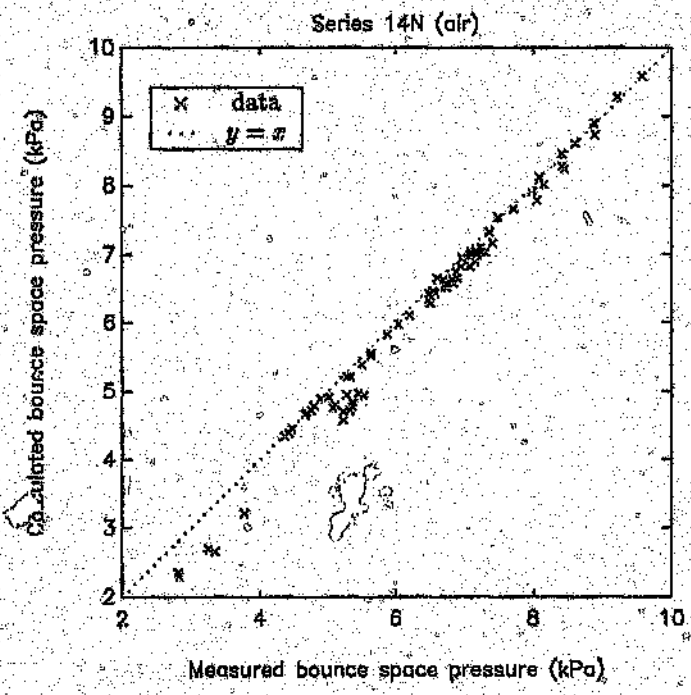

Figure D.3: Comparison of linearized adiabatic simulation and measured bounce-space pressure amplitude (Series BE14N).

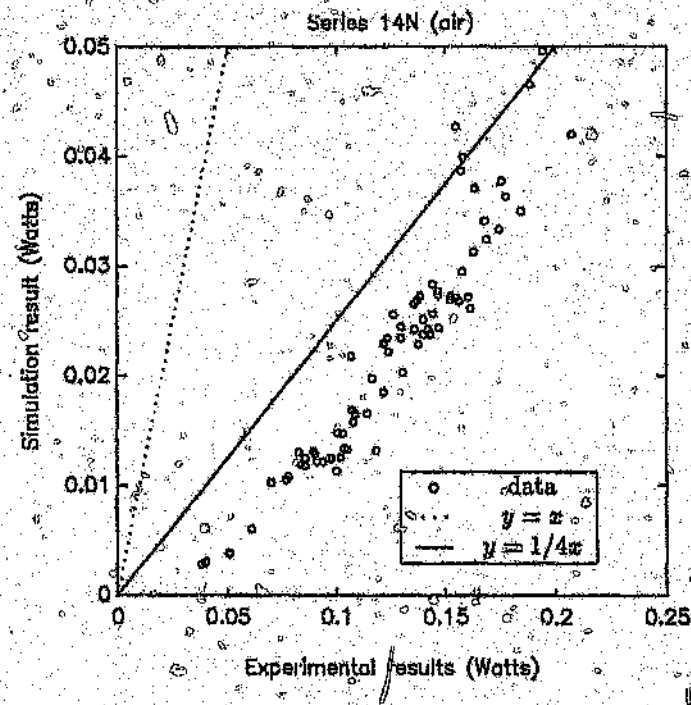

Figure D.4: Comparison of bounce-space hysteresis loss: simulation and experimental data (Series BE14N).

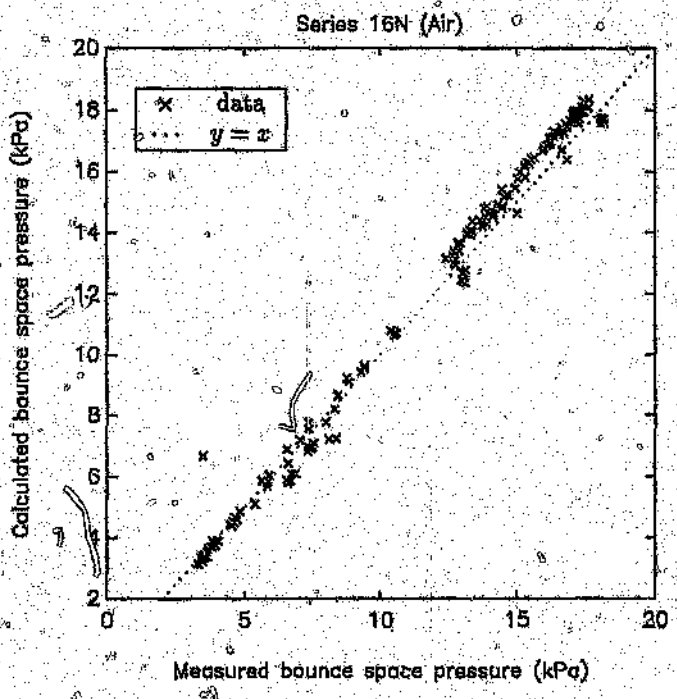

Figure D.5: Comparison of linearized adiabatic simulation and measured bounce-space pressure amplitude (Series BE16N).

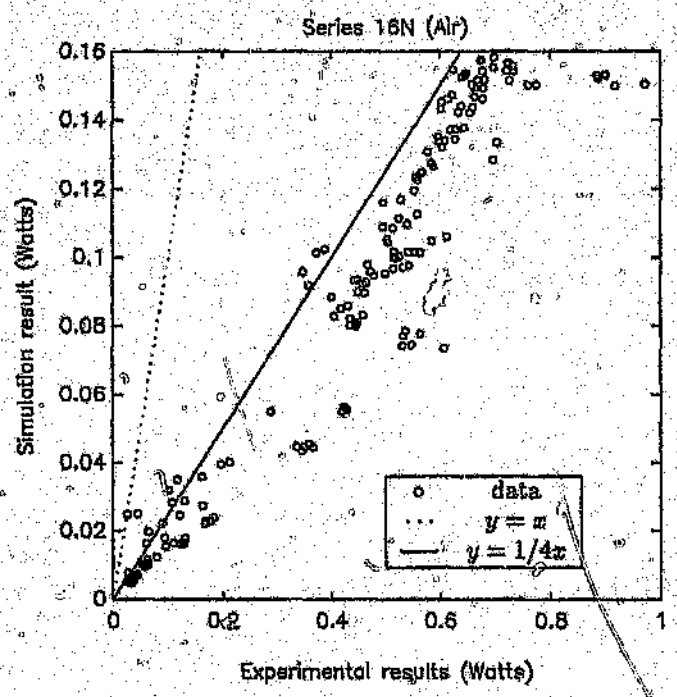

Figure D.6: Comparison of bounce-space hysteresis loss: simulation and experimental data (Series BE16N).

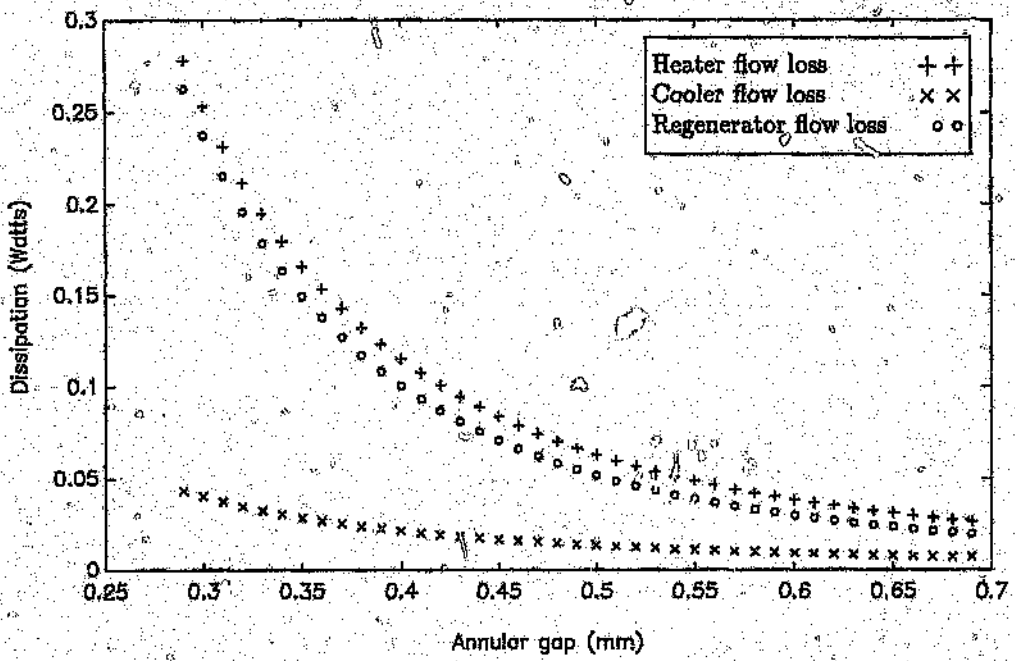

Figure D.7: Heat exchanger flow losses as a function of annular gap dimension

through the heater, regenerator and cooler to the dimension of the gap between displacer and the cylinder wall. Figure D.7 shows the flow dissipation for each of the three components as a function of the annular gap. The component dynamics were fixed at the experimental values for test BE14N14, a case amplitude falling close to middle of the range of case amplitudes for the test series. The sensitivity to the exact value of the gap width is clearly shown (The measured gap width was 0.4 mm). The equations used did not include a factor for eccentricity. Eccentricity would reduce the resistance to flow significantly, and hence reduce the dissipation resulting from gas flow through the heat exchangers.

From the above it is clear that a fudge factor of 0.3 is not unreasonable, given that it was difficult to measure the exact gap width accurately, and that eccentricity was a definite possibility. As annular gap heat exchangers are an unlikely candidate for future FCSE prototype development, the difficulties in determining the dissipation and heat transfer alluded to here will probably not arise. If they are used, then very good control of the exact dimensions, and of eccentricity, will be necessary if repeatable engine performance, and accurate simulation is to be achieved.

D.3 Investigation of the force balance method

In conducting the experimental work reported here, and in developing the simulations discussed in chapter 6, an important area of uncertainty was the determination of damping within the engine. This applies not only to the major pressure drop which occurs across the displacer, but also to the mechanical friction between piston and case, between piston and displacer, between case and ground. The importance of these 'unknown' dissipative forces is highlighted by the not insignificant work required to maintain oscillation of the components (tables 4.2, 5.3 and 5.4)

Not only are the drag forces acting on the internal components difficult to measure, but they are also difficult to determine analytically, being sensitive to precise clearance fit geometry, high spots and imperfections in the hardware (especially in the case of seals). Flow losses occurring in the short Stirling engine heat exchangers under reversing flow conditions are also notoriously difficult to predict accurately.

A force balance can be carried out on the components in order to determine from the experimental data both the magnitude and phase of the unknown interactions. An approach, based on the relatively commonplace measurements of component motion, work- and bounce- space pressures alone is presented below. Although the method has not proved successful for the experimental work undertaken during this project, it is presented here, primarily to explain why it has not been used. It may find application in work where better measurement accuracy is possible, or serve as a warning to others of the pitfalls of adopting this approach. With reference to figure D.8:

If Δp is a pressure drop across the regenerator annulus due to gas flow, then $\Delta p A_{gap} = \Sigma_{\text{shear force on walls}}$. Since the inner wall of the annular gap (part of the displacer), and the outer wall (part of the case) have approximately the same area the shear force on the displacer as a result of the gas flow is equal to that on the case, and is given by $\Delta p A_{gap}/2$. [1]

Simplified equations of motions for the three components are:

$$\begin{aligned} m_d\ddot{x}_d &= p_w(A_d - A_r) - K_{dc}(x_d - x_c) + p_b A_r - (p_w - \Delta p)A_d + \\ &\quad \Delta p A_g/2 + D_{pd}(\dot{x}_p - \dot{x}_d) - D_{dc}(\dot{x}_d - \dot{x}_c) \qquad \text{(D.1)} \\ m_p\ddot{x}_p &= -p_w A_p + p_b A_p - K_{pc}(x_p - x_c) - D_{pd}(\dot{x}_p - \dot{x}_d) - D_{pc}(\dot{x}_p - \dot{x}_c) \qquad \text{(D.2)} \\ m_c\ddot{x}_c &= (p_w - \Delta p)A_c + \Delta p A_g/2 - p_b A_c + K_{pc}(x_p - x_c) + K_{dc}(x_c - x_d) \\ &\quad + D_{dc}(\dot{x}_d - \dot{x}_c) + D_{pc}(\dot{x}_p - \dot{x}_c) + f_{fc} + f_{cg} \qquad \text{(D.3)} \end{aligned}$$

[1] For an engine in which there is a sleeve between the heat exchangers and the displacer (as in the larger 'water pump' engine') then $A_d = A_c$ and this term falls away from both equations.

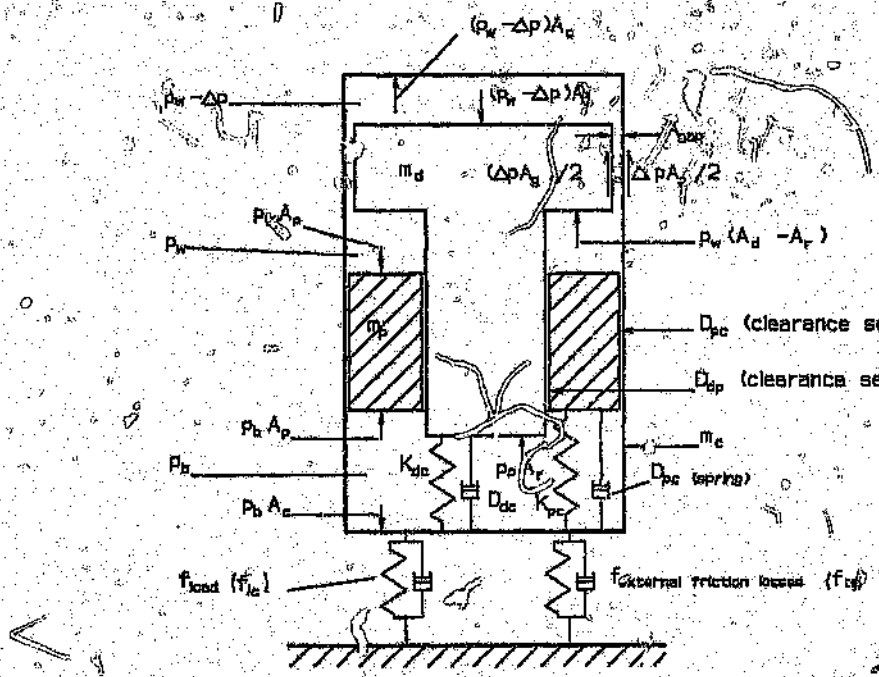

Figure D.8: Free body diagram of B-10 engine

D_{dc} represents possible displacer-case mechanical spring hysteresis losses, D_{pd} refers to the damping effect of the displacer rod clearance seal, while D_{pc} refers to the damping effect of the piston-case clearance seal and the piston-case mechanical spring losses.

From the experimental results, and the static spring calibrations p_w, p_b, K_{dc} and K_{pc} are known, as are the masses, velocities and accelerations of the components. The measured force to the load cell f_{lc} is known, and equation (5.7) can be used to determine the unmeasured external force f_{cg}. It is therefore possible to calculate some of the other unknown coefficients in equations (D.1) to (D.3). They can either be determined as variable coefficients, if general motion and pressure data is available, or as constant coefficients if sinusoidal approximations of pressure and motion data are used. Note, equation (5.7) is the sum of equations (D.1) to (D.3). The internal terms cancel out, so that the force between the case and ground can be determined from the motion of the components only, (or alternatively, if the force between the case and ground is known, and the motion of two components is known, then the motion of the third component can be calculated). This is not restricted to the assumption

of sinusoidal motion.

For the piston, from equation (D.2), let $f_p = m_p\ddot{x}_p + p_w A_p - p_b A_p + K_{pc}(x_p - x_c)$, ie, the known forces. The resistance to motion of the piston as a result of friction losses f_p can therefore be determined. If p_w, p_b and x_d can be reasonably represented by sinusoidal functions, then f_p will be a complex phasor $\overline{F}_p$, rotating at the engine frequency. Real coefficients D_{pd} and D_{pc} can then be determined, either graphically, or by solving the equation below. (If amplitudes and phase angles are used rather than complex phasors, then appropriate techniques are shown in section 3.4.3 and 3.3.2).

$$\left.\begin{aligned} \overline{X}_{pd} &= \overline{X}_p - \overline{X}_d \\ \overline{X}_{pc} &= \overline{X}_p - \overline{X}_c \end{aligned}\right\} \tag{D.4}$$

$$\overline{F}_p = -D_{dp} i\omega \overline{X}_{pd} - D_{pc} i\omega \overline{X}_{pc} \tag{D.5}$$

Since both the real and the imaginary components of the above equation must balance, it is possible to solve for D_{dp} and D_{pc}.

D_{pd} represents damping between the piston and the displacer occurring at the clearance seal. Similarly, D_{pc} represents the combined effects of piston-case spring hysteresis and the piston-case clearance seal. As both coefficients represent unknown, but real dissipative interaction, they should have positive values.

Unfortunately the results are very sensitive to the accuracy of motion and pressure measurements, and reliable results were therefore not obtained from the B-10 data. Of a broad cross-section of tests analyzed, 39% yielded negative and therefore impossible values of D_{pd}, and 37% yielded $D_{pc} < 0$. Sensitivity is a function of both phase and amplitude of the different components, thus it is not possible to carry out a simple sensitivity analysis to indicate the required accuracy of measurements in order to achieve meaningful results. However, if the equations are presented in vector form, then it is clear from the figures that the damping coefficients calculated using the method should be treated with extreme caution, or discarded. Figure D.9 shows the force polygon for the piston. The known forces (inertia, pressure, mechanical springs) have been added, the resultant being the 'unknown' force required to close the diagram, joining the '×' to the origin. The proximity of the '×' to the origin is encouraging, in that it illustrates that the forces resulting from damping between the piston and case, and between the piston and displacer are much smaller than the pressure and inertial forces. However, this proximity makes the estimation of damping coefficients difficult. A small percentage error in the measurement of the pressure or frequency of oscillation will lead to a large percentage error in the 'unknown' force estimate. Trying to take the process

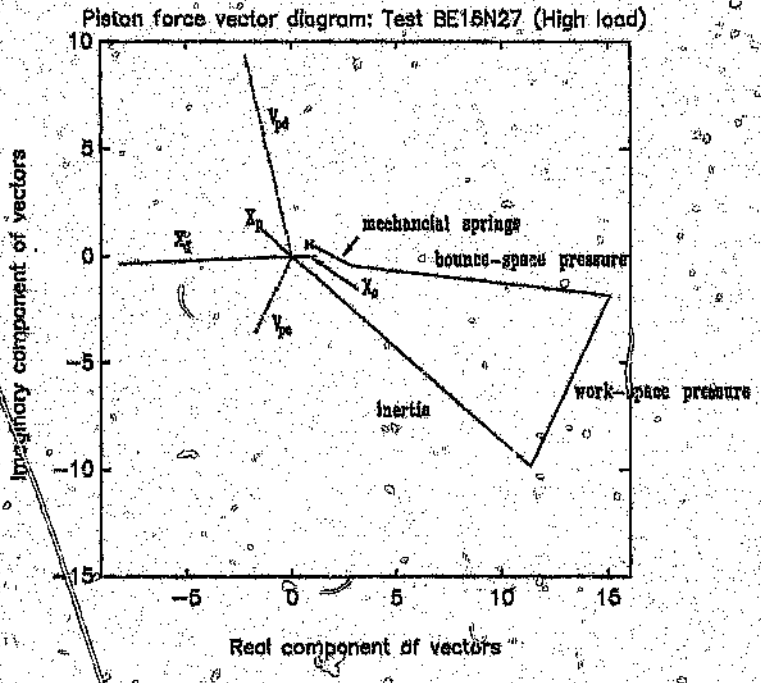

Figure D.9: Piston force vector diagram: Test BE16N27 , high load condition

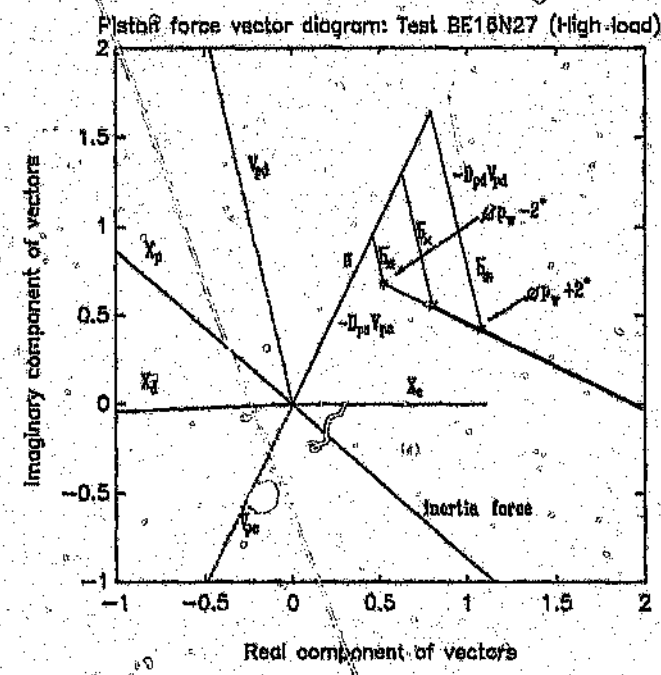

Figure D.10: Enlarged view of portion of piston force polygon

one step further, and estimate the damping coefficients which would lead to the 'unknown' force introduces yet more error as shown graphically in figure D.10, an enlarged view of the force polygon. If the 'unknown' force is the result of damping between the piston and the case, and between the piston and the displacer, then it can be resolved into the two vectors $\bar{a}$ and $\bar{b}$, parallel and proportional to $\overline{V}_{pc}$ and $\overline{V}_{pd}$ respectively. The constants of proportionality are the damping coefficients D_{pc} and D_{pd}. In order to highlight the sensitivity of D_{pc} and D_{pd} to possible measurement errors of the other parameters, three different sets of vectors have been plotted. The '×' symbol corresponds to the recorded values. The asterisks were plotted using the same data, except that the work-space pressure vector phase was adjusted by $+2^\circ$ and -2° (a small change). Note the significant change in the length of vector $\bar{b}$, and hence in the estimated value of D_{pd}.

Figures D.11 and D.12 show the force polygons for the displacer and case respectively. The 'unknown' vector for the displacer includes the effect of Δp, D_{pd} and D_{pc}, while that for the case includes forces resulting from Δp, D_{dc} and D_{pc}. The force polygons for test BE09N06, a low pressure test from the first series of tests are presented in figures D.13 to D.15 in order to show the very different shapes resulting from the different mode of oscillation.

The 'unknown' force acting on the displacer is a more significant element of the force polygon, and there may be some merit in unravelling it further. Rearranging equation (D.1) with all the known terms on the LHS as $\overline{F}_d$, expressing Δp as a phasor, and setting $\overline{X}_{dc} = \overline{X}_d - \overline{X}_p$, we get:

$$\overline{F}_d = \overline{\Delta p}(A_d + A_g/2) + D_{pd} i\omega \overline{X}_{pd} - D_{dc} i\omega \overline{X}_{dc} \qquad \text{(D.6)}$$

Δp would be as a result of gas flow, and could therefore reasonably be assumed to be a function of the relative velocities of the displacer and the piston w.r.t. the case ($\dot{x}_{dc} = \dot{x}_d - \dot{x}_c$ and $\dot{x}_{pc} = \dot{x}_p - \dot{x}_c$) respectively. Therefore set $\overline{\Delta p} = d_1 i\omega \overline{X}_{dc} + d_2 i\omega \overline{X}_{pc}$. For convenience set $A_D = A_d + A_g/2$. D_{pd} is known from the piston force balance.

The above then becomes:

$$\overline{F}_d - D_{pd} i\omega \overline{X}_{pd} = (d_1 A_D - D_{dc}) i\omega \overline{X}_{dc} + d_2 A_D i\omega \overline{X}_{pc} \qquad \text{(D.7)}$$

It is then possible to solve for d_2 and the combined coefficient $(d_1 A_D - D_{dc})$.

If one could determine a reasonable value for D_{dc}, the displacer-case spring hysteresis, it would be possible to calculate both d_1 and d_2, and therefore get a

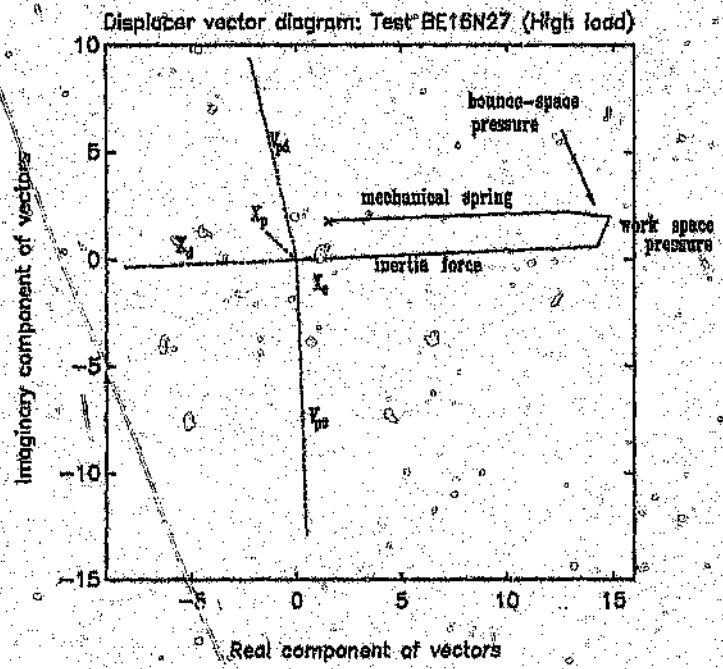

Figure D.11: Displacer force polygon: Test BE16N27, high load condition.

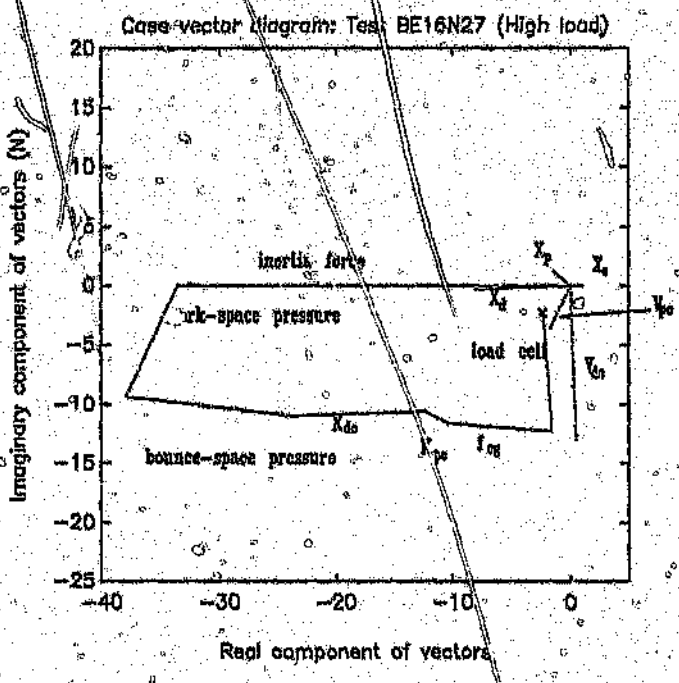

Figure D.12: Case force polygon: Test BE16N27, high load condition.

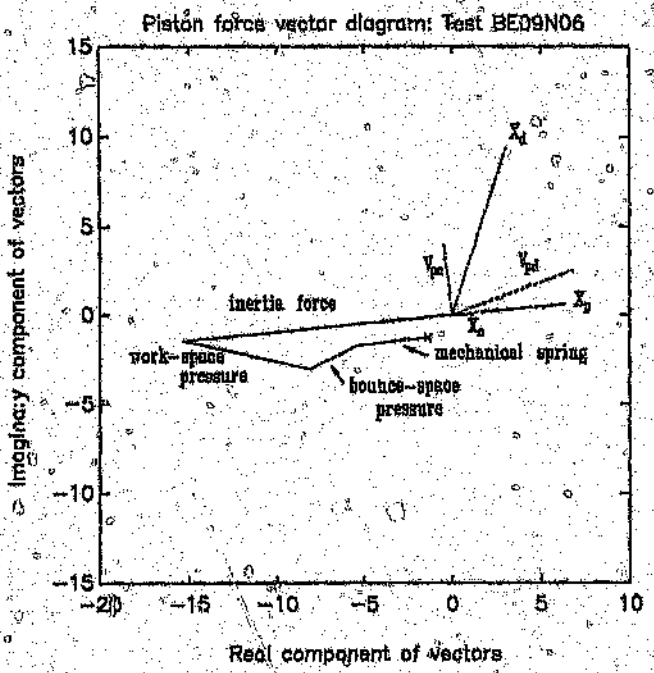

Figure D.13: Piston force polygon: Test BE09N06 (low mean pressure)

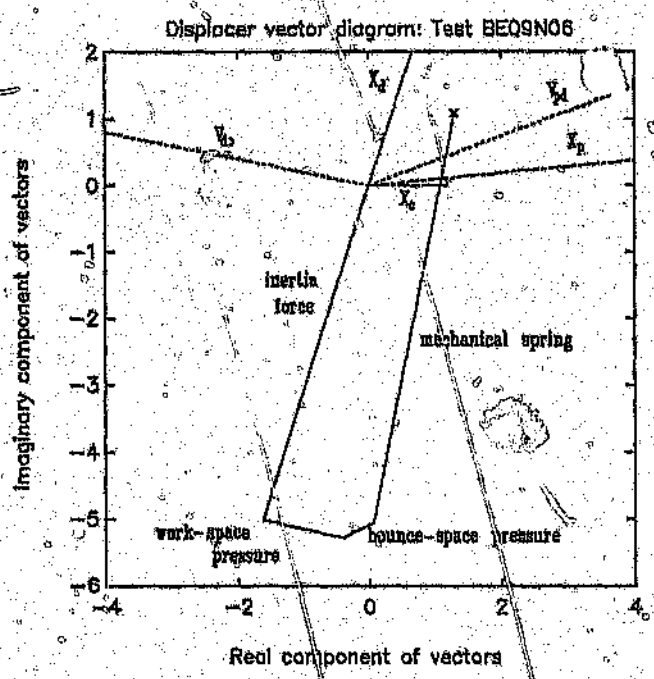

Figure D.14: Displacer force polygon: Test BE09N06 (low mean pressure)

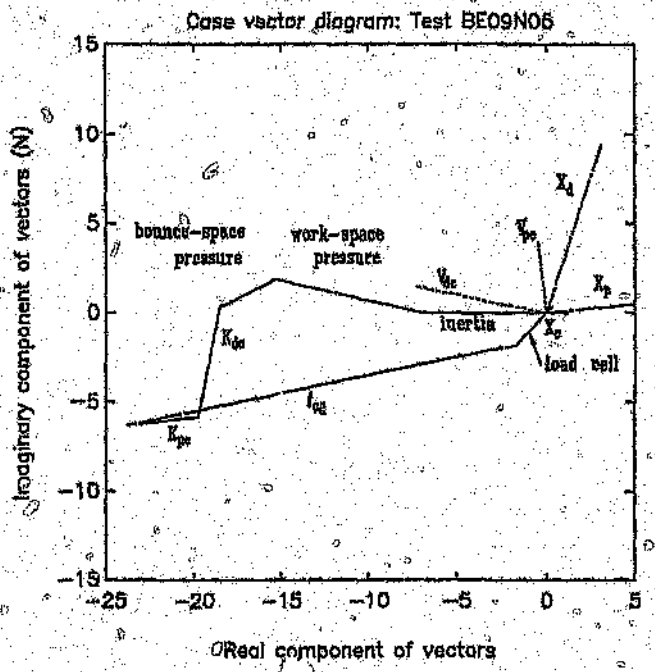

Figure D.15: Case force polygon: Test BE09N06 (low mean pressure)

value for $\overline{\Delta p}$, the pressure drop across the cooler-regenerator-heater annulus. Typically, mechanical spring hysteresis is small enough to be ignored. The pressure drop across the cooler-regenerator-heater annulus can thus be estimated. However, estimates of the coefficients d_1 and d_2 suffer from the same sort of accuracy problems as the above described estimates of D_{pc} and D_{pd} (and are dependant on D_{pd}).

In a system where it is known that D_{pd} and D_{dc} have significantly less influence than the pressure drop Δp, then these terms can be dropped from equation (D.6), and an estimate of $\overline{\Delta p}$ obtained without reference to the piston force balance. Since D_{pd} and D_{dc} represent clearance seal and mechanical spring dissipation this will often be a reasonable approximation. The provisos with respect to accuracy given above still apply. However, as an order of magnitude check, the results for some of the tests are presented in the figures D.16, D.17 and table D.1.

For the purposes of comparison, calculated pressure drops, using the simulation programme in the fixed dynamics mode have been plotted in the same figures. The same heat transfer and flow loss fudge factors were used as in the

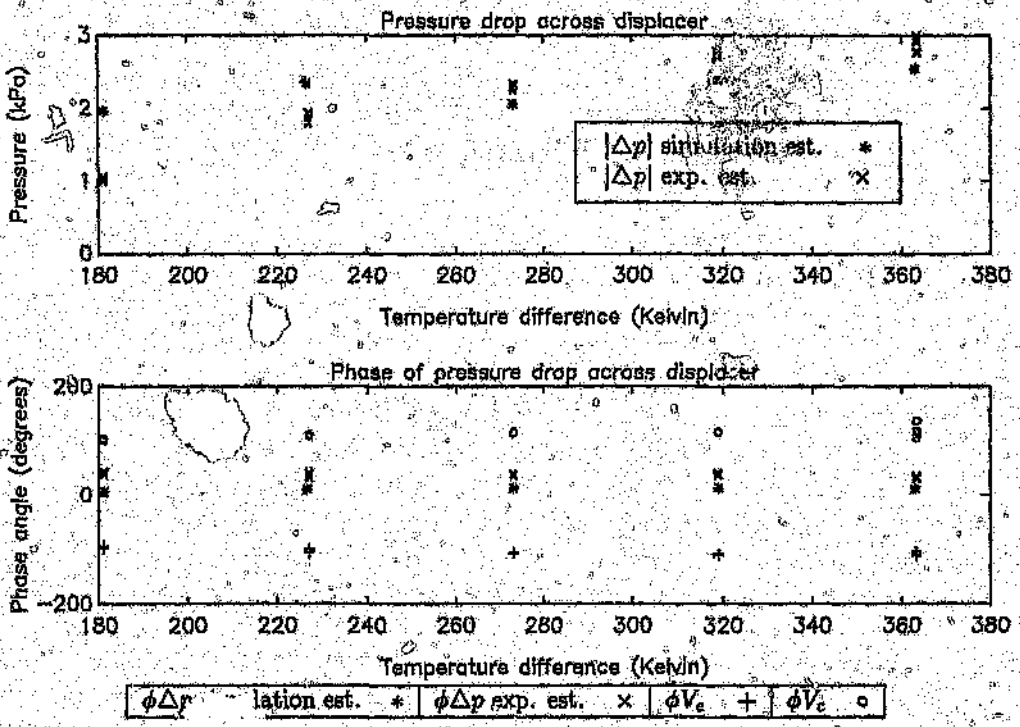

Figure D.16: Pressure drop across the annular heat exchangers: low pressure range of test series BE09N

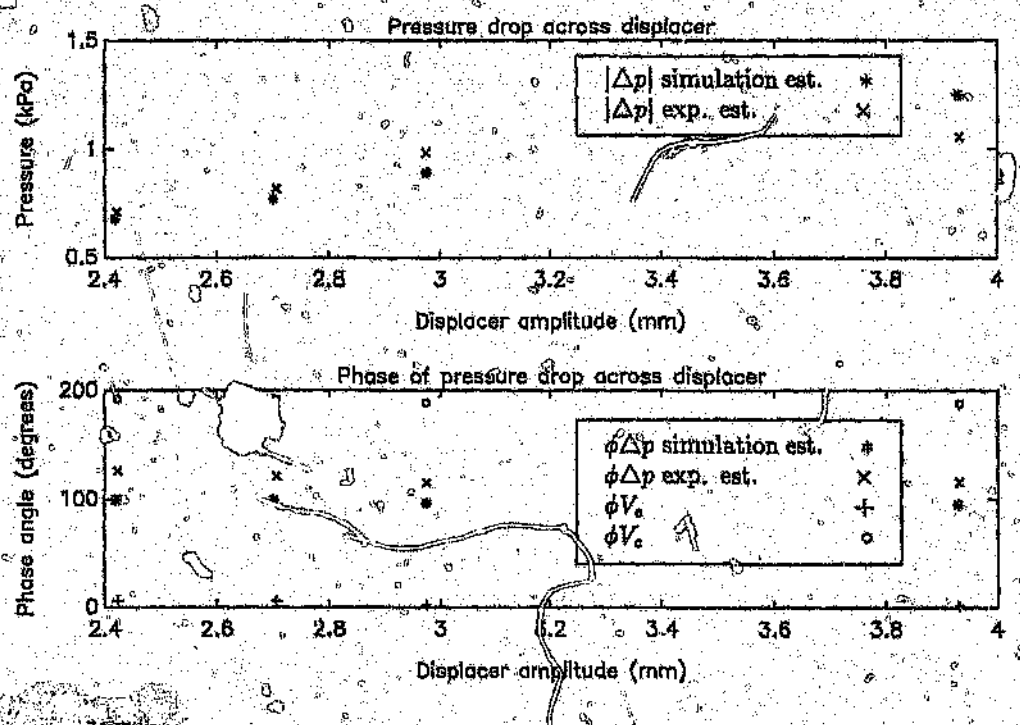

Figure D.17: Pressure drop across the annular heat exchangers: high temperature range of test series BE14N

Table B.1: Estimates of pressure drop across the annular heat exchangers: Test BE16N27

	Low load				High load			
	Experiment		Fixed dyn. calc.		Experiment		Fixed dyn. calc.	
$\|\Delta p\|$	2.14 kPa	56°	2.18 kPa	107°	2.70 kPa	50°	2.68 kPa	98°

simulations reported in sections 6.2 and 6.3.[2] The amplitude of the estimated and calculated pressure drops are reasonably similar. Agreement on phase angles is not as good.

Given the previously noted sensitivity of the estimated balance forces (and hence the estimated pressure drop) to possible errors in primary measurements, the above agreement of amplitudes must primarily be considered fortuitous. It does however lend an added measure of credibility to the flow loss fudge factor of 0.3 applied in the simulation of the series BE14N and series BE16N tests. No satisfactory reason (apart from sensitivity to experimental error) for the differences in phase angle could be determined.

In summary, while vector analysis (or the equivalent complex phasor manipulation) is a useful tool in aiding the visualization of the force interactions, and gives a good representation of the larger forces, its use as a tool for the estimation of specific small but possibly important damping coefficients is not recommended unless very accurate measurement is possible.

[2] No fudge factor was applied for the simulation of the series BE09N tests, while the calculated heat transfer rates were increased by a factor of 2 for the BE14N and the BE16N tests. The flow losses for the latter two test series were multiplied by 0.3.

Appendix E

Regenerator effectiveness calculation

In the original version of the SAUCE subroutine dealing with the regenerator actual heat transfer, and its effectiveness, a discrepancy between the equations listed in the body of Berchowitz's thesis and the subroutine was noticed. The following serves to explain the resulting modification made in an attempt to make the computer programme represent Berchowitz's derived equations more closely. The derivation of regenerator actual heat transfer and regenerator effectiveness equations is not reviewed.

The regenerator effectiveness is calculated using the expressions below (see [13, p 106,p 109])

$$\epsilon = \mathrm{N}r/(\pi + \mathrm{N}r) \tag{E.1}$$

where:

$$\mathrm{N} = \frac{hA_w}{c_p(w_{kr})\mathrm{max}} \tag{E.2}$$

h is the regenerator heat transfer coefficient, A_w the wetted surface area, and w_{kr} the mass rate of flow from the cooler to the regenerator, positive flow being towards the hot end.

$$r = \sqrt{2(1 - \cos\theta_w}$$

where θ_w is defined by the figure E.1. Berchowitz does not give an equation in the text to calculate the value of θ_w. In the figure w_{rh} is the mass rate of

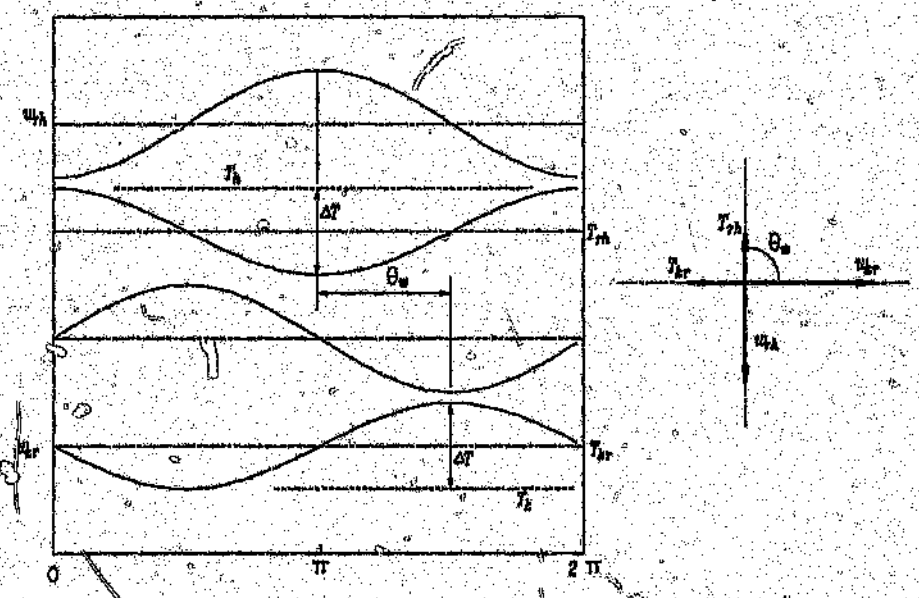

[Redrawn from [13, pg 105]]

Figure E.1: Approximate phase relationships between mass flow and temperature

flow from the regenerator to the heater (positive flow to hot end), while T_{rh} and T_{kr} are the gas temperatures at the same nodes (w_{kr} already described above). If θ_{rh} and θ_{kr} are the phase angles relative to a common reference for the mass rates of flow, then

$$\theta_w = \pi - (\theta_{rh} - \theta_{kr}) \tag{E.3}$$

However in the subroutine HEAT: listed on page 402–403 of [13]:
THW = ABS(PHWH - PHWK)
where PHWK and PHWK are the phase angles of the cooler and heater mass flow rates respectively, and THW $= \theta_w$ of the above equations. The same line appears in the original SAUCE programme used as a basis for the development of 3-D SAUCE. The coded equation will thus yield values of THW close to zero for very short regenerators (where PHWH and PHWK are expected to be approximately in phase). Equation (E.3) yields values close to π for situations when $\theta_{kr} \simeq \theta_{rh}$. In the simulation programme used for the results reported here, the code was therefore altered to:
THW = PI – (PHWH-PHWK)
The above modification resulted in increased regenerator effectiveness (and hence reduced heat load on the cooler and heater) in the simulations reported. As heat loads and heat transfer were not investigated in the experimental work, the situation was not reviewed in any more detail.

Appendix F

Copy of publication

F.1 Errata

A paper written by this author, entitled 'Test results on a free-cylinder Stirling engine' was published at the 24th International Energy Conversion Engineering Conference, 1989 [1]. A copy of the paper is attached for reference purposes. The following errata serve to correct minor errors in the original paper.

The only equation in the text of the published paper should be replaced with the following equation.

$$\oint p_w \mathrm{d}V = \oint p_w A_c \mathrm{d}x_c - \oint p_w A_p \mathrm{d}x_p - \oint p_w A_r \mathrm{d}x_d$$

Figure 1 of the published paper should be replaced with figure F.1.

The data published in table 2 of the paper was based on an incorrect displacer rod area, and an incorrect value for the specific heat capacity ratio (γ) of helium. The corrected table is listed as table F.1 below.

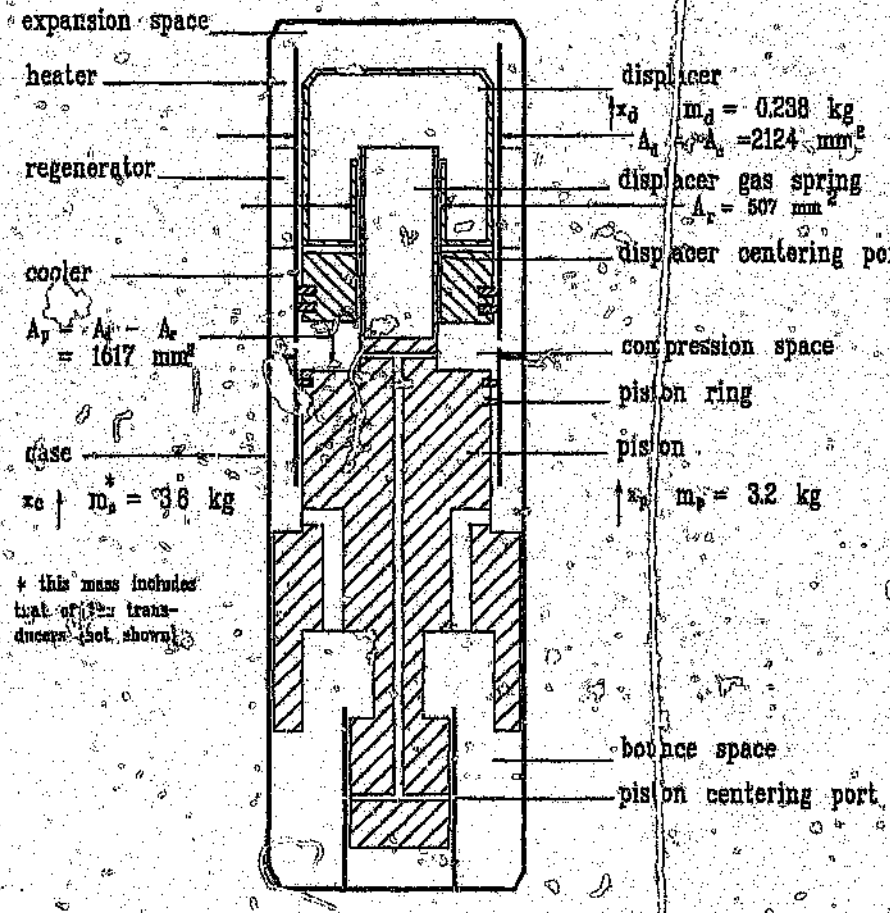

(Not to scale)

Figure F.1: Corrected drawing to replace figure 1 of published paper

Table F.1: Corrected table to replace Table 2 of published paper

	Piston	Displacer	Case	Sum	Test
Work space	0.175	1.682	1.324	3.181	1
	-0.231	0.618	-1.379	-0.993	2
	0.231	0.725	-0.802	0.154	3
Disp. spring	0.678	-0.678	0	0	1
	0.290	-0.290	0	0	2
	0.277	-0.277	0	0	3
Bounce space	-0.342	0	0.046	-.296	1
	0.139	0	-0.402	-.263	2
	0.078	0	-0.419	-0.340	3
Sum	0.512	1.004	1.369	2.885	1
	0.197	0.328	-1.781	-1.256	2
	0.586	0.448	-1.221	-.186	3

899052

TEST RESULTS ON A FREE-CYLINDER STIRLING ENGINE

Douglas I Banks
School of Mechanical Engineering
University of the Witwatersrand
P O Wits, 2050
South Africa

ABSTRACT

In the early 1980's Sunpower Inc, of Athens, Ohio designed and built some prototype free-cylinder Stirling engine powered water-pumps for use in rural areas. In 1986, one of the products of this development was donated to the University of the Witwatersrand. This engine has been comprehensively instrumented and is in the process of being tested. A net output power of 40 watts has been obtained from the engine, using helium at an absolute pressure of 1600 kPa as the working fluid, and an external heater temperature of 624 °C. The frequency of the engine was 33Hz, while the case stroke was 6.8mm. The piston and displacer motion, as well as the energy flow paths through the gas spaces are discussed.

INTRODUCTION

The free-cylinder Stirling engine concept is a natural derivative of the free-piston Stirling engine. Using this as a base, one can describe the free-cylinder Stirling engine as a free-piston engine with a suitably supported light case. As a result the case tends to oscillate with a significant amplitude. Thus a hermetically sealed engine can be used to directly obtain mechanical power. To date the principal application of this device has been as the power source of a water pump.

The free-cylinder Stirling engine was first developed by Beale during 1969 [Ref 1 & 2]. The concept was again taken up by Beale and the Sunpower team ten years later. During the years upto 1984 some successful free-cylinder powered water pumps of approximately 100 watts output had been demonstrated. The intention was to develop a solar or renewable fuel powered water pump for use in developing countries. Despite the nobleness of the venture, and the success of the prototypes, the ways of the commercial world halted further development before an economically viable engine could be produced.

The last free-cylinder prototype built by Sunpower was unfortunately not thoroughly tested or proved. This engine is now being used in the research programme at the School of Mechanical Engineering.

OBJECTIVES

The overall objectives of the FCSE programme at the University of the Witwatersrand are:

1. To establish the performance characteristics of the Sunpower free-cylinder engine under operating conditions.
2. To apply and possibly extend some of the analysis techniques developed by Berchowitz, Urieli and Redlich for free-cylinder Stirling engines [Ref 3,4,5].
3. To continue the development of free-cylinder Stirling engine powered water pumps.

The specific objective of this paper is to report progress under item 1 above.

DESCRIPTION OF THE ENGINE

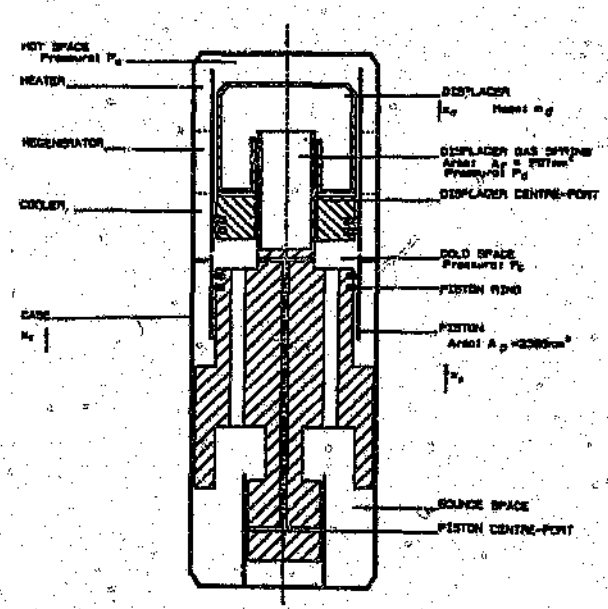

Figure 1 Schematic of Sunpower Free-cylinder Stirling Engine

CH2781-3/89/0000-2363 $1.00 © 1989 IEEE

Figure 1 shows the engine layout. Piston and case have approximately equal mass, while the displacer mass is about 1/15 of the mass of the piston. The engine case, internal heat exchangers and cylinder are manufactured from stainless steel. The heater, regenerator and cooler form a welded single unit about the cylinder bore. There are no external fins on the heat exchangers. The piston is manufactured from brass.

Rulon rings are used for the main piston seal. The other sliding contact surfaces have one member coated with a teflon based product. The piston centring-ports tend to equalize the bounce and working space pressures at piston mid-stroke, thus stopping the piston from drifting towards one end of the engine. The displacer centring-ports serve a similar purpose, equalising the displacer gas spring pressure and the work space pressure at the displacer mid-stroke. The use of piston rings, rather than clearance, seals for the piston and displacer seals significantly relaxes the concentricity requirements of the engine. There is however an increase in the sliding friction of the components.

The engine is heated by means of a simple propane gas burner. Experimentation with both a biogas burner and solar heating has been planned.

INSTRUMENTATION

Fast linear displacement transducers have been attached to both the piston and the displacer. Piezoelectric pressure transducers are used to monitor the working space and piston bounce space pressures. External wall temperatures are measured using thermocouples.

The engine is supported in a frame on a variable spring rate mechanical spring, and guided by ball bearings. During the tests reported the engine was mounted on a large hydraulic ram coupled to a feedback control system. It was thus possible to oscillate the engine in a controlled manner. The motion of the case and the force applied to the case were measured. Thus it was possible to test the engine in a non-power producing state as well as when it produced positive power.

Data acquisition was performed using a computer-scope card which plugged into an IBM-compatible PC.

RESULTS AND DISCUSSION

Figures 2(a-d) show the six dynamic variables recorded over a complete cycle. For this test the charge was helium at a pressure of 16 bar. The power delivered to the ram by the engine was approximately 40 watts. Table 1 is a summary of the data shown in Figure 2. Results from a cold test as well as from a less satisfactory hot test are also shown. The latter was run with nitrogen as the working fluid.

In order to facilitate visualization of the engine dynamics, two conventions have been used for describing the displacer and piston motion. For Figure 2a and for that data which are marked with an asterisk in Table 1 and (in the discussion below), the motion is relative to that of the case. This allows direct comparison of characteristics such as stroke and displacer phase angle with those of free-piston Stirling engines. However, when considering the dynamics of the engine as a mechanical system, it becomes easier to use displacements of the components with respect to ground. Absolute displacements are used in Figures 2b and 2c as well as in the unmarked data in Table 1.

Figure 2a is very similar to that expected from a free-piston Stirling engine. The phase angle between piston and displacer is 67°° degrees. This angle and the displacer amplitude were the principal variables which determined the frequency at which the engine produced positive power. At frequencies lower than 33Hz the displacer amplitude was reduced and the phase lead decreased, resulting in inferior thermodynamic performance. Since the thermodynamic performance affects the displacer amplitude, a negative feedback system can quickly reduce the engine to an inert lump of metal.

Figure 2b shows the force applied by the ram to the case versus the case displacement. It is the area of this curve which is reported as the work output per cycle in Table 1. Although this is positive for the test shown, indicating a net transfer of energy from the engine to the ram, the forces required to maintain oscillation at the correct frequency are high. The case is obviously not oscillating at its natural frequency. However, the frequency could not be altered for the reasons stated above. Hence it is necessary to tune the engine, such that the displacer and case motions are better matched without the need for a sophisticated loading device. Slight free play between the ram and the engine is the primary cause of the somewhat unusual shape of this curve.

Figure 2c shows the absolute motion of the components as a function of theta, where theta is a time based division of the period of oscillation. Reference to Table 1 shows that the piston leads the case by approximately 180°. For those tests in which the engine produced positive work this lead was less than 180°, while for those where the engine did not produce positive work the lead was greater than 180°. During tests this was noted as a sudden change on the oscilloscope as the engine reached operating conditions. There was a slight hysteresis involved in the change. Thus, for example, as the excitation amplitude was increased the phase suddenly shifted to less than 180°, and then remained in the shifted position until the excitation amplitude was reduced to a value slightly below that at which the first shift had occurred.

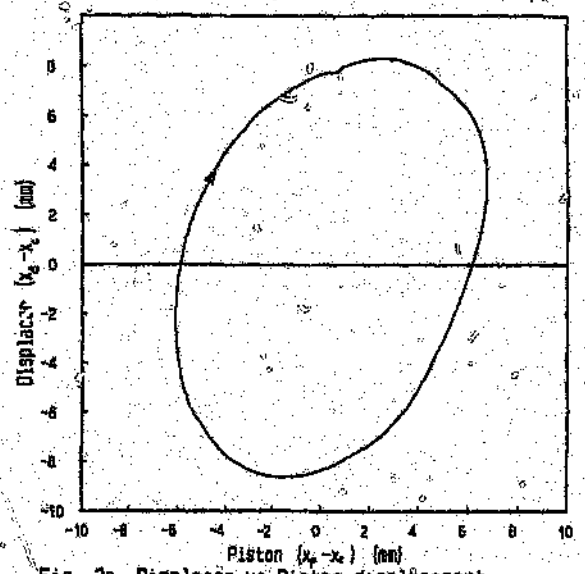

Fig. 2a Displacer vs Piston displacement

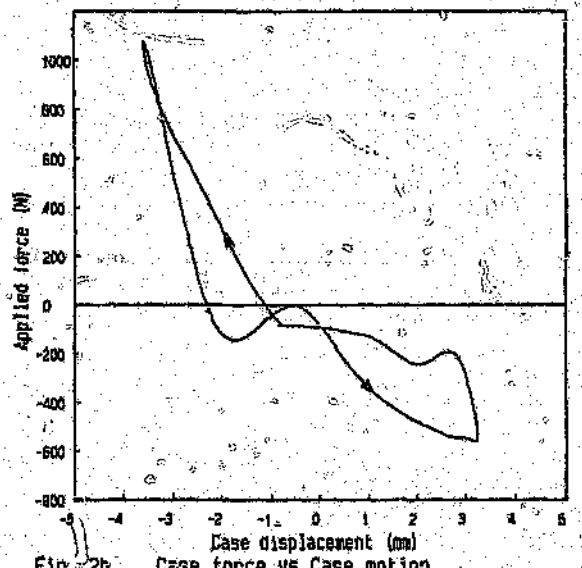

Fig. 2b Case force vs Case motion

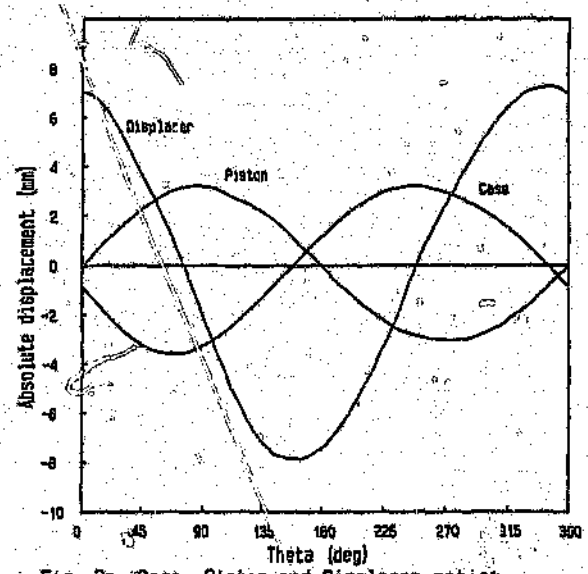

Fig. 2c Case, Piston and Displacer motion

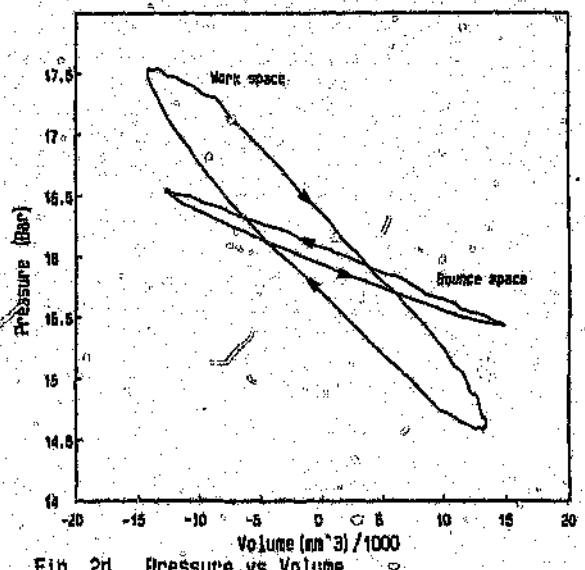

Fig. 2d Pressure vs Volume

The pV diagrams for both the bounce and working space volumes are shown in Figure 2d. The sum of these would be the total energy per cycle available both to drive the components and to deliver power. An indication of the energy flow paths through the engine can be obtained by analyzing the cyclic integrals of the terms which comprise the equation for $\oint pdV$. For the work space:

$$\oint p_w dV = \oint p_w A_p dx_c - \oint p_w (A_p - A_d) dx_p - \oint p_w A_r dx_d$$

The equations for the displacer gas spring and the bounce space are similar. Table 2 uses these cyclic integrals to show the energy flow paths for the test reported in Table 1. For this table it is assumed that $p_c = p_r = p_w$ and that the displacer gas spring behaves in an adiabatic reversible manner. Both these assumptions are incorrect, and therefore the values reported only give an indication of the flow path directions and magnitudes. The results are presented to three significant figures for the sake of comparison only. The change in energy flow paths for the

Table 1 Data Summary

Test		1	2	3
Charge	1600kPa	He	He	Nitrogen
Condition		Work out	Work in(cold)	Work in
Frequency	Hz	32.7	33.8	30.7
Work out per cycle	(J)	1.2	-1.47	-1.0
T heater	°C	624	18	616
T cooler	°C	75	18	72
Piston stroke	(mm)*	23.8	11.4	12.5
Displacer stroke	(mm)*	16.9	8.95	8.1
Displacer/piston phase	°	67	106	66
Work space				
Maximum pressure	(kPa)	1754	1698	1718
Minimum pressure	kPa	1458	1504	1493
Pressure/piston phase	°	-15.5	19.4	4
Bounce space				
Maximum pressure	(kPa)	1656	1649	1647
Minimum pressure	(kPa)	1545	1651	1653
Pressure/piston phase	°	183	194	193
Absolute Motion				
Case stroke	(mm)	6.8	6.5	7.3
Piston stroke	(mm)	8.2	6.8	5.5
Displacer stroke	(mm)	15.1	9.1	8.6
Piston/case phase	°	148	211	314

Values marked with an * refer to piston and displacer motions relative to the case motion, ie, $(x_p - x_c)$ for the piston and $(x_d - x_c)$ for the displacer.

Phase is calculated as the average of the number of degrees (where 360 degrees corresponds to a complete cycle) by which the peak of one signal precedes the peak of the reference signal and by which the trough of one signal precedes the trough of the reference signal.

Table 2 Energy flow paths

	Piston	Displacer	Case	Sum	Test
Work space	0.202	0.845	1.329	2.376	1
	-0.268	0.310	-1.385	-1.342	2
	0.268	0.364	-0.856	-0.174	3
Disp. spring	0.267	-0.267	0	0	1
	0.119	-0.119	0	0	2
	0.135	-0.135	0	0	3
Bounce space	-0.343	0	0.046	-.297	1
	0.139	0	-0.403	-.264	2
	0.079	0	-0.420	-0.341	3
Sum	0.126	0.577	1.376	2.083	1
	-0.010	0.192	-1.788	-1.607	2
	0.482	0.229	-1.226	-.516	3

engine in a non-power-producing state to that when the engine produces positive power are quite marked. It is interesting to note that the bounce space transfers energy from the case to the piston in the negative work running state, while the energy transfer is from the piston to the the case for the test in which the engine was producing positive power. Of significance in all the tests reported is the amount of energy absorbed by the bounce space. This is attributable to heat transfer effects, gas flow dissipation losses, and perhaps most importantly, leakage of piston and centring-port seals. This is a direct loss of available work. In the case of positive power output the bounce space losses are 20 percent of the output energy.

A similar, although less tractable loss must be occurring in the working space, as any leakage across the sliding seals affects both the bounce and working gas spaces. The importance of the piston and centring-port seals in reducing this loss should not be underestimated. The principal modifications to the engine over the past few months have been to improve these seals.

The energy required to drive the displacer is a significant fraction of the output work. However not all of this energy is lost as the damping between the displacer and piston transfers some of this work to the piston.

CLOSURE

This programme has not been successful in producing an efficient stand-alone free-cylinder engine – yet. A positive output power of 40 watts for a helium-charged engine of this size is disappointing, especially as similar engines have produced approximately 100 watts when charged with air. There is thus still room for improvement, although it is expected that the adverse effects of the instrumentation will keep the power output below 100 watts. Particular areas of concentration will be the tuning of the engine (by the appropriate addition or removal of mass from the components), to improve the dynamics, and the use of a new centring-port seal for the piston. This should help to reduce bounce and working space losses.

However, the test results do provide an insight into the workings of the engine. It is hoped that further tests, and more comprehensive analysis of the results will lead to a better understanding, particularly of the dynamics, of free-cylinder Stirling engines.

ACKNOWLEDGEMENTS

The significant contribution of Sunpower Inc to the programme is gratefully acknowledged. Thanks are extended to the Structural Dynamics unit of the University for the loan of the hydraulic ram and control system. Furthermore, this work is part of a wider on-going experimental and theoretical programme on Stirling engines being conducted in the School of Mechanical Engineering of the University of the Witwatersrand. This has been partially funded over the years by the Anglo American Corporation of South Africa and by the Foundation for Research Development of the Council for Scientific and Industrial Research. Both their assistance and that of the other members of the Stirling engine programme, particularly Professor C J Rallis, are gratefully acknowledged.

REFERENCES

1. Beale W T. Free Piston Stirling Engines- Some Model Tests and Simulations, SAE Paper No. 690230: 1969.

2. Beale W T. A Free Cylinder Stirling Engine Solar Powered Water Pump, International Solar Energy Society International Congress, Atlantia, Georgia: 1979.

3. Redlich R W and Berchowitz D M. Linear dynamics of free-piston Stirling engines. Proc Instn Mech Engrs Vol 199 No A3: 1985.

4. Urieli I and Berchowitz D M. Stirling Cycle engine analysis: 1984 (Adam Hilger, Bristol).

5. Berchowitz D M. Design and Optimisation of Stirling Cycle Engines. PhD Thesis. University of the Witwatersrand, Johannesburg, South Africa: 1979.

References

[1] **Banks D I**, Test results on a free-cylinder Stirling engine, *Proc. 24th IECEC*, paper no. 899052, 1989, pp 2363–2368.

[2] **Bauwnes L**, Consistency, stability, convergence of Stirling engine models, *Proc. 25th IECEC*, paper no. 90-5-352, 1990.

[3] **Beale W T**, Free piston Stirling engines– some model tests and simulations, *SAE, International Automotive Engineering Congress*, paper no. 690230, January 1969.

[4] **Beale W T, Wood J G and Chagnot B J**, Stirling engines for developing countries, *American Institute of Aeronautics and Astronautics, Inc.*, paper 809399, 1980.

[5] **Beale W T**, Stirling engines for developing countries, supplement to text printed in: *Energy for Rural Development*, National Academy of Sciences, 1980.

[6] **Beale W T**, A free cylinder Stirling engine solar powered water pump, *International Solar Energy Society International Congress*, Atlanta, Georgia, 1979.

[7] **Beale W T**, Applications of simple Stirling engines, *International Stirling Engine Conference*, paper no. ISEC 1986-11-49, 1986.

[8] **Beck P**, The development of a biogas-driven Stirling engine with generator for a decentralized power supply, *6th International Stirling Engine Conference*, Eindhoven, May 1993.

[9] **Benvenuto G, de Monte F and Farina F**, Dynamic behaviour prediction of free-piston Stirling engines, *Proc. 25th IECEC*, 1990, pp 346–351.

[10] **Benvenuto G and de Monte F**, On the self-regulation of free piston Stirling engines: Comparison of theoretical and experimental results, *Proc. 28th IECEC*, paper no. 9334, 1993, p 2.731–2.738.

[11] **Berchowitz D M, Urieli I and Rallis C J**, A numerical model for Stirling cycle machines, *Journal Eng for Power*, vol 102, no 4, Oct 1980, pp 756–761. Also published as *ASME* paper 79-GT-Isr-16, and in *Proc. Israel Joint Gas Turbine Congress*, Haifa, Israel, 1979.

[12] **Berchowitz D M**, Stirling engines in developing countries, Presented at *Conference on Small Engines and their Fuels in Developing Countries*, University of Reading, September 1984.

[13] **Berchowitz D M**, *Stirling Cycle Engine Design and Optimisation*, PhD thesis, University of the Witwatersrand, South Africa, 1986.

[14] **Burton J D and Lobo-Guerrero U**, Induced flow reciprocating pump theory: Supported by new performance data, *Transactions of the ASME*, December 1972, pp 706–714.

[15] **Carlini M and Kucharski T**, Non-linear simulation model for free piston Stirling engines, dynamic analysis, *Proc. 3rd International Stirling Engine Conference*, paper no. ISEC 86-III-63, 1986.

[16] **Chagnot K**, Personal communication, Stirling Technology Inc. Athens, Ohio, April 1988.

[17] **Cooke P**, *Research on the effects of loading and use of higher mean cycle pressures (1 to 9 bar absolute) on the performance of a free-piston Stirling engine with different displacer mechanical-springs and using nitrogen and helium as working fluids*, Final year BSc (Eng) project, University of the Witwatersrand, Johannesburg, 1990.

[18] **Cooke-Yarborough E H**, Use of an analogue circuit modelling program to study the dynamics of a thermo-mechanical generator, *Proc. 3rd International Stirling Engine Conference*, paper no. ISEC 86-VI-66, 1986.

[19] **Flavin C**, China reviving biogas reliance after several years of neglect, *Solar Energy Intelligence Report*, vol 12. Publisher: Eiserer L A, January 7, 1986, pp 4–6.

[20] **Fraenkel P L**, Development of a Stirling engine for small scale applications, *Project Bulletin* I.T. Power Ltd, United Kingdom. No date given, estimated 1988.

[21] **Fulford D J**, *Running a Biogas Programme: A Handbook*, Intermediate Technology Publications, London, 1988.

[22] **Gaegauf C and Zumsteg H**, Co-generation with a wood chips fuelled Stirling engine *Proc. 6th International Stirling Engine Conference*, Eindhoven, May 1993.

[23] **Griffin N J, Banks D I, Mavrandonis J, Shackleton C M and Shackleton S E**, Fuel use in six rural settlements in Gazankulu, *Journal of Energy in Southern Africa*, vol. 4 no. 3, August 1993, pp68–73.

[24] **Goldberg L F**, *A Computer Simulation and Experimental Development of Liquid Piston Stirling Cycle Engines*, MSc dissertation, University of the Witwatersrand, 1979.

[25] **Goldberg L F**, *A State Space and Continuum Mechanics Analysis of Stirling Cycle Machines*, PhD thesis, University of the Witwatersrand, 1987.

[26] **Greig S W**, *The testing of a free cylinder Stirling engine*, Final year BSc (Eng) project, University of the Witwatersrand, Johannesburg, 1991.

[27] **Ikai J, Kazuhiko T, Kazuyuki Y and Mitsuo K**, Free piston Stirling engine simulation, *2nd International Stirling Engine Conference*, Shanghai, May 1984.

[28] **Jawurek H H, Lane N W and Rallis C J**, Biogas/petrol dual fuelling of SI engine for rural third world use, *Biomass*, vol 13, 1987, pp 87–103.

[29] **Johansson K G**, Report on long term testing of woodgas powered engines, *Proc.: Renewable energy potential in South Africa*, University of Cape Town, September 1986.

[30] **Kaźmierczak J and Żmudzki S**, Relative analysis of free-piston Stirling engine dynamics, *Proc. 3rd International Stirling Engine Conference*, ISEC 86-VI-71, 1986.

[31] **Kinnersly R F**, An innovative low pressure, air charged Stirling engine, *Proc. 6th International Stirling engine conference*, Eindhoven, May 1993.

[32] **Kolin I**, Recent development of the flat plate Stirling engine, *Proc. 21st IECEC*, paper no. 869113, San Diego, California, August 1986, pp 501–508.

[33] **Leroux P**, *Third year laboratory report*, University of the Witwatersrand, Johannesburg, 1988.

[34] **Mathews J and Walker G**, Limitations of Kolin-type Stirling refrigerators, *6th International Stirling Engine Conference*, paper no. 93051, Eindhoven, May 1993, pp 227–232.

[35] **McLean S L**, *The Design of a Free Cylinder Stirling Engine Powered Water Pump*, Final year BSc (Eng) design project, University of the Witwatersrand, Johannesburg, 1989.

[36] **McNelis B**, Solar water pumping– the current status, *Appropriate Technology*, vol. 14, no. 1, 1987.

[37] **Mitchell L**, Series of memos to other members of the Sunpower team on the modelling of an induction pump using an electrical analogue circuit, Sunpower Inc., Athens, Ohio, 1974.

[38] **Morgan P R**, A simple low-cost water pump for shallow wells, *Appropriate Technology*, vol 8, no. 3, 1981, pp 13–16.

[39] **Muche H and Zimmermann H**, *The purification of biogas*, Friedr. Vieweg and Sohn Braunschweig/Wiesbaden, 1985.

[40] **Penswick L B and Urieli I**, Duplex Stirling Machines, *Proc. 19th IECEC*, San Francisco, California, August 1984.

[41] **Rallis C J, Kilgour B D, Taylor A B and Banks D I**, Further tests on a back-to-back free-displacer disciplined-piston Stirling engine, *Proc. 23rd IECEC*, paper no. 889437, 1988, pp 203–208.

[42] **Rallis C J, Kilgour D, Banks D I, Jawurek H H, Taylor A B**, Performance comparisons of a back-to-back free-displacer disciplined-piston Stirling engine with air and helium as working fluids, *Proc. 24th IECEC*, 1989, pp 2379–2384.

[43] **Reader G T and Hooper C**, *Stirling Engines*, E and F N Spon, London/New York, 1983.

[44] **Redlich R W and Berchowitz D M**, Linear dynamics of free-piston Stirling engines, *Proc. Institution of Mechanical Engineers*, vol 199 no. A3, 1985, pp 203–212.

[45] **Rennie L E**, *Research of Back-to-back Stirling Engine*, Final year BSc (Eng) project, University of the Witwatersrand, Johannesburg, 1989, pp 67–72.

[46] **Ross B (Ed.)**, *Stirling Machine World*, September 1993, p 9.

[47] **Sasse L, Kellner C and Kimaro A**, *Improved Biogas Unit for Developing Countries*, Friedr. Vieweg and Sohn, Braunschweig, 1991.

[48] **Sasse L**, *Biogas Plants: Design and Details of Simple Biogas Plants*, Friedr. Vieweg and Sohn, Braunschweig/Wiesbaden, 1988.

[49] **Senft J R**, A mathematical model for Ringbom engine operation *Journal of Engineering for Gas Turbines and Power*, vol. 107, pp 590–595, 1985.

[50] **Stirling Technology Inc.**, Introductory pamphlet on the ST-5 engine, Date not given, estimated: 1987.

[51] **Sunpower Inc.**, Information arising from personal observation and communication with staff at Sunpower Inc., Athens, Ohio, May 1988.

[52] **Talbert** *et al*, The development of a 32 kW solar irrigation pump, *Proc. International Solar Energy Society Congress*, New Delhi, India, 1978 *Cited in [6].*

[53] **Tse F S, Morse I E, Hinkle R T**, *Mechanical Vibrations: Theory and applications*, 2nd ed. Allyn and Bacon Inc., Boston, 1978.

[54] **Thom C and Banks D I**, Biogas as rural domestic energy source: A pilot study, *Proc. Third Southern Africa Anaerobic Digestion Symposium*, Pietermaritzburg, pp 285–293, July 1992.

[55] **Thom C**, *A Socio-technical Feasibility Study to Develop Biogas as an Energy Source for Rural South Africa*, Department of Mineral and Energy Affairs, Pretoria, 1994.

[56] **Tonkin D**, *Research on the effects of pressure, temperature and different working fluids on the performance of FPSE*, Final year BSc (Eng) research project, University of the Witwatersrand, Johannesburg, 1989.

[57] **Urieli I and Berchowitz D M**, *Stirling Cycle Engine Analysis*, Adam Hilger, Bristol, 1984.

[58] **Urieli I and Chen M F E**, The feasibility of a Ringbom Stirling engine combined with a solar pond, *Proc. 23rd IECEC*, paper no. 889118, 1988, pp 55–58.

[59] **Walker G**, *Stirling Engines*, Oxford Science Publications, 1980.

[60] **Walker G, Reader G, Fauvel O R and Bingham E R**, *The Stirling Alternative*, Draft, to be published by Gordon and Breach Inc., Philadelphia, estimated publication date 1994.

[61] **Walker G and Senft J R**, *Free Piston Stirling Engines*, Lecture Notes in Engineering, Springer-Verlag, Berlin, 1985.

[62] **West C D**, *Liquid Piston Stirling Engines*, Van Nostrand Reinhold Company Inc., 1983.

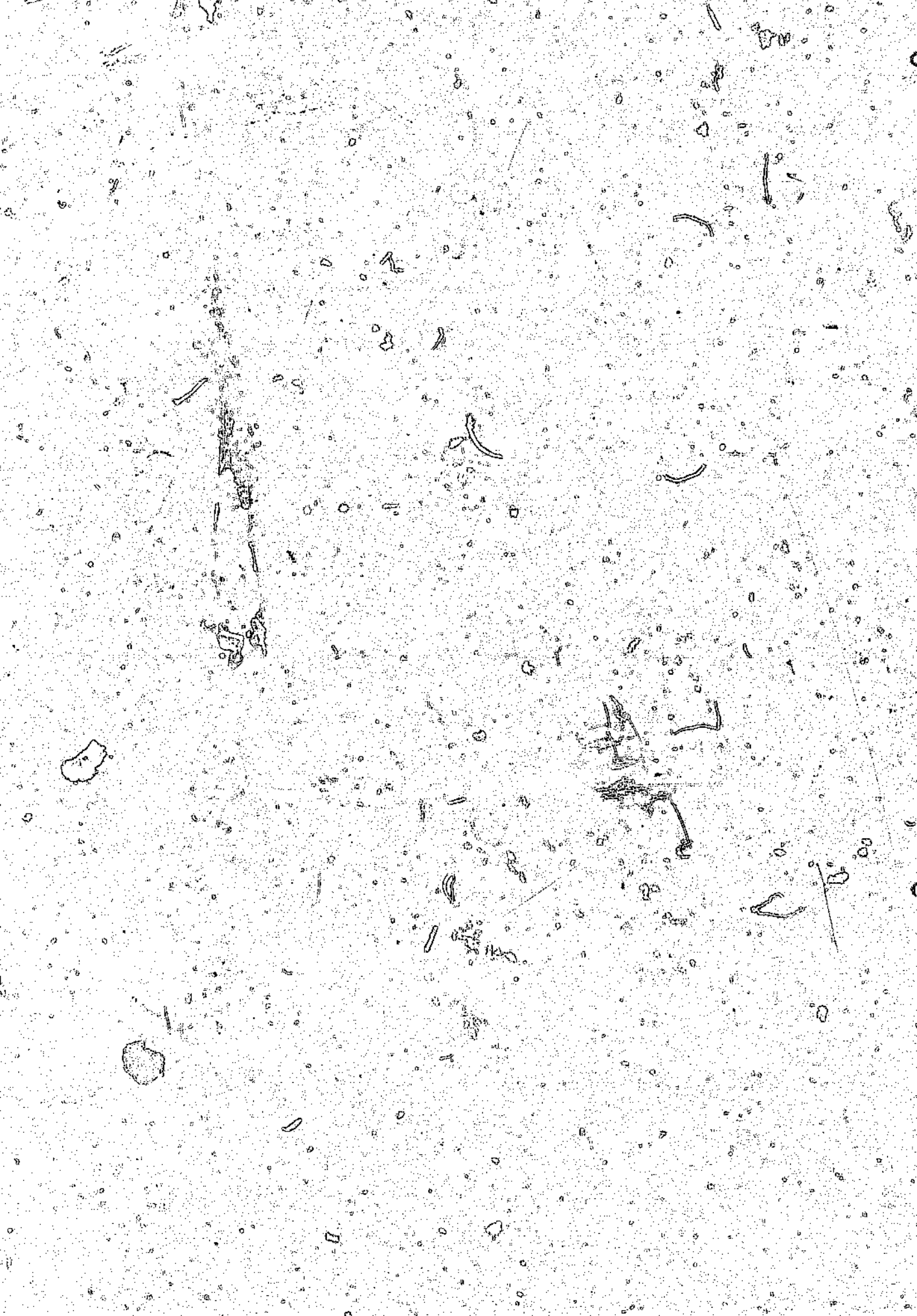

Author: Banks Douglas Ian.
Name of thesis: A numerical and experimental investigation of free-cylinder Stirling engine operation.

PUBLISHER:
University of the Witwatersrand, Johannesburg
©2015

LEGALNOTICES:

Copyright Notice: All materials on the University of the Witwatersrand, Johannesburg Library website are protected by South African copyright law and may not be distributed, transmitted, displayed or otherwise published in any format, without the prior written permission of the copyright owner.

Disclaimer and Terms of Use: Provided that you maintain all copyright and other notices contained therein, you may download material (one machine readable copy and one print copy per page)for your personal and/or educational non-commercial use only.

The University of the Witwatersrand, Johannesburg, is not responsible for any errors or omissions and excludes any and all liability for any errors in or omissions from the information on the Library website.